Structural and residual strength analysis of metal-to-metal adhesively bonded joints.

PRATHURU, A.

2019

STRUCTURAL AND RESIDUAL STRENGTH ANALYSIS OF METAL-TO-METAL ADHESIVELY BONDED JOINTS

A thesis submitted in partial fulfilment of the
requirements of the
Robert Gordon University
for the degree of Doctor of Philosophy

January 2019

Abstract

The aim of this study is to propose a new simulation/experimental methodology to assess the residual strength of defective adhesive bonds. This incorporates detect defection in adhesive bonds and quantification of the effect of these defects on the adhesive bond failure. Finite Element Analysis (FEA) has been used in simulating the failure behaviour of adhesive bonds. Acoustic Emission (AE) has been used to monitor the adhesive bond failure experimentally.

AE based pencil lead break (PLB) tests have been used to detect the defects in adhesive joints manufactured with two different adhesive types (brittle, ductile) and different defect area distributions (0%, 25% and 40%) along one of the interfaces. The chosen type of defects was kissing bonds as these are the most difficult to detect. The signals recorded were processed to establish the AE parameters that can be used to distinguish between the different defective adhesive bonds. 4-point flexure and plane strain (cylindrical wedge) indentation have been chosen as the mechanical testing methodologies to assess the failure of defective adhesive bonds. Cohesive Zone Model (CZM) was used in conjunction with FEA of indentation testing to study the effect of adhesive layer thickness, adhesive modulus, interfacial strength and toughness on the adhesive bond failure. Flexure, indentation and single lap joint tension experiments have been carried out in selected specimens with AE monitoring to record the crack propagation events.

Finite element analysis of the 4-point flexure of adhesive bonds shows that the failure initiation is at the loading points. The failure propagation is because of the strain mismatch between the adhesive and adherends. FEA analysis of indentation testing shows that the failure initiation is under mode-II adjacent to the indentation compressive zone. Increase in the interfacial strength delays the crack initiation under indentation loading and increase in interfacial toughness reduces the total crack length for a given indentation depth. The AE monitoring of experiments shows that the AE event energy as well as number of crack events can be used to assess the residual strength of defective adhesive bonds. The classification of the AE events into mode-I and mode-II events allowed the verification of the crack propagation nature observed in the simulations. Finally, a correlation is proposed between cumulative AE energy and CZM energy release rate to estimate the adhesive bond interfacial strength.

Dedication

To my parents

Uma Devi & Krishna Rao Prathuru

Acknowledgements

I would like to express my deep gratitude to my supervisors Dr. Nadimul Haque Faisal, Dr. Sha Jihan and Prof. John (Iain) A Steel for their constant support and supervision throughout the course of my study, their guidance has been invaluable. I would like to thank the School of Engineering at Robert Gordon University, Aberdeen for providing the scholarship to carry out my studies.

I owe my sincere thanks to Mr. Alan McPherson, Mr. David Smith and Mr. Benjamin Bird for providing valuable support in test rig fabrication and development of instrumentation, Dr. Rosslyn Shanks, Mrs. Kirsty Stevenson and Mrs. Petrena Morrison for their valuable support during the course of my study.

I'm also very thankful to Dr. James Njuguna and Dr. Radhakrishna Prabhu for the interesting discussions which were a source of insight into academia and research.

Finally, I thank my colleagues and friends at the School of Engineering for their moral support and social interactions which made my time at the university enjoyable.

Notations

ADCB	:	Asymmetric double cantilever beam
AE	:	Acoustic emission
CBBM	:	Compliance based beam method
CZM	:	Cohesive zone model
DCB	:	Double cantilever beam
DIC	:	Digital image correlation
ECT	:	Edge crack torsion
EDS	:	Energy dispersive X-ray spectroscopy
EIS	:	Electrochemical impedance spectroscopy
ENF	:	End notch flexure
FE	:	Finite element
FFT	:	Fast Fourier transform
GFRP	:	Glass fibre reinforced plastic
LEFM	:	Linear elastic fracture mechanics
NDT	:	Non-destructive testing
PLB	:	Pencil lead break
PSD	:	Power spectral density
RH	:	Relative humidity
SLJ	:	Single lap joint
SLS	:	Single lap shear
SSY	:	Small scale yielding
UV	:	Ultra-violet
V	:	Voltage
WT	:	Wavelet transform

XPS	:	X-ray photo spectroscopy
G_c	:	Critical strain energy release rate
Γ_o	:	Interface toughness in CZM
σ_c^m	:	Mixed-mode critical traction
Δ_o	:	Reference length used in indentation simulations
K_n	:	Normal stiffness used in the CZM
K_t	:	Tangential stiffness used in the CZM
σ	:	Normal traction in the CZM
τ	:	Tangential traction in the CZM
u_n	:	Normal displacement in the CZM
u_t	:	Tangential displacement in the CZM
d_m	:	Damage parameter used in the CZM
u_{ni}	:	Displacement at damage initiation in CZM
u_n^c	:	Displacement at debonding completion in CZM
σ_{max}	:	Maximum normal traction in CZM
τ_{max}	:	Maximum tangential traction in CZM
G_n	:	Opening mode energy release rate in CZM
G_t	:	Tangential mode energy release rate in CZM
σ_{adh}^y	:	Yield strength of adhesive
E_{adh}	:	Elastic modulus of adhesive
ν_{adh}	:	Poisson's ratio of the adhesive
h_{adh}	:	Thickness of the adhesive
E_a	:	Elastic modulus of adherends
σ_a^y	:	Yield strength of the adherends
ν_a	:	Poisson's ratio of the adherends
R	:	Radius of the indenter

h	:	Indentation depth
P	:	Indentation load
K_I	:	Mode-I stress intensity factor
K_{II}	:	Mode-I stress intensity factor
β	:	Dundur's parameter
θ	:	Mode-mix ratio

Table of Contents

List of publications from this study

Journals (published)

1. **Anil K Prathuru**, N. H. Faisal**,** Sha Jihan, John A Steel, James Njuguna, Stress analysis at the interface of metal-to-metal adhesively bonded composite subjected to 4-point bending: Finite element method, **The Journal of Adhesion**, 93(11), 2017, p. 855-878 (doi: http://www.tandfonline.com/doi/full/10.1080/00218464.2016.1172309)
2. Mohamad Ghazi Droubi, Alan Stuart, John Mowat, Craig Noble, **Anil K Prathuru**, Nadimul Haque Faisal**,** Acoustic emission method to study fracture (Mode-I, II) and residual strength characteristics in composite-to-metal and metal-to-metal adhesively bonded joints, **The Journal of Adhesion**, 2017 (doi: http://dx.doi.org/10.1080/00218464.2017.1278696)
3. M. G. Droubi, J. Mcafee, R. C. Horne, S. Walker, C. Klaassen, A. Crawford, **Anil K Prathuru**, N. H. Faisal**,** Mixed-mode fracture characteristics of metal-to-metal adhesively bonded joints: experimental and simulation methods, **Structural Integrity Procedia**, 5C (2017) pp. 40-47 (doi: https://doi.org/10.1016/j.prostr.2017.07.059)

Conference (published, *presenting author)

4. **Anil K Prathuru***, N. H. Faisal**,** Sha Jihan, John A Steel, Indentation method to evaluate metal-to-metal adhesive bond residual strength, *Proceedings of the 24th Conference on Computational Mechanics, ACME, 31 March – 1 April 2016, Cardiff, UK* [oral presentation and proceedings]
5. **Anil K Prathuru**, N. H. Faisal***,** Sha Jihan, John A Steel, Residual strength characterisation of adhesively bonded joints in wind turbine application, at China-UK workshop on "*Multidisciplinary Issues of Wind Turbines in Cold Environments" Mianyang, China, 14 – 18 August 2016, China Aerodynamics Research and Development Centre (CARDC)* [oral presentation]
6. Ghazi Droubi, N. H. Faisal**,** John Mowat, Craig Noble*, Alan Stuart, **Anil K Prathuru**, Instrumented mechanical testing of composite-to-metal and metal-to-metal adhesive bond strengths, *7th International Conference on Engineering Failure Analysis (ICEFA VII), 3 – 6 July 2016, Leipzig, Germany* [oral presentation]

Journals (under preparation)

7. **Anil K Prathuru**, N. H. Faisal, Sha Jihan, John A Steel, Defect detection in metal-to-metal adhesively bonded joints acoustic emission during pencil-break test (manuscript in preparation for *Journal of Nondestructive Evaluation*)

8. **Anil K Prathuru**, N. H. Faisal, Sha Jihan, John A Steel, Indentation contact mechanics to study interfacial fracture and residual strength in metal-to-metal adhesively bonded joints (manuscript in preparation for *Engineering Fracture Mechanics*)
9. **Anil K Prathuru**, N. H. Faisal, Sha Jihan, John A Steel, Acoustic emission to characterise fracture behaviour during indentation of metal-to-metal adhesively bonded joints (manuscript in preparation for *International Journal of Solids and Structures*)

Chapter-1

1. Introduction

1.1. Research Context

The strength and the failure of adhesive bonds have been extensively studied and several analytical, empirical and numerical models have been formulated to explain the dependence of the said properties on various factors. One of the most important factors difficult to control is the interface quality. Though it can be ensured that the best substrate surface preparation practices are implemented at the time of bonding, the exposure of the bonds to different environmental conditions deteriorates the interfacial strength and the toughness of the bond. The quantification of the relation between the interfacial parameters and the overall strength of the bond is essential to understand the failure mechanics of an adhesive bond of any geometry. Several methodologies have been established to measure the mode dependent fracture properties of adhesive bonds [1]. There exists very limited research on the residual strength of adhesive bonds. A few attempts have been made to quantify the effect of interface conditions on the failure and strength of adhesively-bonded joints [2-4].

Several conventional test methodologies have been used to test the fracture properties of adhesive joints [5-10]. However, these require specific specimen preparation techniques and geometries to keep the data reduction and analysis simple. Similarly, several studies have been conducted to understand the strength reduction caused by the presence of defects. There exists no single methodology to quantify the residual strength of in-service adhesive bonds with weakened interfaces.

The effect of presence of defects, even though investigated, has been confined to defects within specific geometries like single lap joint and confined to specific locations of the adhesively bonded joints. Also, many of these studies deal with defects such as voids within the adhesive layer and in some cases, disbonds along the interface. However, previous studies have indicated that the possibility of void formation within the cured-adhesive layer is very low unless air bubbles are formed due to a faulty fabrication procedure. The interface on the other hand is highly susceptible to moisture ingestion which starts along the bond corners and permeates the entire interface thus significantly weakening the bond [2,16].

Prior to evaluating the strength of bonded joints with defects by mechanical testing, it is prudent to estimate the size, nature and distribution of the defects present. The science of non-destructive testing (NDT) had extensively been made use of for this purpose [17-23]. For example, Xu *et al* [24] used acousto-optical interferometry to detect disbonds between a GFRP

plate and a concrete slab adhesively bonded together. This technique uses an external sound source to excite resonant frequency vibration in the composite plate which acts as a thin circular plate rigidly bonded around the circumference of a circular defect. By varying the defect areas and calculating the corresponding resonant frequencies, the authors have shown that the size as well as the location of the defect can be accurately calculated.

Heller *et al* [25] used a Nd-YAG laser based source generation and detection setup which uses a high intensity laser to trigger various wave propagation modes in adhesive bonded specimens. Spatial measurements were made at various locations of the specimen and two-dimensional fast Fourier transforms (2D-FFTs) and spatial Fourier transforms were calculated to create frequency vs wave number plots for both pristine and aged specimens. They detected significant decay in various wave modes in the aged condition and reported that the bond with the adhesive does not change the behaviour of the plates as far as the frequency vs wave number plots are concerned.

Acoustic emission (AE) is a passive technique which listens to failure within any structure by capturing the elastic wave propagation induced by failure energy release. It has been used extensively in composite failure monitoring and structural health monitoring. Several data analysis techniques such as pattern recognition algorithms, signal classifiers etc. have been developed over the last few decades for AE data analysis. Even though a few studies have made use of AE for defect detection and fracture characterisation of adhesive bonds, it was always in combination with another NDT technique such as ultrasonic scanning or guided lamb wave scanning. In such a case, AE transducer acts as the signal receiver with the other technique emitting the signal. The potential of AE as a standalone method for defect detection with a simpler signal source such as Hsu-Nielsen pencil lead break [26-27] has not been completely explored before.

Senthil *et al* [28] used AE as a monitoring technique in fracture toughness characterisation of adhesive bonded double-cantilever beam (DCB), four-point end notch flexure (4-ENF) and edge crack torsion (ECT) tests. They concluded that a good correlation exists between the load-displacement plots and AE activity. However, no correlation was drawn between the AE energy release rate and experimental energy release rate.

Indentation contact mechanics has been used extensively used in material testing over the past few decades and the science related to indentation of multi-layer materials to evaluate the interfacial quality of coatings, claddings etc. has been developed. Instrumented indentation techniques such as micro- and nano-indentation have been used to assess the interfacial strength and toughness of thin-films, composites [29-38]. In addition, it has been used to evaluate the fracture toughness of brittle coatings by measuring the total indentation induced crack length.

Interfacial indentation has been used to evaluate the adhesion strength of coatings on substrates. Thus, indentation can be considered a prime candidate in material adhesion testing. However, the use of indentation in the field of adhesive bonding is limited at best. Even though a few studies have been conducted [31,39], the analysis of indentation load-displacement data has not been made use of to the full extent. The use of wedge indentation to induce delamination cracks along the interface in thin films can be seen in some studies [38,40]. The effect of the interfacial parameters on the crack parameters such as area and stress state at the crack tip has been investigated by these authors. Similarly, the interfacial energy release rate during indentation has been explored by other investigators where the cohesive zone model (CZM) has been made use of to implement the interfacial de-adhesion.

To summarise, there isn't a comprehensive method to assess the residual strength of defective adhesive bonds. Hence, the current study is on the development of such a tool using numerical/experimental test methodologies to detect interfacial defects and understand the effect of these on the adhesive bond residual strength. The use of AE based instrumented 4-point flexure and indentation as tools to evaluate the interfacial quality of adhesive bonded joints (aluminium metal-to-metal) is explored. This includes the development of numerical models using the finite element software ANSYS Mechanical APDL. The effect of the interfacial parameters on the adhesive joint failure is studied.

1.2. Research objectives

The primary aim of this study thus emerges out of the necessity to develop a simple methodology to detect the presence of defects and characterise the effect of these defects on the residual strength of adhesive bonds. The chosen type of defects is kissing bonds where the adhesive and the adherend are in surface contact, but no-load transfer occurs across them. This type of defects is most commonly caused by interface moisture ingestion leading to interface de-bonding and are of primary interest in this study. AE is chosen as a suitable technique for defect detection and fracture characterisation. Two different mechanical test methodologies namely 4-point flexure and plane-strain indentation were studied, and their feasibility explored.

The objectives of this study are outlined below:

1. Develop an AE based non-destructive methodology using Hsu-Nielsen pencil lead break (PLB) test to detect the presence of defects (kissing bonds) along the interfaces of adhesively bonded joints and find a correlation between the AE parameters and area fractions.
2. Develop and analyse a finite element (FE) model of adhesively bonded joints with different interface conditions and simulate 4-point flexure and plane-strain spherical

indentation test methodologies to evaluate the residual strength of adhesive bonds with weakened interfaces.

3. Develop and analyse an instrumented mechanical test methodology (4-point flexure, plane-strain indentation), of adhesively bonded joints, in combination with AE sensor based monitoring, load and displacement monitoring to validate the FE model findings.
4. Develop a correlation between the numerical (FE) and experimental AE data to quantify the residual strength of adhesively bonded joints.

The first step estimates the defect area percentage along the interface through a simple experimental procedure using AE and PLB tests. The instrumented experimentation procedure estimates the AE energy release rate during the interfacial failure of the adhesive bond. The FE based simulation procedure estimates the energy associated with the crack propagation including the plastic dissipation thus establishing the residual strength of the adhesive bond.

1.3. Research contribution

This work is expected to contribute to the field of adhesive bond structural and residual strength assessment. A defect detection method based on simple pencil lead breaks and AE that can detect a distribution of defects along the adhesive bond line has not been reported in literature. In addition, the capability of this technique to assess the interfacial condition will also be presented. Also, the use of AE in adhesive bond testing is quite limited and its potential has not been fully explored. This study aims to fill in that gap by exploiting various AE parameters such as energy, event duration, number of hits and wavelet transforms (WTs) to quantify the adhesive joint failure behaviour and the interfacial bond quality. A simple method to simulate deteriorated adhesive joint interface is proposed in this study. An unconventional mechanical testing method in detail is being put forth for the first time, that can assess the residual strength of adhesive bonds in combination with AE.

1.4. Thesis outline

Chapter – 1: This chapter gives an overview of the state of the art of adhesively bonded joints. In specific, it explains the current methodologies of residual strength of adhesively bonded joints and outlines the research objectives.

Chapter – 2: This chapter presents the literature review on adhesive bond failure. It explores the mechanics involved in adhesive bond crack propagation, adhesive bond defect detection, and various experimental and FE methods of assessing adhesive bond strength.

Chapter – 3: This chapter outlines the proposed methodology for adhesive bond defect detection using PLB tests and AE sensor. The specimen configurations used, and the test methodologies are explained. Correlations are drawn between various adhesive bond interfacial defect distributions and AE parameters.

Chapter – 4: This chapter outlines the FE methodologies of 4-point flexure and plane strain indentation testing of defective adhesive bonds. The model formulations are explained, and results are presented. The effect of various adhesive bond parameters on the bond failure is explored.

Chapter – 5: This chapter explains the experimental methodologies followed to test the failure of defective adhesive bonds. The correlation between adhesive bond quality and AE parameters is shown and justifications for using different AE data processing techniques are presented.

Chapter – 6: This chapter presents the noteworthy results and compares them with literature reported findings. The use of AE as an adhesive bond residual strength assessment technique is justified. Correlation are made between the FE model findings and the AE parameters to characterise the interfacial quality of adhesive bonds.

Chapter – 7: This chapter presents the significant conclusions drawn from various components of this study and makes recommendations for future studies based on FE and AE methods for assessing adhesive bond interfacial quality.

Chapter-2

2. Literature review

The aim of the present literature review is not to consolidate the entire research, but to pick a handful of articles that are either closely related to the research or which, if studied might lead to a conclusion that might help in further justifying the necessity and validity of the research.

Beginning from the analytical solutions for the shear stress distributions in a lap joint by Hart-Smith [1] and Goland and Reissner [41], adhesive bond research has come a long way and several geometries such as single lap joints, butt joints, strap joints, double strap joints etc have been successfully analysed. Either closed form solutions or numerical solutions have been proposed by these researchers. The entire research in the field of adhesive bonding constitutes thousands of research articles. Due to interdisciplinary nature of the research, this chapter is divided into various sections such as fracture of adhesive bonds, factors affecting failure of adhesive joints and various modes of failure, defects in adhesive joints, effects of environment and defects on bond strength, defect detection, application of AE in adhesive bond characterisation, various modelling of adhesive joints, failure criteria, flexural strength and indentation testing.

2.1. Adhesive bond fracture

The strength of an adhesive joint depends on several factors namely the elastic properties of the adherends and the adhesive, geometry of the joint (lap, scarf, butt etc), surface preparation, loading conditions, dimensions of the joint, uniformity of the adhesive layer thickness, thickness of the adhesive layer, presence of flaws, voids, cracks etc.

All the above have been individually investigated by several studies [42-47]. A typical adhesive joint exhibits different mode of failure (the word ‘mode’ used in this context is not the same as the fracture mode (opening and shear) identified from mode testing). The failure modes of adhesive bonds can broadly be classified into four categories: 1. cohesive failure, failure within the adhesive, 2. adhesive failure, failure along the interface between the adhesive and the adherends, 3. mixed failure, combination of cohesive and adhesive modes of failure and 4. oscillatory failure, crack oscillating between both the interfaces. In addition to these, there are three conventional modes of crack propagation namely opening mode (mode-I), shearing mode (mode-II) and tearing mode (mode-III). Cohesive failure is the most desirable mode as this increases the toughness of the bond [48-51]. Similarly shearing mode (mode-II) is the most desirable mode of crack propagation as the experimentally measured fracture toughness is the

highest in this mode for various bond geometries [52-54]. The fracture of an adhesive bond is characterised by the critical strain energy release rate *Gc* [51,55]. This is a function of the mode mix of loading. The material fracture resistance curve is usually characterised by two critical energy release rates; the crack initiation value and the steady state value. The latter value is higher than the former. The reason being the development of a plastic deformation zone ahead of the crack tip which increases in size with increasing crack length and then reaches a steady state value.

The design of the geometry of the adhesive bonds is done to promote cohesive crack propagation [57]. However, the failure mode of the adhesive depends not only on its inherent properties, but also on the type of loading. Exposure of the bond to certain environmental conditions leads to the deterioration of the bond quality consequently leading to an adhesive failure. The quantification of this strength reduction is a necessary part of the adhesive bond reliability prediction. Jhin *et al* [58] conducted quasi-static, fatigue and creep fracture testing of toughened epoxy adhesive bonds under different environmental conditions to study the transition from cohesive to adhesive failure with a change in the test methodology. They concluded that the higher mode mix leads to interfacial failure. Failure is preceded by the shift of the cohesive crack tip within the adhesive towards the higher strained adherend where the principal stresses are high. The near crack tip fields induce interfacial failure. They reasoned that the interfacial failure plays a key role in joint performance under near threshold fatigue loading. They reported that specimens that exhibited cohesive failure under quasi-static loading and creep are more likely to exhibit interfacial failure under mixed-mode fatigue loading. Furthermore, the presence of moisture at the crack tip when it is near an interface is likely to induce interfacial failure because of a reduction in the plastic zone size near the crack tip.

Ameli *et al* [59] studied the crack propagation in mode-I and mixed mode testing of DCB specimens. They tested both undegraded and degraded specimens. The degraded specimens were prepared through environmental exposure at different temperatures and humidity levels. The resistance curve (R-curve) of the adhesive systems displayed a bilinear behaviour. Under mixed-mode loading, the crack displays oscillatory behaviour between the two interfaces. High stress zones are formed near the upper and lower interfaces because of the constraint exerted by the adherends on the adhesive. When the crack is near the upper interface, high von-Mises stress zone is formed near the lower interface deviating the crack downwards and vice-versa leading to crack oscillation. In the case of degraded specimens however, no crack oscillation was found, and the crack faces were completely flat. This is because of a reduction in the toughness caused by the ingestion of moisture into the adhesive and a transition from ductile to brittle behaviour. In these specimens, the crack propagates in such a way as to maximise the mode-I energy dissipation. This implies a drastic reduction of the toughness of the adhesive from ductile to brittle behaviour.

The T-stress, defined as the compressive stress acting on the plastic zone surrounding the crack tip in an adhesive layer, is found to have a major effect on the crack propagation behaviour. Fleck *et al* [48] studied the crack path selection in a brittle adhesive under remote mixed mode loading. They investigated the effect of local T-stress and the residual stress induced by curing on the crack path stability. For a case with mode-I remote loading and an applied T-stress acting on the crack tip, the postulated that four conditions are possible as shown in **Fig 2.1**.

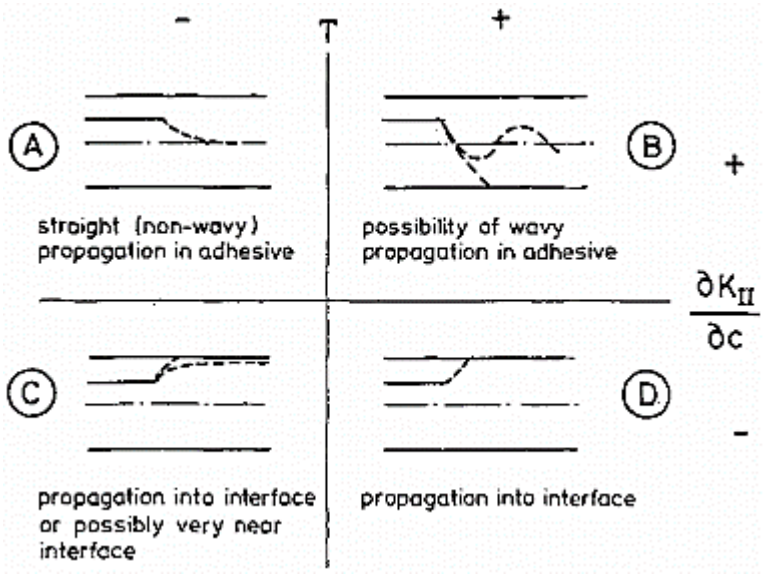

Figure 2.1. Crack path selection in brittle adhesive, X-axis represents the variation of KII through adhesive thickness, Y-axis represents the T-stress [56].

The X-axis in this figure is the variation of the mode-II stress intensity factor with respect to the crack tip height from the lower interface and the Y-axis is the T-stress applied. For a stable crack propagation along the centreline of the adhesive, 1. the adhesive should be highly compliant compared to the adherends, 2. The mode-II stress intensity factor should have a positive variation across the thickness from bottom to top and 3. The net T-stress should be negative. Provided all these conditions are satisfied, if the crack tip is located away from the centreline, it kinks towards the centreline to satisfy the condition $K_{II}=0$ locally. The local T-stress is a function of the material property mismatch, the residual stress and the remotely applied T-stress. By understanding the local variations of the stress intensity factors and the local T-stress, the authors successfully predicted the crack propagation paths in several cases. In the case of aluminium-epoxy joints under remote mode-I loading, they predicted that the crack will run along the centreline of the adhesive.

Chai [57], tried to explain the oscillatory nature of the cohesive crack. He hypothesised that the crack stability is directly related to its length. Hence, after shifting towards one of the interfaces, the crack behaves as if it's a short local crack and hence stably propagates for some

distance which is a multiple of the adhesive layer thickness, before becoming unstable again and shifting towards the other interface. However, this behaviour is possible only if the interface is strong enough. In the case of a weak interface, it is possible that the crack, once reaching one of the interfaces, propagates rapidly along the interface thus leading to the collapse of the joint. Thus, the interface condition is important to maintain the toughness of the adhesive bond.

Chen and Dillard [60] investigated the effect of adherend thickness and T-stress on the crack path selection in adhesive bonded aluminium DCB specimens by developing an analytical solution for the T-stress acting on a crack plane. Experimentally, they varied the T-stress levels in the bonds by stretching the specimens until the adherends underwent various levels of plastic deformation to induce residual elastic stresses in the adhesive layer. They concluded that the negative T-stress supports a stable crack path through the adhesive, whereas a positive T-stress leads to an unstable crack path. Furthermore, they found that as the adherend thickness decreased, the T-stress increased, promoting unstable crack path. However, irrespective of the crack path, the fracture toughness remained the same across joints with different adherend thicknesses and T-stress values. The effect of the T-stress is shown as a difference in the crack paths in **Fig 2.2**. They demonstrated the effect of T-stress by experimentally capturing the oscillating crack path where the crack deviates towards an interface, kinks abruptly parallel to the interface and then propagates roughly 2-3 times the adhesive layer thickness and then deviates towards the other interface and repeats this behaviour at regular distance intervals as shown in **Fig 2.3**.

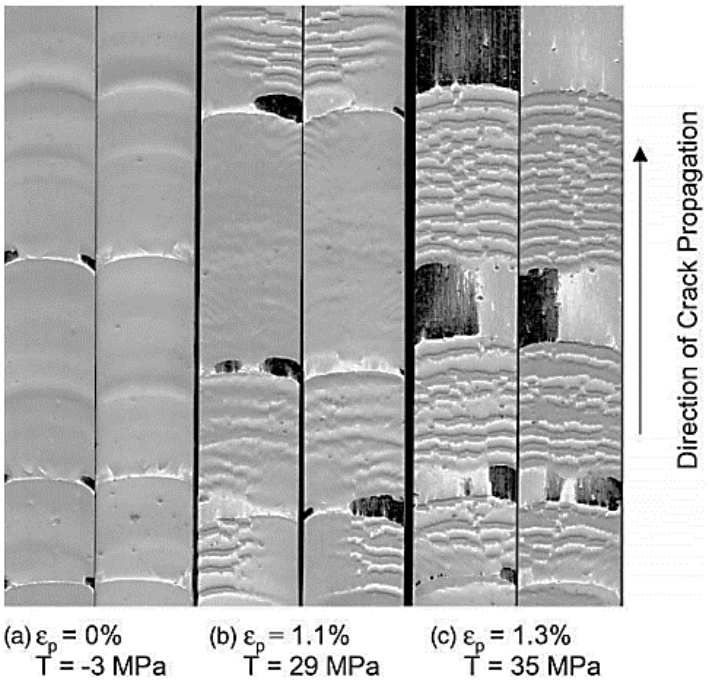

Figure 2.2. The effect of T-stress (shown as 'T') on the crack path in epoxy bonded aluminium DCB specimens [60].

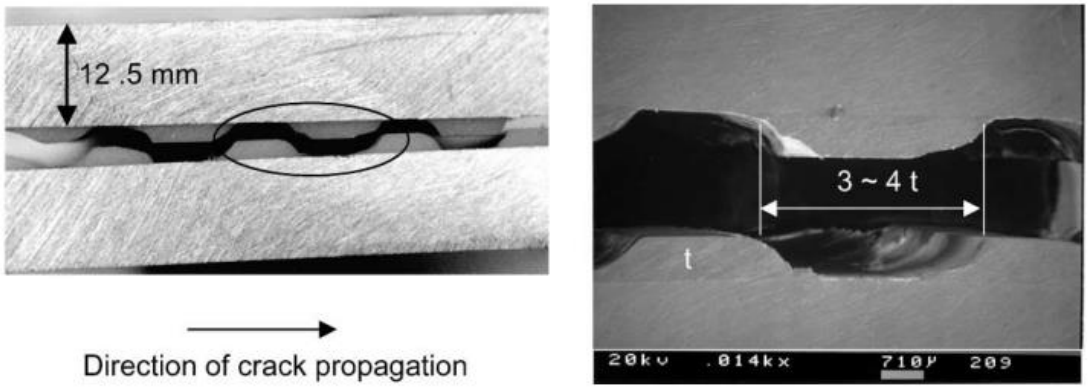

Figure 2.3. Crack path in the adhesive layer of an aluminium-epoxy DCB specimen at aT-stress of 35MPa [60].

2.2.Factors affecting failure of an adhesive joint

As mentioned in **section 2.1**, the failure of an adhesive bond can be of the cohesive type, adhesive type or mixed type. Several factors determine this behaviour. This section considers the effect of the geometry, adhesive properties such as the modulus, thickness and the adherend properties.

Pardoen *et al* [50] studied the effect of adhesive thickness on the crack growth resistance in wedge peel test of adhesive bonds. A parametric study was conducted to understand the effect of intrinsic and extrinsic constraint effects on the toughness of adhesive bonds. An increase in the toughness was reported with increasing adhesive layer thickness till a steady state value was reached. They attributed this to an increase in the plastic zone size ahead of the crack tip with increasing adhesive thickness. At lower adhesive thicknesses, the plastic zone extends through the adhesive layer and interacts with the adherends. The extent of this plastic zone is constrained by the adherends because of their higher stiffness. As the thickness increases, the size of the plastic zone increases and then reaches a stable value which does not increase with further increase in thickness. However, the increase in toughness with increase in adhesive thickness is dependent on the stiffness of the adherend and its own elastic-plastic behaviour. They reported that the increase in toughness is higher at lower adherend thickness and higher adhesive ductility in a wedge peel test.

Tvergaard and Hutchinson [51] arrived at a very similar conclusion. They investigated mode-I crack propagation in an elastic-plastic adhesive layer bound by semi-infinite elastic adherends remotely loaded in mode-I. They observed an increase in the normalized steady state

fracture toughness with increasing adhesive layer thickness at various levels of interface strength and adhesive residual stress (**Fig 2.4).** This trend continued till a critical value of thickness beyond which no further increase in the toughness was seen. This phenomenon is directly related to the constraint of the adhesive because of the stiffer adherends. At lower adhesive thicknesses, the plastic zone ahead of the crack tip in the adhesive is highly constrained by the adherends across the interface. At higher thicknesses, this constraint is reduced, and the plastic zone evolves to its complete size thus reaching a maximum value. The toughness is dependent on the plastic zone ahead of the stress singularity and is assumed to be a function of the joint geometrical parameters and the modulus of the adhesive [54]. Furthermore, the critical (failure) load depends on the interface quality and the geometry of the adhesive layer. The presence of fillets and round ups is known to decrease the stress singularity at the interface corner to a significant level [61]. Thus, it can be concluded that the adhesive layer thickness has a significant effect on the fracture toughness and consequently the load bearing capability of any adhesive bond.

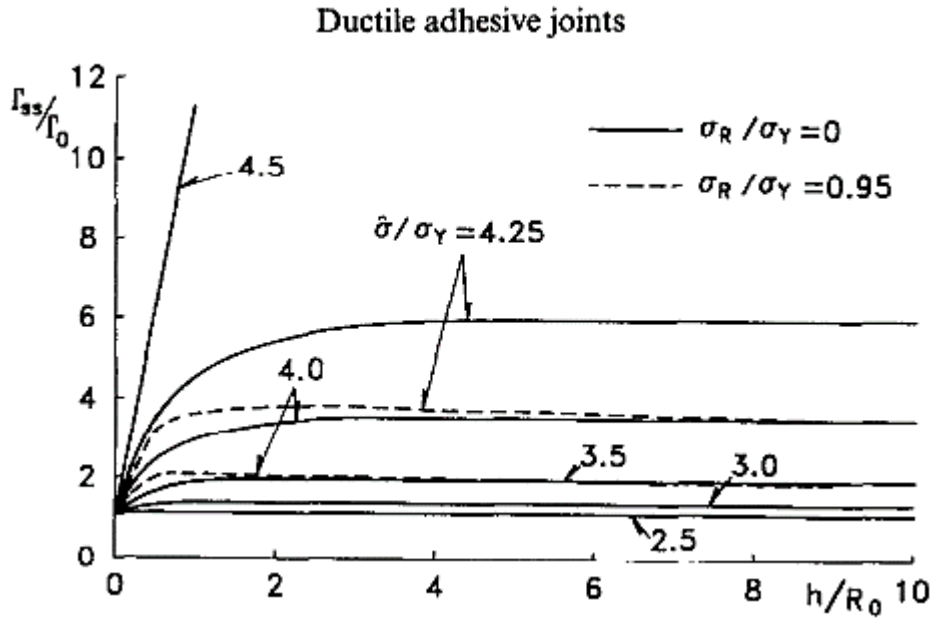

Figure 2.4. Relation between the normalised adhesive layer thickness and the normalised steady state fracture toughness at various levels of interfacial strength and residual stress [54].

Wei and Xu [62] investigated the effect of adhesive layer thickness on the load bearing capacity of single lap joints under tension. They utilised the cohesive zone model (CZM) to represent the adhesive layer as a single layer of cohesive elements and finite element analysis (FEA) to simulate various test conditions. Using the intrinsic parameters of the adhesives tested, they proposed a dimensionless constant called 'η' to estimate the total toughness of an adhesive bond. They have derived analytical equations for the non-dimensional toughness and strength

using the parameter 'η '. The toughness of the bond increased with increase in the adhesive thickness and this increase is governed by the parameter 'η'. Higher values of 'η' yield higher values of toughness.

Adhesive	Adherend	Adhesive modulus (GPa)	Test configuration	Adhesive thickness (mm)	Reference
Epoxy (Brittle), silicone rubber (Ductile)	Aluminium	--	Dog bone tensile, 3-segment shear, SLJ	1, 0.8, 0.6, 0.5, 0.4, 0.3	[63]
Polyvinyl ester	Carbon fibre composite	--	DCB (mode-I), 3-ENF (mode-II)	1, 2, 3, 4	[64]
Polyimide	Aluminium alloy-5052-H34	--	Butt joint tension, single lap shear	0.1-0.75	[65]
AV138/HV998 (Brittle), Hysol EA 9361(Ductile)	High strength steel	4.59 (Brittle), 0.67 (Ductile)	Scarf joint tension	0.1, 0.5, 1	[66]
Hysol EA 9321(Brittle), Hysol EA 9361(Ductile)	High strength steel	3.87 (Brittle), 0.67 (Ductile)	Single lap joint tension	0.2, 0.4, 0.6, 0.8, 1	[62]
Toughened epoxy	Aluminium alloy AA6061-T651	1.5	DCB (mode-I), ADCB (mixed mode), quasi-static and fatigue	0.13, 0.38, 0.79	[44]
Epoxy (Araldite 420)	Aluminium	2.45	Mixed mode (modified arcan fixture)	0.33, 0.65, 1.23	[67]
SikaPower 498	Tool steel	--	DCB, TDCB (mode-I), ENF, ELS (mode-II)	0.2 to 4	[68]
Epoxy	Aluminium alloy, Steel	5 (Brittle), 3(Ductile)	DCB (mode-I), ADCB (mode-II)	0.05, 0.08. 0.19, 0.24, 0.89	[50]
Epoxy (Loctite Hysol 9460)	1018 low carbon steel	--	DCB (mode-I)	0,09, 0.2, 0.4, 0.6, 0.8,	[69]

Table 2.1. Test conditions from literature to study effect of adhesive layer thickness.

The peak (failure) strength, a parameter of the CZM, however, decreased with increasing thickness and this is attributed the decreased constraint exerted on the adhesive layer by the adherends. Finally, the effect of adhesive layer thickness is quantified by the traction-separation laws for different thicknesses. Ji *et al* [69] used experimental and numerical analysis techniques to investigate the effect of the adhesive layer thickness on the fracture toughness of single leg

bending specimens. Data reduction has been done by deriving analytical solutions to energy release rates using the *J*-integral which is further used to calculate the mixed-mode traction separation curves for specimens with different adhesive layer thicknesses. They reported increasing values of steady state toughness values with increasing adhesive thickness. Furthermore, they reported that increasing the thickness did not increase the peak strength parameter of the CZM, but rather increased total area under the traction-separation curve. However, this study treats the entire adhesive layer as a single layer of elements and does not throw light on the mechanics behind the plastic deformation in the adhesive and its effect on the crack propagation. Also, the change in the mode-mix ratio with increasing crack length has not been addressed and the effect of adhesive thickness on this parameter has not been considered. **Table 2.1** gives a summary of some of the available literature on the effect of adhesive layer thickness.

In metal-metal joints, the high degree of mismatch between the adhesive and adherend properties might result in either a cohesive or interfacial failure of the adhesive. This degree of mismatch has been known to govern the deformation mechanism and failure in the adhesive layer [50]. The toughness of an adhesive joint can be classified into two components: intrinsic and extrinsic toughness [55]. The intrinsic toughness is due to the plastic and elastic deformation in the adhesive layer and is a property of the adhesive. The extrinsic toughness is because of the plastic deformation of the adherends and depends on the geometry of the joint. In this study of opening mode deformation of DCB specimens [55], it has been observed that the increased adhesive thickness has no considerable effect on the intrinsic toughness of the adhesive joint. Also, the constraint exerted by the adherends is found to be negligible. The independence of the toughness of the adhesive thickness is attributed to the simultaneous variations in the peak stresses and the critical displacements associated with the adhesive joint failure. On the contrary, several studies have established the effect of the adhesive thickness on joint toughness. As the adhesive layer thickness increases, the peak stress at failure decreases because of the reduced constraint and the toughness increases. This behaviour is seen till the thickness reaches a critical value beyond which the adhesive layer exhibits bulk adhesive properties [51].

In addition to the adhesive layer thickness, the deformation and the failure of the adhesive bond is dictated by the adherend behaviour. As previously explained the adherends are known to exert a constrain on the adhesive layer deformation. The thickness of the adherends and their plastic deformation upon loading determine the joint load-displacement response and failure initiation and propagation. Kafkalidis *et al* [49] investigated the effect of adherend plasticity on the failure of single lap joints fabricated with brittle and ductile adhesives at various thicknesses. Mild steel and medium carbon steel were used as the adherends. The initiation and propagation of the crack was captured using a camera and correlated to the load-displacement curves.

Significant plasticity was observed in both the mild steel and medium carbon steel adherends leading to high bending moments acting at overlap edges. This yielding was observed well before the failure initiation. The crack initiated at the overlap edges and propagated laterally across the width. It further propagated inwards stably. The initiation and propagation of the crack frees the adherend length behind the crack leading to rotation of the joint about the tip location. Thus, the mechanical response of the joint depends entirely on the plastic deformation of the adherends. This phenomenon is more apparent at lower overlap lengths.

Adherend material	**Adherend thickness (mm)**	**Test configuration**	**Adhesive type**	**Reference**
Aluminium alloy AA6082-T651	1, 2, 3, 4	DCB (mode-I)	Polyurethane – SikaForce 7888	[45]
Aluminium alloy AA6061-T651	1.6, 3.2, 12.7, 25.4	DCB (mode-I), ADCB (Mode-II) fatigue	Toughened epoxy	[43]
Aluminium alloy 7075-T6	0.7, 1.3, 1.7, 3	Portable adhesion tension testing	Epoxy- FM-300	[70]
Aluminium alloy, Steel	0.78, 1.2	DCB (mode-I), ADCB (mode-II)	Epoxy	[50]
Aluminium alloy-5758, Cold rolled steel	1, 1.3, 1.6, 2, 2.6, 3 (Aluminium alloy), 0.5, 0.7, 0.9, 1.1, 1.4 (Steel)	Wedge peel test	Toughened epoxy	[71]

Table 2.2. Literature on effect of adherend thickness on joint strength.

Campilho et al [45] investigated the effect of adherend thickness on the steady state energy release rates of polyurethane bonded aluminium DCB specimens. Two techniques were used to calculate the energy release rate, compliance-based beam method (CBBM) and J-integral method. The toughness values calculated using both the techniques displayed the same increasing trend with increasing adherend thickness. This phenomenon was observed in the case of ductile adhesives.

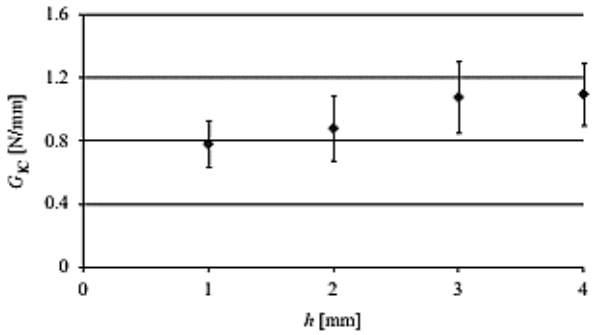

Figure 2.5. Average values and deviation of GIC obtained from DCB testing as a function of adherend thickness [72].

The development of a damage zone ahead of the crack tip is proposed as the reason for this difference. In the case of the ductile adhesive, this damage zone is constrained by the stiffer adherend and this increases with increasing thickness. Similar results were reported by several researchers [54,63,71]. **Table 2.2** gives a summary of some of the literature on the effect of adherend thickness on adhesive bond failure.

Azari *et al* [72] investigated the effect of adherend thickness on the fatigue energy release rate and crack growth behaviour in aluminium-epoxy DCB and ADCB joints (**Fig 2.5**). The increase in the adherend thickness reduced the fatigue threshold energy release rate and increased the crack growth rate at a given value of the energy release rate. However, increasing the adherend thickness increased the failure load in absolute terms. However, no such effect was observed in mixed mode fatigue test at low mode-mix ratios. The relation between the adherend thickness and the energy release rate is applicable till a certain thickness value beyond which the fatigue parameters are independent of the adherend geometry. It was concluded that at higher adherend thicknesses, the deformation is higher around the crack tip in the adhesive layer as shown in **Fig 2.6** and hence failure propagates faster. The same authors [43] studied the effect of adherend modulus on the fatigue crack growth rate by testing steel-epoxy and aluminium-epoxy adhesive ADCB and DCB joints in fatigue. They observed an 8% decrease in the threshold energy release rate when the adherends were changed from aluminium to steel. This implies that the increase in the elastic modulus increases the overall damage of the adhesive layer and has the same effect as decreasing the adhesive layer thickness. The difference in modulus is seen as an appearance of a high stress zone near the interface. In addition to the above, the interface re-entrant corners of the adhesive bond present a spot for high stress concentration when the joint is loaded [61,73,74]. This is caused by the discontinuity of the material elastic properties such as elastic modulus and Poisson's ratio. This occurrence is called the stress singularity which has been the major field of study for several years. The interface stress distribution at the corners of an adhesive joint has been analysed and formulated as a function of the stress concentration factor by Reedy and Guess [74].

However, the use of this model has been restricted to very thin adhesive layers bonded with highly stiff adherends wherein the plastic yield zone of the corner stress concentration is very small compared to the adhesive layer thickness. This condition is called small scale yielding (SSY). By using this model, they accurately predicted the critical local stress at a given adhesive thickness, making it possible to predict the strength of a butt joint. However, this formulation is limited to elastic adherends. Similarly, Qian and Akisanya [61], on the failure behaviour of scarf joints of varying scarf angles, implemented a similar criterion to predict the failure loads. They identified the failure initiation at the interface corners based on stress singularity fields. The analytical solutions proposed were found to be adequate in explaining the crack initiation along the high stress intensity corners, bridging of the crack and subsequent cohesive failure. The validity of this criterion is studied in the specific field of plastic zone size and the elastic singularity zone. Since the validity of this criterion is based on the comparison of the above two parameters, the plastic zone obtained from finite element analysis of butt joints is compared to that from the stress singularity-based criterion and a relation for selection of parameters based on the material properties and the geometry of the joint was obtained.

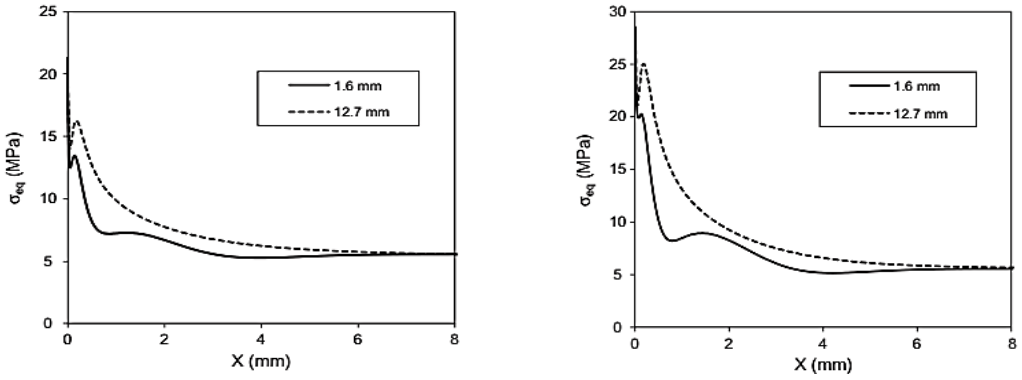

Figure 2.6. von-Mises stress distributions ahead of the crack tip at mid thickness in bonds with 1.6 mm thick adhrends and 12.7 thick adherends at applied energy release rates of a. 200J/m2 and b. 500J/m2 [43].

The interfacial failure happens when the degree of bond between the adhesive and the adherend is not properly formed or if the adhesive strength of the interface is less compared to the cohesive strength of the adhesive. The adhesive bond to form requires a process of adherend surface preparation, application of the adhesive and consecutive curing which requires accurate maintenance of the thickness of the joint. This requires special jigs and fixtures specially designed to suit the geometry of the joint thus making the fabrication procedure troublesome.

2.3. Failure mode characterisation

It is necessary to characterize the bond in terms of load bearing capacity and toughness in different modes of loading. Even though the adhesive joints employed in practical applications are subjected to complex states of stress, the strength of the joint is estimated in each mode of failure separately. The DCB test (ISO 25217:2009) and the ENF tests are used to find the failure toughness in mode-I and mode-II types of loading respectively and SLJ in mode –III for the failure initiation traction. There exist no standardised test methodologies for mode-II and mode-III fracture toughness measurements. The parameter of interest in each of these tests is the steady state fracture toughness. The DCB specimen consists of an initial crack introduced at one of the specimen edges. The fracture toughness of the adhesive in mode-I and mode-II are given by the beam theory solution as:

$$G_{IC} = \frac{3P^2C(a)^{\frac{2}{3}}}{2A_1bh} \quad \ldots\ldots\ldots\ldots \quad \text{Equation 2.1}$$

$$G_{IIC} = \frac{P^2}{2b}\frac{\partial C(a)}{\partial a} \quad \ldots\ldots\ldots\ldots \quad \text{Equation 2.2}$$

Where ‘a’ is the crack length, P is the load, ‘A_1’, ‘C(a)’ are the calibration terms of the joint compliance, ‘b’ is the width of the joint, ‘h’ is the thickness of the adherend. The critical value of the fracture toughness is obtained by using the fracture load in the above relation. The fracture load can be defined as the point of initiation of crack or visual fracture or point of non-linearity of the load displacement curve etc. Hence, the choice of the value of ‘P’ plays a crucial role in determining the fracture toughness of the joint and if not chosen properly might result in erroneous predictions. The steady state fracture toughness is obtained after the crack propagation is stabilised. This value is crucial in the case of plastic deformation around the propagating crack tip. The test parameters such as load and displacement are monitored on the time scale and the area of the load-displacement curve gives the toughness of the adhesive. These parameters are utilised in the models to predict the failure of the adhesive joints under a given loading condition. However, there exists some error in the correlation of the experimental results to the model parameters. This error results in inaccurate prediction of joint failure. Usually, an iterative method, wherein the model parameters are continuously modified till the numerical predictions match the experimental ones is employed. However there exist some assumptions in such models such as linear or non-linear behaviour of the adhesive which introduce further errors in the numerical predictions. In addition, the conventional experimental test output data i.e., load-displacement curve can only be used to predict the macro-scale behaviour of a joint. It is difficult to accurately understand the crack initiation and propagation in such test. Furthermore, it is difficult to isolate the effects of voids, cracks, interface de-laminations etc., on the failure behaviour and crack propagation. Also, in most of the practical applications, the loading and

failure of the joint is such that the failure is rapid and catastrophic. Hence, understanding the failure (crack) initiation and propagation in the joint is crucial.

2.4.Adhesive bond defects

Adhesive bond defects are usually caused either because of the manufacturing methodology or because of the environmental effects. Defects in adhesive bonds can be classified as disbonds, voids, zero volume disbonds or kissing bonds, porosity, under-cured adhesive and cracks [75]. Disbonds are localised debonded areas present along the adhesive-adherend interface caused due to thermal expansion differences between them. They are also caused by impact loads. Voids are usually because of the coalescence of small pores caused within the adhesive layer. This can be because of foreign gases or air entrapped within the adhesive during fabrication. Kissing bonds or zero-volume disbonds are areas along the adhesive-adherend interface where there is a contact between the two but no load transmission occurs. These are usually caused because of moisture ingestion along the interface when the adhesive joint is exposed to high humidity conditions. They also occur because of improper surface preparation, residual stress within the constituents or contamination. Porosity in the adhesive layer is caused by entrapped air during fabrication. It is also caused by some volatile compounds mixed with the adhesive which tend to evaporate during the curing process. Cracks are formed in the adhesive layer usually because of thermal shrinkage of the adhesive and are most common in brittle and high temperature curing adhesives. **Figure 2.7** gives an illustration of the common defects in adhesive bonds. Kissing bonds are regarded as the most detrimental as they are very difficult to detect and lead to significant reduction in the interfacial bond strength. It is highly likely that the interfacial moisture ingestion leads to corrosion of the adherend if metallic, and thus compromises the structural integrity of the bond. They lead to adhesion type failure which is highly undesirable. The major dimension of the above defects usually varies from below 1 mm to higher than 100 mm depending on the loading and environmental conditions.

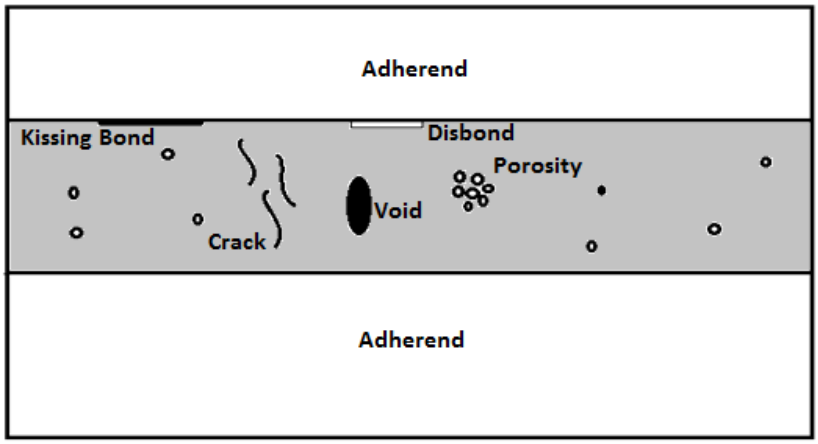

Figure 2.7. Various defects in a typical adhesive bond (as per current understanding).

2.5. Effect of environment and defects

This section looks into the available literature on the study of environment and defect induced reduction in adhesive bond strength. Many of the studies conducted characterised the bond strength as a function of exposure to hot and humid environments. The exposure of the adhesive bond to humid environments leads to a change in the glass-transition temperature of the adhesive [76]. This leads to a weakened cross-linked structure within the adhesive leading to degradation in the load-carrying capacity.

The effect of defects is studied by artificially inducing defects either along the interface by applying various contaminants or within the adhesive layer by creating voids and inclusions. Most of the studies report a steady decrease in the bond strength with increase in the defect area or volume percentage. In some cases, a change in the failure mode has also been reported.

Zhang *et al* [77] studied the effect of hygro-thermal exposure on the shear strength of single lap shear (SLS) joints of aluminium and steel adherends. Specimens were made with both the same and different material adherends to study the different interfacial degradation mechanisms when exposed to moisture. The residuals strength of the bonds after environmental exposure at 80ºC and 90% RH for just 60 days was only 34% of the initial strength. At lower humidity levels however (<30%RH), the strength increased after 60 days of exposure. This is deemed to be because of the secondary curing effect. Exposure to high humidity levels deteriorated the interface quality. The moisture reacted with the aluminium surface and formed an oxide layer which reduced the interfacial strength. The artificial defects were introduced by applying a thin layer of oil along the adherend surfaces before bonding. As expected, the bond strength reduced considerably with increasing oil film thickness.

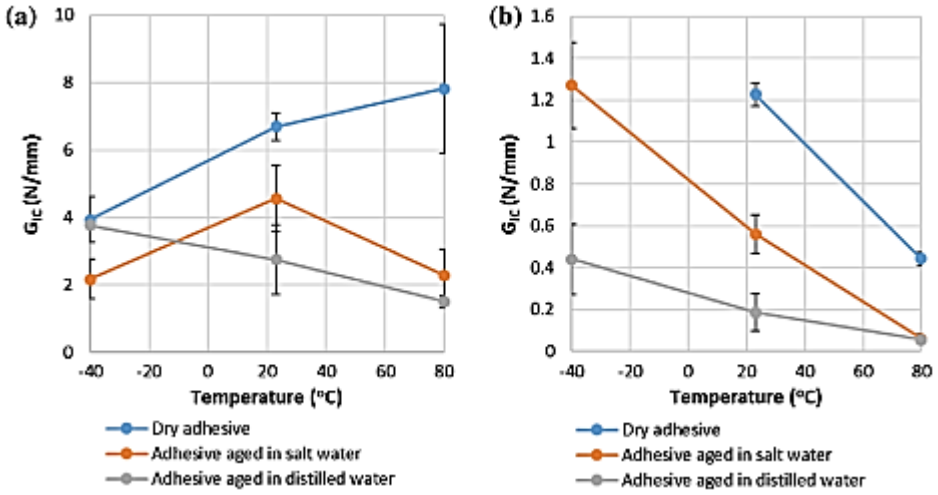

Figure 2.8. Effect of temperature on mode-I fracture toughness of a. XNR-6852-1 adhesive and b. SikaPower 4720 adhesive at different ageing conditions [78]

Silva and Biscala [82] investigated the effect of cycles of salt fog, moisture, temperature and salt water immersion on the degradation of FRP-concrete adhesive bonds. Temperature

cycles and moisture cycles led to failures in the concrete substrate whereas the samples exposed to salt fog cycles exhibited failure at the concrete-adhesive interface. Moreover, samples exhibited to temperature cycles exhibited significant strength decrease compared to samples subjected to salt water immersion.

Adhesive	**Adherend**	**Test Method**	**Exposure conditions**	**Failure mode**	**Reference**
Epoxy	Aluminium alloy	Single lap shear	40ºC, 98%RH - 240 hours	Interfacial	[79]
Loctite-ESP110, Araldite-2015, Araldite AV138	Aluminium alloy, Steel	Single lap shear	80ºC, 25ºC, -30ºC, 20%RH	Cohesive	[4]
Polyurethane	Mild steel-S235	Raman spectroscopy, FE-SEM	Water immersion at 60ºC	Interfacial	[80]
Epoxy-Araldite 2011	CFRP/Steel	Double strap joint tension	23ºC, 40ºC, 50oC, 60ºC, 70ºC	Cohesive, Interfacial	[81]
Epoxy-NVT201E	CFRP/Carbon steel	Floating roll peel testing	5% NaCl immersion-0 days, 30 days, 90 days	Cohesive, Interfacial	[3]
Epoxy	CFRP/Concrete	3-point bend	Salt fog, temperature, moisture cycling, salt water immersion	Interfacial	[82]
Epoxy Loctite Hysol-9466	GFRP	Single lap shear	50ºC, 70ºC, 90ºC, 1 1 week, 2 weeks	Fibre tear	[83]
Epoxy – XNR 6852-1, SikaPower 4720	Aluminium alloy – 6082 T6	DCB	Immersion in distilled water, 75% RH, -40ºC, 23ºC, 80ºC	-40ºC – Cohesive 23ºC, 80ºC - Adhesive	[78]
Epoxy-3M AF-163-2K	Aluminium Alloy 7075-T6	Single lap shear fatigue	Thermal cycling – 74.5ºC-39ºC; <10% - 100% RH	Cohesive	[84]
Acrylic-3M VHB	Aluminium alloy-2024 T4	Single lap shear, 3-ENF; Tension and impact, EIS, Vibration	Freeze-thaw cycling -10ºC to – 12ºC	Interface	[85]

Table 2.3. Literature on effect of environmental conditions on adhesive joint performance and failure

Weiss *et al* [53] conducted a thorough study on the surface morphology and composition of steel plates before adhesive bonding and after bonding followed by water immersion ageing at 60^{o}C. Prior to bonding, the substrates were grit blasted with alumina particles. Hence the surface composition of the plates showed traces of aluminium oxides. The specimens were tested in shear after ageing. The principal failure mode was interfacial. Spectroscopy on the fracture surfaces showed significant amount of oxides and hydroxides of iron. The adhesive, however, was in a pristine state. Hence, adherend substrate corrosion accelerated by the presence of water at the interface resulting in the formation of metallic oxides and consequent separation and deterioration of the interface was concluded to be the cause of the adhesive failure of the specimens. Very little traces of iron oxides were also found on the adhesive fracture surface, thus showing that its adhesion to the oxide layer sustains the joint. However, this may not be sufficient to carry higher loads. Stazi *et al* [86] reported similar behaviour in pultruded GFRP single lap and butt joints when bonded with epoxy, acrylate, methacrylate and polyurethane adhesives. The specimens were aged at elevated temperatures and high humidity. Exposure to elevated temperature however, led to strengthening of bond because of the secondary curing effect. However, ageing for longer periods at temperatures close to the glass-transition temperatures led to permanent deformation in the adhesives and higher elongations of the bond at a given load or in other words, lower stiffness. The failure mode changed from cohesive to adhesive because of the high temperature exposure. UV radiation on the other hand only deteriorated the epoxy bonds. This was because of the possible difference in the absorption capacities of various adhesives.

Frietas *et al* [3] tested epoxy bonded steel-CFRP specimens under peel type loading. They considered three types of specimen conditions. Pristine, 30-days salt sprayed and 90-days salt sprayed. The pristine specimens exhibited 100% cohesive failure. No notable change in the average peel load was observed between the pristine and 30-day salt sprayed specimens. A slight tendency towards interfacial failure was however seen. After 90-days salt spraying, extensive interfacial failure was seen, and the average peel load was reduced by 23%. EDS of the fracture surfaces showed deposits of NaCl on the surface thus revealing accumulation of the salts along the interfaces thus reducing the interfacial strength. The moisture and salt ingress started from the corners of the joint where the interface is exposed.

Zheng *et al* [79] conducted lap shear tests on epoxy bonded aluminium plates exposed to high humidity-high temperature and high humidity-low temperature conditions. They found out that the high humidity though does not affect the chemical state of the adhesive, leads to accelerated corrosion of the aluminium substrate along the interface. They postulated that the interfacial bonding between the adhesive and the adherend is not due to chemical reaction but rather due to the Vander Waal force and attraction between polar molecules. At high temperatures, these break down leading to reduction in bond strength.

Several conventional test methodologies have been used to test the fracture properties of adhesive joints. However, these require specific specimen preparation techniques and geometries to keep the data reduction and analysis simple. There exists no single methodology to quantify the residual strength of in-service adhesive bonds with weakened interfaces. Similarly, several studies have been conducted to understand the strength reduction caused by the presence of defects. For example, Ribeiro *et al* [12] studied the distributions of peel and shear stress distributions in SLJs with varying overlap lengths and defect sizes. They used CZM to model the interface peel and shear behaviour. They studied two different adhesives (brittle and ductile) to understand the effect of deformability of the adhesive on the strength of the adhesive bonds. They reported that the effect of the defects is more dominant on the ductile adhesive joints than the brittle ones. The defects, being in the central portion of the overlap do not affect the high stress zones formed at the end of the overlaps in the case of the brittle adhesives. However, the strength of the ductile adhesive is because of the global yielding in the adhesive after reaching the maximum load. Hence the total overlap area plays an important role in determining the load bearing capacity of the joint. For a non-defective joint, however, the ductile adhesive joint has a higher load capacity than the brittle joint. Hence, they concluded that the defects do not play a major role in the brittle adhesive joint strength whereas there exists a linear relation between the defect area% and the joint strength in the case of ductile adhesive joints.

Xu *et al* [13] studied the presence of various types of defects namely voids, interfacial de-bondings and weak interfaces on the load carrying capacities of single lap joints with aluminium adherends. The interfacial de-bondings were implemented as a layer of cohesive zone elements with zero interfacial toughness. Similarly, weak bonds were implemented as reduced toughness interface elements and voids were modelled by using the Gurson-Tvergaard-Needleman function which correlated the void nucleation and growth with the effective yield strength. They reported that the location of the defect relative to the overlap ends determines the peak load in tension testing. Also, the increase in the defect length leads to a change in the joint behaviour from brittle to ductile as a whole. Similarly, decreasing peak strength parameter of the CZM decreases the peak load for a given weak bond length and interfacial strength. For a given interfacial strength, decrease in the peak strength shows higher discrepancy in the peak load at higher weakly bonded interface length. They also reported that increasing void fraction drastically decreases the peak load and the displacement corresponding to the peak load.

Karachalios *et al* [14] studied the tension testing of single lap joints with different adherend materials and adhesives. They reported that the adherend plasticity plays a major role in determining the failure load of ductile adhesive joints. The presence of defects in this case does not significantly affect the load carrying capability of the adhesive joint. In the case of brittle adhesive joints however, the defect size is directly related to the peak load. This is because of a

transition from the failure of the adhesive at the overlap ends to complete plasticisation of the adhesives at higher defect lengths. However, in 4-point bending, the correlation between defect % and peak load is not straight forward. This is considered to be because of the stress concentrations acting at the overlap edges in flexural loading rendering the mid overlap ineffective in the load transmission across the joint.

Galy *et al* [15] investigated the effect of various interfacial qualities on the tensile testing of single lap joints. They did this by varying the interfacial treatment before bonding. They considered three different surface treatment conditions and showed that sanding in combination with degreasing gives the optimum strength. They have used ultrasonic C-scan to qualitatively measure the adhesion across the interfaces. In addition, AE monitoring was used in combination with tension testing to understand the failure mechanisms. It was found that lower interfacial quality leads to interfacial adhesive failure and higher interfacial quality leads to a combination of adhesive and cohesive failure. However, this study does not consider the presence of localised defects such as kissing bonds and voids along the interface. In addition, the AE analysis reported only concentrates on amplitude analysis based classification and does not report on the frequency analysis.

2.6. Defect detection

It is quite apparent that the interface plays an important role in the load transmission through the adhesive joint. However, the estimation of the interface parameters namely the strength and fracture toughness is an arduous task as the crack propagation along the interface is always accompanied by plastic deformation either in the adhesive or the adherends or both [55]. The formation of a plastic dissipation zone ahead of the crack tip and the size of this zone determine the steady state fracture toughness and thus the inherent toughness of the interface [51]. The size of the plastic zone varies with the thickness of the adhesive layer. The use of linear elastic fracture mechanics is limited to small-scale yielding conditions where the size of the plastic dissipation zone in front of the crack tip is negligible compared to the dimensions of the geometry. LEFM breaks down where large-scale yield conditions exist as an interfacial crack in adhesive joints. Liu *et al* [87] have proposed a parametric study based methodology to estimate the interface parameters by reducing the adhesive layer thickness to a near zero value to minimise the plastic dissipation energy.

The estimation of the interface toughness can be carried out through the calculation of the work of adhesion of the adhesive on the adherend material which is estimated to be around 0.1 J/m^2 [88] using the surface free energy of the adhesive and the contact angle of an adhesive droplet on the adherend surface. This estimate is assuming an interface without defects and 0^o contact angle. However, in the presence of improper adhesion or other such defects this value can be quite lower than the estimated value. Tvergaard and Hutchinson [51] reported a strong

dependency of the steady state energy release rate on both the interfacial strength and toughness in addition to adhesive layer thickness and modulus. The failure prediction of adhesive joints has largely been carried out using failure criteria that have been established for various geometries and loading conditions. The effect of the presence of the above defects on the load capability of the adhesive bond has not been properly addressed. Defects have been known to occur in adhesive bonds due to a variety of factors.

Adhesive	Adherend	Type of defects	Size of defect	NDE Method	Reference
Epoxy	Aluminium	Environmentally degraded interface	--	Ultrasonic scanning	[89]
Epoxy	Aluminium	Environmentally degraded interface	--	Ultrasonic angle-beam spectroscopy	[90]
Epoxy	CFRP	Porosity, Disbonds	--	Ultrasonic scanning	[91]
Epoxy	Aluminium	Interfacial defects	--	Ultrasonic angle-beam spectroscopy	[92]
Epoxy	Aluminium	Softened adhesive-cohesive strength	--	Longitudinal ultrasonic scanning	[93]
Epoxy	Steel	Adhesive voids and interfacial defects	--	Ultrasonic pulse-echo	[10]
Epoxy-araldite AV138	CFRP	Degraded interface	--	Ultrasonic oblique scanning	[94]
Epoxy-QY8911	CFRP	Defect evolution	--	Lamb wave based pitch-catch method	[95]
Epoxy-FM1515-3	CFRP	Indentation damage	100 mm diameter	Guided lamb wave	[39]
Epoxy-Araldite AV138M	GFRP	Kissing bonds	50 x 50 mm^2	Water immersion scanning, Digital image correlation	[96]
Epoxy	CFRP	Kissing bonds	10 x 10mm^2	Pulsed Phase Thermography	[97]
Epoxy	Aluminium	Voids	5 mm, 10 mm, 16 mm, 21 mm, 44 mm diameter	Leaky lamb wave based guided wave detection	[98]
Epoxy-AME6000 INF	CFRP	Disbonds	0-48% of bond area	Ultrasonic C-scan, Lock-in thermography	[99]

Table 2.4. Literature on adhesive bond defect detection using NDT.

The previous section gives a brief overview of the literature available on the effect of environmental exposure and consequent defect evolution. However, mechanical testing to estimate the residual strength may not always be possible. Empirical relations may be developed between the defect size (area or volume percentage) and the residual strength of a bond if the size of the defect can be estimated prior to testing. This section considers the available literature on defect detection using various techniques. It should be noted that though defect detection is a well-developed science by itself, the current review only considers defect detection in adhesive bonds. **Table 2.4** gives a summary of some of the literature available on defect detection in adhesive bonds. The quality of the bond in terms of the presence of irregularities such as voids, cracks and impurities need to be determined and the effect of these on the failure initiation and propagation must be understood. Various techniques such as X-ray photo spectroscopy (XPS), Electrochemical Impedance Spectroscopy (EIS) and Thermal analysis have been used respectively to evaluate the compositional changes in the adhesive chemistry leading to failure, moisture or water ingress along the interface, differential thermal expansion between the adhesive and the adherends.

The amplitude and frequency response of the output of the ultrasound monitoring is a function of the integrity of the degree of the cohesion and the interfacial strength of the joint. It has been shown that the minimum peak in the output spectrum shifts towards the negative side, the shift being proportional to the degree of interfacial void. Also, the peak amplitude of the reflected signal is found to be a direct indicator of the cohesive or adhesive failure of the bond. Ultrasonic inspection has been extensively used in defect detection in adhesive bonds. Several types of defects such as fracture cracks, voids, delamination and kissing bonds have been successfully detected using this technique. Ultrasonic investigation of adhesive bonds is usually carried out using a range of techniques principally based on using an ultrasonic transducer to initiate various modes of wave propagation along the interface. Few of the techniques are acousto-ultrasonics, ultrasonic spectroscopy and pulse-echo method. This type of testing is usually carried out using either one or two transducers simultaneously in the pulse-echo configuration or the pitch-catch configuration respectively. Pulse-echo method has the capability of detecting disbonds, voids and porosity in adhesive bonds. The presence of defects appears as an echo on the time domain signal usually between the front face echo and back face echo. It is possible to estimate the location of the defect by calculating the arrival time of the corresponding echo compared to the one from the back face of a specimen.

Ultrasonic wave that produces shear stress on the interface is sensitive to interfacial properties. Rokhlin and Rosen [100] measured the effective modulus using shear waves. This characterises not only the interfacial properties but also the cohesive properties of the adhesive. Claus and Kline proved that the surface finish of the substrate is directly related to the attenuation

of the interface wave. Rokhlin *et al* [90] used ultrasonic angle beam spectroscopy to estimate the degraded thickness across the adhesive-adherend interface. This model was modelled as a visco-elastic material along the interface and the model optimisation was achieved through iterative minimisation of the error between the experimental and model minimum reflection coefficient values. Experimentally, the viscoelastic layer was simulated using a very thin epoxy layer at different curing levels.

Her and Lin [93] used experimentally obtained ultrasonic longitudinal wave reflection coefficients at weak epoxy-aluminium interfaces to calculate the interfacial bond stiffness. They then correlated these values for three different bonding conditions to the experimentally obtained tensile bond strengths of the said joints. They obtained a linear relation between the interfacial stiffness and the reflection coefficient thus demonstrating the simplicity of this method. However, the mode of failure has not been reported and the correlation between interfacial reflections and the overall bond strength has not been explained. It is difficult to understand the applicability of this method in the case of cohesive failure of the adhesive. Goglio and Rosetto [23] proposed an index 'i' based on the reflection coefficient obtained through ultrasonic scanning from the metal-adhesive interface. They proposed a statistical technique for calculating an acceptable value of 'i' to distinguish between good and bad adhesion. They considered thin adhesive bonds where the adherend thicknesses are less than 2 mm.

Teles & Chimenti [101] developed a leaky lamb wave based defect detection technique using a pitch-catch methodology using ultrasonic transducers. The method was developed to detect kissing bonds along the interface of a glass-epoxy plate bonded to a balsamic wood core, a commonly used composite structure in aerospace applications. The principle is based on the fact that the presence of a kissing bond induces lamb wave propagation within the debonded part of the plate. This produces extraneous reflections which interfere with the reflections from a pristine part of the bond. They were able to successfully map a 1.1-inch diameter defect along the interface induced by quasi-static indentation.

Brotherhood *et al* [19] used three different techniques to detect the presence of kissing bonds in aluminium-epoxy adhesive bonds; longitudinal wave, shear wave and high power ultrasonic inspection techniques. They conducted ultrasonic transmission tests at various compressive loads applied to the specimen surface. Also, the specimen surface roughness was varied to determine the sensitivity of each technique to the various bonding conditions. The pressure-reflected signal correlations were made by calculating reflection co-efficients for the techniques. The reflection co-efficients were then normalised by those calculated for a perfectly bonded specimen. They concluded that longitudinal wave ultrasonic inspection has the best sensitivity to the presence of kissing bonds at various pressure levels and surface roughness. The shear wave although has good sensitivity at low loads and roughness, does not perform well at

higher loads. The high power ultrasonic inspection is the least sensitive of the three and is reliable only at near zero loads.

In addition to UT, a few other methods such as digital image correlation, Infrared thermography (lock-in), fibre optic interferometry etc have been successfully implemented to detect the presence of debonding along the interface.

Tighe *et al* [97] investigated the plausibility of kissing bond detection using infrared thermography. The adhesion defects along the bond lines were created by using teflon inserts and silicon grease. The eligibility of these two to be classified as kissing defects has been investigated using pulse phase thermography (PPT) and thermo-elastic stress analysis (TSA). It has been concluded that the silicon grease induced defects are undetectable at no load conditions as they do not alter the thermal conduction of the bond. However, when a small load is applied the defects open up and are detectable by the PPT phase difference ($\Delta\Phi$).

Kumar *et al* [94] used digital image correlation (DIC) to detect kissing bonds artificially introduced into GFRP-epoxy single lap joint specimens. They found very good correlation between the ε_{yy} strain field and the defect area% evolution when the specimens were loaded in tension. Also, they found a very good correlation between FE calculated strain fields and DIC calculated strain fields. They concluded that DIC can detect the kissing bonds even at 50% of the failure load. However, this technique requires the specimen to be loaded for effective defect detection.

Heller *et al* [25] used a Nd-YAG laser based source generation and detection setup which uses a high intensity laser to trigger various modes in adhesive bonded specimens. Spatial measurements were made at various locations of the specimen and 2D-FFTs and spatial Fourier transforms were calculated to create frequency vs wave number plots for both pristine and aged specimens. They detected significant decay in various modes in the aged condition and reported that the presence of adhesive does not change the behaviour of the plates as far as the frequency vs wavenumber plots are concerned. They also concluded that the adhesive, though transmits the energy from the metal plates across it's thickness, does not play a role in determining the mode propagation in the plates as they behave as if they are independent of each other instead of behaving as a plate with thickness equal to the sum of the two. Furthermore, they observed that as long as the aging temperature is below the glass transition temperature of the adhesive, the mode propagation behaviour does not change significantly.

2.7. AE in adhesive bond strength analysis

Another technique that is being successfully implemented in monitoring dynamic behaviour of engineering structures is AE. It has been demonstrated that AE can predict the crack growth in its initial stages in steel structures. Yu *et al* [102] monitored the growth of fatigue crack inside steel bridge components and the correlated the crack growth and temporal evolution of AE energy through an empirical model. Acoustic emission has first been implemented in testing of adhesive joints by authors such as Hill [103] and Curtis [104]. The latter showed that the AE cumulative energy relates to the fracture energy release rate in shear testing of lap joint specimens. Hill showed that the energy released from lap shear specimens can be related to the failure initiation along the overlap edges. Furthermore, the failure initiation can be detected very early using AE.

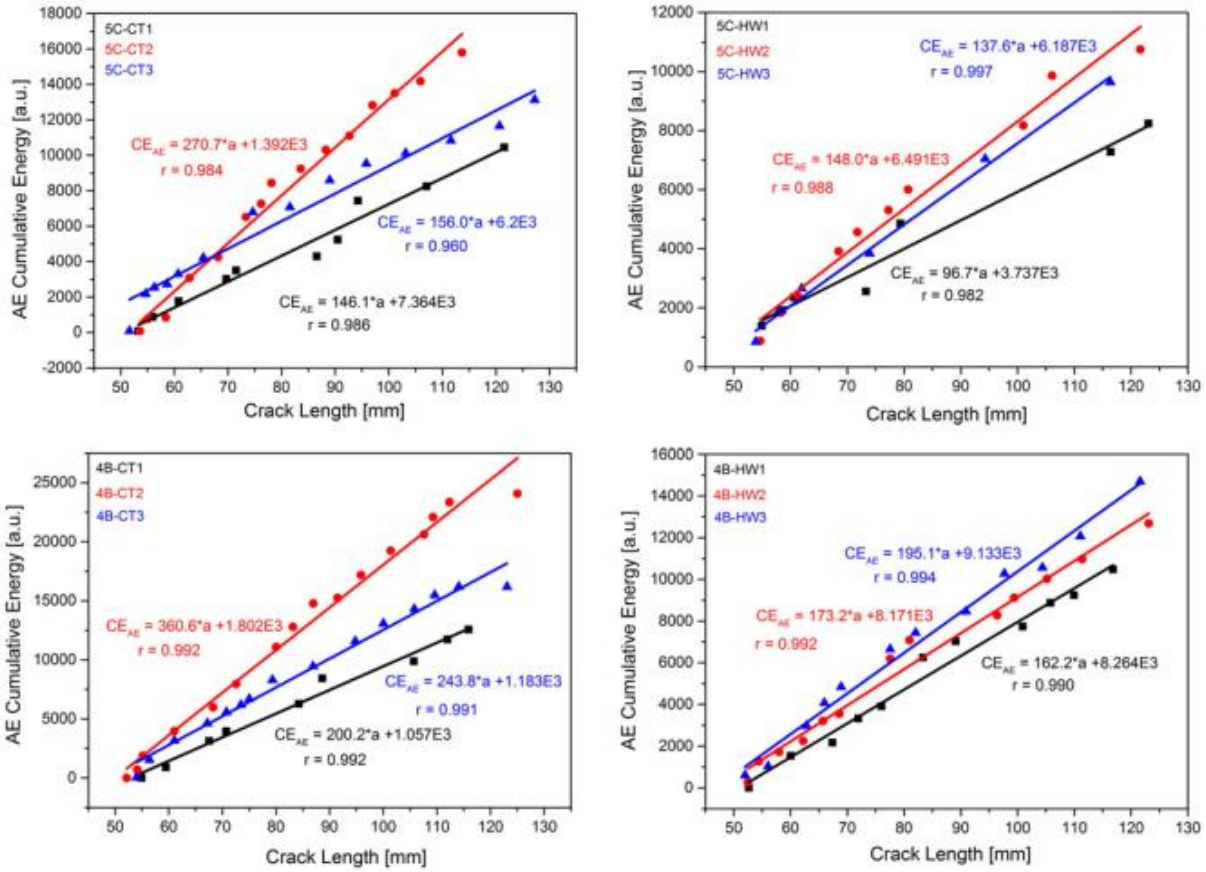

Figure 2.9. Relation between crack length and AE cumulative energy at various specimen environmental conditions [16].

Michalkova *et al* [16] investigated the relation between the AE cumulative energy release rate and analytically calculated energy release rate in DCB tests of laminated composite layers under different environmental conditions. They conducted the tests at 80 °C and -55 °C and observed a linear relation between the crack length and AE cumulative energy. They also investigated the effectiveness of AE source localisation based crack length measurement and

reported mean absolute percentage errors of <5% compared to a camera based visual method. They proposed a moving average based method for estimating the source location and hence the crack tip location between two sensors placed between the two ends of an initial crack.

Adhesive	Adherend	Test	Techniques	AE system	Sensor band width	Reference
Epoxy-FM300-2M	Graphite-Epoxy composite	DCB, ENF, single lap tension	AE	AMS3-vallen system (DAQ), B1025 AE sensor	--	[105]
Epoxy-FM300	Composite	Single lap shear	Acousto-Ultrasonics	AET 5000 signal processing unit, AET AC 379L sensor	125-1000kHz	[106]
Polyurethane-SikaForce 7851	GFRP	Double lap shear	Acousto-Ultrasonics	AMS-3 vallen system, SE-45H and SE-150M	30-1000kHz	[20]
Epoxy	CFRP	DCB	AE	Dakel-Xedo measuring system, IDK-09 PZT	25-600kHz	[16]
--	CFRP/Steel	Uniaxial tension (dog-bone)	AE	Physical acoustics corporation	--	[107]
Epoxy-AF163-2K	Aluminium alloy-2024 T3	Single lap shear	AE	LOCAN-AT apparatus	--	[108]
Terokal 5045	CFRP, GFRP	Single lap shear creep	AE	LOCAN-4 channel system, R15I AE sensors	--	[109]
Epoxy-Araldite LY556	GFRP	Repair patch-Tension	Acoustic emission + Digital Image Correlation	SAMOS E3.10 DAQ,	100-900kHz	[17]
Epoxy	GFRP	DCB, MMB	AE	Pacbus system, R15 AE sensors	--	[9]

Table 2.5. Literature on the use of AE in adhesive bond failure characterisation

They found that the damage index increases at a drastic rate once the yield point is reached and hence this parameter can be used in structural health monitoring to predict failure. However, they did not investigate the signal parameters such as amplitude and frequency content for possible indications of material failure initiation. Furthermore, the correlation between the

failure mechanism and AE features is yet to be completely established. Chen *et al* [92] proposed three AE based parameters to characterise the strengths of FRP/steel composite plates; a sentry function based on the ratio of strain energy derived from load-displacement plots of a tensile test to the cumulative AE energy, a damage index defined as the cumulative AE energy at any given time during the test to the cumulative AE energy at the yield point and a modified damage index defined as the ratio of cumulative AE energy at any given point to the AE energy at the half yield point. There is a possibility that different failure mechanisms namely opening shear and mixed mode have a characteristic signature because of their inherent nature. Preliminary research in this area has been carried out by Dzenis *et al* [105] who classified the AE signals from DCB and ENF tests into clusters using pattern recognition algorithms. They proved that mode-I and mode-II have different signal characteristics which are distinguishable. In addition, they carried out tensile fatigue tests on lap joints and established that the failure mode in these joints is closer to mode-II than mode-I. However, this classification is not based on wave propagation characteristics, but rather based on expected failure mechanisms. Ducept *et al* [9] used AE in composite mode testing to primarily identify the fracture initiation load. At the same time, AE was also used to monitor the energy release rate during the fracture testing. However, no significant AE data analysis has been conducted and no correlations have been drawn between the AE data and the calculated fracture energy release rates. Thus, the possibility of such correlation has been identified as one of the objectives of this thesis. Brunner *et al* [20] investigated the difference in theoretical and experimental failure loads of GFRP double lap joints by monitoring their tensile testing using AE sensors. They observed significant AE activity well below the failure load (at 50%). This seems to show that the damage mechanism is a combination of microscopic damage initiation and accumulation beginning at low loads at specific points followed by material softening and stress redistribution. They were successfully able to predict the failure loads for three adhesive thicknesses.

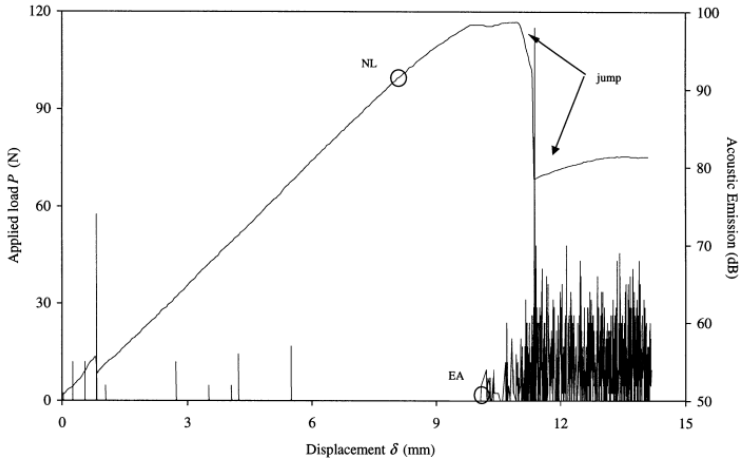

Figure 2.10. Load and AE events vs displacement in a DCB test of epoxy bonded CFRP composite joint [9].

Tanary *et al* [106] worked on something similar wherein they investigated the transmission of ultrasonic longitudinal waves through an adhesive bond with two different types of defects; voids and disbonds. They proposed the use of an acousto-ultrasonic parameter (AUP) to characterise the effects of defects on the overall amplitudes of the transmitted signal and the resonance of the signal within the bond. They then correlated this parameter to the tensile shear strength of lap joints and reported a linear relationship. The same applies to aging of the joint. The presence of defects also induces the excitation of low frequency components. However, the quantification of the energy of these low frequency components in relation to the disbond and void sizes has not been reported. Magalhaes and de Moura [109] used AE monitoring to characterise the tensile creep failure of epoxy bonded CFRP plates. They also studied the creep behaviour at different values of temperature and moisture. A linear increase in the AE cumulative count was observed in the initial stage of the joint failure. In the case of adhesive failure, the hit rate was lower compared to interlaminar failure of the plates. They defined a 'damage acoustic coefficient' as the slope of the plot between the cumulative count and time. A value of less than 10 per second predicts that no failure occurs.

2.8. Modelling failure in adhesive joints

The modelling and prediction of failure initiation and propagation is primarily done using a range of techniques such as FEM, virtual crack closure technique (VCCT), *J*-integral method, CZM etc. In general, the FEM analysis of adhesive joints is done either a 2-dimensional or 3-dimensional model of the joint. In 2D either plane stress or plane strain analysis is conducted depending on the relative dimensions of the adherends. Plane stress is used in the cases where the width of the joint is smaller than the thickness. In cases where the width is considerably higher, plane strain condition is implemented. The stress in third direction is assumed to be zero in this case. 2D analysis is easier to implement and less demanding computationally and the error when compared to a full 3D analysis is small enough to be ignored. In continuum mechanics approach, the singularity of stress at the interface formers and the cracks introduced because of fabrication cannot be accounted for as the stress ends to infinity at high stress concentration zones.

The basic assumption in the continuum damage approach is the continuity and uniformity of the material and stress. Hence at crack edges, continuum damage mechanics cannot be used to predict the stress field. Finite element method has the ability of predicting the stress distribution or concentration in the inter-layer joints and locating the plausible locations of failure initiation. This technique has been extensively implemented in studying the stress distributions in single lap joints [14,110] scarf joints [42,46,76,111-112] etc. However, the theory of Linear Elastic Fracture Mechanics (LEFM) can only be implemented in the case of brittle materials where the pre-failure plastic deformation is negligible and the material behaviour can be expressed by a linear relation between the stress and strain. However, the technique called VCCT has been successfully

implemented in some cases to predict the failure critical fracture toughness [113]. In this technique, the tip of the crack is advanced in a progressive manner between nodes, and the relative separation along the co-ordinate directions of the initially co-incident nodes is measured. This gives an estimate of the total displacement of the nodes away from each other and the traction required to achieve this relative displacement is measured. The integration of these values over a given length of the crack gives the total critical fracture toughness of the crack which then is compared to the experimental fracture toughness of the crack.

Several studies have been conducted on the prediction of the failure loads of various joints based on this technique. Advances in computational studies have brought forth the CZM which is being extensively used in failure predictions of a wide variety of joint geometries. Cohesive zone modelling is a damage mechanics based approach that incorporates the interface and cohesive failure of the adhesive into a layer of elements that are placed between the adherends. The CZM models the interface as a series of springs whose stiffness is a function of the normal and tangential displacements [114-115]. The principal advantage of CZM is that the stress state at any node is defined by the traction-separation law and is independent of its distance from the crack tip [**50**]. Many have utilised the CZM to model the interface and have used the energy release rate (Γ_o) and the interface strength (σ_c) as the variable parameters. Emphasis has been made on the study of the relative effect of these parameters on the crack propagation behaviour.

The failure behaviour of the adhesive is described by a traction-separation law the shape of which defines the maximum traction, deformation at failure initiation, toughness of the adhesive and initial stiffness. The failure initiates at the maximum traction and failure is complete at the failure deformation. The softening is governed by a damage parameter '*D*'.

The cohesive zone model can be implemented in all the three principal modes of failure and in mixed modes of failure. The mixed mode failure criteria linear and quadratic forms which are shown in **Equations 2.3** & **2.4** below.

$$\{ \frac{t_n}{t_n^c} \}^2 + \{ \frac{t_s}{t_s^c} \}^2 = 1 \qquad \textbf{Equation 2.3}$$

$$\{ \frac{G_n}{G_n^c} \} + \{ \frac{G_s}{G_s^c} \} = 1 \qquad \textbf{Equation 2.4}$$

The above two equations define the failure initiation surface in the case of a 2-dimensional model. In the case of a 3-dimensional implementation, an additional term for the mode-III failure will also be considered along with the above two terms of each equation. The 3-dimensional failure surface is defined by the following equations:

$$\{ \frac{t_n}{t_n^c} \}^2 + \{ \frac{t_s}{t_s^c} \}^2 + \{ \frac{t_t}{t_t^c} \}^2 = 1 \qquad \textbf{Equation 2.5}$$

$$\{\frac{G_n}{G_n^c}\}+\{\frac{G_s}{G_s^c}\}+\{\frac{G_t}{G_t^c}\} = 1 \qquad \textbf{Equation 2.6}$$

where t_n is the normal traction, t_s is the shear traction, t_t is the tear traction. Similarly, G_i (i=1,2,3) denote the toughnesses for the three corresponding failure modes.

The damage parameter 'D' in two dimensions is given by

$$D_{n,s} = \frac{\delta_{n,s}^f(\delta_{n,s}-\delta_{n,s}^D)}{\delta_{n,s}(\delta_{n,s}^f-\delta_{n,s}^D)} \qquad \textbf{Equation 2.7}$$

Where $\delta^f_{n,s}$ is the failure deformation in tensile or shear mode. The same can be applied to 3 dimensions. The gross deformation in two dimensional analysis $\delta_{n,s}$ is given by

$$\delta_{n,s} = \sqrt{\delta_n^2 + \delta_s^2} \qquad \textbf{Equation 2.8}$$

Failure of the joint occurs only in tension but not in compression. This model has been implemented in predicting failure adhesive joints in numerous studies [67]. For example, Xu *et al* [**62**] utilised cohesive zone model in finding the effect of adhesive thickness on the strength of lap shear specimens. They also studied the effect of varying the toughness parameter of the CZM on the failure deformation and the maximum strength of the lap joints.

Mohammedi *et al* [116] have attempted to combine both the CZM and continuum damage model to predict the displacements of interfacial layers of a metal-adhesive joint subjected to a 4-point bend test. The cohesive deformation of the adhesive was modelled with elastic-plastic response and the interface failure was modelled using CZM. Excellent agreement was found between the predicted and experimental values and the error was below 2%. However, they did not take into consideration the presence of stress singularity at the interface corner in the model.

Since the failure behaviour of an adhesive is highly variable depending on numerous parameters, a unified failure criterion and failure model does not exist. Moreover, for the same adhesive used, the stress field in the adhesive layer depends on the adherend properties and geometry and type of loading. Also, it has been suggested that a single criterion based either on stress, strain or toughness is not able to completely predict the failure initiation in an adhesive layer. Hence there exists a necessity to further understand the failure behaviour of adhesive joints under different loading conditions.

2.9. Failure criteria

The failure criteria vary depending on the nature of the adhesive i.e. ductile or brittle, joint geometry, loading conditions and presence of stress singularity areas such as the interface corner where the bond line meets the edge of the joint [61,73,74,117].

The most common joints such as single lap, double lap, butt and scarf have been studied extensively and failure criteria have been established for the same. This involves the study of the effect of the loading conditions and the induced peel and shear stresses in the joints. In the continuum mechanics approach, the behaviour of the adherends and the adhesive is assumed to be elastic or elastic-plastic. The failure behaviour of the adhesive is assumed to depend on the principal stresses or principal strains or strain energy density. One of the criteria used in the early studies is the von-Mises stress and strain criterion. These were implemented for brittle and ductile adhesives respectively. Similarly, maximum shear stress criterion has been used to predict the strengths of single lap joints [111,118]. Recently the maximum shear strain criterion has been implemented in failure assessment of ductile adhesives. Dan *et al* [46] have studied the effect of parameters such as scarf angle, adhesive young's modulus and thickness of the adhesive layer on the interface stress distribution and the failure of the adhesive joint. Two different failure criteria based on the maximum principal stress and maximum principal strain have been evaluated by comparing numerical failure loads to experimental values and it has been found out that the maximum principal strain criterion is more accurate in predicting the failure loads of the adhesive joints.

Similarly, Park *et al* [119] have modelled lap shear tests on thick aluminium to aluminium adhesive joints to assess the failure behaviour. The adhesive is assumed to be elastic-plastic in nature and the interfaces between the adhesive and adherends are considered perfect without flaws. They used a damage zone model based on equivalent strain based criteria in assessing the strengths of the bonds. However, the rotation of the loading axis is not taken into consideration. They could predict the failure of the lap joints to within 15% of the experimental value. Also, Sawa *et al* [120] studied the behaviour of scarf joints subjected to bending moments and observed that the failure behaviour of the joints is best described by the maximum principal stress criterion. The failure behaviour of the joint is also found to depend on the properties of the adherends. For example, Liao *et al* [111] studied the effect of adherend modulus on the rupture stress of the joints. They have observed that the stress increased with decreasing adhesive-adherend modulus mismatch.

2.10. Flexural strength and flexural testing

The studies of an inter-layer joint under flexural loading configurations (e.g. 4-point bending) are minimal, in particular for adhesive inter-layers with different moduli. The flexural

loading strength, or bend strength, can be defined as a material's ability to resist deformation under load acting in the transverse direction. Under 4-point bending, the specimen is subjected to a larger region of force (inducing a constant maximum bending stress over the whole large section between the loading points, testing conditions specified in ASTM D6272-00-Procedure B [121], whereas, under the 3-point bending, a concentrated bending stress acts under the central loading point (maximum bending stress occurs at the cross section where the load is applied), leading to premature failure.

In bi-material systems such as composite panels, there exists a property mismatch between the epoxy matrix and the fibres which might lead to a load or stress concentrations at the interfaces which act as a bridge to transfer the loads and can act as high stress concentration zone especially at the interface corners. In the study of the 4-point bending, the analysis is primarily dictated by the modelling of the load transfer between the loading and support pins and the adhesive joint. The elastic theory of bending is developed on the assumption that forces act at a point on the beam, whereas the actual loads are distributed over a small area of contact, which reduces the stress concentration significantly. Also, the plasticity of the material can bring about a considerable change in the stress levels in the joint, particularly in the vicinity of the loading and the support pins.

Following the above reasoning, a comparison of 3- and 4- point bend tests of unidirectional composites done by Cui and Wisnom [122] revealed a higher damage of the composite under the loading roller in three-point loading. They reported a decrease of transverse compressive and tensile stresses by a factor of 20% under 4-point loading compared to 3-point loading. They also reported a decrease of 20% in the bending stresses when the non-linearity of the materials is considered.

The study by Xie and Adams [123] concentrates on the shear testing of composite materials using 3- and 4-point flexural testing. Finite element and analytical methods were implemented to calculate the shear stress distributions in the composite laminates. The dependence of inter-laminar shear strength on the chosen support-span-length to specimen-thickness ratio has been reported.

Feraboli and Kedward [10] conducted a similar study on uni- and multi-directional composites of a constant span-to-thickness ratio subjected to 4-point loading configuration. The delamination has been reported to initiate at a small distance from the loading roller causing inter-laminar failure. Similarly, the mode-III failure of carbon/epoxy laminates has been studied by De Morais and Pereira [124] by subjecting them to a 4-point flexure loading. They implemented FE modelling in combination with cohesive zone modelling (CZM). The 3-point flexure loading configuration has been extensively used in various mode-II and mixed-mode fracture tests of adhesive joint.

However, the above studies consider specimens either with low support span-to-specimen thickness ratio or the existence of a pre-crack which acts as the failure initiation point. In addition, the 4-point flexure test has so far been utilised in finding the inter-laminar shear strength (ILSS) of composites and the mode-II and mode-III fracture toughness of adhesive joints. The literature on the study of the stress distribution in the adhesive interlayer in perfect bonding conditions without defects under flexural loading is minimal. Furthermore, the study of geometrically dissimilar adherends joined with an adhesive is crucial to assess the adhesive joints behaviour in real world applications.

Adhesive bonds inherently multi-layered materials with the mechanical properties varying with different depth levels. In this respect, they are similar to other multi-layer materials such as surface coatings, cladded metals and laminated composites. Though all these have interfaces across which the mechanical properties jump, they differ in terms of the type of bond. Indentation testing is a versatile tool used to assess the bond strength several multi-layer materials including composites which by nature are similar to adhesive joints. Hence, this technique could potentially be used to estimate the interfacial quality of adhesive joints. The section below presents an overview of available literature on the use of indentation testing of interfacial strength in multi-layer materials.

2.11. Indentation testing

Indentation contact mechanics (e.g. Hertzian contact stress analysis) provides necessary information for the study of localised surface and sub-surface loading behaviour. There is little literature where indentation method has been applied to adhesively bonded samples to analyse through-thickness stress distribution. However, indentation method has been extensively used in thin films to evaluate the adhesion properties and the elastic properties of coatings. In addition, the fracture properties of polymeric coatings on bulk materials, fibre de-bonding in composites [31,34,115], fracture toughness of brittle coatings etc have been studied using indentation. These studies have utilised the CZM to understand the interfacial delamination behaviour of the thin film under wedge indentation. In thin films, interface toughness is a more suitable parameter than interface strength to control the crack propagation. She *et al* [126], in the case of 3D wedge indentation on thin films, reported increase in critical load with increasing interfacial strength. In addition, they observed a transition in crack profile from 3-D to plane strain with increasing indenter length. Moreover, a transition from 2D to 3D crack propagation behaviour with increasing indentation depth has been found under wedge indentation. At lower indentation depths, a plane strain condition (2D) prevails. Indentation has also been used to study the delamination of polymer films on brittle substrates. All these findings lead to the conclusion that wedge indentation is a suitable technique to study interfacial crack propagation in multi-layer structures. It is clear from the foregoing that indentation based stress analysis of adhesively

bonded samples is possible to appreciate the interfacial delamination and crack propagation behaviour.

2.12. Gaps in the current field

Although considerable research has been done in the field of experimental, analytical and numerical aspects of the failure of adhesive joints, the understanding of their failure behaviour is still highly subjective and varies between different joint types and different adhesives. The research done so far is highly concentrated on macro-mechanical behaviour and failure strength prediction. There still exists a need to understand the relation between the microstructural aspects of the adhesive such as voids, cracks etc and the macro-mechanical behaviour of an adhesive joint. Also, even though the standard testing methods to assess the strength of a joint, describe the failure strength, cannot give a complete picture of the failure phenomenon from an energy point of view. It is certain that there is a lot to be gained by further understanding the failure behaviour of adhesives from the roots of its structure.

Techniques such as ultrasound scanning and AE can make this a possibility as they can be implemented to understand the physical structure and the dynamic behaviour respectively. Moreover, the presence of defects further complicates the number of variables to be simultaneously considered to properly assess the adhesive bond strength. Studies carried out so far in the literature put forth methods to detect defects whose size is higher than 5cm in diameter. However, these defects usually form due to the coalescence of smaller defects. Hence to assess the life of any structure, it becomes essential that the defects be detected in the early stages before they coalesce to form one big defect. No such study exists where the presence of a distribution of defects over the bonded area is assessed. Furthermore, the potential of AE as a defect characterisation technique has not been fully explored. This is partially because of it's being a passive technique unlike ultrasonic scanning where an external pulse is fed into the structure to extract defect information. AE relies on the elastic strain energy released from within the structure. Hence this study puts forth the research to support the claim that AE can be used, along with PLB tests as the source, to detect presence of a defect distribution along an adhesively bonded area and to characterise the effect of these on the adhesive bond strength.

It is important to estimate the residual life of an adhesively bonded structure based on the defect distribution. Many of the available studies utilise the conventional test methodologies such as single lap shear testing, DCB testing (mode-I) and ENF testing (mode-II) to assess the effect of defects. However, it may not always be practical to perform these tests on bonded joints with different geometries. Hence, there is a need to formulate a simple yet robust methodology capable of quantifying the residual strength of adhesive bonds.

Castaings [127] investigated the lamb wave propagation through the interfaces of different adhesive bonded aluminium specimens. The surface preparation technique was varied between different specimens. The reference specimen was sand blasted, cleaned and degreased. The other three specimens had interfaces with no sand blasting but cleaned and degreased surface, Cleaned, degreased but with a thin oil film applied and sand blasted, cleaned, degreased and with a thin layer of glass-epoxy inserted within the adhesive layer. Wang *et al* [11] investigated the effect of different surface pre-treatments and environmental exposure conditions on the fatigue crack growth performance of adhesive bonded single-edge notch bend specimen. They reported that exposure of the cured adhesive joint specimens to hot and humid conditions significantly deteriorates the bond quality. In specific, when exposed to humid environments the interfacial bonding degrades considerably because of moisture ingress along the interphase region loosening the inter-molecular bonds. This conclusion was supported by the observation that the exposure to moisture did not cause significant damage within the adhesive layer as the moisture absorption capability of the adhesive is significantly low and negligible when compared to the moisture ingress along the interfaces. This leads to a predominant interfacial failure mode in fatigue tests. This study proves that the interfacial bond quality significantly changes with changes in environmental conditions and hence needs to be dealt with as the weakest link in the adhesive joint.

The effect of presence of defects, even though has been investigated, has been confined to defects within specific geometries like SLJ and confined to specific locations of the adhesively bonded joints. Also, many of these studies deal with defects such as voids within the adhesive layer and in some cases, disbonds along the interface. However, previous studies have indicated that the possibility of void formation within the cured-adhesive layer is very low unless air bubbles are formed due to faulty fabrication. The interface on the other hand is highly susceptible to moisture ingestion which starts along the bond corners and permeates the entire interface thus significantly weakening the bond. Very few studies have considered the possibility of the entire interface being weakened.

Prior to evaluating the strength of bonded joints with defects by mechanical testing, it is prudent to estimate the size, nature and distribution of the defects present. The science of non-destructive testing had extensively been made use of for this purpose. Xu *et al* [128] used acousto-optical interferometry to detect disbonds between a GFRP plate and a concrete slab adhesively bonded together. This technique uses an external sound source to excite resonant frequency vibration in the composite plate which acts as a thin circular plate rigidly bonded around the circumference. By varying the defect areas and calculating the corresponding resonant frequencies, the authors have shown that the size as well as the location of the defect can be accurately calculated. However, this method is limited by the maximum frequency that can

detected using the optical fibre based interferometry and in this size the minimum defect size is limited to 2 mm.

AE is a passive technique which listens for failure within any structure by capturing the elastic wave propagation induced by failure energy release. It has been used extensively in composite failure monitoring and structural health monitoring. Several data analysis techniques such as pattern recognition algorithms, signal classifiers etc. have been developed over the last few decades. Even though a few studies have made use of AE for defect detection and fracture characterisation of adhesive bonds, it was always in combination with another NDT technique such as ultrasonic scanning or guided lamb wave scanning. In such a case, AE transducer acts as the signal receiver with the other technique emitting the signal. The potential of AE as a standalone method for defect detection with a simpler signal source such as Hue-Nielsen pencil lead break has not been completely explored before. Senthil *et al* [28] used AE as a monitoring technique in fracture toughness characterisation of adhesive bonded DCB, 4-ENF and ECT tests. They concluded that a good correlation exists between the load-displacement plots and AE activity. However, various AE parameters such as the energy, amplitude and power spectral density have not been studied as possible fracture characterising parameters.

2.13. Thesis topic identification

The above review has provided insights into the basics related to fracture of adhesive bonds, factors affecting failure of adhesive joints, various modes of failure, defects in adhesive joints, effects of environment and defects on bond strength, defect detection, application of AE in adhesive bond characterisation, various modelling of adhesive joints, failure criteria, flexural strength and indentation testing. However, there appears to exist no methodology to correlate the presence of defects and the mechanical strength of an adhesive bond. Some relationships have been observed (mainly in flexural testing of composite samples), but none of these have been applied to adhesively bonded samples. Moreover, there is no comprehensive study that correlates experimental and numerical modelling fracture predictions in adhesive bonds. The strength characterisation methods for defective adhesive bonds currently available involve the use of multiple techniques for the defect detection followed by mechanical testing. Thus, the correlation of data across these various techniques is crucial to obtain meaning interpretation of the failure scenarios. Furthermore, the results obtained from the mechanical testing methods rely completely on either empirical or fracture mechanics based data analysis techniques that depend heavily on the experience of the user. This data does not give any insight into the material behaviour in the micro-scale. Also, the current experimental methods fail to predict an accurate fracture initiation point. The use of AE in this scenario has the possibility of revealing several details regarding the material behaviour that have not been investigated before. AE based detection has the potential

to detect the smallest of cracks that occur prior to the macroscopic failure of the material through crack propagation. Thus, if used it can predict early on-set failure.

Thus, the present study is aimed at using numerical and experimental techniques to detect and characterise the effect of presence of defects on the adhesive bond strength. Thus, this study proposes a methodology to characterise the residual strength of adhesive bonds.

Chapter-3

3. Defect detection - Pencil lead break based AE tests

3.1. Specimen preparation methodology

The following section explains the methodology of specimen preparation and specimen quality control. The geometrical properties of the specimens for all the prepared specimens were the same. However, the interface bonding conditions were varied. For defect detection tests, the specimens have been prepared with different defect area densities along one of the interfaces. The adhesive joints were made by joining aluminium plates whose dimensions are shown in **Table 3.1**. The adhesive layer thicknesses and material properties including the parameters for the bi-linear plasticity models are also shown in the same table.

Properties	**Young's modulus, *E* (GPa)**	**Poisson's ratio (*ν*)**	**Yield strength (MPa)**	**Tangential Modulus (GPa)**	**Length, *l* (mm)**	**Width w (mm)**	**Thickness, *t***
Lower adherend (aluminium)	68.4	0.3	105	5	120	50	1.5 mm
Upper adherend (aluminium)	68.4	0.3	105	5	120	50	0.5 mm
Brittle adhesive (Epoxy)	3.34	0.38	48.07	0.1	--		(100, 250, 500) µm
Ductile adhesive (Acrylic)	0.300	0.2	34	0.01	--		(100, 250, 500) µm

Table 3.1. Material properties and dimensions of the adherends and adhesives used.

The aluminium plates were procured from the manufacturer in the cut state with a thin oil film on each to prevent oxidation. This oil film was cleaned using the Loctite®7063™ degreaser by spraying it on to the plates and wiping with a clean paper towel. This was done on both the faces of the adhesive joint. Next, the plate surfaces were sprayed with Loctite®7649 ™ activator. Temper half hard (AL000730, size: length 120 mm, width 50 mm and thickness 1.5 mm, and AL000645, size: length 120 mm, width 50 mm and thickness 0.5 mm; GoodFellow Ltd., Cambridge UK) aluminium plates were selected for this study. The Vickers micro-hardness of the 2 mm thick aluminium sheet was 37± 2 $HV_{1.96\ N\ (200\ g)}$ measured using Mitutoyo HM 210A machine.

Two types of adhesive bond materials (ductile bond: Loctite®326™, elastic modulus: 0.3 GPa ; brittle bond: Loctite® 3430™, elastic modulus: 3.34 GPa were used between two aluminium

plates (size: 120 mm × 50 mm; thicknesses 0.5 mm and 1.5 mm). **Figure 3.1** describes the scheme of the adhesive bond specimen preparation. As received aluminium metal plate surfaces were degreased using a surface cleaner (Loctite®7063™) and then activator (Loctite®7649 ™) was applied.

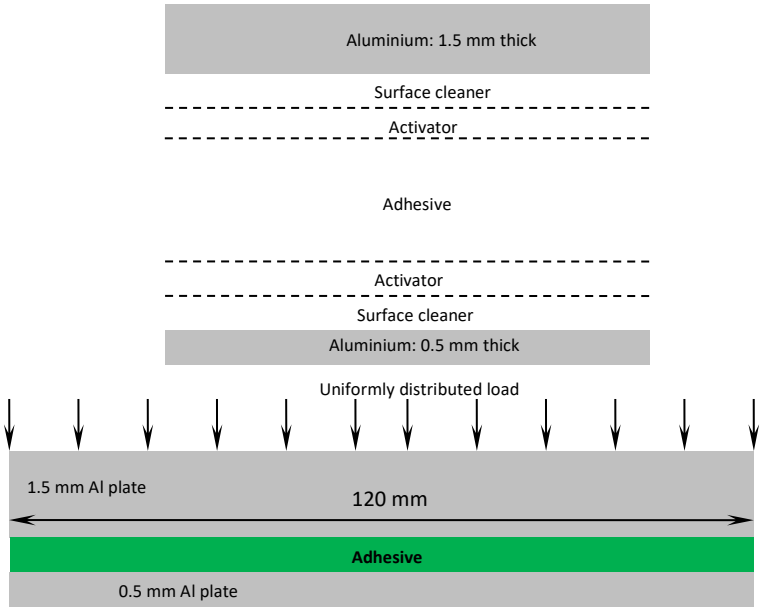

Figure 3.1. Schematic of specimen preparation methodology.

The bond gap was controlled using thin aluminium shims, introduced to maintain a gap of 100 µm and 250 µm, respectively. The shims of very small size (2 mm x 1 mm each) and thicknesses 100 µm and 250 µm were adhesively bonded permanently to the lower plate at the four plate corners and at the centre of two 120 mm sides. These shims were adhesively bonded permanently to ensure that they do not squeeze out during the application of uniform compressive pressure on top of the plate. A uniform distributed load (UDL) using known weights (20 N) was applied and specimens were cured for 2 days at 25^{o}C and a relative humidity of 30%.

The defective specimens were prepared using pre-fabricated templates prepared using composite plates. The use of the template method ensures that there is no overspray on the plate surface and hence prevents overlap between neighbouring circular defects. Since the aim of this study is to detect the presence of distributed kissing bonds. The defects were introduced along the interface between the 0.5 mm thick plate and the adhesive layer. This was done by placing the template on the plate and spraying PTFE through the template on to the plate. This introduces an array of circular defects on the surface of the plate.

The number of passes of the spray over the plate was kept constant across all the specimens prepared. The thickness of the circular defects was not more than 20 µm. The templates used and the plate with the circular defects are shown in **Fig 3.2**. The total defect area was

measured as a percentage of the total face area of the aluminium plate. Two defect area densities were considered in this study (25% and 40%).

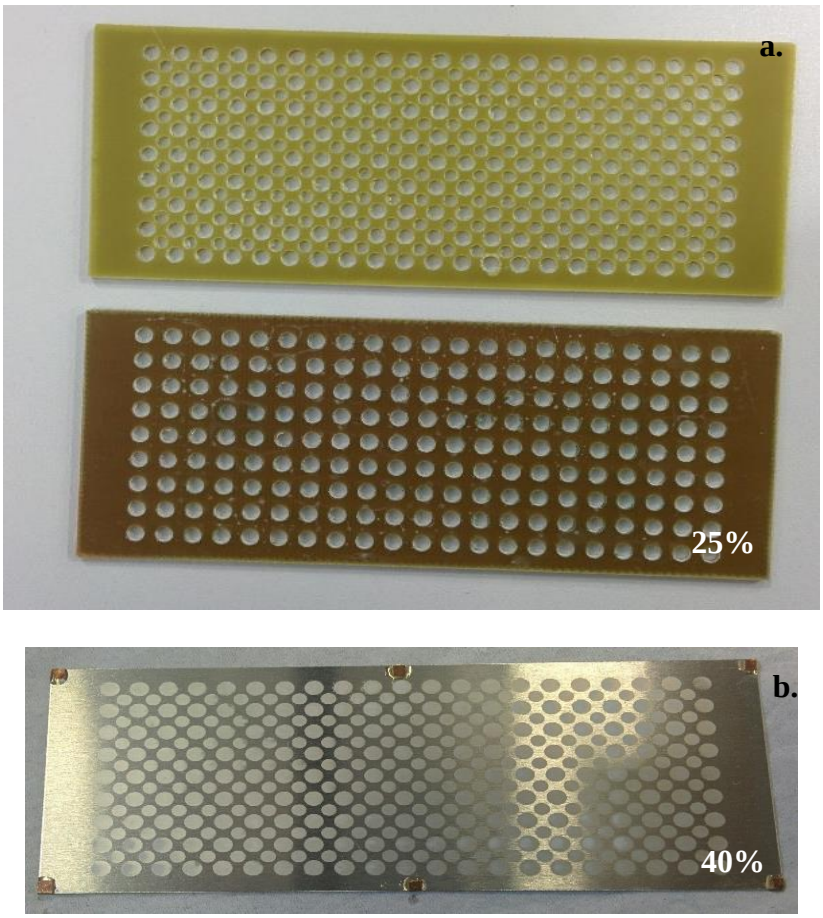

Figure 3.2.a. Templates used for the defective specimen manufacture for flexure experiments, and **b.** prepared specimen with 40% defect area percentage.

The activator was sprayed on to the plate surface before spraying on the PTFE. The rest of the specimen fabrication was the same as with the non-defective adhesive bonds. The specimens were then allowed to cure for 2 days at room temperature. This was according to the curing conditions prescribed by the manufacturer. Both the adhesives reach 100% of their post-cure strength after 4 hours of cure at room temperature. The extra curing time was to allow for complete curing of the adhesives in the presence of impurities.

3.2. Pencil lead break based AE test experimental set-up

The Micro-80D AE sensors were from Physical Acoustics Corporation (PAC, see ***Appendix A***), based on lead zirconate titanate (PZT), with a frequency response range of 100 kHz to 900 kHz and 325 kHz as resonant frequency. Pre-amplifiers of type PAC series 1220A with three amplification levels (20 dB,40 dB and 60 dB) were used in combination with the sensors.

An in-house developed signal conditioning unit was used in addition for further amplification or de-amplification as required.

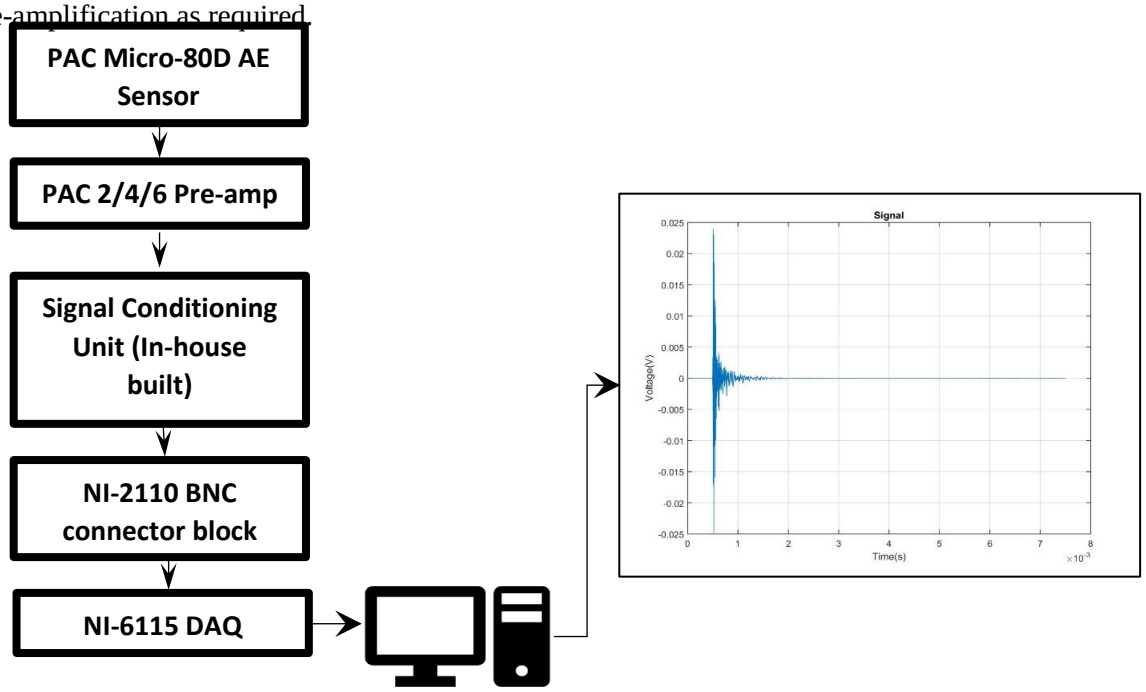

Figure 3.3. Block diagram of the experimental set-up used.

Co-axial BNC cables were used to connect the sensors and the amplifiers to a BNC block (National Instrument, NI-2110) which was connected to a NI-6115 PCI-express data acquisition card. This card has the capability of recording 10 MS/s on four channels (2.5 MS/s on each channel when used simultaneously). A visual interface (VI) built using LabVIEW was used to setup the data sampling and recording. This VI lets the user choose the sampling rate, number of data points to be recorded, trigger voltage level, number of pre-trigger data points, number of data channels and the storage location. The block diagram of the setup used is shown in **Fig 3.3.** A screenshot of the VI is shown in ***Appendix B***. The specimens considered were either aluminium plates or adhesive bonded joints. Each specimen was placed on a wooden block with a V-shaped groove in the middle so that the specimens were simply supported at the two ends (***Appendix-C***). To damp any reverberations passing from the specimen into the wooden block and back, multiple layers of soft paper were placed between the two. The AE sensor was mounted on the specimens using aluminium tape. The thickness of the aluminium tape was less than 15µm and hence does not significantly affect the wave propagation characteristics of the specimen. Silicone coupling grease supplied by RS components was used as the sealant between the sensor and specimen to prevent air gaps (to avoid impairment in wave transmission).

Two different sensor-source location configurations were considered. The first has the sensor and the source (pencil-lead break) on the opposite faces of the specimen. The sensor was located at the geometrical centre of the face in this configuration. This configuration was chosen to study the wave transmission and attenuation through the thickness of the adhesive layer. The

second configuration has both the source and sensor on the same face of the specimen. 7 different points were marked on both the faces of each specimen and the pencil leads were broken at these points. The location of these points is shown in **Fig 3.4**.

The various specimen-sensor configurations are shown in **Table.3.2**. Two different adhesives were considered. The choice of these adhesives was based on their elastic modulus and elongation to failure. Based on these values, they were classified as brittle and ductile adhesives. The adhesive layer thicknesses chosen were 100µm, 250µm and 500µm. The total variables were 5 as shown in **Table 3.2**. In total, 2340 different signal recordings were analysed. The thickness was controlled using shims and later measured using a screw gauge. Defects were introduced along one of the interfaces towards the 0.5 mm thick plate.

Configuration	Number of points	PLB tests per point	Adhesive layer thickness (A)	Adhesive type
0.5-A-1.5-D	6	5	100µm, 250µm, 500µm	Brittle, Ductile
1.5-A-0.5-D	6	5	100µm, 250µm, 500µm	Brittle, Ductile
S-0.5-A-1.5-D-P	7	5	100µm, 250µm, 500µm	Brittle, Ductile
S-1.5-A-0.5-D-P	7	5	100µm, 250µm, 500µm	Brittle, Ductile

***S-**Sensor**, A-**Adhesive layer thickness**, D-**Defect area percentage**, P-**Pencil break

Table 3.2. Configurations of sensor-source combinations tested. This table is for both the brittle and ductile adhesives

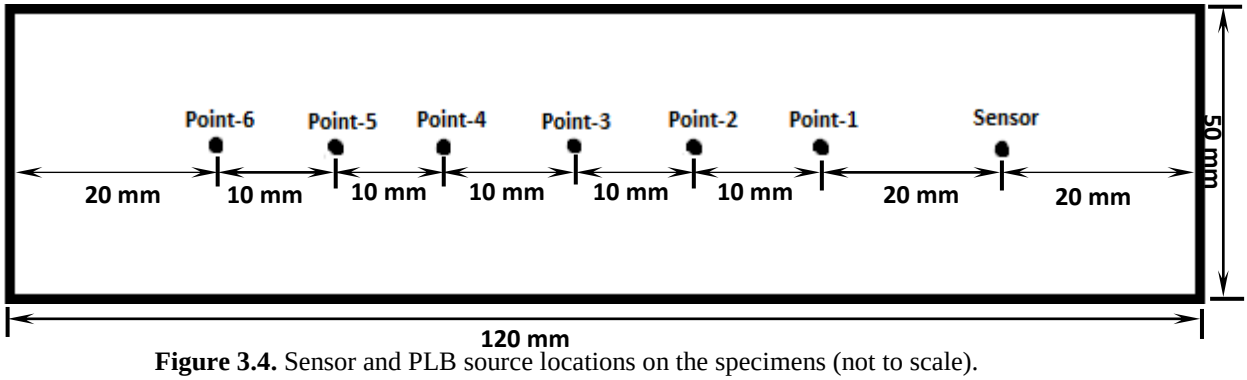

Figure 3.4. Sensor and PLB source locations on the specimens (not to scale).

The defects were introduced as small circular areas distributed in a symmetric grid. These defects were produced by spraying PTFE through a template. This template has a uniform distribution of holes which when sprayed through lead to the grid pattern on the metal plate. The size and distribution of these defects were chosen to simulate localised kissing bonds along the interface. Previously, several methods have studied the suitability of various techniques in identifying a single defect with a large size located within the adhesive layer. However, the

present study is aimed at studying the suitability of AE in combination with PLB tests to identify small defects distributed over the interface of the specimen.

3.3. Specimen naming convention for adhesive bonded specimens

The letter ‘S’ denotes the sensor and the letter ‘P’ denotes the pencil break (Source). The first configuration is when the AE sensor and the source (pencil break) are located on the opposite faces of the specimen. In this case, the specimen name begins with ‘S and is succeeded by the thickness of the plate on whose face the sensor is located on. This is followed by the adhesive layer thickness and the thickness of the plate on whose face the pencil leads are broken. This is followed by the letter ‘P’ which is again followed by the defect percentage (if applicable).

It must be noted here that the interfacial defects are always located towards the interface between the 0.5 mm thick plate and the adhesive layer. The configurations tested are listed in **Table 3.2.** For example, ‘S-0.5-0.1-1.5-P-25%’ indicates that the sensor is located on the 0.5 mm thick plate and the PLB sources are located on the 1.5 mm thick plate of the bonded specimen, the adhesive layer thickness is 0.1 mm and the defect percentage area is 25%.

The second case is when both the sensor and the source are located on the same face of the specimen. In this case, the letters ‘S’ and ‘P’ are omitted altogether, and the specimen name begins with the thickness of the plate on which the sensor and the source are located. For example, the configuration name ‘0.5-0.1-1.5’ indicates that both the sensor and source are located on the 0.5 mm thick plate of the adhesive sandwich, the adhesive layer thickness is 0.1 mm and the defect percentage area is 0% (since the defect area is not shown). The configuration name ‘0.5-0.1-15-25%’ has the same source and sensor locations as before in addition to a 25% defect area along the interface between the 0.5 mm thick plate and the adhesive layer. In the first configuration, the sensor was always placed at the geometrical centre of the plate face. The sources on the opposite face of the specimen were located at the 7 points as shown in **Fig 3.4**. The configurations are shown in **Fig 3.5**. In the second case, the sensor was always placed at 2cm along the central axis parallel to the long edge of the specimen. PLB sources were on the remaining six points on the same face as shown in **Fig 3.4**.

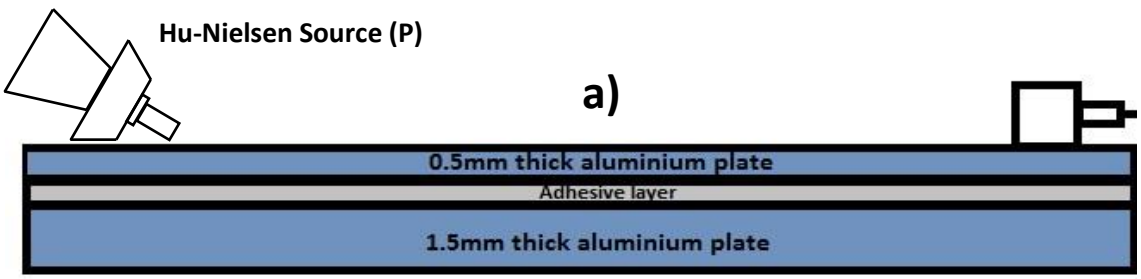

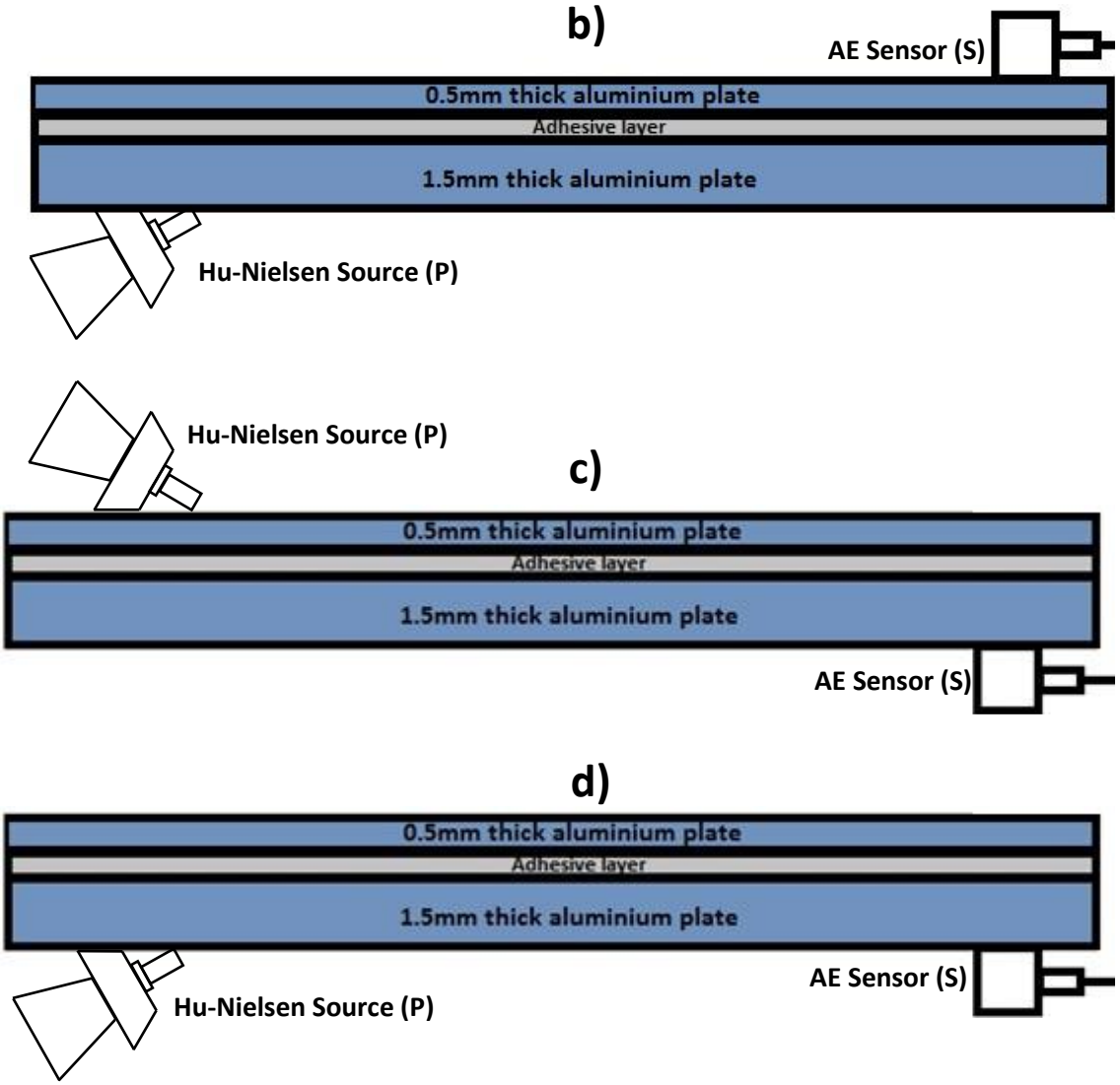

Figure 3.5. Sensor -Specimen-Source configurations **a.** 0.5-A-1.5, **b.** S-0.5-A-1.5-P, **c.** S-1.5-A-0.5-P and **d.** 1.5-A-0.5

3.4. AE signal processing

Signals were acquired at a rate of 2MHz during all the experiments conducted. 5 repetitions were conducted at each point on the specimen and the acquired signals after each test were stored as binary (.bin) files. Signal processing was done using the codes written in the commercial data analysis software MATLAB. The energy content of the signal was measured by calculating the total area under the absolute voltage-time profile.

$$E = \int |V| dt \qquad \textbf{Equation 3.1}$$

The rise time, decay time and hit count were calculated for each signal record by using a threshold value. Different values of the threshold were considered so as to maximise the defect detection capability of the data processing technique. In some cases, the threshold value was

selected based on the peak value of the amplitude instead of the noise. Digital filters were used to separate the high and low frequency components of each signal record. These filtered components were further processed to extract the energy, rise, decay and total times, hit count etc (using MATLAB (ver 7.9.0.529 (R2009b), codes provided in ***Appendix D***). In addition, selected data files were processed using the wavelet transform (WT) technique to identify the prominent frequencies and their variation with time.

3.5. Results

3.5.1. PLB tests on aluminium plates

Before the tests on the bonded specimens, PLB tests were conducted on the 1.5 mm and 0.5 mm thick aluminium plates. Sample signal and corresponding power spectral density(PSD) distribution plot for the 1.5mm plate are shown in **Fig 3.6**. As seen, the plate has a frequency response ranging from 10kHz-400kHz with different energy distributions. However, there are two frequency bands of significant energy density, one in the region below 100kHz and another above 300kHz (~resonant frequency of the sensor). These bands were taken as the basis for further signal processing. To understand the plate wave propagation, dispersion curves were calculated for the 0.5 mm and 1.5 mm plates and the corresponding phase and group velocity curves are presented in **Fig 3.7**.

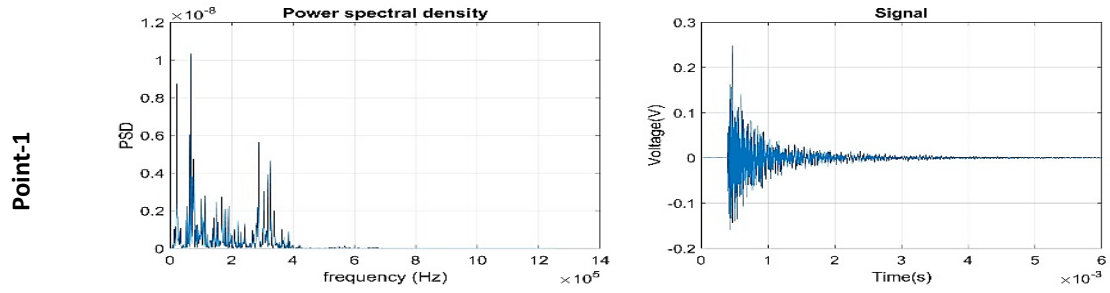

Figure 3.6. Power spectral density vs Frequency and Signal amplitude vs Time plots of PLB tests at various points on the 1.5mm thick Al plate.

From the figure, within the frequency response range of the sensor (0.1MHz to 0.9MHz), there are only two fundamental modes of wave propagation, A_0 (first anti-symmetric mode) and S_0(first symmetric mode), in both the plates. The velocity of the symmetric mode is higher than the anti-symmetric (asymmetric) mode within the frequency range. As a PLB source is being used in this study, the exact application time is unknown and cannot be used to align the theoretical dispersion curves with the recorded signal. To allow analysis of the recorded AE waveforms in both time and frequency domains the wavelet transform (WT) has been utilised.

Wavelet transforms (WT) were calculated for the recorded signals at various points along the plate.

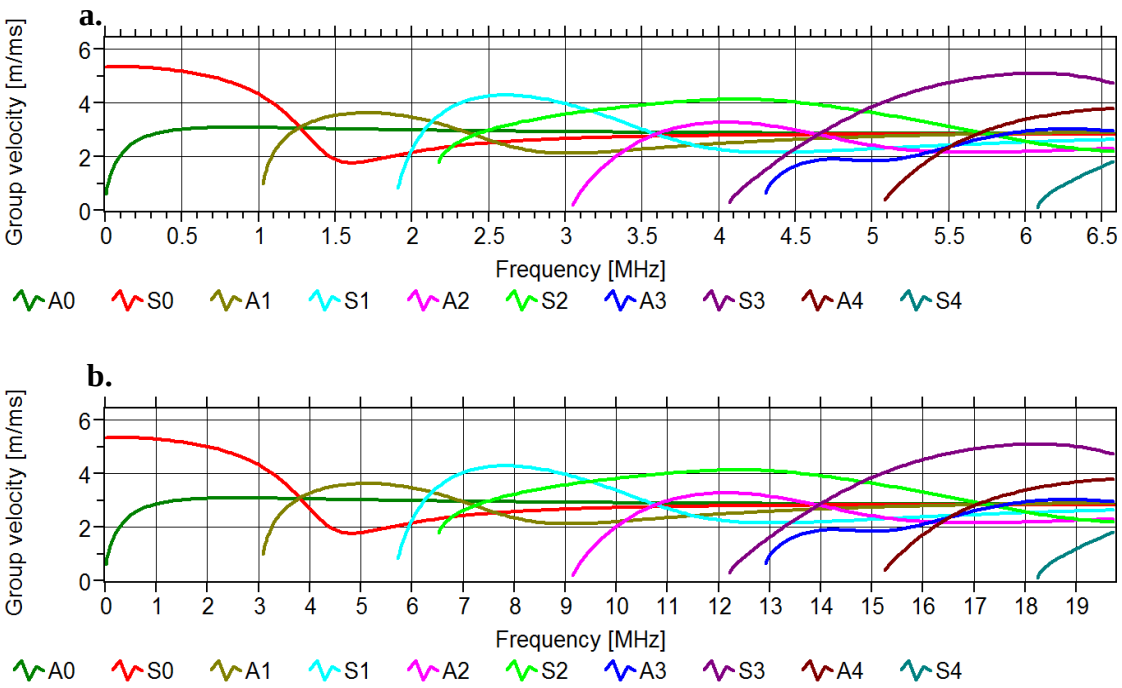

Figure 3.7. Dispersion curves of **a.** 1.5 mm thick and **b.** 0.5 mm thick aluminium plates.

In this study wavelet transforms were implemented using open access AGU-Vallen Wavelet software (ver. R2015.0430.6). The wavelet software utilises a Gabor-type wavelet as this is known to provide the best combination of time and frequency resolution of any available wavelet as the product of its standard deviations in both time and frequency domains are minimised. The dispersion curves calculated for the plates earlier were then superimposed over the WTs of the PLB tests done on the plates.

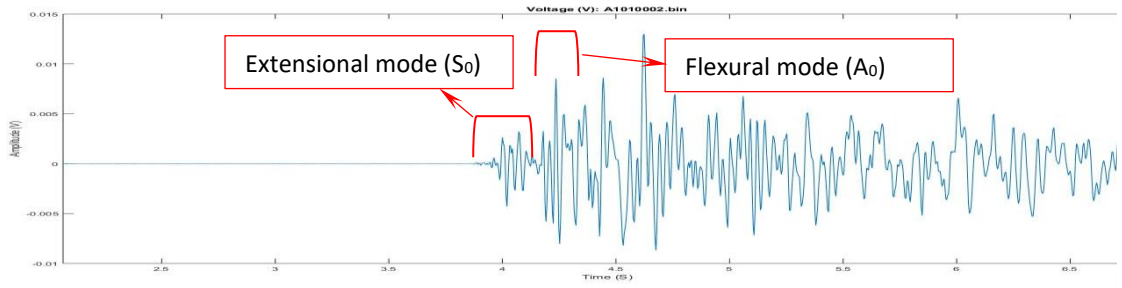

Figure 3.8. Magnified view of signal from PLB test at 60 mm from sensor on 1.5 mm thick aluminium plate.

In this study, the group-velocity curves have been generated using open-access Vallen Dispersion software (ver. R2015.0430.6), using 6420 m/s and 3040 m/s for longitudinal and shear wave velocities in aluminium. This was to identify the first arrival of the principal wave modes.

The dispersion curves calculated were under the assumption that the dimensions of the plate are infinite and the reflections from the specimen edges are negligible in amplitude. However, the plates used in this study were of finite dimensions and hence the recorded signal had multiple reflections from the edges of the plate.

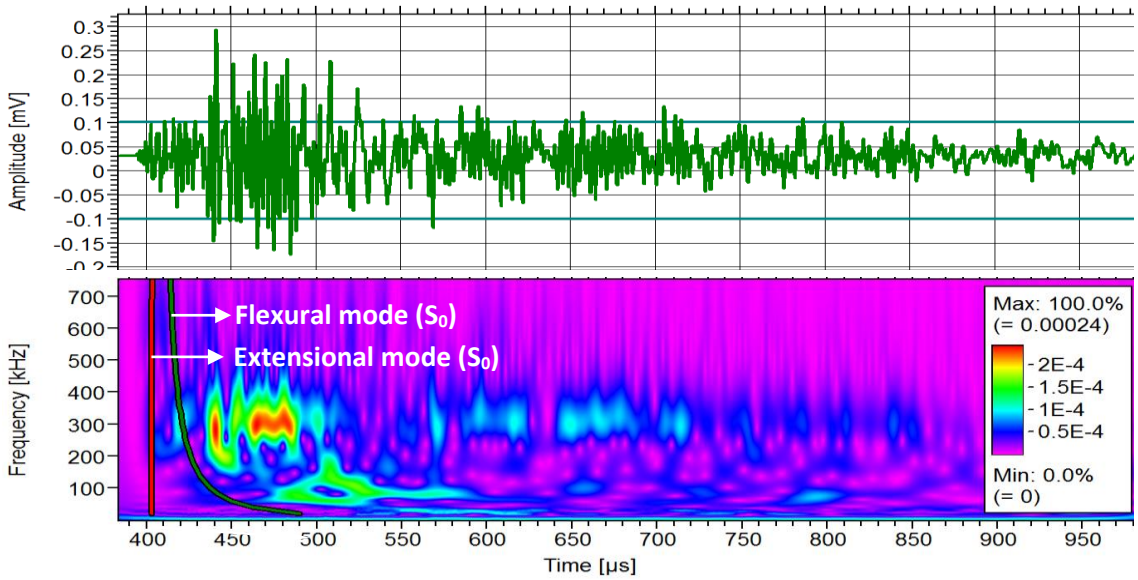

Figure 3.9. Wavelet transforms (WT) of signal from PLB test on 0.5 mm thick Aluminium plate.

Fig 3.8 shows the magnified view of the signal acquired from the PLB test on the 1.5 mm thick plate. The signal clearly shows a low amplitude high frequency component arriving first at the sensor followed by a high amplitude high frequency component. The WT of a signal acquired at 6cm from the sensor on the 0.5 mm thick plate is shown along with the superimposed dispersion curves in **Fig 3.9**. As seen, the extensional (symmetric-S_o) mode arrives first at the sensor followed by the flexural mode (anti-symmetric-A_o).

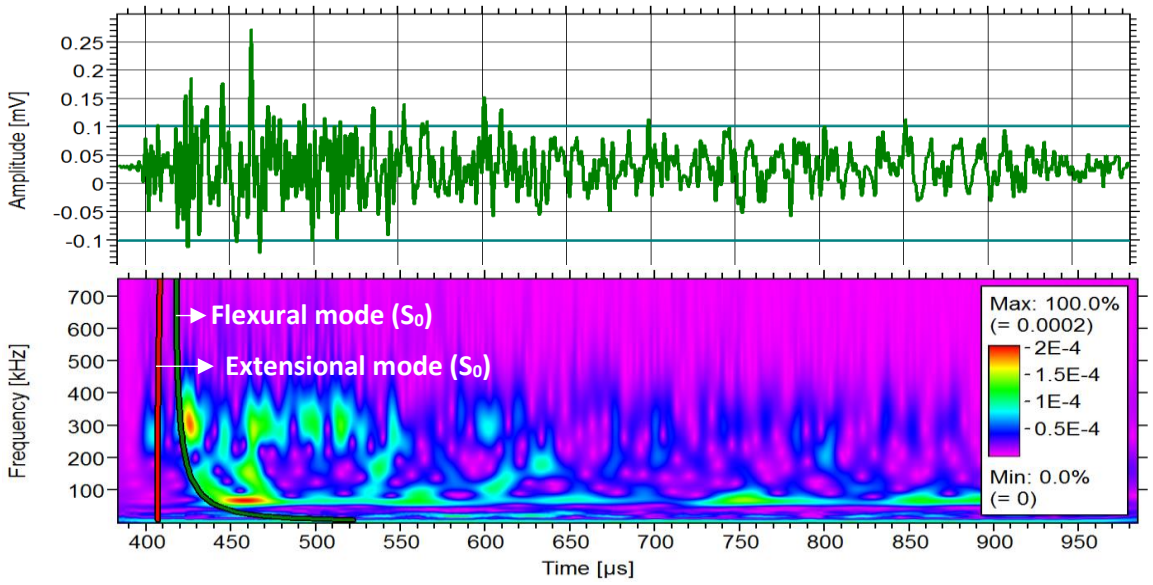

Figure 3.10. Wavelet transforms (WT) of signal from PLB test on 1.5 mm thick Aluminium plate.

The amplitude of the extensional mode is smaller compared to the flexural mode as seen from **Fig 3.9**. Another important observation from **Fig 3.9** is that the low frequency flexural mode is not as damped as the high frequency flexural mode. The low frequency component resonates within both the plates (0.5 mm thick and 1.5 mm thick) (**Fig 3.9** & **Fig 3.10**) longer whereas the high frequency component is damped and reaches a negligible level quickly. Also, the energy content of the PLB test signals on the 1.5 mm thick plate is higher than those on the 0.5 mm thick plate.

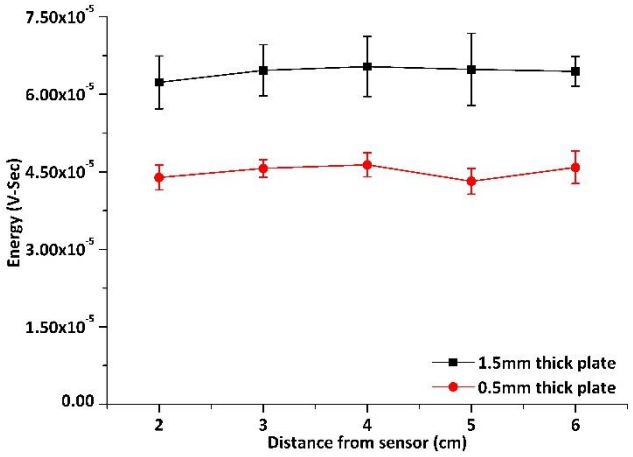

Figure 3.11. Average energy values of signals from PLB tests on 1.5 mm thick and 0.5 mm thick aluminium plates.

Figure 3.11 shows the average energy values of the PLB test records and the standard deviations calculated from different repetitions. As seen, the energy content of the signals from PLB tests on the 1.5 mm thick plate is higher. **Figure 3.11** also shows that the distance from the sensor has no considerable effect on the energy in both the 0.5 mm thick and 1.5 mm thick plates. It must be mentioned here that the energy was calculated over the entire time span of the signal recording so that all the reflections from the plate edges were included. The calculation was based on the area under the absolute amplitude vs time profile. The sensor was mounted onto the specimen using an adhesive aluminium tape and no external load was applied on the sensor. PLB tests were then conducted on adhesive bonded specimens. The configurations tested are as mentioned earlier in **Fig 3.5**. The results obtained are presented separately for the brittle and ductile adhesives and comparisons and observations are made.

3.5.2. Effect of adhesive layer and thickness

3.5.2.1. Brittle adhesive

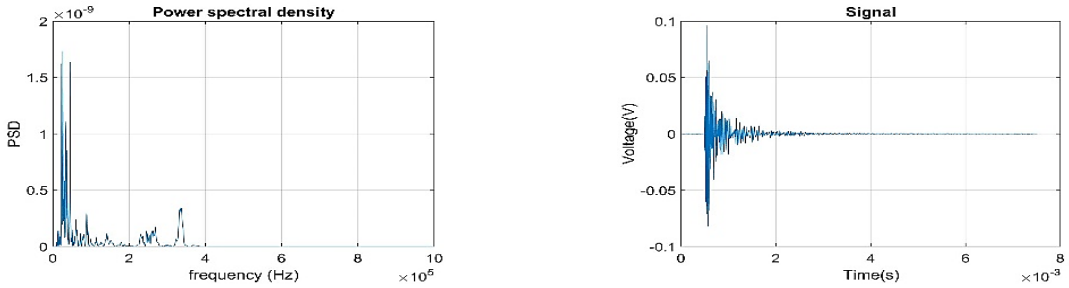

Figure 3.12. Time domain signals and corresponding PSD plots of PLB tests done at various distances from sensor on '0.5-0.1-1.5' brittle adhesive specimen.

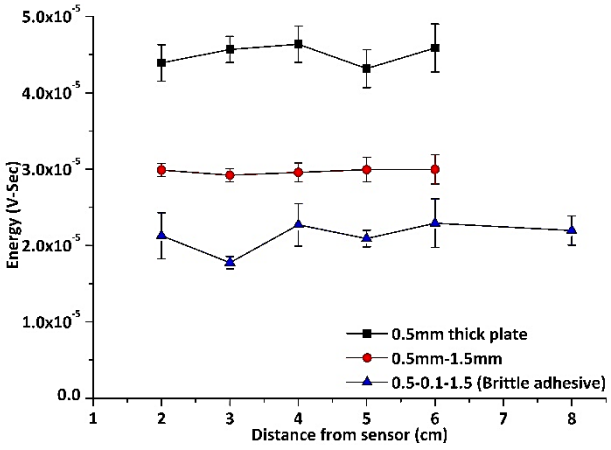

Figure 3.13. Comparison of average energy values from signals of PLB tests at different points on 0.5 mm thick aluminium plate, '0.5-1.5' configuration and '0.5-0.1-1.5' configuration.

Three adhesive layer thicknesses (100µm, 250µm, 500µm) were considered in both the brittle and ductile adhesive bonded specimens. **Fig 3.12** shows the signal amplitude vs time plot and corresponding PSD plot of a sample PLB test done on the specimen configuration '0.5-0.1-1.5'. One observation that can be made from these plots is that the addition of the adhesive layer seems to damp the high frequency components within the multi-layer structure. To further understand the effect of the adhesive layer, a comparison was made between the energy content of the signals of PLB tests on the above adhesive bonded specimen and a 0.5 mm plate. This plate was chosen as both the source and the sensor were on the 0.5 mm thick plate side of the specimen in this configuration. **Figure 3.13** shows the comparison. Even though there is not a significant difference in energy levels at different points within the same specimen, there is considerable reduction in the average energy (~100%) with the addition of an adhesive layer.

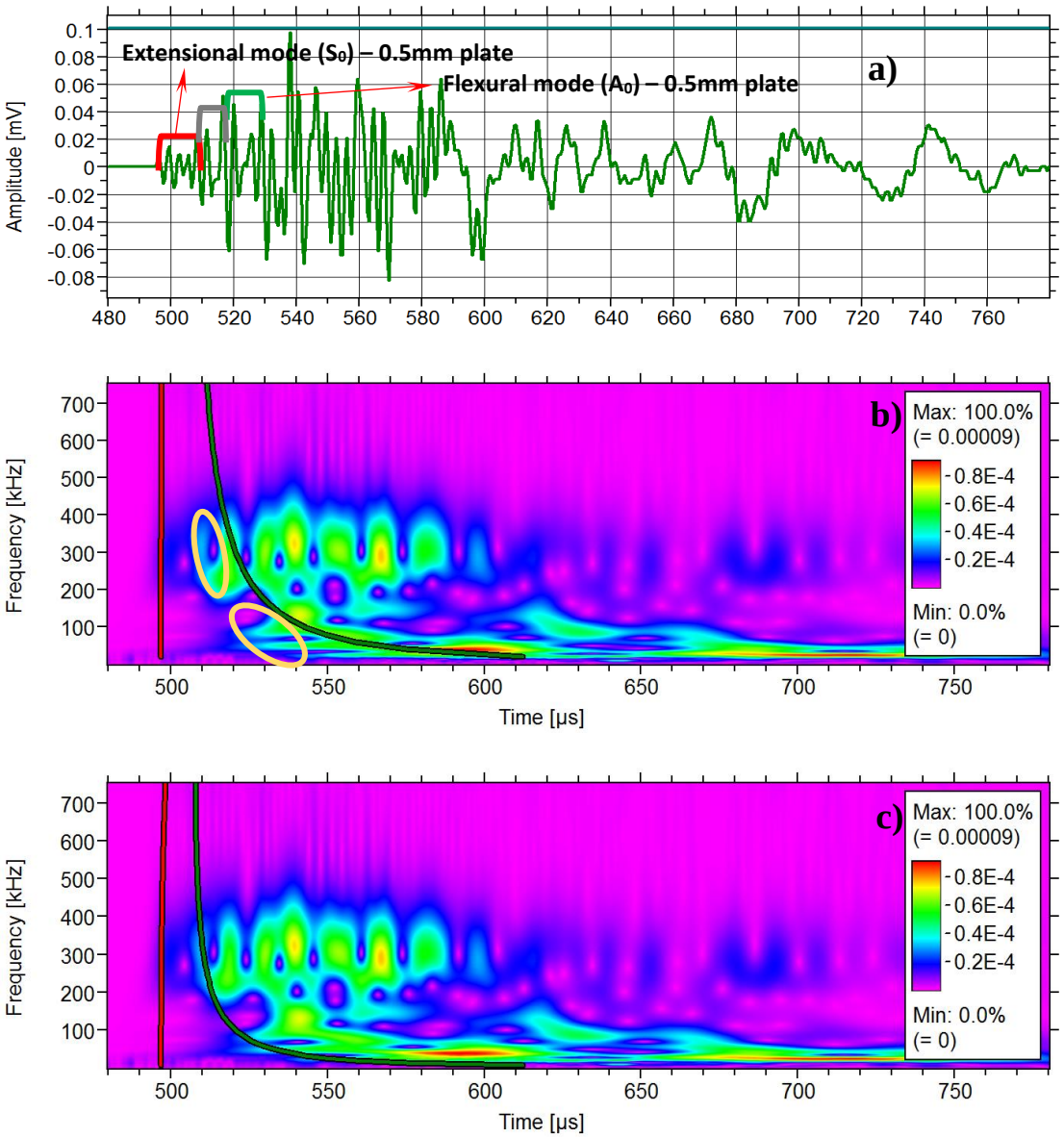

Figure 3.14. a. Time domain signal and WTs of signal acquired from PLB test at 50 mm from sensor on the configuration '0.5-0.1-1.5' with **b.** 0.5 mm dispersion curve fit and **c.** 1.5 mm dispersion curve fit.

The average energy values obtained from PLB tests on the configuration ‘0.5-1.5’ are also shown in this **Fig 3.13.** This test was done by taping together both the plates in close contact. However, it is expected that there exists a small air gap and this is responsible for damping of the signal between the two plates. The damping effect of the adhesive was higher than in the case of the two plates in contact. Next, WT was performed on the acquired signals. **Figure 3.14** shows the time domain signal and the corresponding WT of a signal of a PLB test at 50 mm from the sensor on the configuration ‘0.5-0.1-1.5’. The dispersion curves of the 0.5 mm plate were superimposed on the WT plot. As seen in the individual plates, the amplitude of the extensional mode is quite low compared to that of the flexural mode. Also, the flexural mode exhibits both

the low and high frequency components. For a given threshold value, the low frequency flexural wave has a higher time duration than the high frequency flexural component. From **Fig 3.14**, the total frequency response can be divided into two components. A 175 kHz low pass component and a 175 kHz high pass component. These frequency bands will be used to build digital filters later to study the effect of the thickness of the adhesive layer. There are a few differences between the present WT and that of the signal from the 0.5mm plate. The most noticeable one being that there seems to be another wave packet that appears between the extensional and flexural components emanating from the 0.5 mm thick plate.

This is indicated with a grey bracket in **Fig 3.14a**. This could be one of the wave modes from the 1.5 mm thick plate. The dispersion curves corresponding to A_0 and S_0 modes of the 0.5 mm thick and 1.5 mm thick plates have been superimposed on the WT. These are shown in **Fig 3.14b** & **3.14c**. The same wave packet is highlighted with orange ovals in **Fig 3.14b**. From **Fig 3.14c**, this corresponds to the flexural component from the 1.5 mm thick plate. The velocities of the extensional and flexural waves in both the plates were found and presented in **Table 3.3**.

Thickness	**Extensional wave group velocity(m/s)**	**Flexural wave group velocity(m/s)**
0.5mm	5349	2085
1.5mm	5295	2185

Table 3.3. Wave-mode velocities in 0.5 mm thick and 1.5 mm thick plates at a frequency of 300kHz.

From the table, the extensional wave generated in the 0.5 mm thick plate should be the first to arrive at the sensor. Next will be the extensional wave generated in the 1.5 mm thick plate followed by the flexural wave in the 1.5 mm thick plate and finally the flexural wave in the 0.5 mm plate. To confirm this hypothesis, a simple calculation was made of the time required by the latter three wave modes to reach the sensor after the extensional wave in the 0.5 mm plate first appears. The time estimate 't' can be estimated using

$$V_2 = \frac{V_1 d}{V_1 t + d} \qquad \textbf{Equation 3.2}$$

Where

V_1 = Velocity of the extensional wave that first reaches the sensor.

V_2 = Velocity of the wave mode whose arrival time difference with respect to the first wave is to be estimated.

d = Distance of the sensor from the location of the PLB.

t = Time taken by the wave mode to reach the sensor after the first extensional wave reaches the sensor.

From the above equation, the calculated arrival times of the above-mentioned modes were 9.532×10^{-8}s, 1.353×10^{-5}s and 1.463×10^{-5}s for the extensional mode in 1.5mm thick plate, flexural wave in 1.5 mm thick plate and the flexural wave in the 0.5 mm thick plate respectively. The respective wave packets in the signal were identified using the WT and the time difference between them was calculated. In the case of the signal in **Fig 3.14**, the extensional wave from the 1.5 mm thick plate either cannot be seen or is so close to the extensional wave from the 0.5 mm thick plate that it cannot be distinguished. It is also possible that it is completely damped by the adhesive layer. The time differences of the remaining two wave packets were found out to be 1.35×10^{-5}s and 1.51×10^{-5}s respectively. These values match closely with those calculated, thus proving that the extra wave packet seen in the WT was the flexural wave from the 1.5 mm thick plate. These observations show that the addition of the adhesive layer does not impact the propagation velocities of the plate wave modes. The adhesive layer only reduces the amplitude of the wave modes.

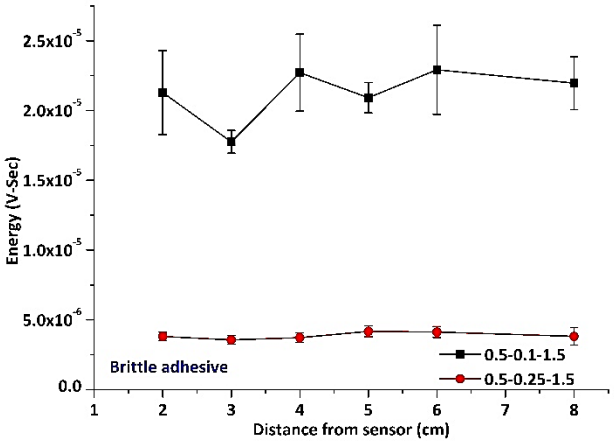

Figure 3.15. Average energy of signals from PLB tests at various locations for the configurations '0.5-0.1-1.5' and '0.5-0.25-1.5'.

The effect of increasing the adhesive layer thickness can be seen from **Fig 3.15**. The average energy levels of two different adhesive layer thicknesses have been compared in this plot. The specimen-sensor configuration is the same between the two. As seen, as the adhesive layer thickness increases, the overall energy content of the recorded signals decreases, thus demonstrating the damping effect of the adhesive layer. However, the energy decrease with increasing thickness might be confined to a particular frequency band. To find out if this is the case, further analysis using digital filters designed using MATLAB filter design and analysis tool

was carried out. The frequency ranges have been selected by visually determining the differences between the WTs of the metal plates and those of the adhesive bonded specimens (not shown here). To compare the relative damping of different frequency components of the signal, the ratio of the energy contents of the low and high frequency components was calculated for different thicknesses. These values for PLB tests at different points for the different configurations are shown in **Fig 3.16a**. It can be seen from the figure that as the adhesive layer thickness increases, the energy ratio decreases. Here, 'E1' represents the energy of the 175kHz-lowpass component and 'E2' represents that of the 175kHz-highpass component. From **Fig 3.16b**, the low frequency component has higher energy than the high frequency component at lower adhesive thickness, whereas the energy levels of the low and high frequency components are similar at higher adhesive thickness.

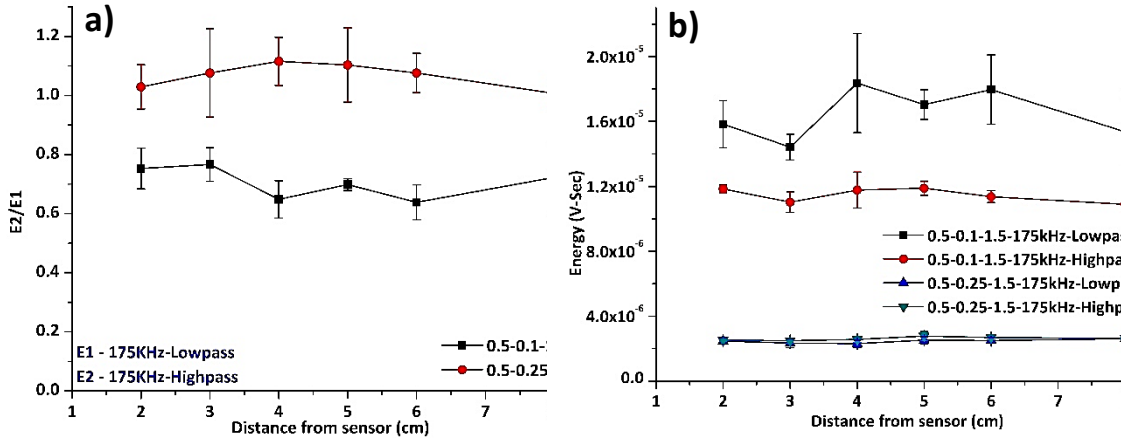

Figure 3.16. Energy ratio comparison of PLB tests on the configurations **a.** '0.5-0.1-1.5' and **b.** '0.5-0.25-1.5'.

Thus, at higher adhesive layer thickness, the low frequency components are relatively damped. To further investigate the effect of the adhesive layer thickness on signal damping, the total duration of each signal above a set threshold was calculated. In addition, this parameter was also calculated for the filtered components for various signals from different configurations. **Figure 3.17** shows the comparison of the total duration above threshold of the 175kHz-Highpass component of the signal acquired on the configurations '0.5-0.1-1.5', '0.5-0.25-1.5'. As seen, the high frequency component exhibits longer duration on the specimen with 250µm thick adhesive layer. This is despite the fact that the overall energy content was lower in this case as shown in **Fig 3.15**. Threshold values in this case were calculated as a fraction of the peak value of the signal record instead of as a multiple of the maximum value of the noise level, though it was ensured that the threshold value is higher than the noise. Both the extensional and flexural wave modes exhibit high frequency components as seen from the WTs of the metal plates. However, as mentioned before, the energy associated with the

extensional mode from both the 0.5 mm thick and 1.5 mm thick plates is too low to produce any reflections. Hence, it can be inferred that the resonating wave mode seen in the adhesive bonds is the flexural wave mode associated with the metal plates.

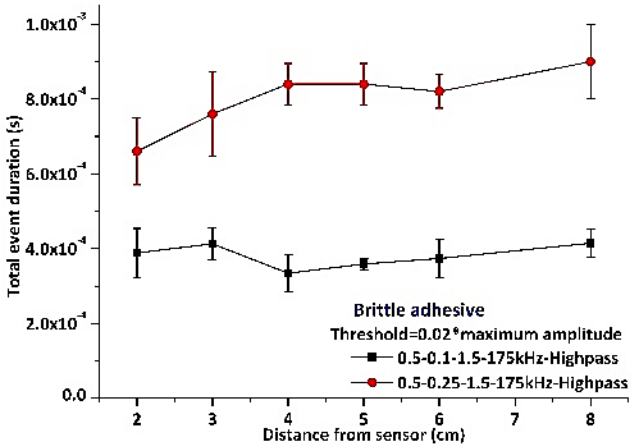

Figure 3.17. Total duration above threshold of 175kHz-High pass component of PLB tests on '0.5-0.1-1.5' and '0.5-0.25-1.5'.

3.5.2.2. Ductile adhesive

This section presents the results obtained from the PLB tests on the ductile adhesive specimens. **Figure 3.18** shows the PSD vs frequency plot and the time domain plot of a sample signal on the configuration '0.5-0.1-1.5'.

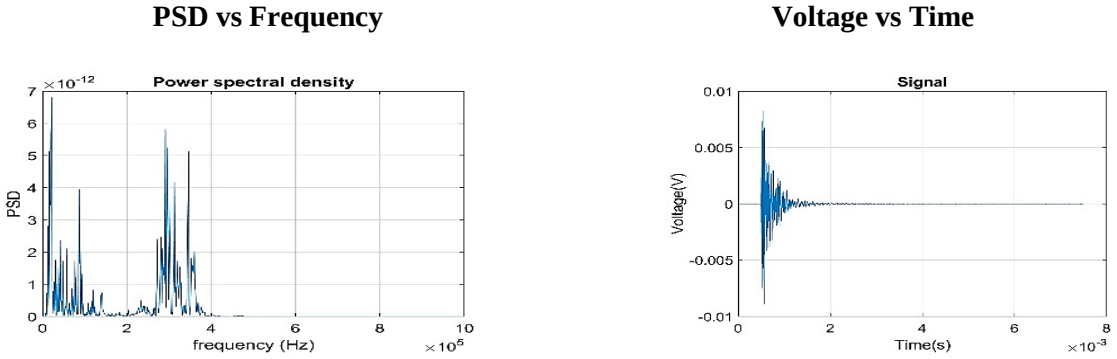

Figure 3.18. PSD vs Frequency plots and Voltage vs Time lots of PLB test on the configuration 'DA-0.5-0.1-1.5'.

From visual observation, the frequency response of the PLB tests exhibits two separate high energy zones, similar to the brittle adhesive specimens. These are 0-175 kHz and 175 kHz-~400 kHz. Also, the decay time associated with the signal is quite low compared to the brittle adhesive specimen PLB tests, showing the higher damping effect of the ductile adhesive layer. Wavelet transforms were also performed on selected signal records to identify the presence of the different plate wave modes from both the aluminium plates. **Figure 3.19** shows the zoomed view

of a signal recorded from a PLB test at 80 mm from the sensor and the corresponding WT. Compared to the WT of the signal from the brittle adhesive specimen (**Fig 3.14**), the AE activity in both the high and low frequency domains looks highly damped in the ductile adhesive specimen.

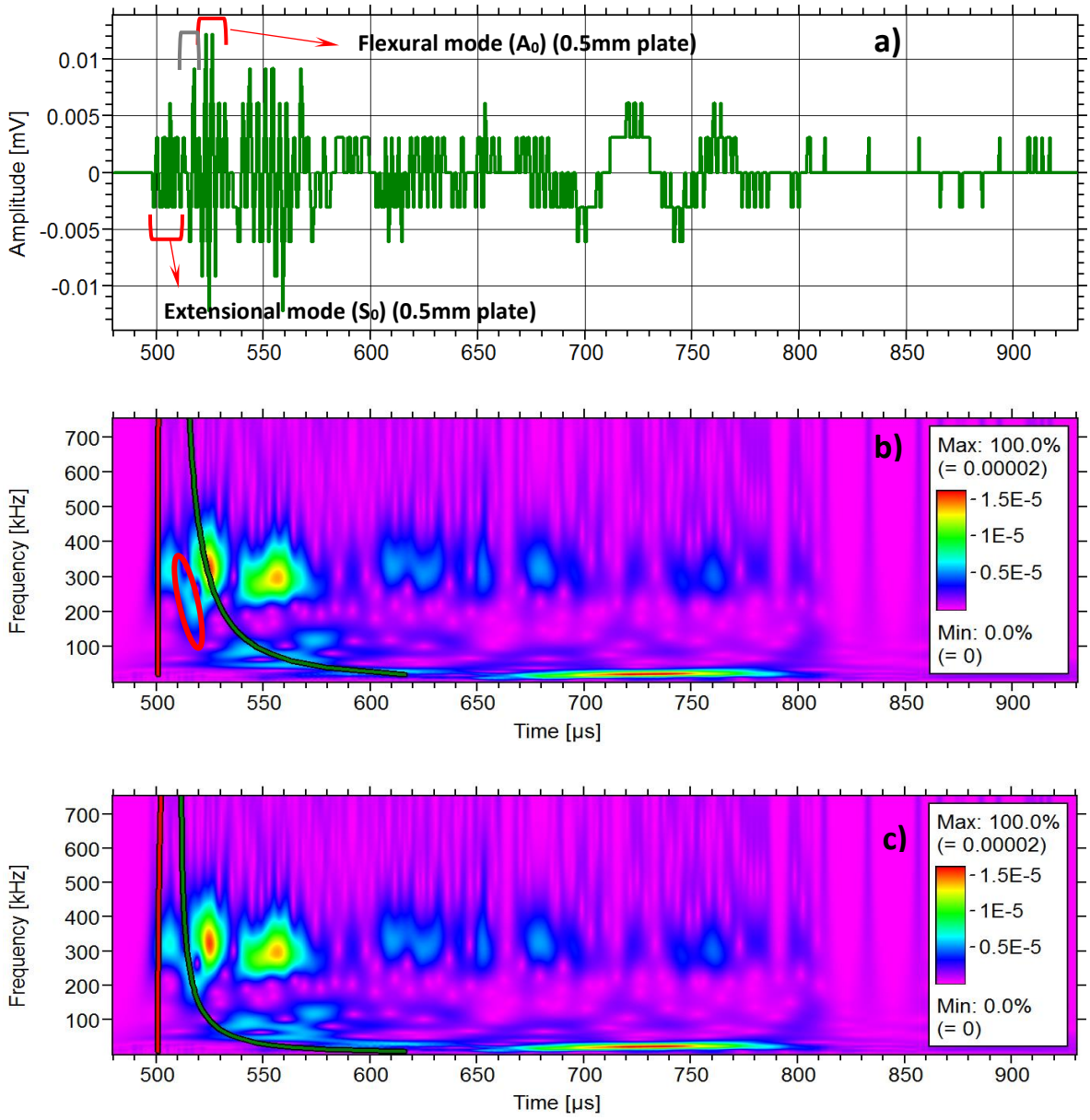

Figure 3.19 .a. Zoomed in view of signal from PLB test on 'DA-0.5-0.1-1.5' at 80 mm from sensor, corresponding WTs with **a.** 0.5 mm dispersion curve fit, **c.** 1.5 mm dispersion curve fit.

As seen, a high frequency-low amplitude wave arrives at the sensor first followed by a high frequency-high amplitude wave (highlighted with red oval in **Fig 3.19b**). The extra wave packet seen between the extensional and flexural waves from the 0.5 mm plate can be identified by calculating the arrival times as was done for the brittle adhesive specimen.

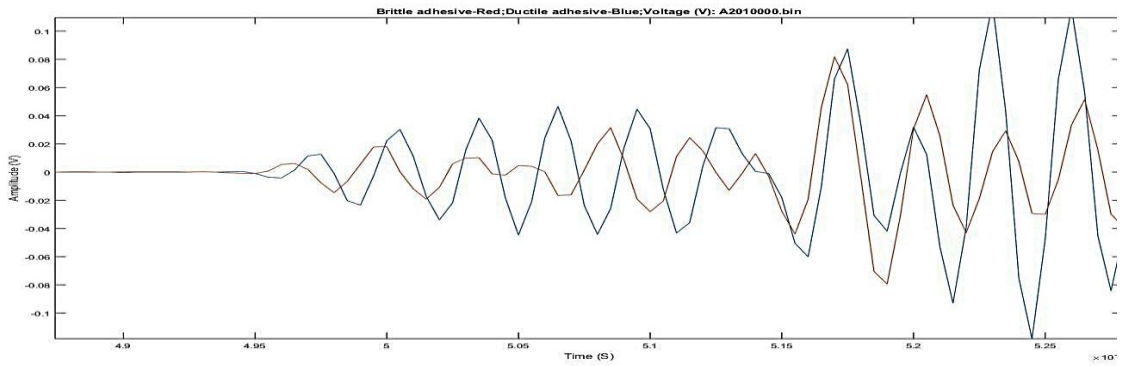

Figure 3.20. Comparison of time domain signals from PLB at 80 mm from sensor on 'BA-0.5-0.1-1.5' (Red) and 'DA-0.5-0.1-1.5'(Blue).

However, there is one obvious difference between the signal recorded on the brittle adhesive specimen and the one from the ductile adhesive specimen. This is shown in **Fig 3.20** in which both the time domain signals are plotted together and the extensional wave that first arrives at the sensor is zoomed into. As seen, the signal from the brittle adhesive specimen shows two distinct wave packets within the first 500µs, whereas the signal from the ductile adhesive specimen shows only one. This difference might be because of change in the degree of damping with the change in the elastic modulus of the adhesive from 3.21GPa of the brittle adhesive to 0.3GPa of the ductile adhesive. As done for the WT of the brittle adhesive specimen signal, the dispersion curves of the 1.5 mm thick plate have been superimposed on the WT shown in **Fig 3.19c.** As seen, the wave packet unaccounted for previously is the flexural wave emanating from the 1.5 mm thick plate. This is similar to what was observed in the brittle adhesive specimen. Using **Equation 3.2**, the estimated time of arrival of the flexural mode from the 1.5 mm thick plate is 2.1×10^{-5}s. This value from the time domain plot of the signal is ~2.05×10^{-5}s. Hence, it is concluded that this wave packet corresponds to the flexural wave from the 1.5 mm thick plate. **Fig 3.21** shows the average energy values of the PLB tests done on the specimens with the three different (ductile) adhesive layer thicknesses and all the different specimen-sensor configurations. The energy decrease with increase in adhesive layer thickness can be seen. There is a significant decrease in the energy as the adhesive layer thickness increases from 100 µm to 250 µm. However, increasing the thickness from 250 µm to 500 µm does not seem to decrease the energy value to a similar level. This is the case where the sensor and the source were on the same face of the specimen. However, in tests where they were on the opposite sides no change was seen across specimens of different adhesive layer thicknesses.

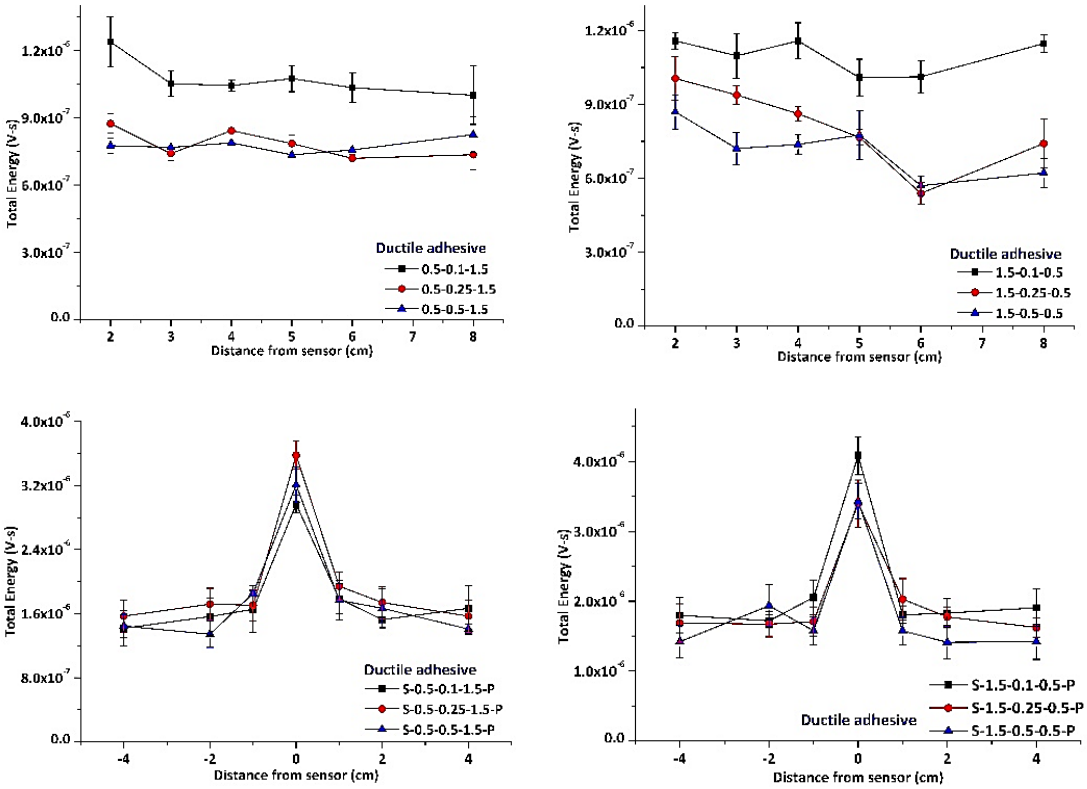

Figure 3.21. Average energy values at different points for PLB tests on adhesive bonded specimens with adhesive layer thicknesses 100 µm, 250 µm, 500 µm.

The above behaviour might be because of the non-uniformity of the adhesive layer thickness across the span and the width of the specimen. Even though spacers were used for maintaining uniform thickness, the externally applied load on the specimen during the curing procedure might have made the metal plates to sag. This leads to the adhesive being squeezed out of the areas with less support. At lower thicknesses, the viscosity of the uncured adhesive prevents the adhesive to be squeezed out and hence expected thickness values can be easily achieved. The effect of the adhesive layer thickness was further investigated by calculating the total event durations of the PLB tests at various locations.

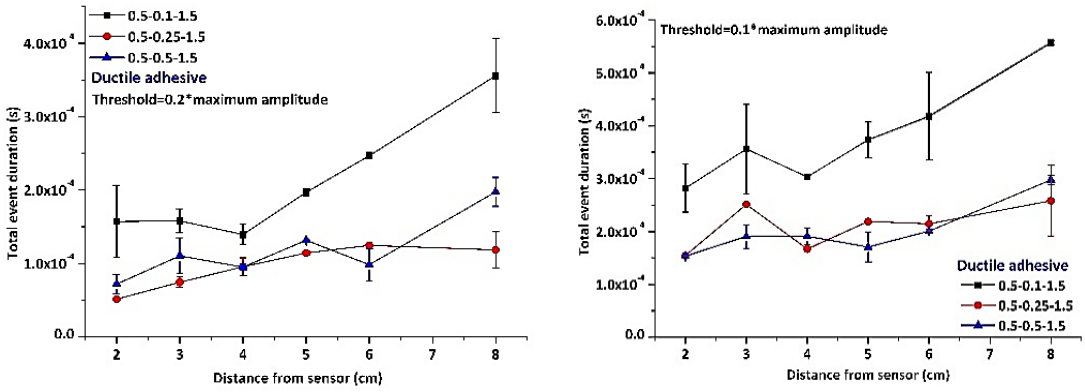

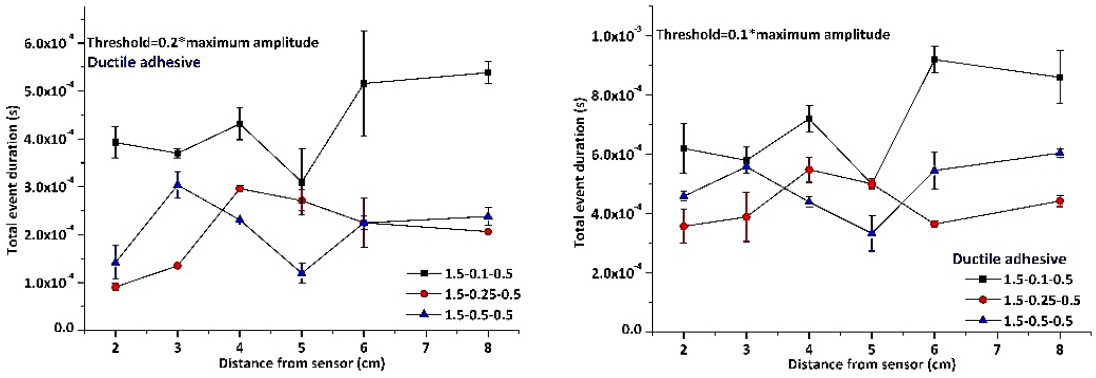

Figure 3.22.Total event duration with threshold equal to a. 20% and b. 10% of maximum amplitude on '0.5-A-1.5' and c. 20% and d. 10% of maximum amplitude on '1.5-A-0.5'

The threshold was set at two values i.e., 20% of the maximum amplitude and 10% of the maximum amplitude. These values were chosen arbitrarily to include majority of the hits (threshold crossings) in the calculation. **Figure 3.22** presents the plots of the total event time of the PLB tests on the configurations '0.5-A-1.5' and '1.5-A-0.5'. These were chosen as these were the only configurations which showed some degree of difference in the energy levels between different adhesive thicknesses. From the figure, the event duration is higher at lower adhesive thicknesses. However, again, there is no significant difference in event duration between the higher adhesive thicknesses. The same observation can be made with respect to the number of hits calculated with the various configurations (**Fig 3.23**). The elastic modulus of the ductile adhesive is 0.3GPa compared to 3.21GPa of the brittle adhesive. Because of the lower elastic modulus, the ductile adhesive is expected to have a higher damping nature compared to the brittle adhesive. To test this hypothesis, the energy content of the PLB tests on a ductile adhesive specimen is compared to that of a brittle adhesive specimen (Configuration – '0.5-0.1-1.5') in **Fig 3.24**. As seen, the energy content of the ductile adhesive specimen is lower.

However, the energy content calculated over the entire record of the signal does not give a complete picture of the energy re-distribution over the frequency response spectrum caused by the change in adhesive elastic modulus. To further understand the effect of the elastic modulus of the adhesive on the frequency response of the bonded joint, the signals from the ductile adhesive specimen have been filtered using the same filters as in the case of the brittle adhesive (175 kHz-Lowpass, 175 kHz-Highpass) and the component energy ratio has been compared between the brittle and ductile adhesive specimens in **Fig 3.24a**. The corresponding energy values of the filtered components have been compared in **Fig 3.24b** & **3.24c**. As seen, the energy ratio decreases with an increase in the elastic modulus. However, the decrease in this ratio, considering the increase in the elastic modulus (~10 times) does not appear to be considerably high. The absolute values of the energy content however, show a clear difference between the brittle and ductile adhesives.

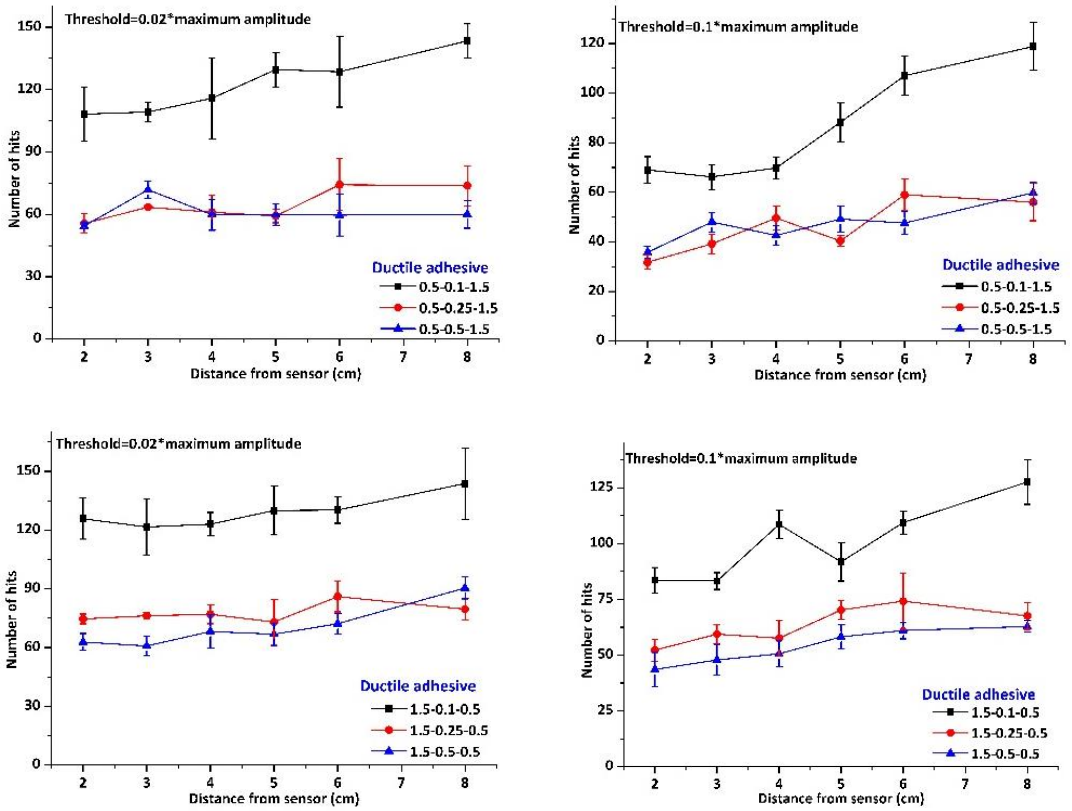

Figure 3.23. Number of hits with threshold equal to a. 2% and b. 10% of maximum amplitude on '0.5-A-1.5' and c. 2% and d. 10% of maximum amplitude on '1.5-A-0.5'

The energy values calculated for the ductile adhesive specimen are an order of magnitude smaller than those of the brittle adhesive. Another important observation that can be made from **Fig 3.24** is that the 175 kHz-highpass component increases in magnitude relative to the low pass component. This shows a redistribution of the energy content of the signal across the frequency spectrum. In the brittle adhesive specimen, the average energy of the high-pass component is about 54% of the average total energy value. In the ductile adhesive specimen, this value rose to 63%.

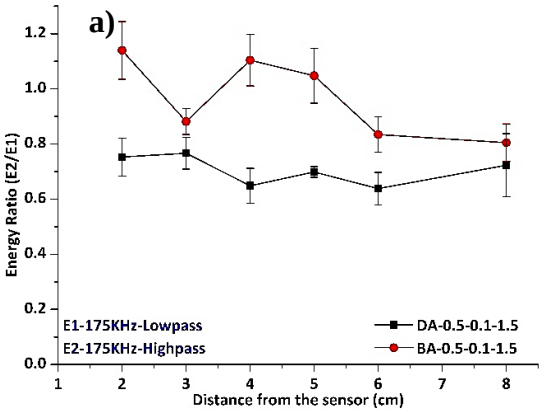

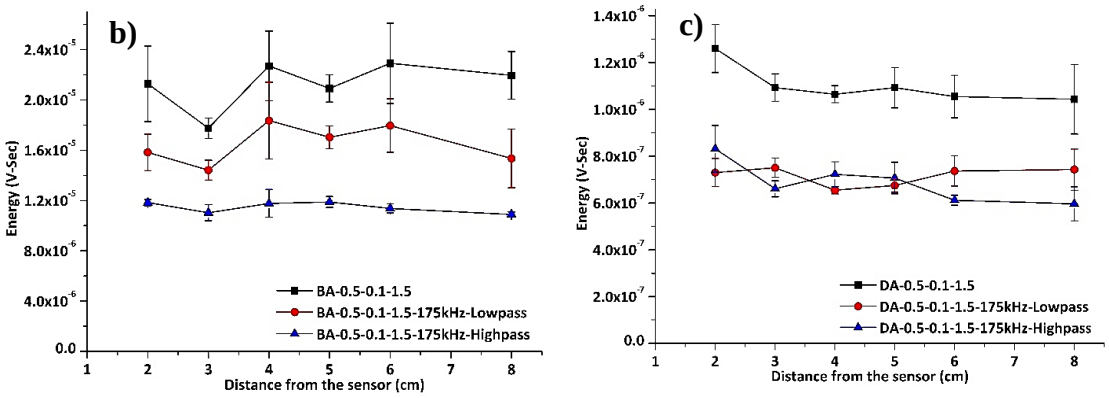

Figure 3.24. Comparison of **a.** energy ratio between 'DA-0.5-0.1-1.5' and 'BA-0.5-0.1-1.5' configurations, **b.** Total energy and energy of filtered components for 'BA-0.5-0.1-1.5', **c.** Total energy and energy of filtered components for 'DA-0.5-0.1-1.5'

However, the energy estimate only gives an overall picture of the signal energy distribution in the frequency domain and tells nothing about the time domain. To understand this, the total signal durations above a chosen threshold value were calculated for a ductile adhesive specimen at different points and compared with those of the corresponding brittle adhesive specimen (**Fig 3.25**).

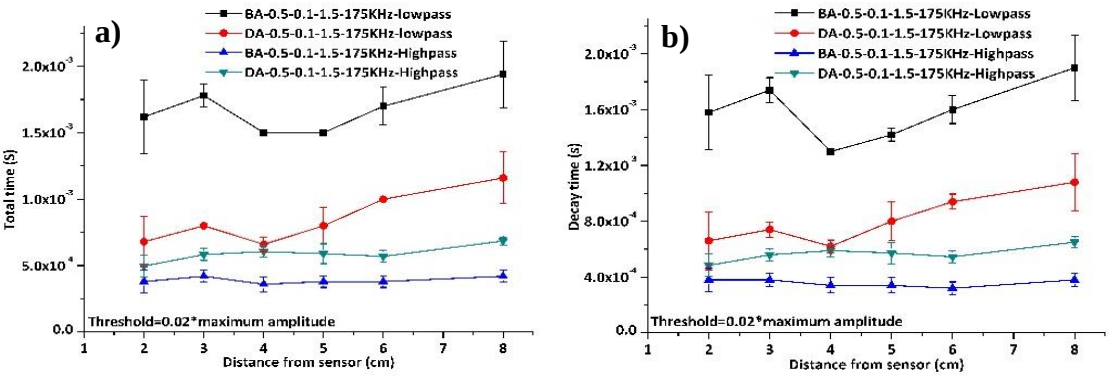

Figure 3.25. Comparison of time above threshold of **a.** 175 kHz-lowpass and **b.** 175 kHz-highpass filtered components of PLB tests on 'BA-0.5-0.1-1.5' and 'DA-0.5-0.1-1.5'.

The plot shows that the high frequency component has a higher total duration in the ductile adhesive specimen compared to the brittle adhesive one. Thus, as the adhesive modulus decreases, damping is higher. However, the signal resonates within the structure for a longer time at lower adhesive modulus. **Figure 3.25b** shows the decay time of the lowpass and high-pass components of the brittle and ductile adhesive signals. The trend is identical to that of the total time plots. This shows that the rise time of the signals is very short and hence is insignificant compared to the total time.

3.5.3. Effect of presence of defects

The suitability of AE to detect the presence of defects along the interface (kissing bonds) of an adhesive bond is investigated in this section. For this study, the same two adhesives, brittle and ductile, have been used. Defects have been introduced along one of the interfaces, by applying PTFE spray sprayed through a template onto the plate surface. This template has holes cut through its thickness, the dimensions and pattern of which have been chosen to constitute a percentage of the face area. This template and the produced PTFE spray grid pattern on the plate surface are shown in **Fig 3.2**. As mentioned earlier, two defect area percentages were chosen, 25% and 40%. In the previous section, to explain the effect of the elastic modulus and thickness, only one configuration has been made use of, '0.5-A-1.5' ('A' represents adhesive layer thickness) for both the brittle and ductile adhesives. In this part of the study, however, different configurations have been explored to maximise the differences in the parameters characterising the effect of the defects. Also, total duration calculation, digital filtering, energy calculations have been made use of.

3.5.3.1. Brittle adhesive

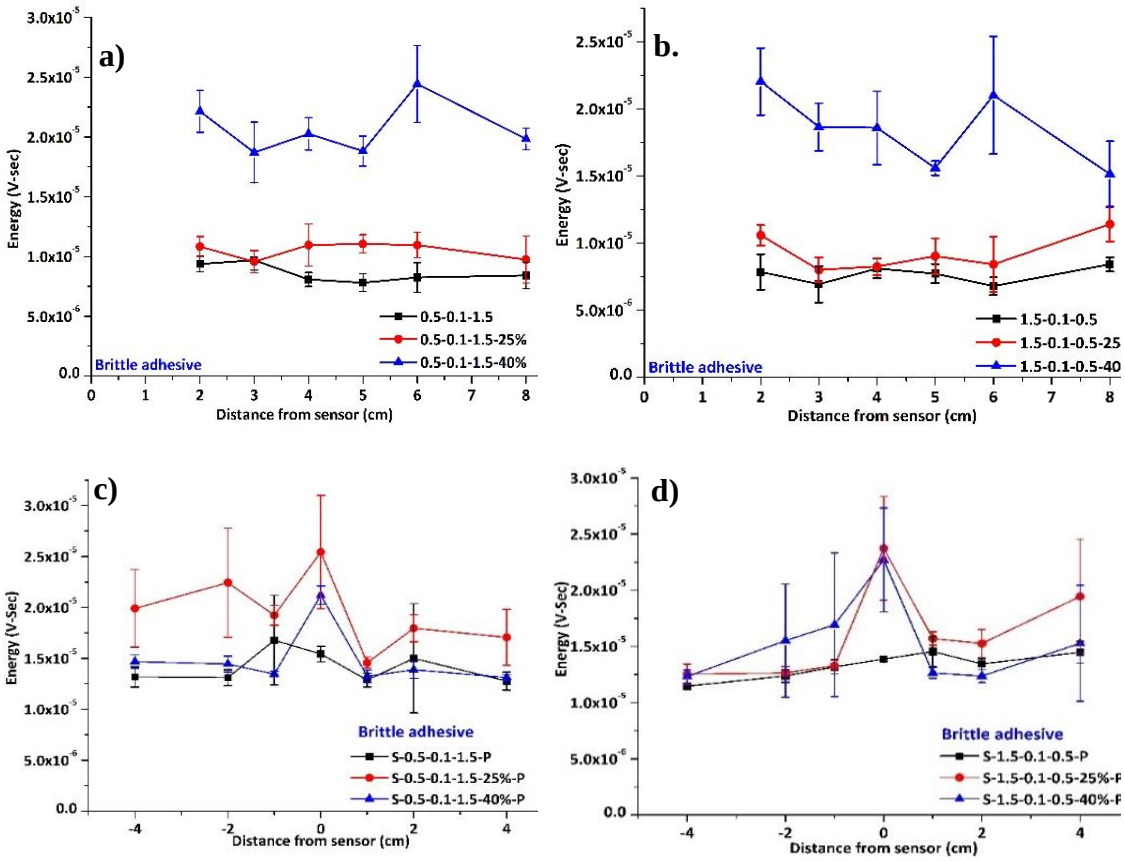

Figure 3.27. Average energy values of PLB tests done on the brittle adhesive specimen configurations **a.** 0.5-0.1-1.5, **b.** 1.5-0.1-0.5, **c.** S-0.5-0.1-1.5-P, **d.** S-1.5-0.1-0.5-P.

Figure 3.27 shows the average energy content plots of 100µm thick brittle adhesive layer specimens with different defect area percentages and different configurations. The energy calculation, as done before, includes the total area under the time domain signal. As seen from the figure, as the area percentage of the defects increases, the total energy content decreases in some configurations and stays almost the same in the remaining. In those configurations with the sensor and the PLB source on the same side of the specimen, there seems to be a large enough difference in the energy to differentiate between the defective and non-defective specimens. However, there is not a significant difference between the specimens with 25% and 40% defect area to consider total energy to be a reliable parameter in any configuration in this case, though it may be used as an indicator of whether the adhesive bond has defects along the interface. **Fig 3.28** shows the average energy of PLB tests at different locations on various configurations for the 250µm thick brittle adhesive specimens. As seen, in this case too, energy does not show a distinguishable difference between the specimens with 25% defect area and 40% defect area.

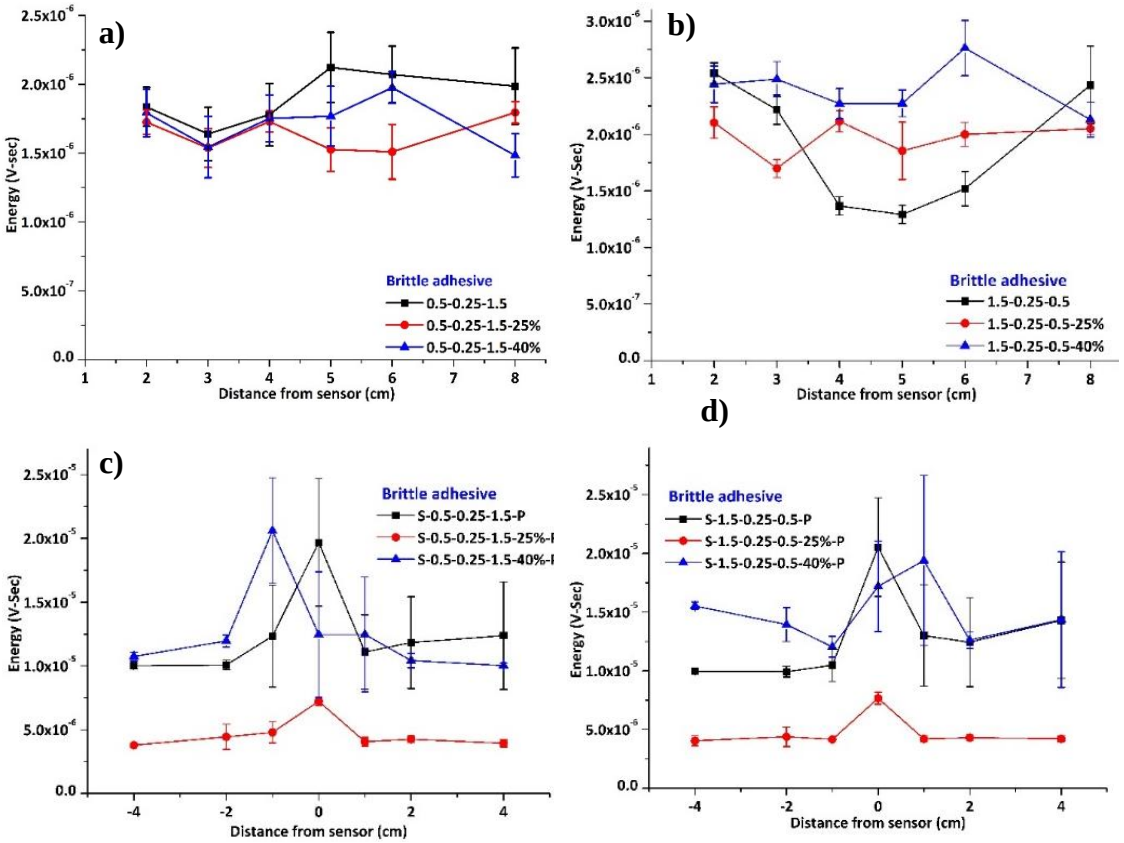

Figure 3.28. Average energy values of PLB tests done on the brittle adhesive specimen configurations **a.** 0.5-0.25-1.5, **b.** 1.5-0.25-0.5, **c.** S-0.5-0.25-1.5-P, **d.** S-1.5-0.25-0.5-P.

Furthermore, it cannot be used to differentiate between the bonds with 25% defect area and 40% defect area in any configuration. To further understand the effect of the defects on the signal behaviour in the time and frequency domains, WT is performed on the signals acquired with the different configurations. **Fig 3.29** shows sample WTs from PLB tests done at 80 mm

from the sensor on the configurations ‘0.5-0.1-1.5’, ‘0.5-0.1-1.5-25%’ and ‘0.5-0.1-1.5-40%’. The zones of significant activity were identified and further processing of data is done on these zones. From the figure, as the defect density increases, the WT co-efficient of the low frequency component decreases relative to the high frequency component. Another observation is that there is a major redistribution of energy across the entire frequency spectrum as the defect density increases. A closer look at the WTs shows that the low frequency response of all the specimens shows significant activity below 50 kHz and above 200 kHz.

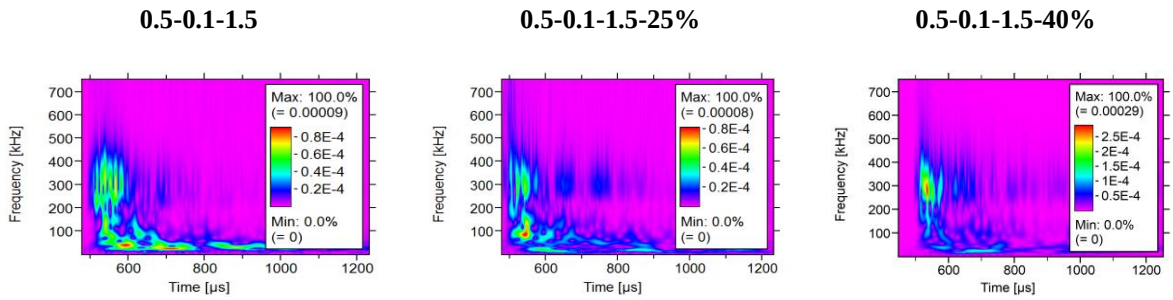

Figure 3.29. WTs of PLB tests at 80 mm from sensor on configurations **a.** 0.5-0.1-1.5, **b.** 0.5-0.1-1.5-25%, **c.** 0.5-0.1-1.15-40% with the adhesive joint with 100 µm thick brittle adhesive layer.

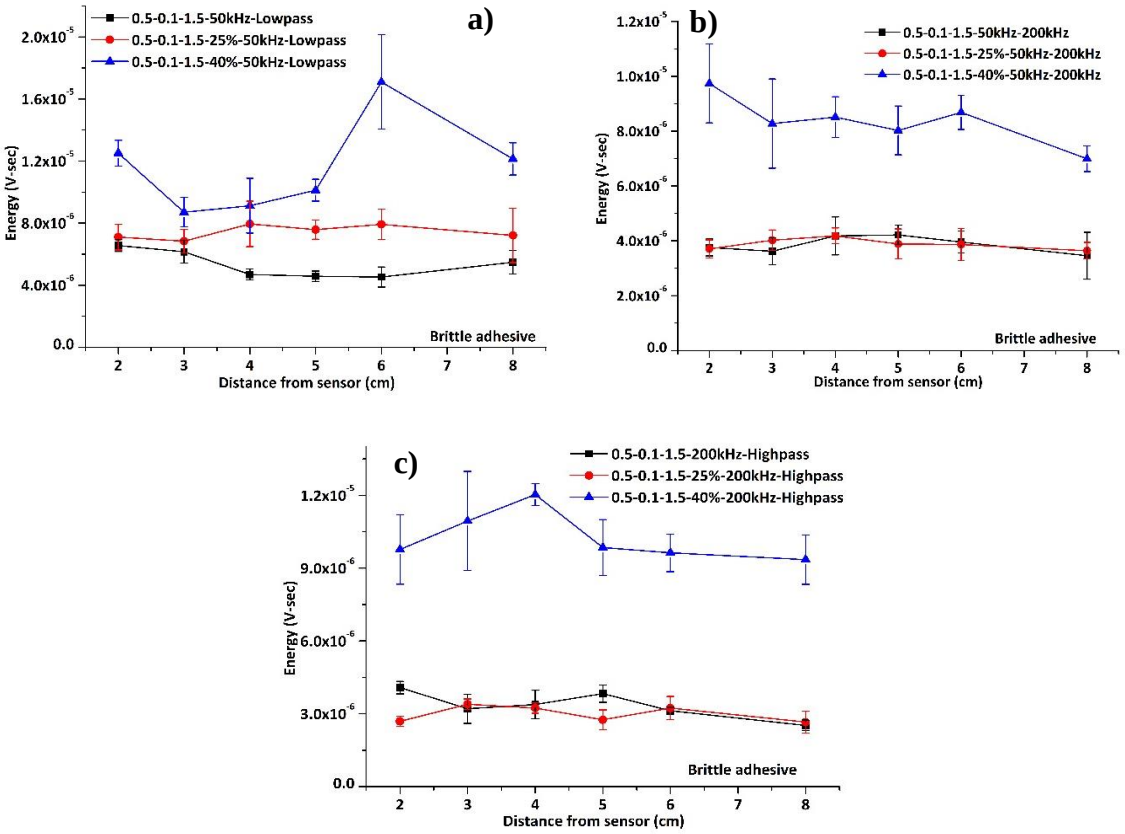

Figure 3.30. Average energy values of filtered components of PLB tests, **a.** 50kHz-Lowpass, b**.** 50kHz-200kHz, **c.** 200kHz-highpass.

Hence, the individual signals are filtered into three components; 50 kHz-lowpass, 50 kHz-200 kHz-bandpass and 200 kHz-highpass. **Figure 3.30** shows the spectral energies of three components for the three configurations in **Fig 3.29.**

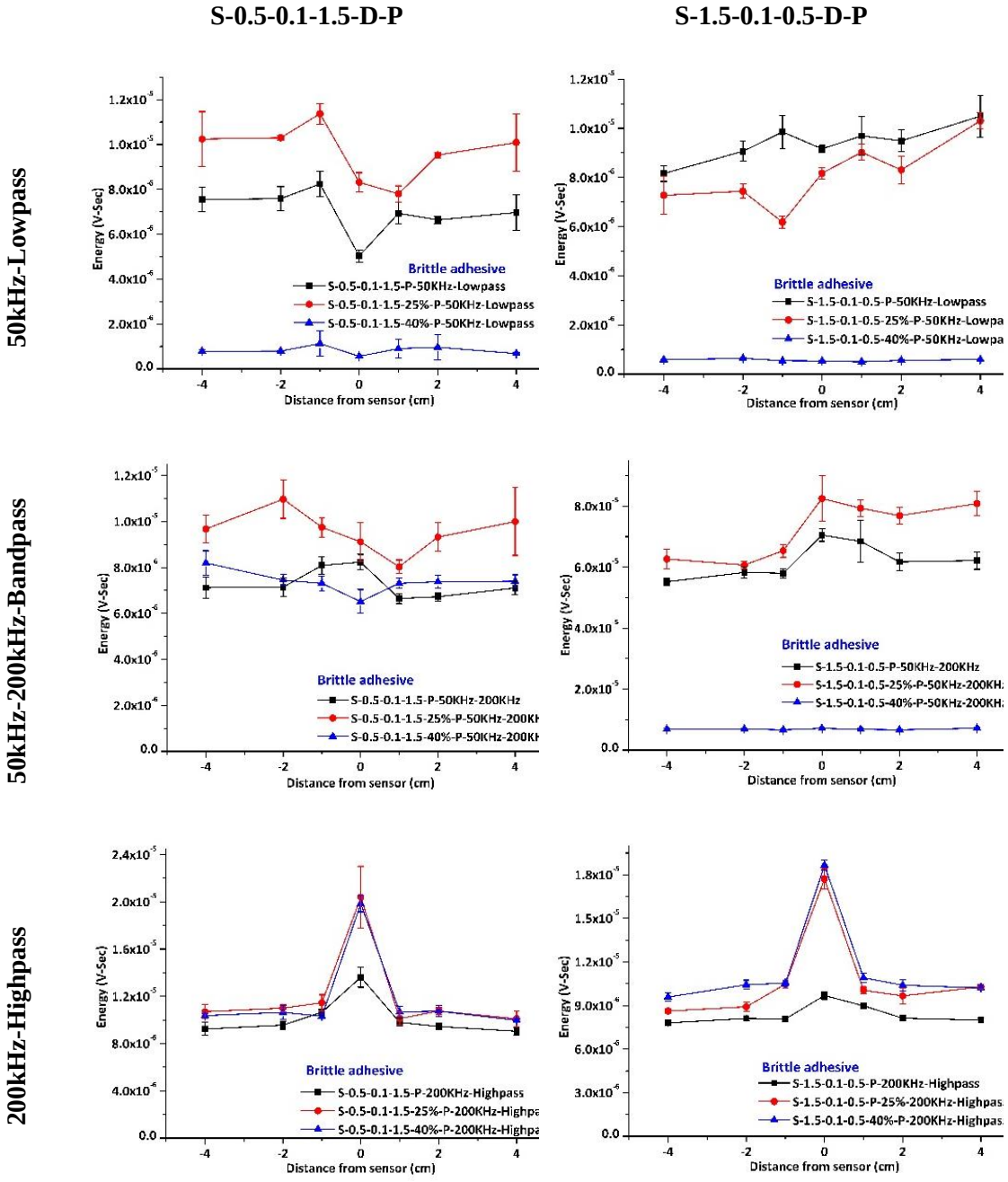

Figure 3.31. Average energy values of filtered components of PLB tests on configurations 'S-0.5-0.1-1.5-D-P' and 'S-1.5-0.1-0.5-D-P'.

From this figure, it can be clearly seen that there is a large enough difference between the energies of the 50kHz-lowpass filtered component from the different specimens to distinguish between non-defective and defective adhesive bonds. However, the energy difference between

adhesive bonds with 25% and 40% defect area density is high enough throughout the entire span to conclusively use this parameter (**Fig 3.30a**).

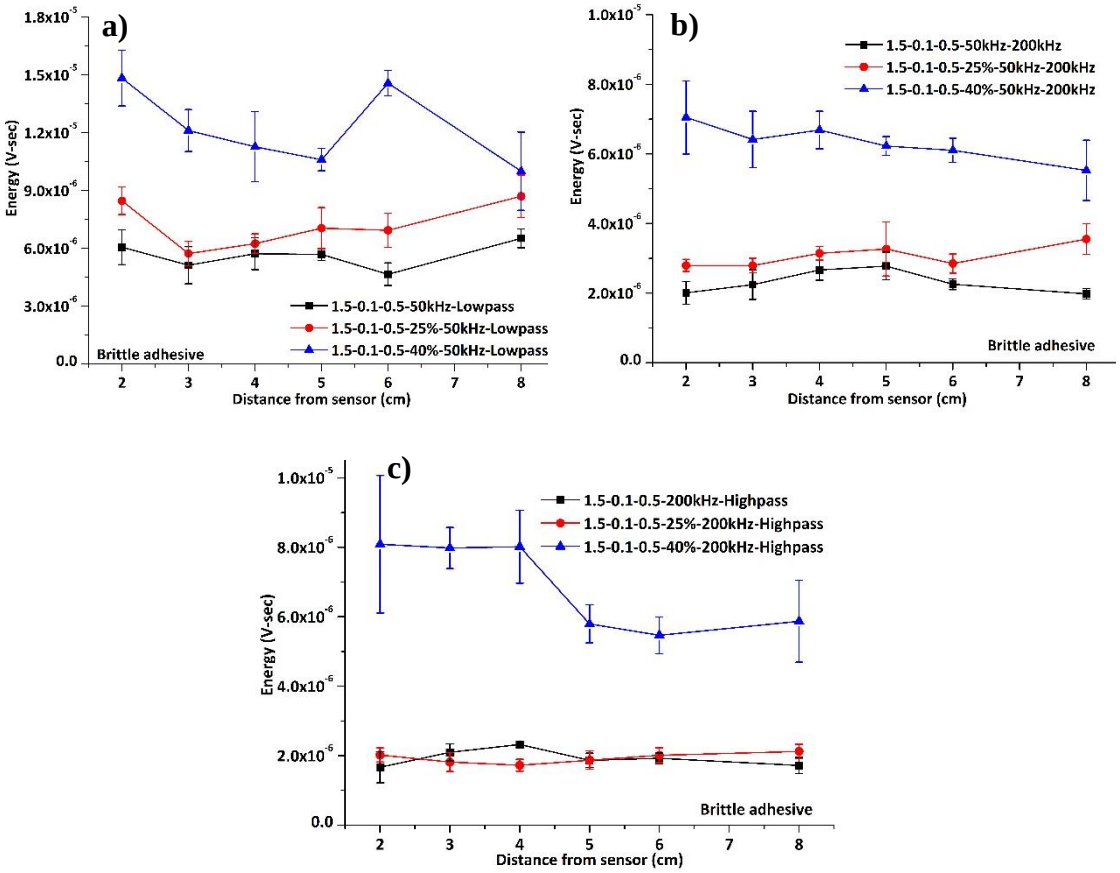

Figure 3.32. Average energy values of filtered components of PLB tests on configuration '1.5-0.1-0.5-D'.

This is the case when both the sensor and the source are on the same side of the adhesive bond specimen (0.5 mm side). To understand the effect of the configuration on the detectability of the defect density, the same procedure has been repeated for all the configurations listed in **Table.3.1. Fig 3.31** compares the average energy values of various defect area density specimens with the sensor and source on the opposite faces of the specimen. These figures show that the PLB tests on the configurations 'S-0.5-0.1-1.5-D-P' and 'S-1.5-0.1-0.5-D-P' may not be suitable for defect density detection if this set of signal filters were used. **Figure 3.32** presents the calculated energy values of the filtered components with the configuration '1.5-0.1-0.5-D'. As seen, the overlap between the non-defective and 25% defect area specimens rules out the signal energy as a differentiating AE parameter.

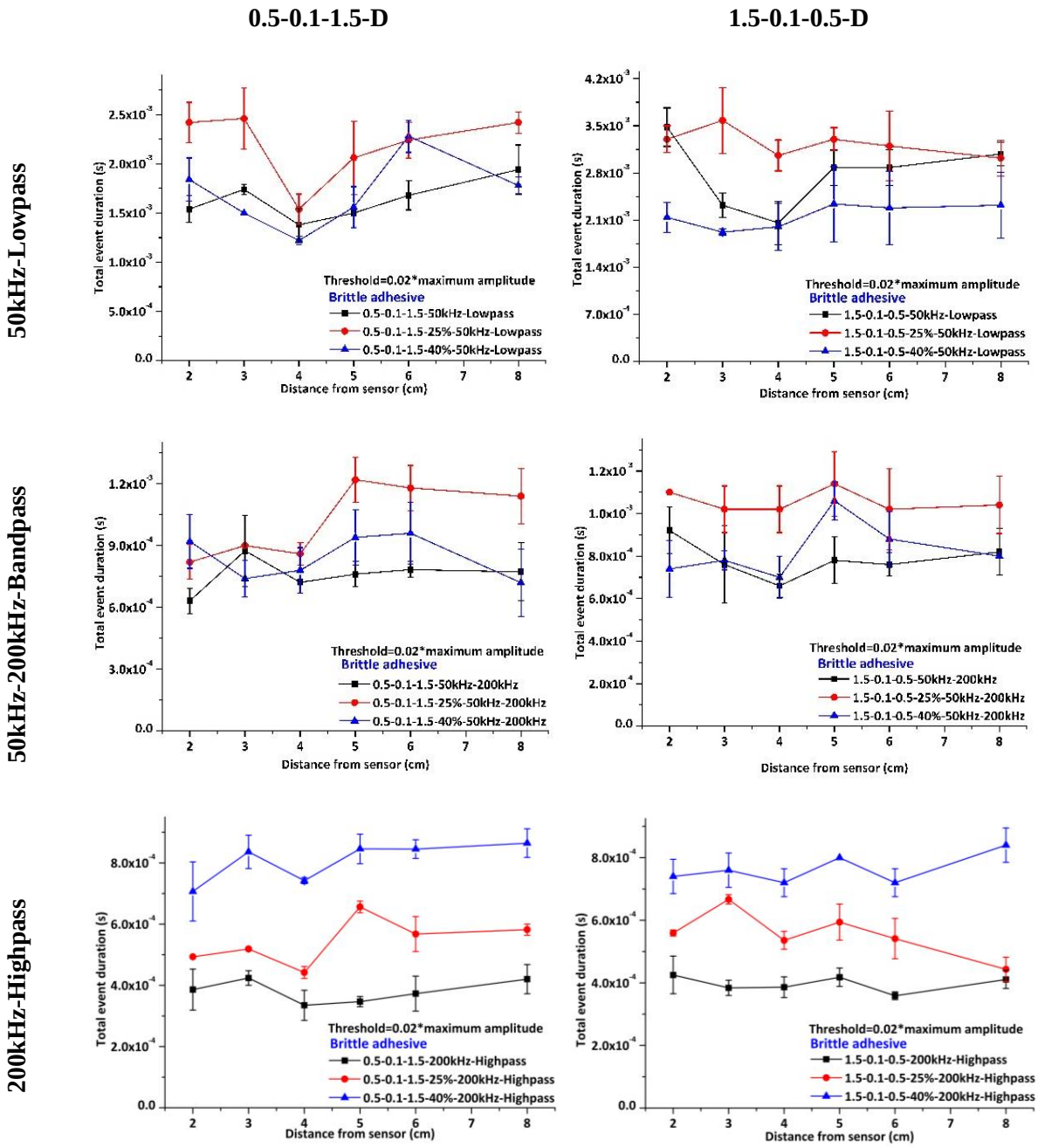

Figure 3.33. Total duration above threshold of filtered components from PLB tests on configurations '0.5-0.1-1.5-D' and '1.5-0.1-0.5-D' of brittle adhesive specimen.

As was previously mentioned, the addition of an adhesive layer between the plates increases the damping of the signal which may be reflected in the time duration of the recorded signal. Keeping in mind that the frequency response of the different adhesive bonds depends on the defect density, the time duration of the filtered components was calculated individually and presented in **Fig 3.33** for the configuration '0.5-A-1.5-D' and '1.5-A-0.5-D'. It is clear from this figure that the time duration above threshold of the 200kHz-highpass component with both the configurations can be used as a distinguishing parameter.

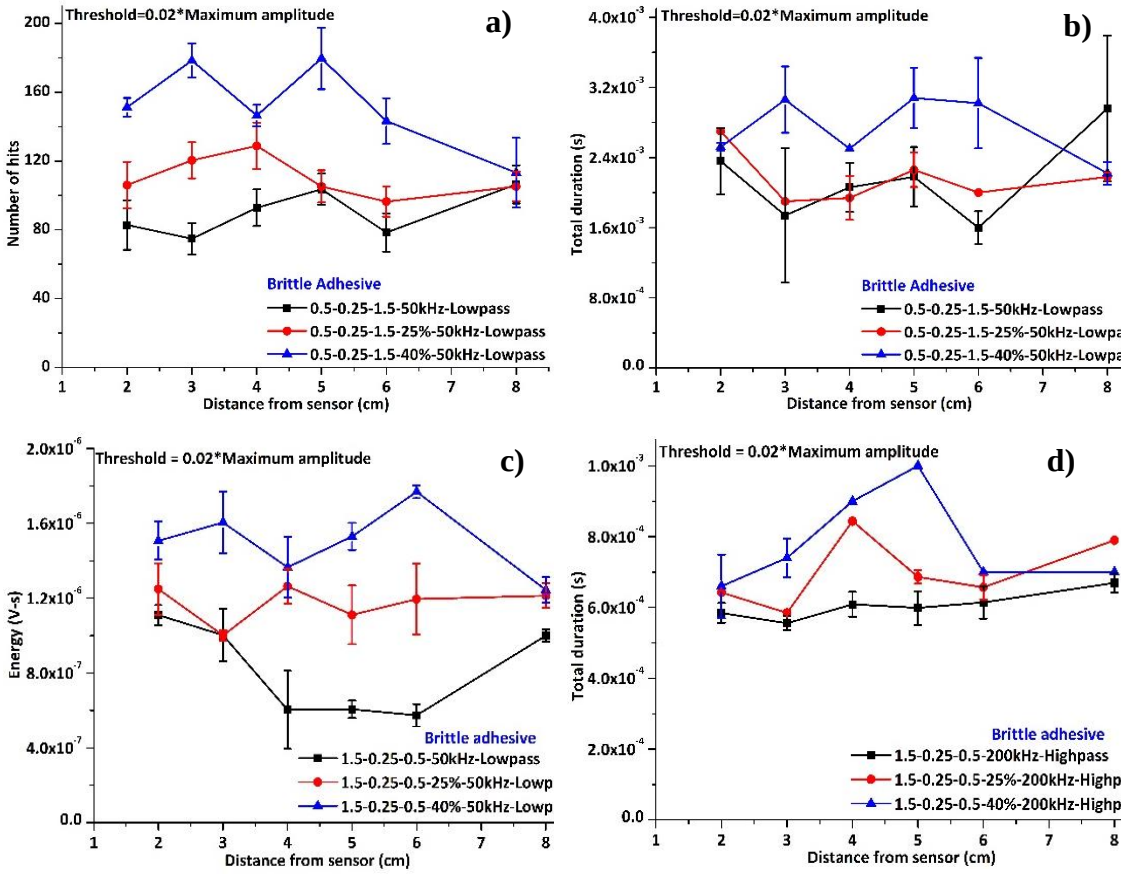

Figure 3.34. Variation of AE parameters with defect densities with configuration 0.5-0.25-1.5-D, **a.** number of hits, 50 kHz-lowpass, **b.** total duration above threshold, 50 kHz-Lowpass, and with configuration 1.5-0.25-0.5-D **c.** number of hits, 50 kHz-lowpass, **d.** total duration above threshold, 50 kHz-Lowpass.

Also, the signal component corresponding to a frequency band >200 kHz is a combination of the extensional and flexural modes of wave propagation. The extensional mode energy, however, is found to be quite low as the energy input through the PLB test is not enough to excite high amplitude extensional waves and hence, it can be inferred that the flexural wave mode is sensitive enough to detect different defect densities to characterise the quality of adhesive bonds. However, this is not the case with the configurations with the sensor and the source on the opposite faces of the specimen. This could be because of the damping of the signal energy through the adhesive layer and the multiple reflections of the waves at the interfaces. The digital filtering analysis has been conducted on the signal records on the 250µm thick brittle adhesive bonded specimen as well. After several iterations on optimising the analysis technique, the number of hits (threshold crossings) and the total duration above threshold of the 50 kHz-lowpass and 200 kHz-highpass components have been found to be moderately sensitive to the defect density.

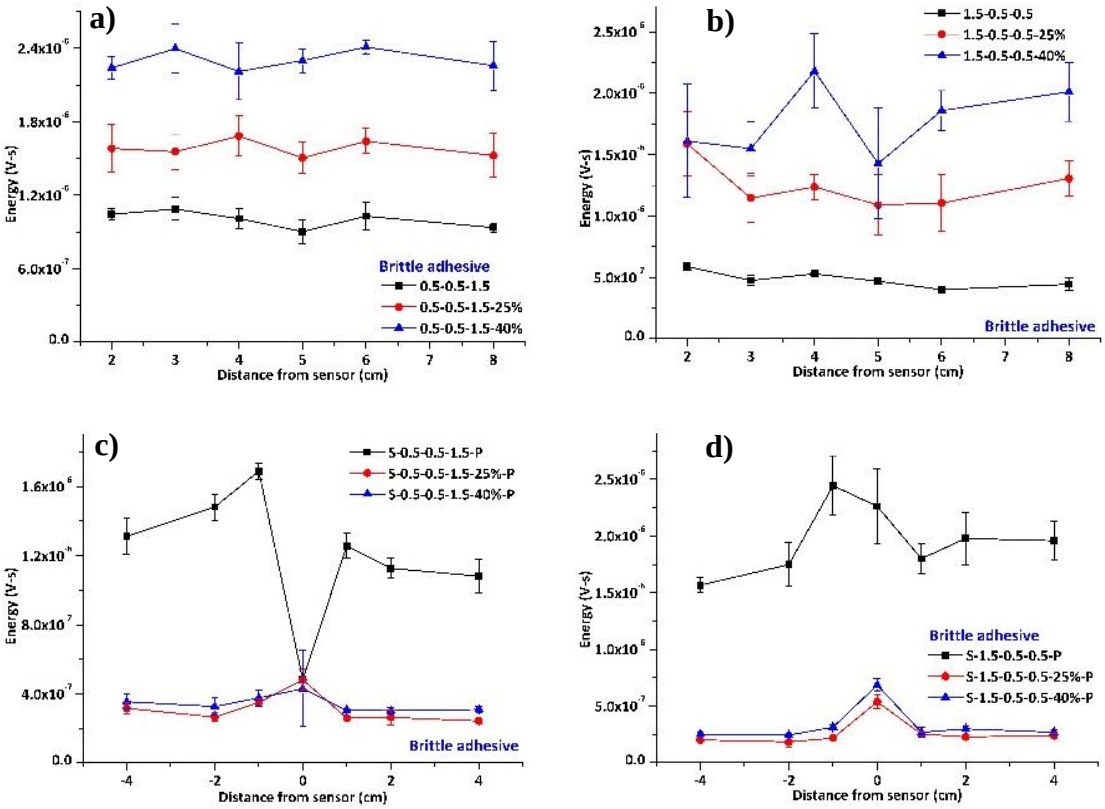

Figure 3.35. Average energy plots of PLB tests on **a.** 0.5-0.5-1.5-D, **b.** 1.5-0.5-0.5-D, **c.** S-0.5-0.5-1.5-D-P, **d.** S-1.5-0.5-0.5-D-P configurations of brittle adhesive joint with 500 mm thick adhesive layer.

From **Fig 3.34**, though there exist distinct differences between the average values of the different AE parameters with configuration 0.5-0.25-1.5-D (**Fig 3.34a**) from different defective adhesive bonds, the overlaps in the standard deviations leads to the inference that there are irregularities in the signal generation technique. However, the configuration 1.5-0.25-0.5-D seems to show decent amount of separation in the AE parameter.

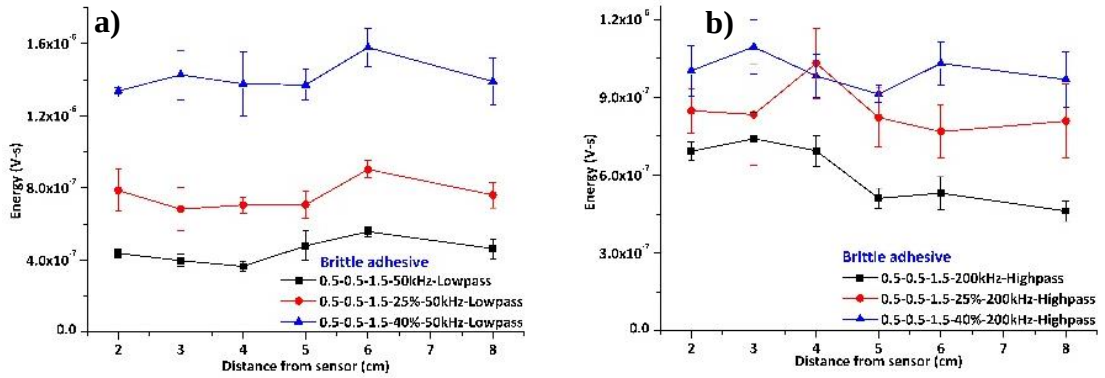

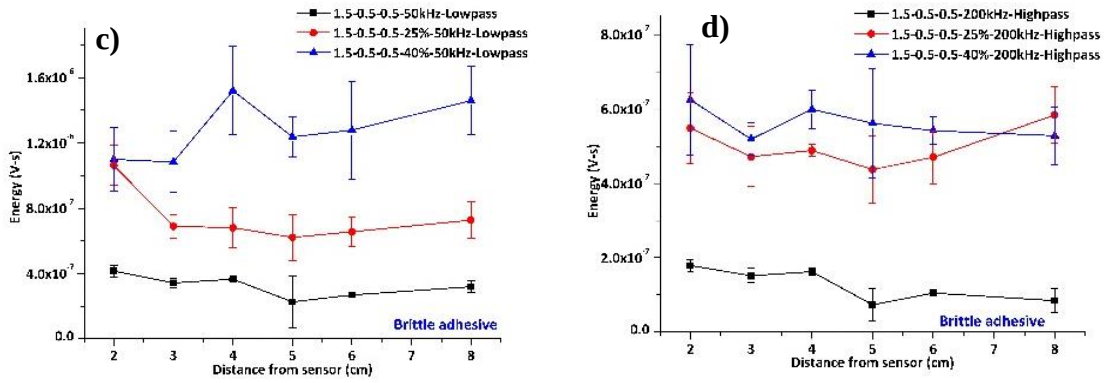

Figure 3.36. Average energy values of **a.** 50 kHz-lowpass, **b.** 200 kHz-highpass component of signals from '0.5-0.5-1.5-D' configuration and **c.** 50 kHz-lowpass, **d.** 200 kHz-highpass components of signals from '1.5-0.5-0.5-D' configuration.

Fig 3.35 shows the effect of defect area percentages on the average energy values obtained from adhesive joints with 500µm thick adhesive layer. The energy value calculated is from the entire signal record and no threshold has been applied. All the four source-sensor configurations are shown. As seen, there exists a clear distinction between the various defective joints, especially with the configurations where the source and sensor are on the same side of the adhesive joint. Hence, the signal energy can be used as a defect detecting parameter directly with the recorded signal without further signal processing. However, like the earlier adhesive layer thicknesses studied, digital filtering was applied to the signals from the 500 µm thick adhesive layer as well. Filtering was done with a 50 kHz-lowpass and a 200 kHz-highpass filter and the corresponding signal characteristics namely the energy and total duration above threshold were calculated. **Fig 3.36** shows the energies of filtered components of the test signals on this specimen.

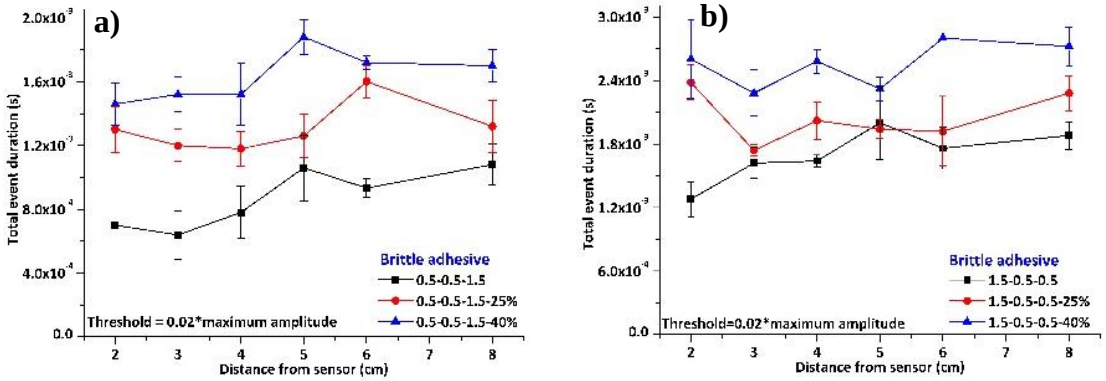

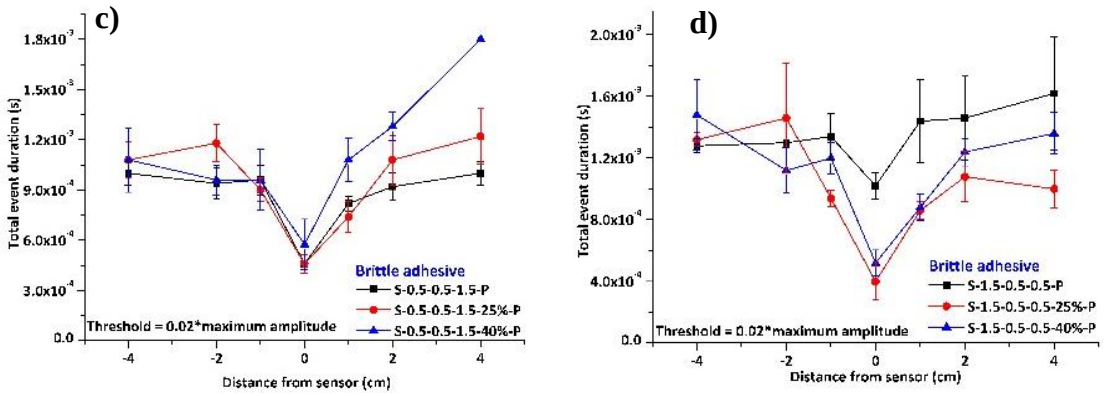

Figure 3.37. Total duration above threshold of signal records from PLB tests on configurations **a.** 0.5-0.5-1.5-D, **b.** 1.5-0.5-0.5-D, **c.** S-0.5-0.5-1.5-D-P, **d.** S-1.5-0.5-0.5-D-P.

From **Fig 3.36**, it can be said that the 50kHz-lowpass filter applied to the signals acquired from PLB tests on configurations '0.5-0.5-1.5-D' and '1.5-0.5-0.5-D' can be used to distinguish between the various defective joints. The average energies of the filtered components of the signals from the other configurations are not shown here as the results exhibited significant overlaps between the energies corresponding to different defective specimens.

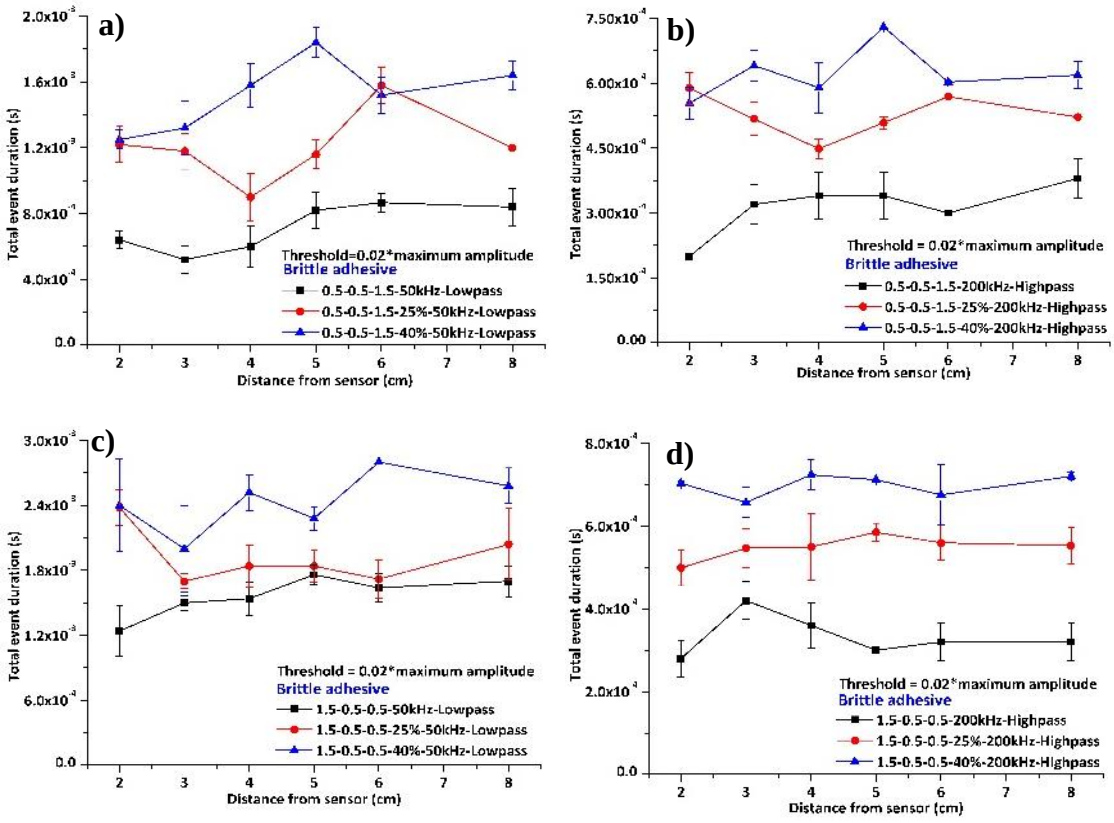

Figure 3.38. Time above threshold values of **a.** 50 kHz-lowpass, **b.** 200 kHz-highpass component of signals from '0.5-0.5-1.5-D' configuration and **c.** 50 kHz-lowpass, **d.** 200 kHz-highpass components of signals from '1.5-0.5-0.5-D' configuration.

In addition to energy values, the event duration values have also been calculated for all the configurations (**Fig 3.37**). The calculations have been done using a threshold value of 2% of the signal peak amplitude. From the figure, it can seen that the time duration of the signals shows overlaps between different specimens across the specimen span. This leads to the observation that the confidence level associated with choosing time duration as the AE parameter is low. Hence, the time above threshold of the filtered components is also calculated for all the signal records for all the configurations. The filters used are the same as used in the energy calculations. **Fig 3.38** shows the time above threshold of 50 kHz-lowpass and 200 kHz-highpass components of the configurations '0.5-0.5-1.5-D' and '1.5-0.5-0.5-D'. The threshold value used is 2% of the maximum amplitude of each signal record. From the plots, it can be seen that the 200kHz-highpass component exhibits decently separated values of the time duration above threshold to effectively distinguish between the defective specimens.

3.5.3.2. Ductile adhesive

This section presents the effect of the presence of defects on the PLB test characteristics conducted on ductile adhesive bonds. Parameters such as energy content, event durations, number of hits etc. are investigated to distinguish the adhesive bonds with various defect area percentages.

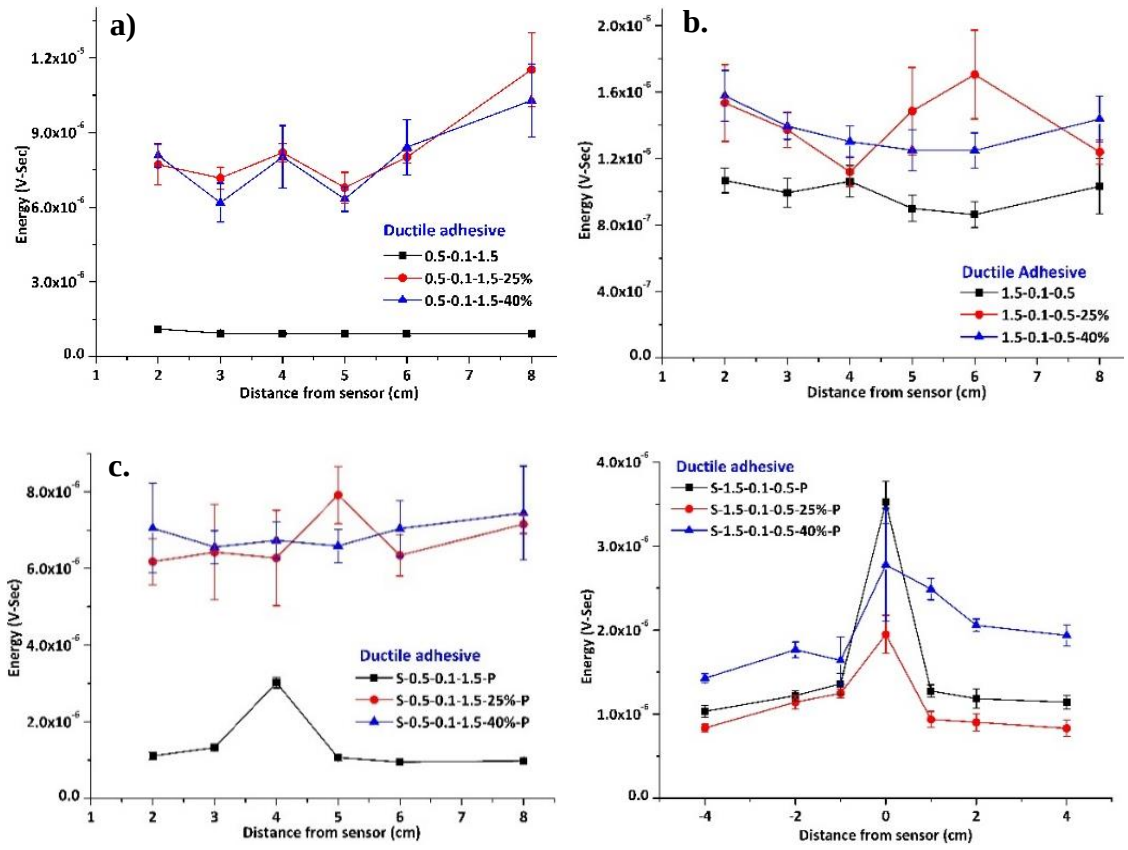

Figure 3.39. Average energy values of PLB tests on **a.** 0.5-0.1-1.5-D, **b.** 1.5-0.1-0.5-D, **c.** S-0.5-0.1-1.5-D-P, **d.** S-1.5-0.1-0.5-D-P configurations of 100 µm thick ductile adhesive layer bonds.

Figure 3.39 presents the average energy content of PLB test records at various locations on the ductile adhesive bonds. As seen, the average values are higher for the defective adhesive bonds, especially in those configurations where the sensor is on the 0.5 mm thick plate. This is understandable, as the defects are on the interface between this plate and the adhesive layer. Hence it can be said that the AE energy content of the PLB tests is sensitive to the presence of the defects along the interface.

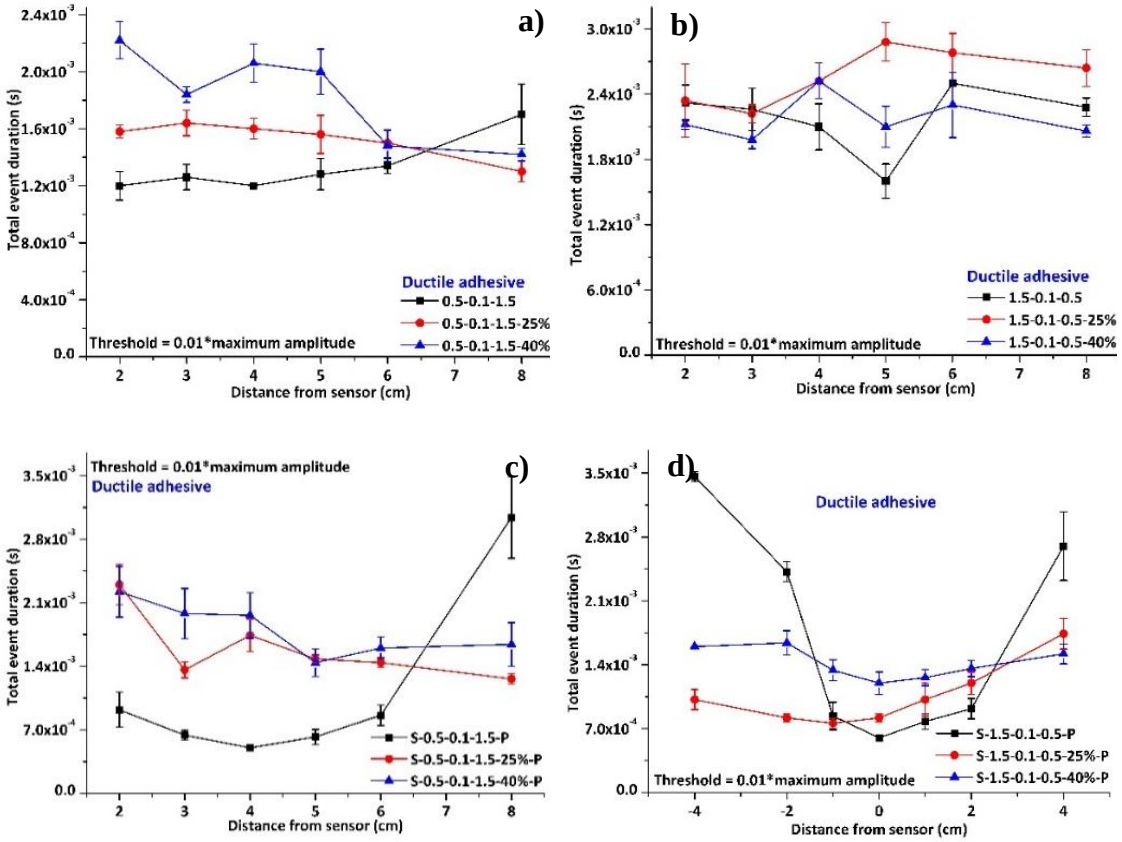

Figure 3.40. Average total event durations of PLB tests on **a.** 0.5-0.1-1.5-D, **b.** 1.5-0.1-0.5-D, **c.** S-0.5-0.1-1.5-D-P, **d.** S-1.5-0.1-0.5-D-P configurations of 100 µm thick ductile adhesive layer joint.

This also implies that the configurations where sensor is in closer proximity to the defects is more likely to exhibit a change in the PLB test signal. This observation might be made use of in identifying the interface along which the defects are in an adhesive bond. One more observation is that the difference in energy levels between the bonds with 25% and 40% defect area densities is negligible. Hence, even though the signal energy content can be used to identify the presence of a defect, the relative area of the defects cannot be effectively identified using this parameter. The effect of the adhesive interface defects on the total event duration of the PLB tests on various configurations is presented in **Fig 3.40**.

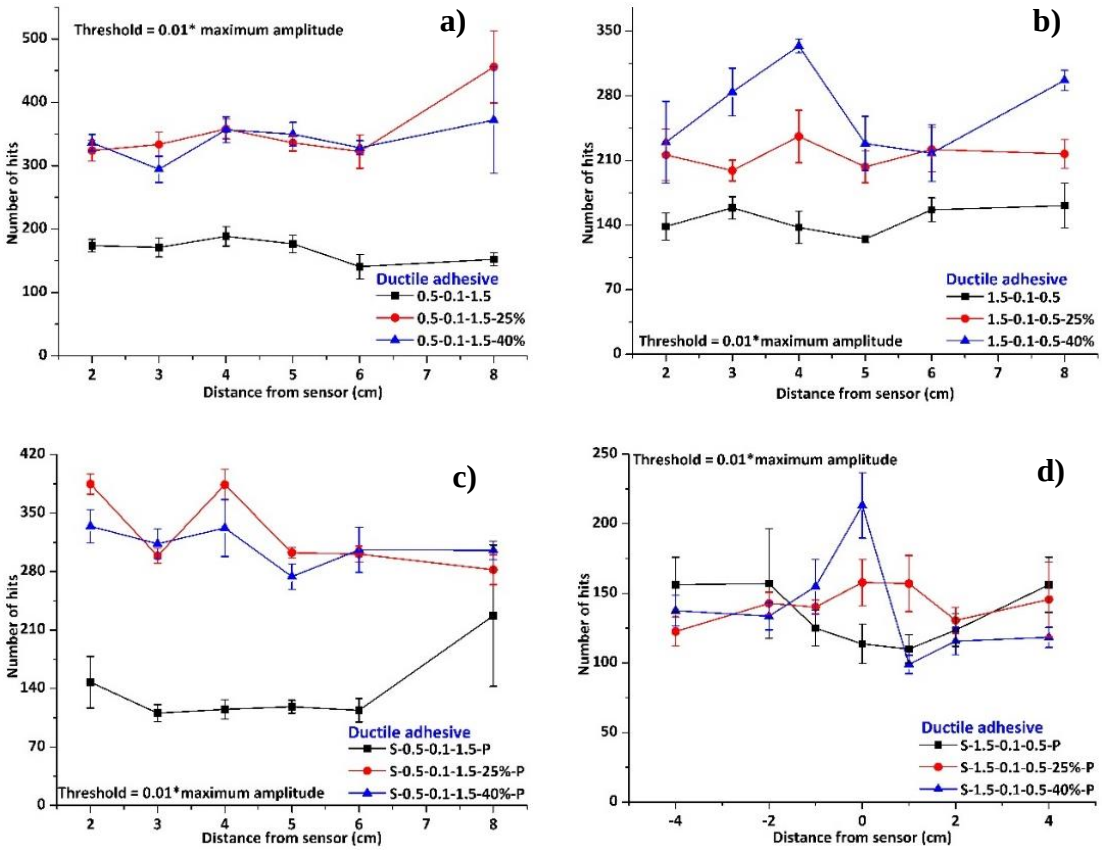

Figure 3.41. Average number of hits from PLB tests on **a.** 0.5-0.1-1.5-D, **b.** 1.5-0.1-0.5-D, **c.** S-0.5-0.1-1.5-D-P, **d.** S-1.5-0.1-0.5-D-P configurations of bonds with 100 µm thick ductile adhesive joint.

The values shown are average values. As seen, even though there is an observable difference in the average event durations between the various defect percentages within a configuration, only the configuration '0.5-0.1-1.5-D' seems to show a quantifiable difference. It should be noted that the threshold used in this case is equal to 1% of the maximum amplitude.

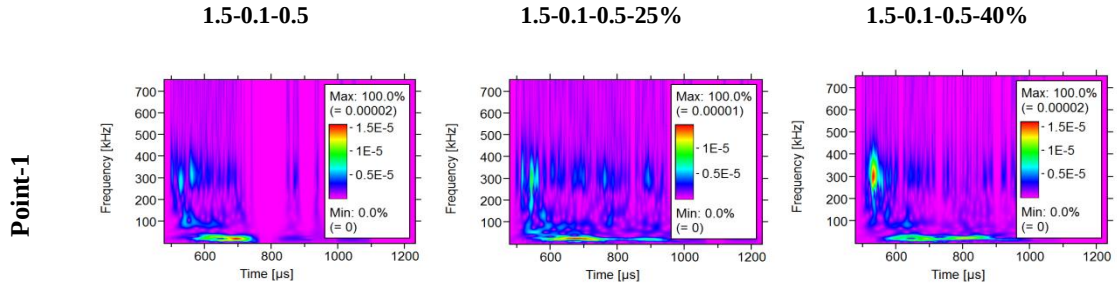

Figure 3.42. WTs of PLB tests at various points on configurations '0.5-0.1-1.5', '0.5-0.1-1.5-25%' and '0.5-0.1-1.5-40%'.

As in the case of the brittle adhesive joints, the configuration with both the sensor and the source on the same side of the bonded sandwich has the highest sensitivity to the defective interface. The process of choosing the optimum threshold value to obtain the maximum difference

in the parameter is can be automated by writing an algorithm in MATLAB. However, for the scope of this study, the threshold values are chosen arbitrarily.

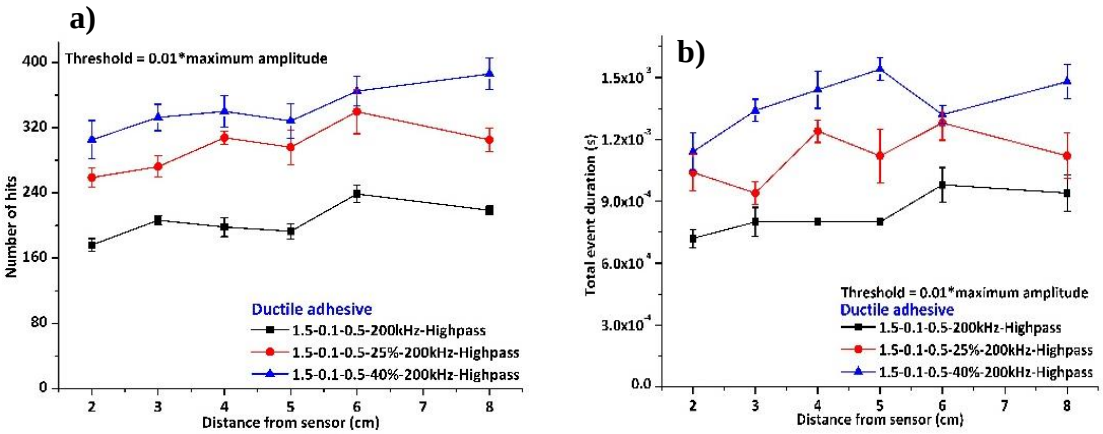

Figure 3.43.a. Hit count of 200 kHz-Highpass component of PLB tests on ductile adhesive configuration '1.5-0.1-0.5-D', **b.** Corresponding total event duration.

The values were varied between 1% and 20% of the maximum amplitude of the recorded signal and the optimum value was identified. However, all these results are not shown here except the ones with the largest difference between the AE parameters corresponding to various defective joints. **Figure 3.41** shows the average number of hits from PLB test records on various configurations on the bond with 100 µm ductile adhesive layer. The number of hits increases in the defective adhesive bonds. However, as is the case with energy, there is no clear distinction between the bonds with 25% and 40% defect areas. This is the case in all the configurations except with '1.5-0.1-0.5-D' where there is a considerable difference in the parameter though not over the entire span of the specimen.

To further investigate the reason behind this behaviour, the WTs of the recorded signals on the configuration '1.5-0.1-0.5-D' were calculated and samples are presented in **Fig 3.42**. From this, the major difference between the various defective bonds is that the decay of the high frequency component is over a longer period in in defective bonds. This observation is further explored by calculating the number of hits of the 200 kHz high pass component on the configuration '1.5-0.1-0.5-D'. The corresponding plot is shown in **Fig 3.43a**. As shown, there is a clear distinction between the defective bonds.

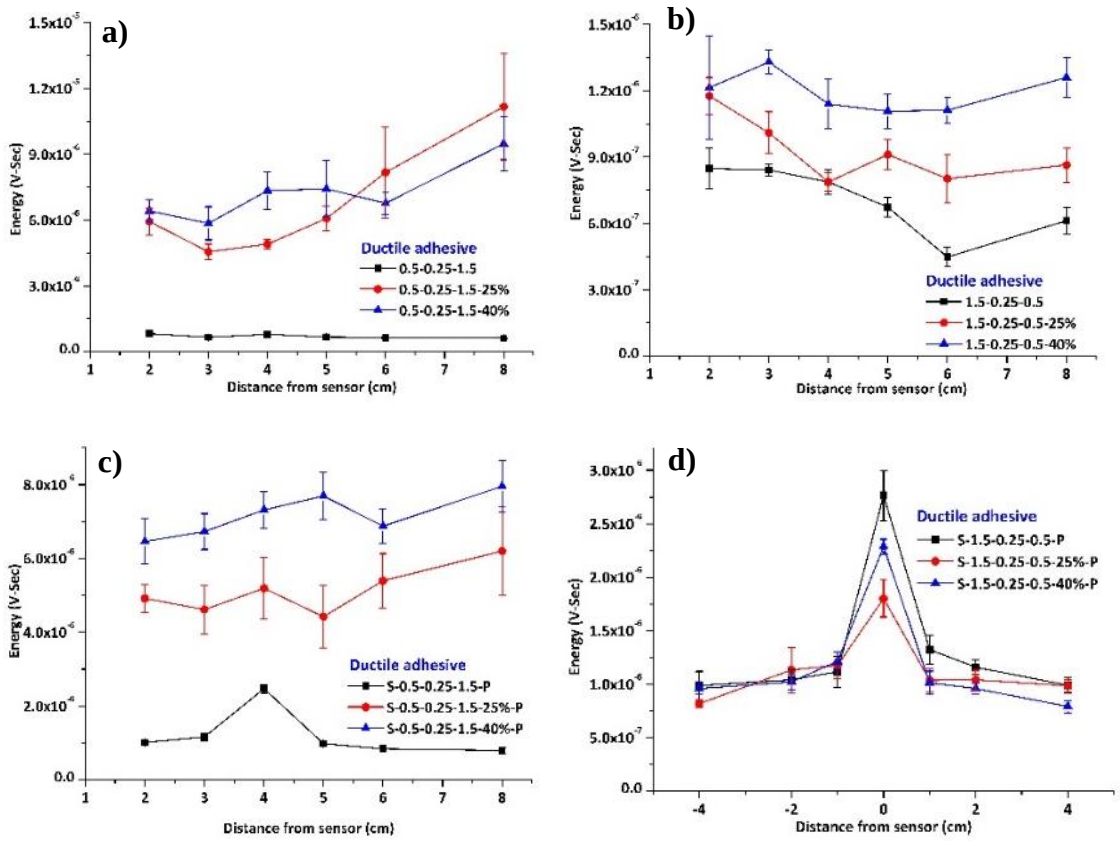

Figure 3.44. Average energy values of PLB tests on **a.** 0.5-0.25-1.5-D, **b.** 1.5-0.25-0.5-D, **c.** S-0.5-0.25-1.5-D-P and **d.** S-1.5-0.25-0.5-D-P configurations of adhesive bonds with 250 mm ductile adhesive layer.

Thus, the hit count (threshold crossings) can be used as a distinguishing parameter between the non-defective and defective specimens. The total time duration of this component with this configuration is also presented in the same figure (**Fig 3.43b**). **Figure 3.44** shows the average energy values from PLB tests on various configurations of the 250 µm ductile adhesive layer joint.

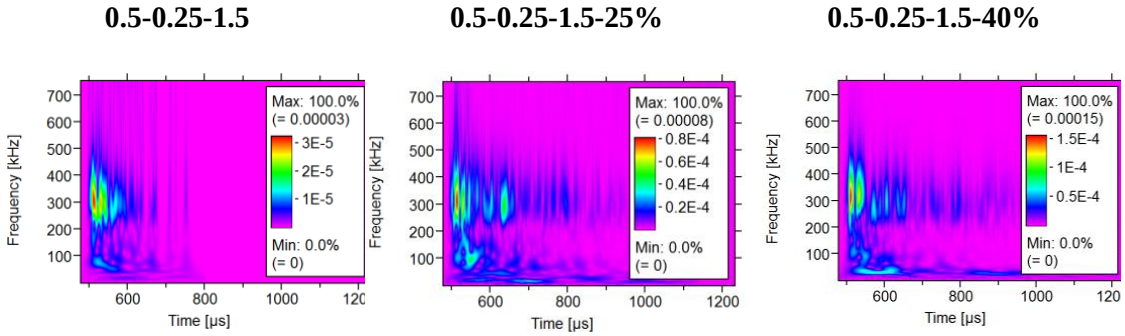

Figure 3.45. WTs of PLB tests on the configuration '0.5-0.25-1.5-D'.

From the plots, it is quite apparent that energy itself is enough to distinguish between the various defective adhesive bonds. This is the case with the configuration ‘S-0.5-0.25-1.5-D-P’ and ‘1.5-0.25-0.5-D’. The remaining, however, do not show a clear difference. It should be noted that in both the cases, the sensor is on the 1.5 mm thick aluminium plate. The conclusion that can be drawn from this is that the ductility of the adhesive layer is affecting the through thickness signal transmission across the joint. As the defect area percentage increases, the transmitted signal from the source side to the sensor side reduces in magnitude. The primary difference that can be seen is that the high frequency component prevails over a longer period. This leads to the next set of results that comprise the total duration and the hit count for the high frequency component. The filtering has been done using a 200 kHz-highpass component. Moreover, the signal, once transmitted to the other side of the specimen stays within the thicker plate as the transmission to the thinner plate is hindered by the defects along the interface. The effect of the defects can further be understood by looking at the WTs of the PLB tests.

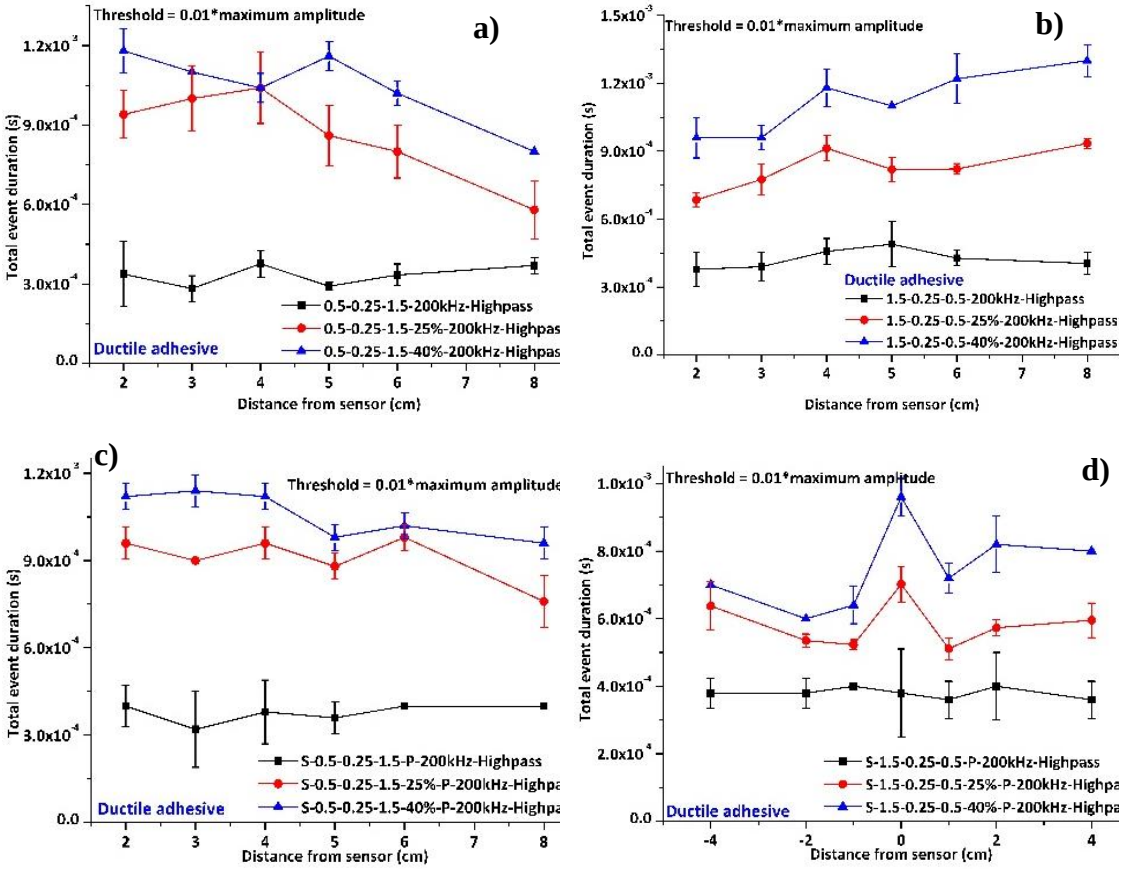

Figure 3.46. Average total durations of the high frequency components of PLB test records on **a.** 0.5-0.35-1.5-D, **b.** 1.5-0.25-0.5-D, **c.** S-0.5-0.25-1.5-D-P, **d.** S-1.5-0.25-0.5-D-P configurations of the 250µm thick ductile adhesive layer joint

Fig 3.45 shows the WTs of PLBs at various tests on the configuration ‘0.5-0.25-1.5-D’. The average values of the total duration and the hit count of the high frequency components of

various configurations with the 250 µm ductile adhesive layer are shown in **Fig 3.46** & **Fig 3.47.** As seen, the total duration is higher at higher defect percentages. The same is the case with the hit count. These observations are true for the configurations '0.5-0.25-1.5-D' and '1.5-0.25-0.5-D'. For the remaining, there is a slight overlap between the parameter values for the joints with 25% and 40% defect areas. Thus, it is recommended that these configurations may not be used for defect detection. It is to be noted that the threshold values used for the time and hit count calculations is 1% of the maximum amplitude of a test record.

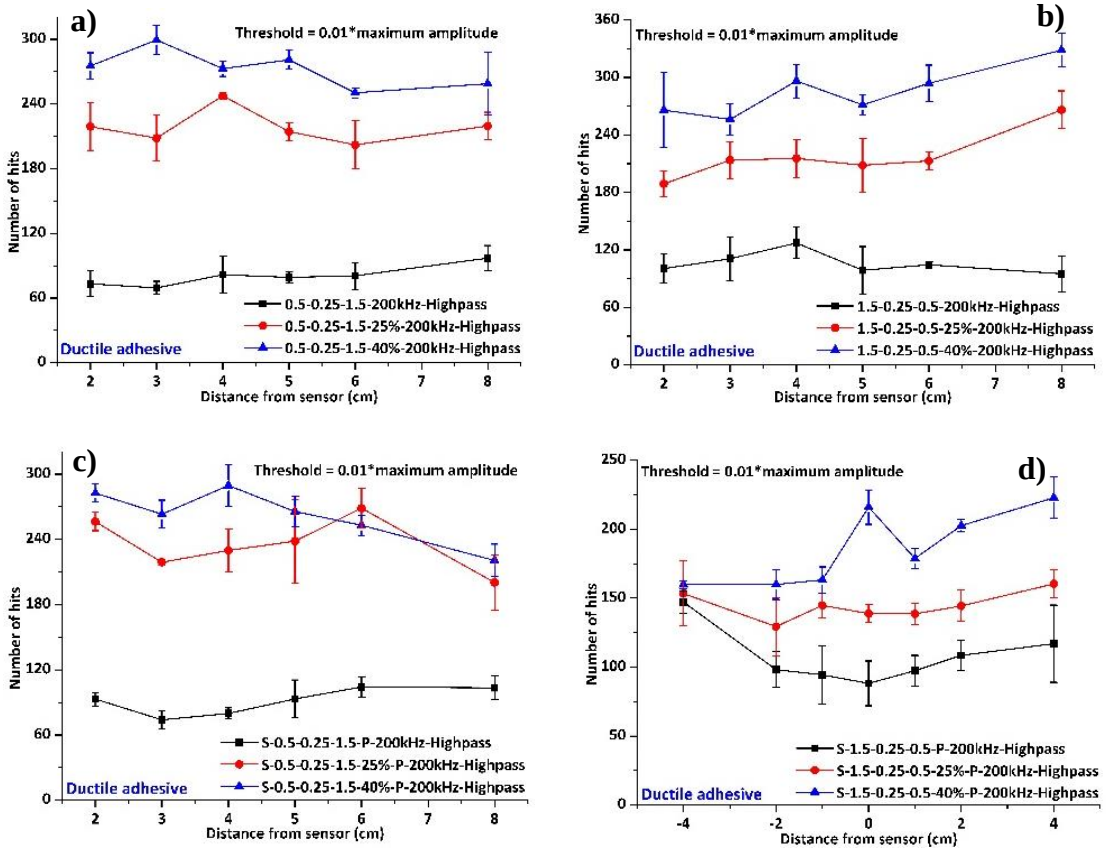

Figure 3.47. Average hit counts of the high frequency components of PLB test records on **a.** 0.5-0.35-1.5-D, **b.** 1.5-0.25-0.5-D, **c.** S-0.5-0.25-1.5-D-P, **d.** S-1.5-0.25-0.5-D-P configurations of the 250µm thick ductile adhesive layer joint.

The threshold is calculated for every test record and hence, it varies between different records. The threshold can also be calculated based on the noise level. Calculations based on such a threshold value have also been conducted, but the results obtained showed no distinction between the various defective joints.

Hence, it is recommended that the threshold value be calculated based on the maximum amplitude of the records seen, even though the total duration of the 200 kHz-highpass component can be used to estimate the defect area percentage, there is still a slight overlap between the

calculated parameter values between the defective joints. However, the parameter hit count gives a good distinction between various defect area percentages as seen in **Fig 3.47**.

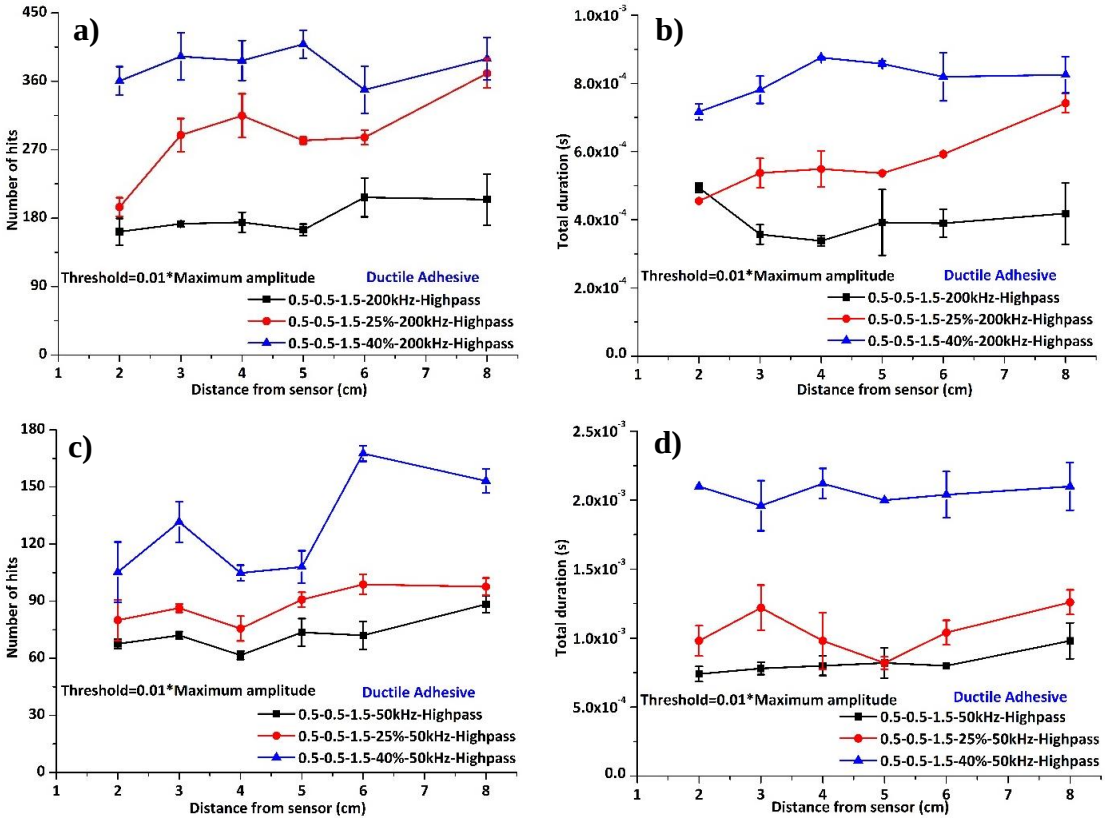

Figure 3.48. Variation of AE parameters with defect densities with configuration 0.5-0.5-1.5-D, **a.** number of hits, 200 kHz-highpass, **b.** total duration above threshold, 200 kHz-highpass, **c.** number of hits, 50 kHz-lowpass, **d.** total duration above threshold, 50 kHz-lowpass.

This is the case with the two configurations where the sensor and the source are on the same side of the specimen. Even though there is a clear difference in the hit count between the various joints it is not along the entire span of the specimen in configurations with the source and sensor on the opposite sides of the specimen. Hence, in the case of adhesive joints with 250 µm thick ductile adhesive layer, the defect area can easily be estimated using the configuration with the sensor and the source on the same side. Similarly, the number of hits (threshold crossings) and the time duration above a threshold of 1% of the peak voltage have been calculated for the different sensor-source configurations of the 500 µm thick ductile adhesive layer specimen. This analysis has been conducted on the different filtered components, the filters being 50 kHz-lowpass, 50 kHz – 200 kHz-bandpass and 200 kHz-highpass. The results are shown in **Fig 3.48**. The plots show that the number of hits (threshold crossings) and the total duration above threshold of both the 50kHz-lowpass component and the 200kHz-highpass component can be used to differentiate between the different defect densities of the 500 µm thick ductile adhesive layer

specimen. These results have been arrived at after multiple iterations to optimise the threshold value. The signal energy associated with the different frequency bands have also been calculated. However, all the above results have not been presented here for brevity.

3.6. Summary

Adhesive Type	Thickness (μm)	Filter	Parameter (features)	Defect-AE parameter correlation
Brittle	100	200kHz-Lowpass	Event duration	Linear
	250	50kHz-Lowpass 200kHz-Highpass	Threshold crossings (No. of hits) *	Linear
	500	50kHz-Lowpass	Energy	Linear
Ductile	100	200kHz-Highpass	Threshold crossings (No. of hits)	Quadratic
	250	200kHz-Highpass	Event duration, Threshold crossings (No. of hits)	Linear
	500	50kHz-Lowpass 200kHz-Highpass	Event duration, Threshold crossings (No. of hits)	Linear

Table 3.6. Summary of AE parameters used in defect detection in adhesive bonds

*Not conclusive because of overlaps in the standard deviation values

In summary, this chapter presents the experimental procedures proposed to utilise AE in combination with simple PLB tests, as a defect estimation technique in adhesive bonds. The experiments were carried out with two different adhesives, chosen based on their elastic moduli to be treated as brittle and ductile in behaviour. The defects were introduced along one of the interfaces. Various source-sensor location combinations were tested and the configuration which yields the maximum difference in AE parameters between the adhesive bonds with different defect area percentages is chosen. The correlations between the AE parameters and the adhesive layer defect density are shown in **Fig 3.49**. The following observations have been made from the results analysis (**Table 3.6**).

- By superimposing the dispersion curves of the aluminium plates used, the flexural and symmetric modes propagating within the adhesive joint have been identified in the WTs of the PLB test records. The symmetrical mode is found to be of low amplitude whereas the flexural mode is of a relatively larger magnitude. It has been observed that the energy input from the PLB test in not enough to induce the symmetrical mode in the adhesive joint.
- The introduction of the adhesive layer induces the damping of higher frequency component of the PLB test record. Compared to the brittle adhesive joints, the ratio of high

frequency (175 kHz-highpass) energy content to the low frequency (175 kHz-lowpass) energy content is lower in the ductile adhesive joints. Also, the energy content of the records with the brittle adhesive joints was higher compared to ductile adhesive joints.

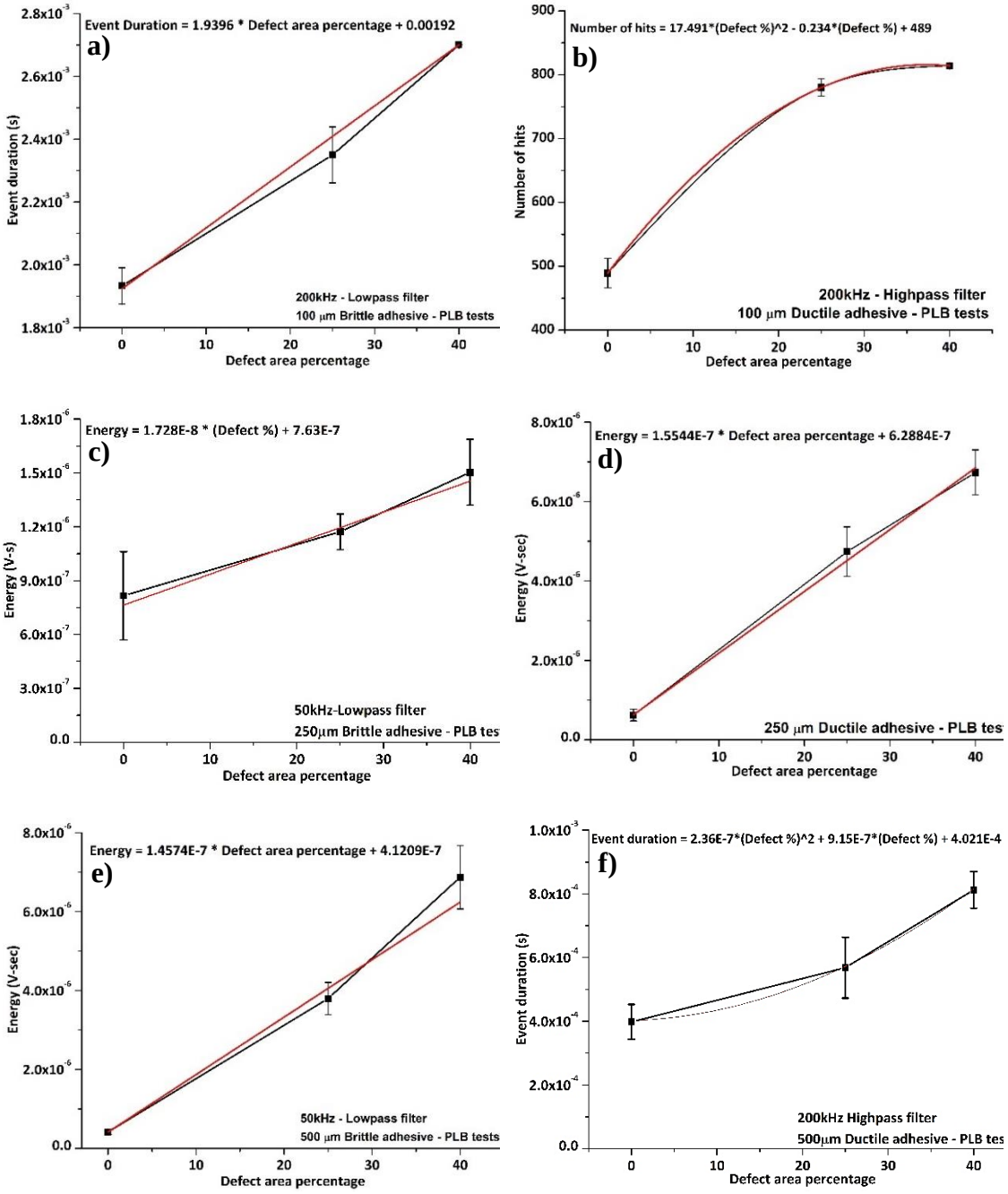

Figure 3.49. Effect of the defect area density on the AE parameters with different adhesive layer thicknesses and types (from PLB tests).

- The high frequency (200 kHz-highpass) component of the recorded signals was found to be highly sensitive to interfacial defects in the case of brittle adhesive joints. Both the total duration above threshold and the number of hits can be used as distinguishing parameters

between the defective joints. However, the threshold value must be optimised so as to increase the disparity between the various defective joints.

- In addition, the energy content of the high frequency component, calculated as the total area under the voltage-time record, also can be used as a distinguishing parameter.
- In the case of ductile adhesive joints, the same parameter as in the case of the brittle adhesive joints can be used to detect and estimate the presence of defects. In addition, in the case of joints with 250 μm thick adhesive layer, the hit count of both the unfiltered signal and the high-pass filtered component can also be used as an indicator of defects.
- In most of the tests conducted, the configuration with the sensor and source (PLB) on the 0.5 mm thick aluminium plate seems to be the most sensitive to defective interfaces.

The results presented in this chapter present a methodology to quantify the defects along the interface of an adhesive bond. The effect of these defects on the residual strength of the adhesive bond will be quantified in the subsequent chapters.

Chapter-4

4. Finite element analysis of adhesive bonded joints

The aim of the current chapter is to understand the fracture of defective adhesive bonds. Finite element analysis has been used in many occasions to understand the failure of adhesive bonds [28-30]. Often, the cohesive zone model has been used to represent the interfacial behaviour of adhesive bonds [11,23,28]. The combination of these two presents a viable option to understand the crack propagation along the interface of adhesive bonds. In combination with elastic-plastic fracture mechanics, the present chapter models the fracture of adhesive bonds. The 4-point flexure method and plane strain indentation have been chosen.

This chapter presents finite element analysis of adhesively bonded joints subjected to 4-point flexural and spherical indentation loading. In 4-point flexural simulation section, first, the formulation of models is presented, and then the effect of adhesive thickness and adherend deformation were analysed. This was followed by the analysis of the effect of adhesive modulus and peak stress variation in adhesive layer. In the indentation simulation section, first, formulation and definition of non-dimensional parameters are presented where the interfacial crack propagation was simulated by embedding cohesive zone model in the finite element model, followed by the analysis of the indentation of perfectly bonded joints, effect of normalised interfacial strength, interfacial toughness, adhesive elastic modulus and layer thickness.

4.1. Model Formulation

4.1.1. 4-Point flexure

Figure 1a shows a model of an adhesively bonded metallic joint (e.g. aluminium, often selected for use where weight is critical) with an adhesive thickness under the 4-point flexural loading condition. The present analysis can be useful to understand the out of plane bending of the bonded zone of a simple lap-joint geometry and panel bonding. The Cartesian coordinate system was used with the origin at section XX′ (**Figs. 4.1.a** and **4.2.b**). Two-dimensional (2D) FE simulations were done using ANSYS (14.0) Mechanical APDL package. The behaviour of both the adherends and the adhesive layer were modelled using a simple bi-linear law embedded in the package. This law models the plasticity of the isotropic materials as a straight line**;** the slope of which determines the hardening of the material after yield. Two different adhesives were considered (**Table 3.1**). Eight different thicknesses of the adhesive layer were varied (50 μm, 100 μm, 250 μm, 500 μm, 750 μm, 1000 μm, 1250 μm and 1500 μm).

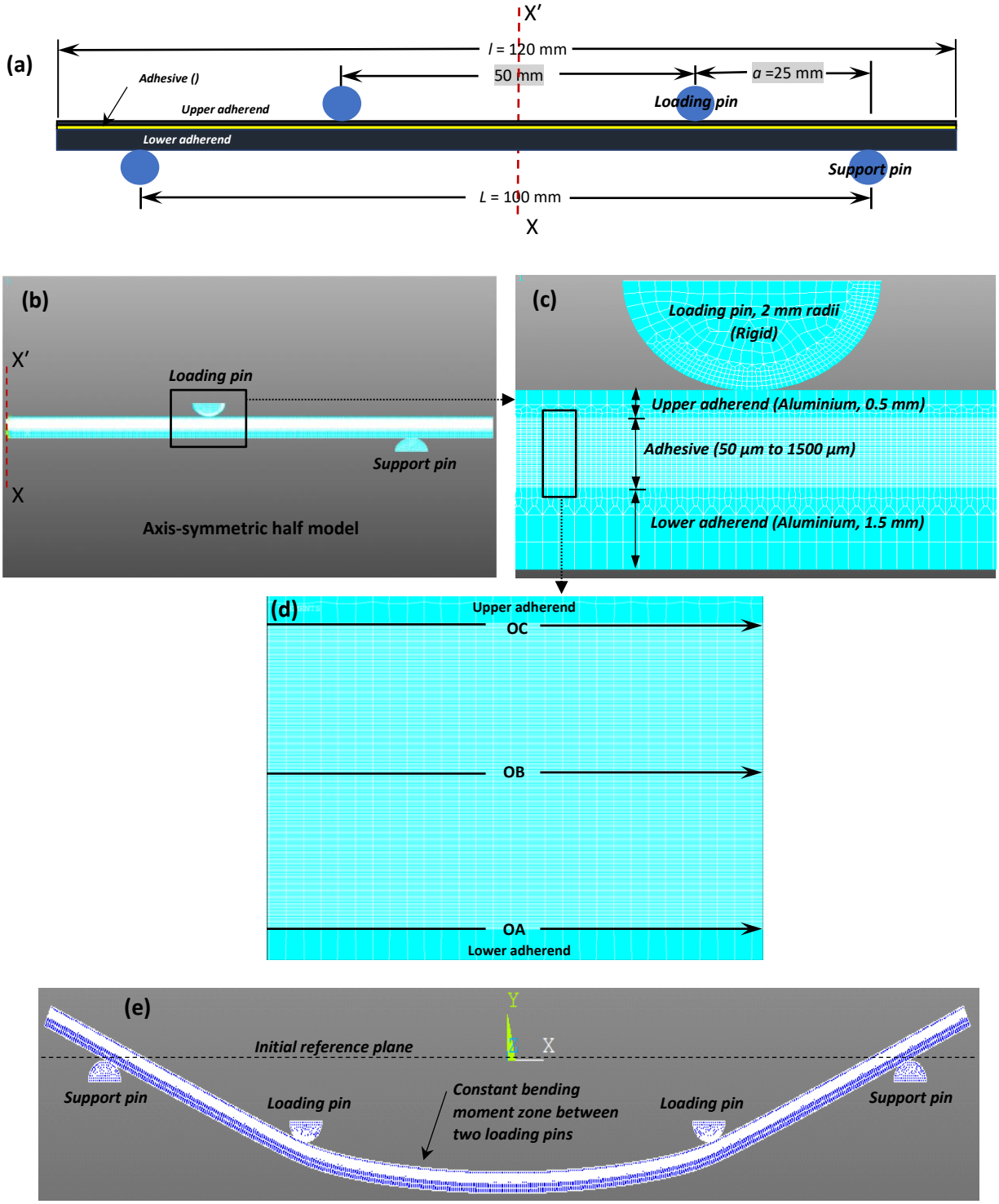

Figure 4.1. 4-point flexure FE schemes for metal-to-metal adhesive bond: (**a**) geometrical model, (**b**) half-symmetric model, (**c**) meshing of the model, (**d**) paths OA, OB and OC in the adhesive, and (**e**) deformed model.

The dimensions and properties of the adherends and the adhesives are shown in **Table 3.1** and the geometrical parameters are schematically represented in **Fig 4.1a**. The dimensions of

the adherends were chosen to understand the effect of adherend thickness and plastic deformation on the adhesive layer stress states. The study focuses on this aspect and endeavours to explain this in context of varying adhesive layer thickness for the two types of adhesives. Only half of the entire model has been considered because of symmetry of the load and support configurations. Both the adherends and the adhesive interlayers were meshed using PLANE 182 elements with plane-strain option. The sample mesh is shown in **Fig 4.1b**. The element size was maintained at 5 µm (finer size) [120] along the thickness of the adhesive layer. The loading and support pins are modelled as rigid semi-circular bodies with radii of 2 mm (**Fig 4.1c**).

The rigidity of loading and support pins was attained by considering a very high elastic modulus (value 100 times that of steel which has an elastic modulus of 210 GPa). Contact 172 and target 169 elements were used to model the contact between the adhesive joint, the load and support pins. These elements monitor the normal and frictional loads between the contact surfaces. The frictional co-efficient value of 0.2 was assumed between all contacting surfaces.

For all the models, a constant downward displacement boundary condition of 10 mm of the loading pin was applied which was constrained in the horizontal direction to prevent sliding on the upper adherend. The lower support was constrained in all directions. The adhesive was assumed to be perfectly bonded with the adherends at both the interfaces. The displacement increment in the solution stage was chosen to ensure a smooth loading of the model. Solution iterations were carried out until convergence was achieved. Convergence in this case was highly affected by the shift in the contact region between the joint, loading and support pins. To restrict the solution instability caused by the frictional effects, program chosen time stepping was selected. This ensures sub-division of the load steps under highly unstable conditions.

Since the behaviour of the adhesive is the object of primary interest, various result items have been extracted along different paths parallel to the span within the thickness of the adhesive (namely OA, OB and OC) as shown in **Fig 4.1d**. The 4-point bending model at the maximum displacement of 10 mm is shown in **Fig 4.1e**. The nomenclature is the same for all the thicknesses and the two types of adhesives considered in this study. In addition, the effect of the modulus mis-match on the adherend side of the interface was also observed. The total element and nodes employed in the calculations for 50 µm and 1500 µm thick adhesives are (3600, 4326) and (108000, 108871), respectively. 120 data points were considered for result extraction along each path (OA, OB and OC, each 60 mm long). This number was optimised on such that the result contour does not change considerably even with a higher number of data points.

The stress results obtained were normalised with respect to the tensile strength (σ_0) of the brittle adhesive and the yield strength (σ_y) of the ductile adhesive (**Table 3.1**). To validate the 4-point bending, the FE model was implemented on a 2 mm thick aluminium (defined here as control specimen), and the elastic modulus calculated from the 4-point bending FE model using **Equation 4.1** was 75 GPa, which is close to the literature value (elastic modulus of aluminium 68.4 GPa). It

is important to note that the elastic modulus has been calculated for a plane strain condition and the literature value of elastic modulus has been taken for a plane stress condition (about 9% difference in this case). Plane strain condition has been chosen as the sandwich structures simulated is assumed to have high width to thickness ratio. The FE mesh was optimised based on the validated elastic modulus value of aluminium and then the obtained optimised mesh was implemented in the adhesive joint model.

$$\delta = \frac{P(L-a)}{6LEI}\left[\frac{L}{L-a}\left(x-a\right)^3 - x^3 + \left(L^2 - (L-a)^2\right)x\right] + \frac{Pa}{6LEI}\left[\frac{L}{a}\left(x-(L-a)\right)^3 - x^3 + \left(L^2 - a^2\right)x\right]$$

Equation 4.1

where δ is the displacement, P is the load within the elastic limit, L is the span length between the supports, a is the distance of the load point from the support, E is the modulus of the material, I is the second moment of the cross sectional area (rectangular) and x is the distance of the section considered from one of the supports. In this case, since the FE model is two-dimensional, the load is considered per unit width and I is calculated accordingly.

The results of this analysis are divided into two components, i.e. stress determination for the brittle and the ductile adhesives of various thicknesses that characterises the critical condition over the length of span. Each component will be discussed within the assumptions in the FE simulations.

4.1.2. Indentation testing of adhesive bonds

The finite element simulations have also been performed using ANSYS Mechanical APDL (release 14.0), as shown in **Fig 4.2**. The 2D models of the adhesive joints have been created and meshed using PLANE 182 (2D quadratic) elements with large deformation behaviour with the plane strain option enabled. A unit length Δ_0 (equal to 100 μm) has been used to normalise the geometry in the model. The length of the model has been taken as $250\Delta_0$. The thickness of the lower adherend is $15\Delta_0$ and that of the upper adherend is $5\Delta_0$. Three different adhesive layer thicknesses have been considered (Δ_0, $2.5\Delta_0$, $5\Delta_0$) in the simulations. The indenter (Rockwell diameter = 4 mm) has been modelled as a material of very high elastic modulus so as to make it rigid. Frictionless contact has been assumed between the indenter and the upper adherend surface.

The through thickness element size within the adhesive was 5μm and element length along the interface was maintained at 15μm to ensure proper resolution of crack propagation. The dimensions of the adherends have been kept constant for all the models. The indenter axis (downward arrow) has been taken as the axis of symmetry of the model. As shown in **Fig 4.2a**, the lower edge of the lower adherend has been constrained along the vertical axis and the entire model is free to move along the horizontal direction (except along the symmetry axis). The load

was applied vertically downward (i.e. displacement mode) to the indenter. Aluminium has been chosen as the material for both upper and lower adherends. Both the adhesive and the adherend have been assumed to be elastic-plastic in nature with their behaviour modelled using a bi-linear material model. The properties of the materials are also shown in **Fig 4.2a**.

A simulation on a joint with no interfacial bonding (defined here as control specimen) has also been done to understand the effect of the interfacial bonding on the load-carrying capability of different geometrical configurations.

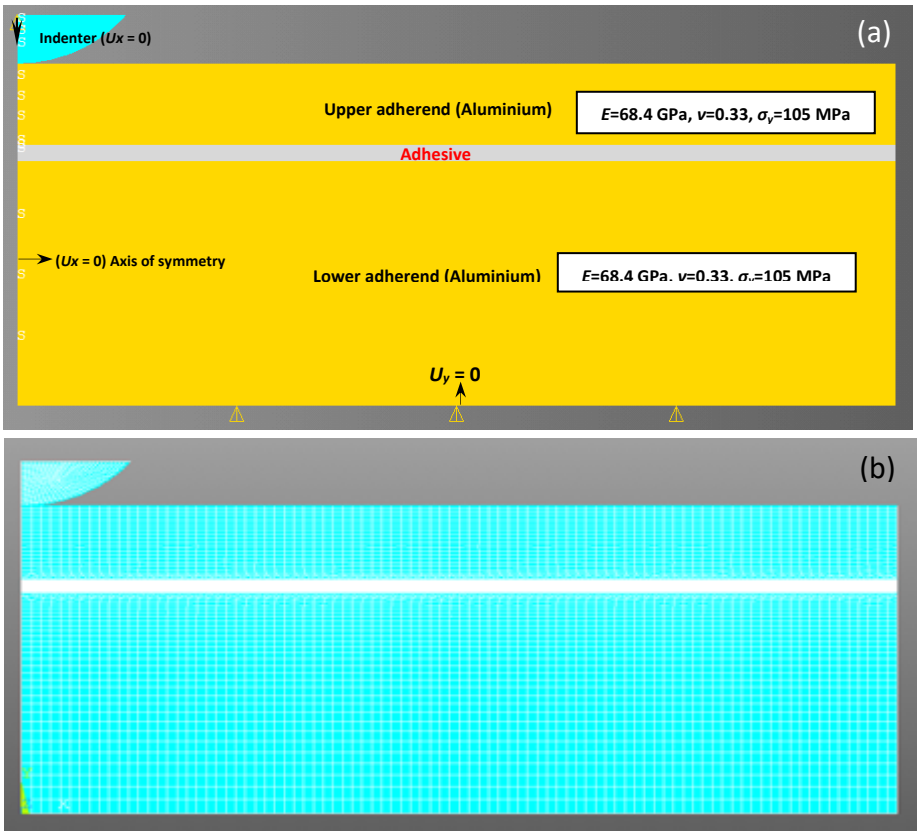

Figure 4.2. Indentation of metal-to-metal adhesively bonded joint: (**a)** model geometry and material properties, (**b**) sample mesh of adhesively bonded joint, adhesive layer thickness = 100 µm.

4.1.3. Cohesive zone model (CZM) formulation and definition of non-dimensional parameters

The interfaces of the adhesive and adherend were modelled using CONTACT 172 and TARGET 169 elements. The element traction-separation behaviour is governed by a traction-separation law employed as shown in **Fig 4.3.** Even though a variety of laws are used (e.g. triangular, trapezoidal and exponential) in de-bonding analysis, in the present study, a triangular law has been selected. This is because of its simplicity of formulation and relative ease of numerical convergence. Moreover, in the case of brittle adhesives, similar to the one used in this

study; it has been proven that the cohesive zone model (CZM) law shape has negligible effect on the loading behaviour of an adhesive joint [129]. Also, the triangular law has been implemented in various multi-layer indentation and adhesive joint studies [36], [38], [62]. The failure initiation and propagation criteria are given below. In the present case, the critical traction in both mode-I and mode-II have been varied as fractions of the adhesive yield strength 'σ_y' (i.e. 0.25σ_y, 0.5σ_y, 0.75σ_y, σ_y) keeping the interfacial toughness constant. In addition, to study the effect of the interfacial toughness (Γ_o), the interface strength has been maintained at σ_y and the interface toughness has been varied (at 0.00625$\sigma_y\Delta_0$, 0.0125$\sigma_y\Delta_0$, 0.025$\sigma_y\Delta_0$, 0.05$\sigma_y\Delta_0$). The normal and tangential toughness values have been assumed to be equal and so are the normal and tangential maximum tractions. The normal and tangential contact stresses are given by:

$$\sigma = K_n u_n(1\text{-}d_m) \qquad \textbf{Equation 4.2}$$

$$\tau = K_t u_t(1\text{-}d_m) \qquad \textbf{Equation 4.3}$$

where d_m is the damage parameter and is defined by:

$$d_m = \left\{\frac{\Delta_m - 1}{\Delta_m}\right\} \chi \qquad \textbf{Equation 4.4}$$

'K_n' is the normal stiffness, 'K_t' is the tangential stiffness, 'P_n' is the normal traction and 'P_t' is the tangential traction, and Δ_m is given by:

$$\Delta_m = \sqrt{\Delta_n^2 + \Delta_t^2} \qquad \textbf{Equation 4.5}$$

$$\text{with } \Delta_n = \frac{u_n}{u_{ni}} \text{ and } \Delta_t = \frac{u_t}{u_{ti}} \qquad \textbf{Equation 4.6}$$

$$\text{and } \chi = \left\{\frac{u_n^c}{u_n^c - u_{ni}}\right\} = \left\{\frac{u_t^c}{u_t^c - u_{ti}}\right\} \qquad \textbf{Equation 4.7}$$

where u_n, u_{ni}, u_n^c are the normal components of the displacement, displacement at damage initiation and displacement at debonding completion respectively. The suffix 't' denotes the tangential components of the corresponding displacements. The tangential stiffness K_t is given by:

$$K_t = \left\{\frac{\tau_{max} u_n^c}{\sigma_{max} u_t^c}\right\} K_n \qquad \textbf{Equation 4.8}$$

where σ_{max}, τ_{max} are the peak normal and tangential tractions. The de-bonding completion is defined by a power law based energy criterion:

$$\left\{\frac{G_n}{G_{cn}}\right\}^2 + \left\{\frac{G_t}{G_{ct}}\right\}^2 = 1 \qquad \textbf{Equation 4.9}$$

where $G_n = \int \sigma \, du_n$ and $G_t = \int \tau \, du_t$. G_n, G_{nc} are the opening mode energy release rate and its critical value. G_t, G_{tc} are the shear mode energy release rate and its critical value. After

delamination happens along the interfaces, the crack surfaces behave as two surfaces in sliding contact. Frictionless contact has been assumed between the crack faces.

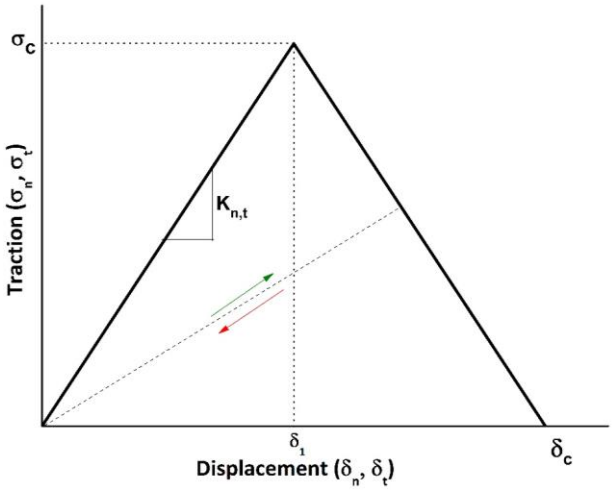

Figure 4.3. Traction-separation law implemented for the cohesive zone model.

The following relation describes the behaviour of the adhesive bond under indentation load. The relation explains the dependence of the indentation load on the various geometrical parameters and material properties of the adhesive bond.

$$P = f\big(\underbrace{h, E_{adh}, \sigma_{adh}^{y}, \nu_{adh}, h_{adh},}_{\text{Adhesive properties}} \quad \underbrace{\Gamma_c, \sigma_c}_{\text{CZM parameters}} \quad \underbrace{E_a, \sigma_a^{y}, \nu_a}_{\text{Adherend properties}} \quad \underbrace{h_{adh}, R}_{\text{Geometrical parameters}}\big)$$

Equation 4.10

where

P = Indentation load per unit width.

h = Indentation depth.

$E_{adh(a)}$ = Elastic modulus of the adhesive (adherend).

$\sigma_{adh(a)}^{y}$ = Yield stress of the adhesive (adherend).

$\nu_{adh(a)}$ = Poisson's ratio of the adhesive (adherend).

$h_{adh(a)}$ = Thickness of the adhesive (adherend).

R = Radius of the indenter.

Γ_o = Interfacial toughness from the CZM.

σ_c = Critical stress parameter of the CZM.

In the present analysis, the adherend dimensions and material properties are the same in all the simulations. Thus, the dependency on the adherend properties is eliminated in this study. After simple dimensional analysis, the above model can be simplified to a relation between a group of non-dimensional parameters as shown in **Equation 4.11**

$$\frac{P}{\sigma_{adh}^{y} R} = f\left(\frac{\Delta}{R}, \frac{E_{adh}}{\sigma_{adh}^{y}}, \frac{\sigma_c}{\sigma_{adh}^{y}}, \frac{\Gamma_c}{\sigma_{adh}^{y} R}, \frac{h_{adh}}{R}\right) \qquad \textbf{Equation 4.11}$$

Thus, the normalised indentation load is a function of the normalised indentation depth, normalised elastic modulus, normalised yield strength of the adhesive, normalised interfacial toughness and normalised interfacial strength of the CZM. This dependency was investigated through systematic variation of the dimensionless parameters. The variation of the parameters such as the critical indentation depth, total crack length with respect to the above non-dimensional parameters has also been investigated. In the present study, the load has been normalised with respect to corresponding load on an adhesive joint with similar geometry without any interfacial bonding (P_o). Thus, the parameter '$\frac{P}{\sigma_{adh}^{y} R}$' changes to '$\frac{P}{P_o}$'.

4.1.4. Energy release rate and mode-mix ratio calculations

The normal and tangential tractions along a bi-material interface are given by the expression:

$$\sigma_{yy} + i\sigma_{xy} = \frac{K_I + iK_{II}}{\sqrt{2\pi r}} r^{-i\varepsilon} \qquad \textbf{Equation 4.12}$$

Where

K_I = Mode-I stress intensity factor

K_{II} = Mode-II stress intensity factor.

r = distance from the crack tip along the interface.

The above equation can be further modified to find the normal and tangential traction components acting on the interface. This leads to

$$\sigma_{yy} = \frac{1}{\sqrt{2\pi r}} \left[K_I \cos(ln\, r^{\varepsilon}) + K_{II} \sin(ln\, r^{\varepsilon})\right] \qquad \textbf{Equation 4.13}$$

$$\sigma_{xy} = \frac{1}{\sqrt{2\pi r}} \left[K_I \sin(ln\, r^{\varepsilon}) - K_{II} \cos(ln\, r^{\varepsilon})\right] \qquad \textbf{Equation 4.14}$$

where

'ε' is given by

$$\varepsilon = \frac{1}{2\pi} \, log\left(\frac{1-\beta}{1-\beta}\right)$$ **Equation 4.15**

and 'β' is given by

$$\beta = \frac{\mu_2(k_1 - 1) - \mu_1(k_2 - 1)}{\mu_2(k_1 + 1) + \mu_1(k_2 + 1)}$$

Equation 4.16

μ_i is the material shear modulus and k_i is given by $(3 - 4\nu)$ for plane strain and $(3 - 4\nu)/(1 + \nu)$ for plane stress.

By using the opening and tangential stresses at the crack tip calculated through the FE analysis, the stress intensity factors can be estimated. The mode-mix ratio can then be calculated using

$$\theta = \, tan^{-1}\left(\frac{K_{II}}{K_I}\right)$$ **Equation 4.17**

The above set of equations were used to calculate the energy release rates of cracks propagating along the interfaces of adhesive joints with the interfacial strengths lower than the adhesive yield stress ($\sigma^c/\sigma^y < 1$), as no plastic deformation can be seen within the adhesive layer. In the case of adhesive bonds where the interfacial strength is higher than the yield strength, plastic deformation is expected within the adhesive layer, the elastic energy release rate itself is not enough, but the plastic deformation also needs to be considered. Hence, the deformation J has been calculated for all these adhesive bonds using the following relations

$$J = J_{el} + J_{pl}$$ **Equation 4.18**

The term J_{el} is the elastic term of the total energy release rate and is equal to the above calculated value of 'G' and the term 'J_{pl}' represents the total plastic deformation energy around the crack tip.

J_{pl} can be calculated by invoking the deformation theory based definition of *'J'* incrementally and is given by:

$$J_{pl} = \left[\frac{\eta_{i-1}}{b_{i-1}} \frac{(P_i + P_{i-1})(h_i - h_{i-1})}{2}\right]\left[1 - \gamma_{i-1} \frac{(a_i - a_{i-1})}{b_{i-1}}\right]$$ **Equation 4.19**

Where

a_i = Crack length at the current step.

b_i = Ligament length at the current step = Total interface length-a_i.

P_i = Load per unit width at the current step.

h_i = Indenter displacement at the current load step.

$\gamma_{i-1} = 1 + 0.76\left(\frac{b_i}{Interface\ length}\right)$

$\eta_{i-1} = 2 + 0.522\left(\frac{b_i}{Interface\ length}\right)$

The calculations are made on the load-displacement curve after crack initiation and propagation. It should be noted here that the load value used in the calculations is the interface load (P-P_o) obtained by subtracting the no-bonding indentation load from the indentation load at the corresponding depth.

4.2. Results

4.2.1. 4-point bending

This work has two basic components, i.e. stress determination for the brittle and the ductile adhesives of various thicknesses that characterises the critical condition over the length of span. Each component will be discussed within the assumptions in the FE simulations. This section discusses the key results.

4.2.1.1. Effect of adhesive thickness and adherend deformation

An observation of the stress distribution plots shows that the span between the mid-axis and the load point is under a uniform stress condition. There exists a considerable difference in the through thickness stress distribution between the 50 μm and 1500 μm thick adhesives (**Figs 4.4a** and **4.4b**). The path OA is at a lower stress state at higher thicknesses (e.g. **Fig 4.4b** for 1500 μm thick adhesive) because of its association with the thicker (1.5 mm) adherend whose degree of plastic deformation being lower compared to the upper adherend (thinner, 0.5 mm). The adherends are known to have a constraining effect on the adhesive layer which is dependent on the modulus mis-match between the adherends and the adhesive and the adhesive thickness [49] [50] [52].

Tvergaad and Hutchinson [51] have investigated the effect of the adhesive layer thickness on the steady state toughness of an adhesive joint tested in mode-I. They reported an increase in the toughness with an increase in the adhesive layer thickness with all the other parameters remaining constant. They attributed this behaviour to the elastic shielding of the adhesive layer at lower thicknesses. This constraining effect is due to the interaction of the stress field in the adhesive with the stiff adherends which modifies the shape and size of the plastic zone in the adhesive layer [53] [67]. In the particular case of the brittle adhesive, this effect might further

be assisted by its relatively higher stiffness (elastic modulus 11 times higher compared to ductile adhesive, **Table 4.1**) which confines the load to the upper layers.

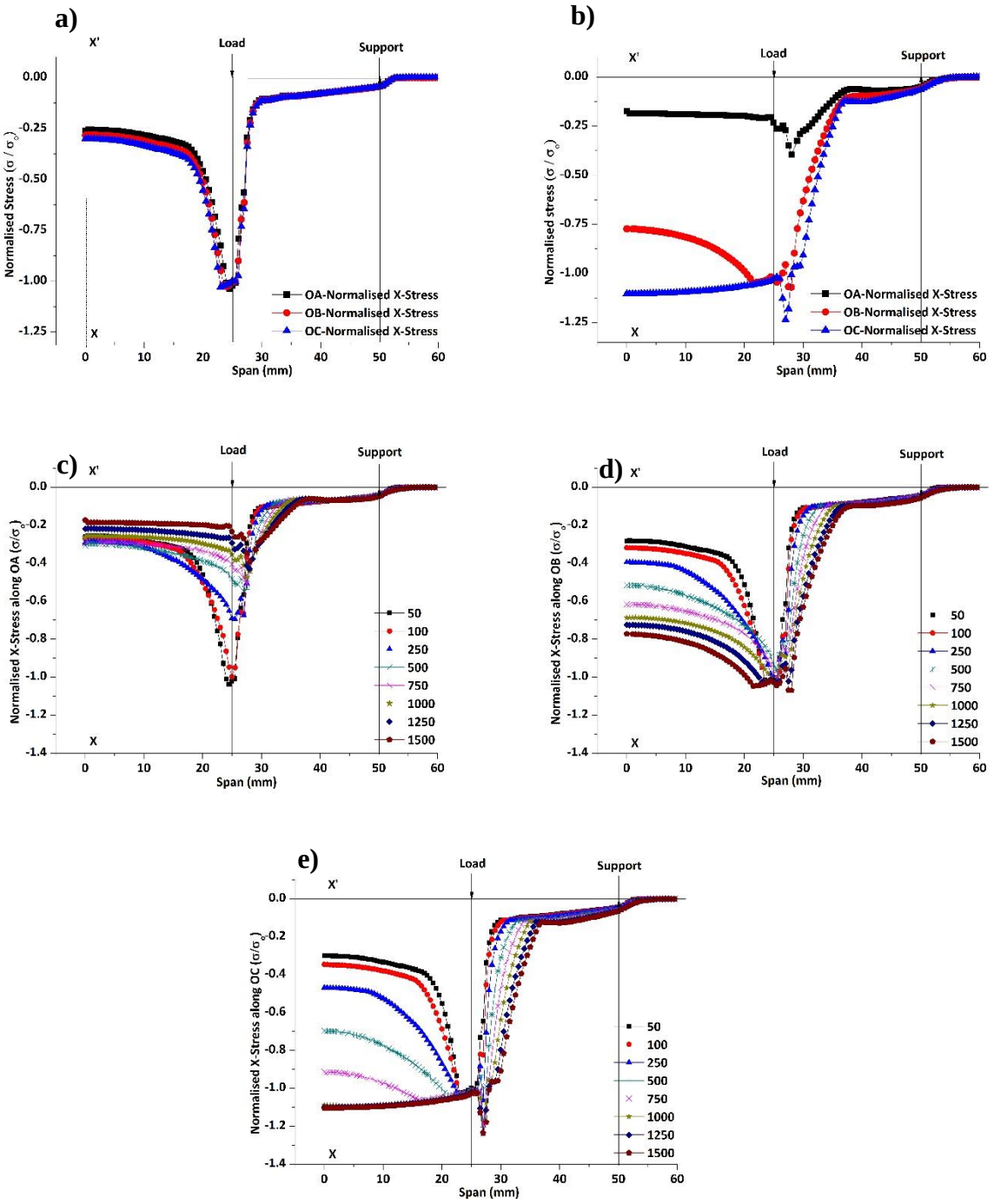

Figure 4.4. Normalised X-directional stress profile along OA, OB and OC with brittle adhesive: (a) 50 µm thick, and (b) 1500 µm thick, (c) along OA for all thicknesses, (d) along OB for all thicknesses, and (e) along OC for all thicknesses.

The term 'stiffness' has been used to refer to the deformability of the adhesive in this context implying the load-deformation behaviour of the adhesive. The variation of the stress

between layers OA and OB (**Figs 4.4c** and **4.4d**) can also be attributed to this combined effect (i.e. stiff lower adherend and brittle adhesive). Also, the distance of the layer concerned from the thicker (lower, 1.5 mm) adherend appears to affect the state of stress (i.e. the higher the distance, the higher is the stress state). The opposite can be said about the distance from the upper adherend due to the higher degree of plastic deformation because of its lower thickness.

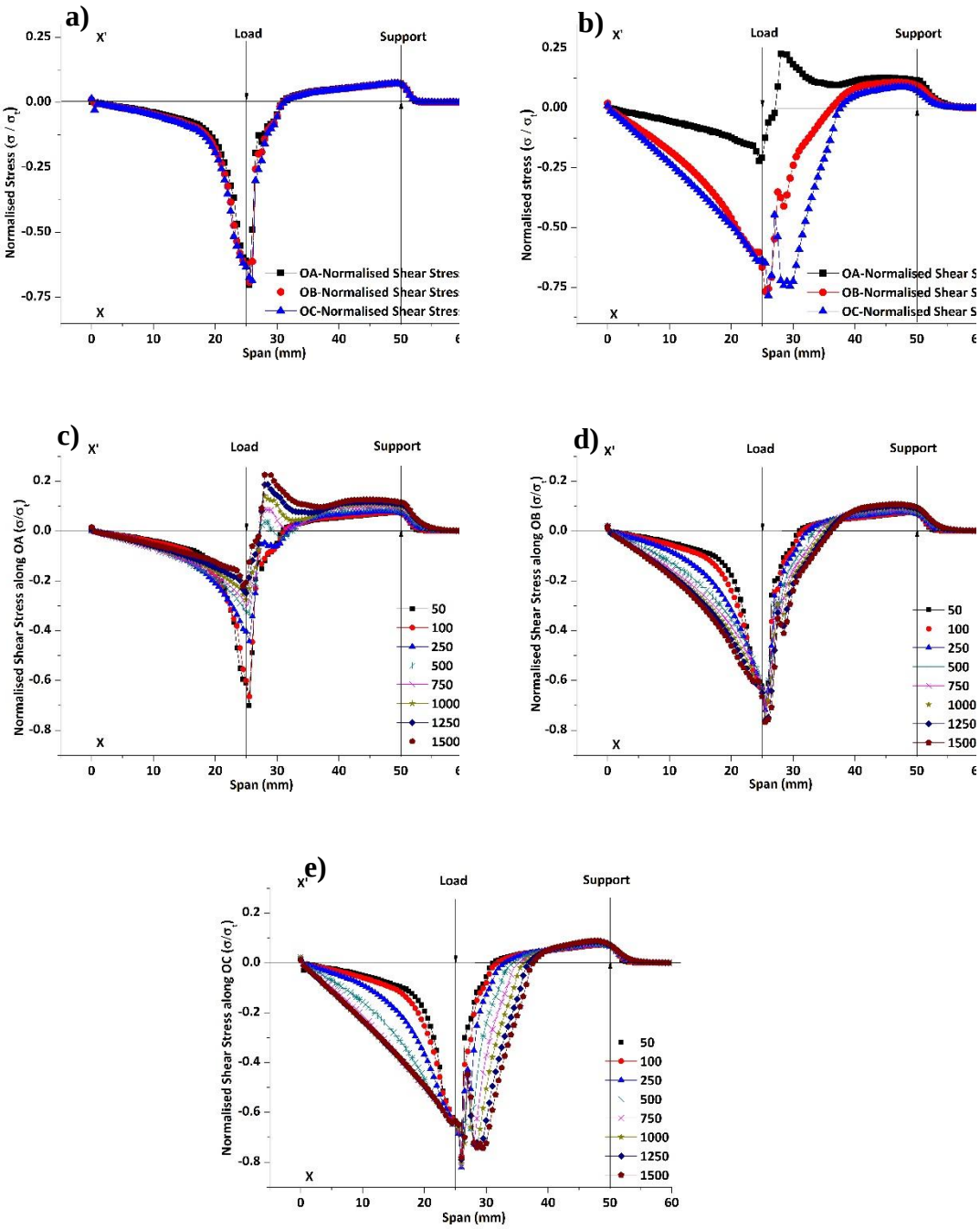

Figure 4.5. Normalised shear stress profile along OA, OB and OC with brittle adhesive: (a) 50 µm thick, and (b) 1500 µm thick, (c) along OA for all thicknesses, (d) along OB for all thicknesses, and (e) along OC for all thicknesses.

The increase in the adhesive thickness decreases the stress concentration because of

higher degree of plastic deformation within the adhesive. Marzi *et al* [68] reported an increase in the flexibility of adhesive joints with increasing adhesive thickness. The span along which higher stress states (stress higher than the compressive strength) can be seen, increases with increasing thicknesses along OB and OC (**Figs 4.4d** and **4.4e)**. This is because of the distribution of the stress over a larger area with the increasing thickness.

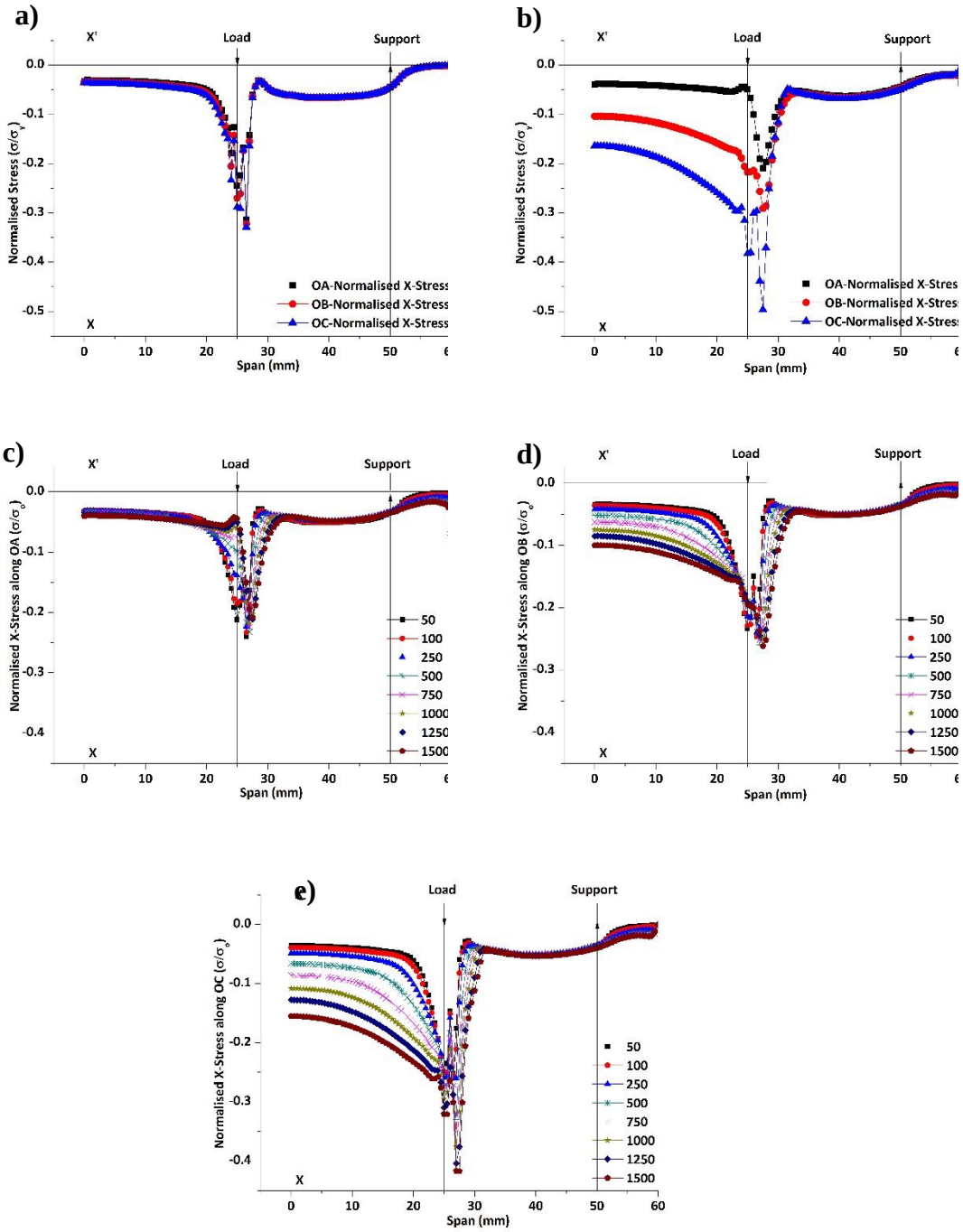

Figure 4.6. Normalised X-directional stress profile along OA, OB and OC with ductile adhesive: (a) 50 µm thick adhesive layer, and (b) 1500 µm thick adhesive layer, (c) along OA for all thicknesses, (d) along OB for all thicknesses, and (e) along OC for all thicknesses.

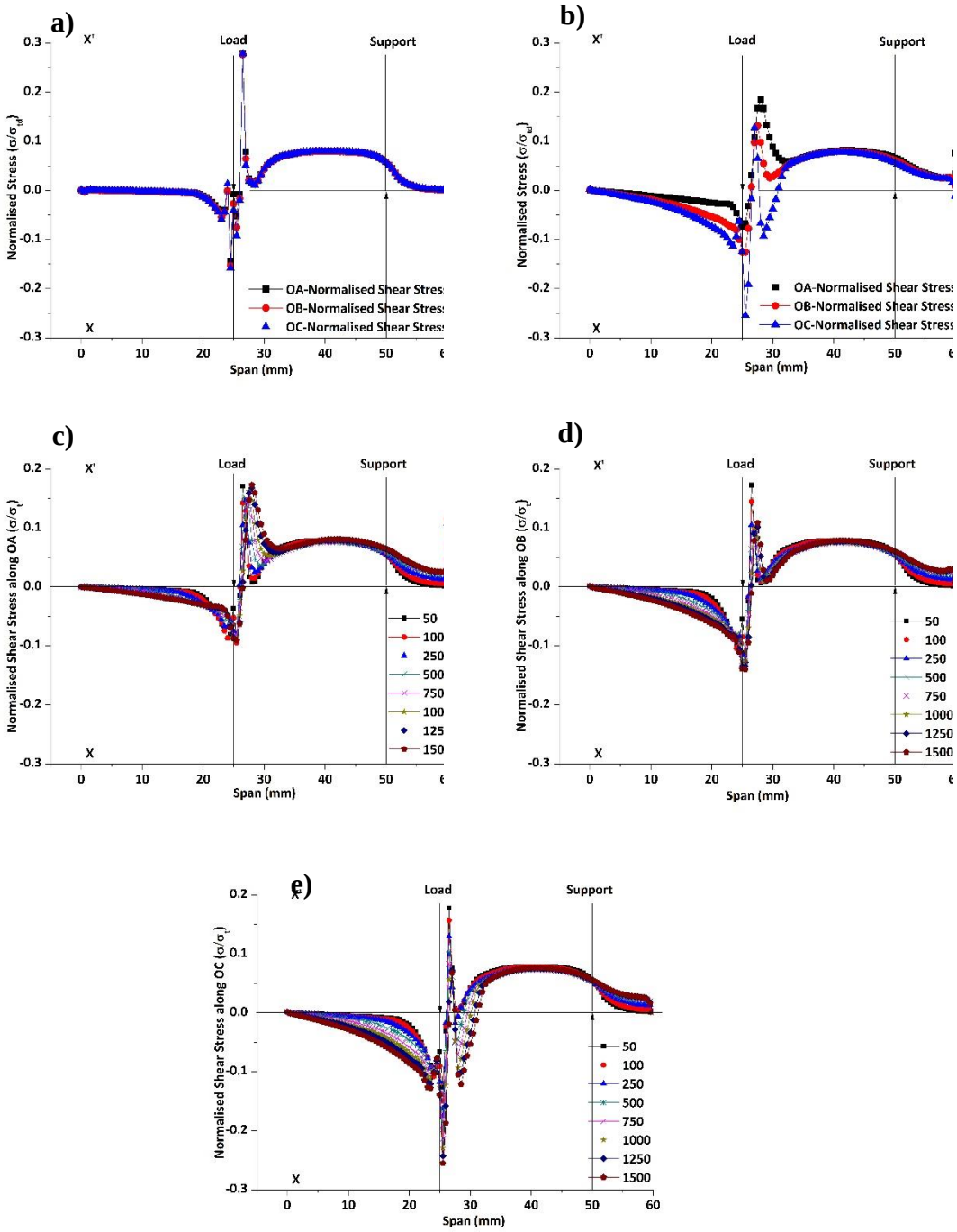

Figure 4.7. Normalised shear stress profile along OA, OB and OC with ductile adhesive: (a) 50 μm thick, and (b) 1500 μm thick, (c) along OA for all thicknesses, (d) along OB for all thicknesses, and (e) along OC for all thicknesses.

At lower thicknesses, the constraint of the adherends prevents the adhesive from straining to relieve the stress from the high load-concentration point. However, at higher thicknesses, restraint decreases, distributing the stress. A similar observation has been made by Xu *et al* [62] that the increase in thickness increases the toughness by increasing the size of the plastic zone. The higher stress state along OC observed in all the simulations was probably because of two reasons:

(a) OC is the upper interface (between the upper adherend and the adhesive), and (b) the upper adherend thickness is 1/3rd of the lower adherend thickness and hence has undergone higher degree of plastic deformation which increases the degree of stress along the upper interface. It is important to note that the X-directional stresses investigated here corresponds to the in-plane tensile or compressive component. This particular component has been chosen instead of the Y-directional peel component as the failure was expected to occur within the adhesive layer because of the bending stress induced during loading.

The contours of Y-directional stresses have also been studied but not presented in this manuscript as they are predominantly compressive within the sandwich structure and failure has not been deemed possible in such test configuration. The shear stress distribution in the adhesive layers seems to be uniform and close to zero along all the adhesive layer combinations simulated (**Figs 4.5a** to **4.5e**). This is consistent with the beam theory which states that there is no shear stress between the loading points in 4-point bending. However, at higher thicknesses of the adhesive layer, the shear stress exhibited a sharp decline from mid-span towards the load-pin location followed by high variations near the loading point since the shear stress is a result of the differential normal stress acting on the adhesive and as the interface with the upper and lower adherends are subjected to higher stress variations due to localised loading at the load pins.

The stress concentration among the upper layers at higher thicknesses similar to brittle adhesive (discussed above) was not observed in the ductile adhesive (e.g. **Figs 4.6c** and **4.6d**). The lower elastic modulus (of ductile adhesive) leads to a higher degree of deformation and strain transfer to the lower portions of the adhesive layer. Sawa *et al* [120] reported a similar observation where in lower principal stresses were observed in ductile adhesive layers under combined tensile and bending loads. The similarity in the stress profiles for all the thicknesses can also be explained by the same. Even though the shear stress is consistently close to zero for all the thicknesses considered, the change in nature of the shear stress profiles for the various thicknesses of the ductile adhesive at the load point (**Figs 4.7c** to **4.7e**) is attributed to the sudden change in the slope of the deflected beam at this location which induces a high degree of stress (and strain) concentration in the upper and lower adherends (i.e. lower adherend is under a high tensile strain at this point and the upper adherend is under a high compressive strain).

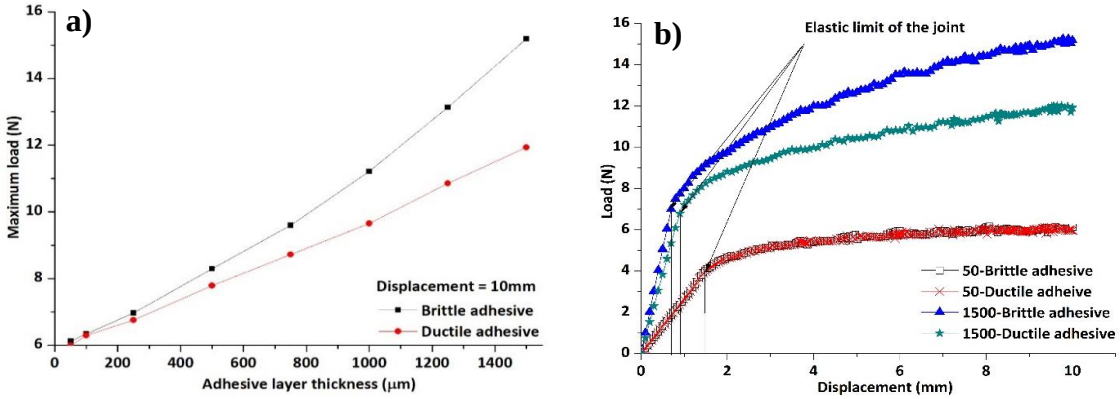

Figure 4.8. (a) Load vs thicknesses profiles of the brittle and ductile adhesives at a displacement of 10 mm, and (b) load vs displacement profiles of 50 μm and 1500 μm brittle and ductile adhesive layer joints.

The increase in the adhesive thickness increases the load capacity of the joint (**Fig 4.8a**). When compared to the ductile adhesive, the rate of increase of the load capacity with adhesive thickness is higher with brittle adhesive, though the difference is high only beyond a certain thickness. If the adhesive stress state is assumed to be a result of the relative deformation of the adherends, the load capacity increase with increasing adhesive layer thickness cannot be explained. The load increase with increasing thickness suggests that the adhesive layer has some load carrying capacity of its own and this is affected by the modulus of the adhesive.

4.2.1.2. Effect of adhesive modulus

The effect of the adhesive modulus can be seen in terms of the stress concentration and the degree of deformation along OA, OB and OC in the adhesive. A simple comparison of the stress state along path OA for the brittle and ductile adhesive s of similar thicknesses reveals interesting facts. As shown in **Fig 4.9a**, the degree of stress concentration is considerably lower for the 50 μm ductile adhesive compared to the brittle adhesive. Similar trend can be seen (in **Fig 4.9c**) with the shear stress distribution. However, for the 1500 μm thick adhesive layer, similar comparison (**Figs 4.9b** and **4.9d**) shows that the difference between the brittle and ductile adhesives along the path OA is relatively less compared to that for the 50μm thick adhesive layer.

This, as discussed, is a combined effect of the adhesive modulus and constraints because of the adherends and the adhesive layer thicknesses. From **Fig 4.6c**, for the ductile adhesive, increase in the adhesive thickness does not show a significant effect on the stress distribution along OA (both the X-stress and shear stress), thus effectively showing the stress propagation from upper to lower interface in the ductile adhesive.

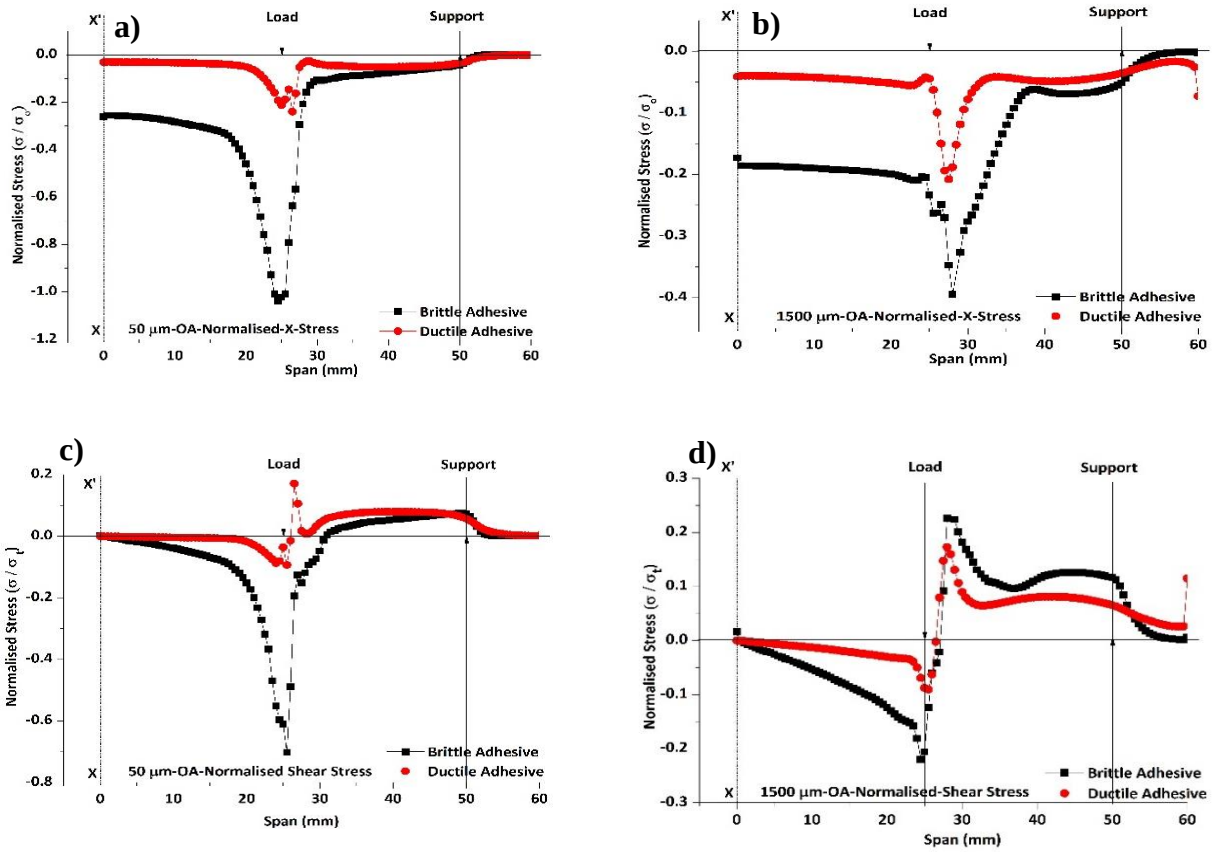

Figure 4.9. Comparison of stress profiles between brittle and ductile adhesive s along the path OA: (a) X-directional stress profile in 50 µm thick, (b) X-directional stress profile in 1500 µm thick, (c) shear stress profile in 50 µm thick, and (d) shear stress profile in 1500 µm thick.

The 4-point bending force-displacement profiles (**Fig 4.8b**) show an increase in the stiffness of the joint with an increase in the adhesive interlayer thicknesses and at the same thickness, the stiffness increases with increasing modulus. The nature of the adhesive elastic modulus appears to have no effect on the force-displacement profile at an adhesive thickness of 50 µm (even beyond the elastic limit). The influence of the adherends appears to be dominant in this case and completely masks the relatively ductile nature of the adhesives.

From **Figs 4.8a and 4.8b**, the variation of load at the maximum displacement can be seen as a function of the adhesive layer thickness. It can be seen that at lower thicknesses, the adhesive joint with the brittle layer and the one with ductile layer have almost similar load carrying capabilities, irrespective of the adhesive modulus. This observation supports the claim that at lower adhesive layer thicknesses, the deformability of the adhesive layer and hence the flexibility of the joint are dictated by the adherend behaviour to a large extent. At higher adhesive layer thicknesses, the load carrying capacity is governed also by the adhesive material properties which can be seen as a higher load capacity at higher thicknesses of the brittle adhesive and also a larger difference in the load capacity of the brittle and ductile adhesive joints with similar adhesive layer thickness.

4.2.1.3 Peak stress variation in adhesive layer

Even though the stress variations along the span of the joint are quite high at specific locations (e.g. in the vicinity of the loading pin) because of St. Venant's effects, the overall distribution seems to follow a similar trend in all the geometries. The shear stresses are almost zero in the mid-span (XX´-loading pin) in the ductile adhesive and in the brittle adhesive the adherend plasticity has led to a slight deviation from this trend. The shear stress is believed to be induced by the relative motion of the adherends. The variation of the mid-span normalised von-Mises stress with the adhesive layer thickness is shown in the **Fig 4.10a** and **Fig 4.10b** for the brittle and ductile adhesives respectively.

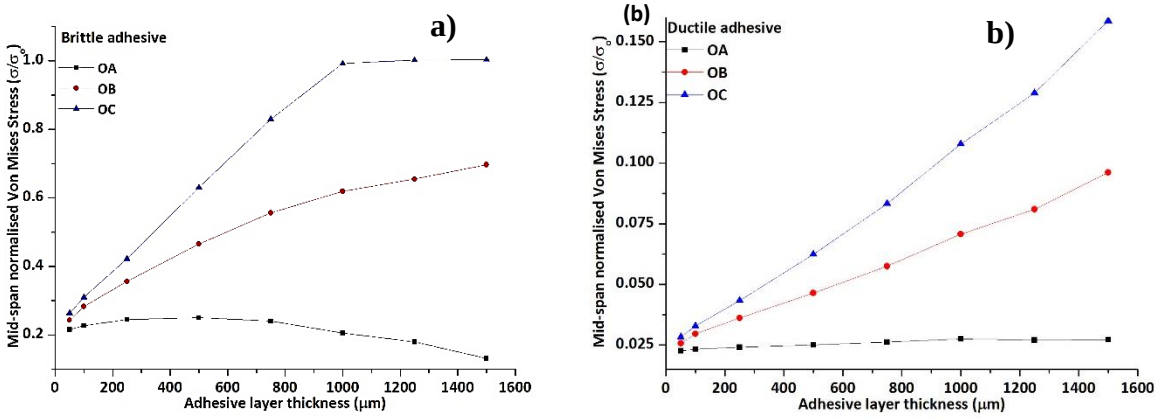

Figure 4.10. Mid-span normalised von-Mises stress vs adhesive layer thickness plots: (a) brittle adhesive, and (b) ductile adhesive.

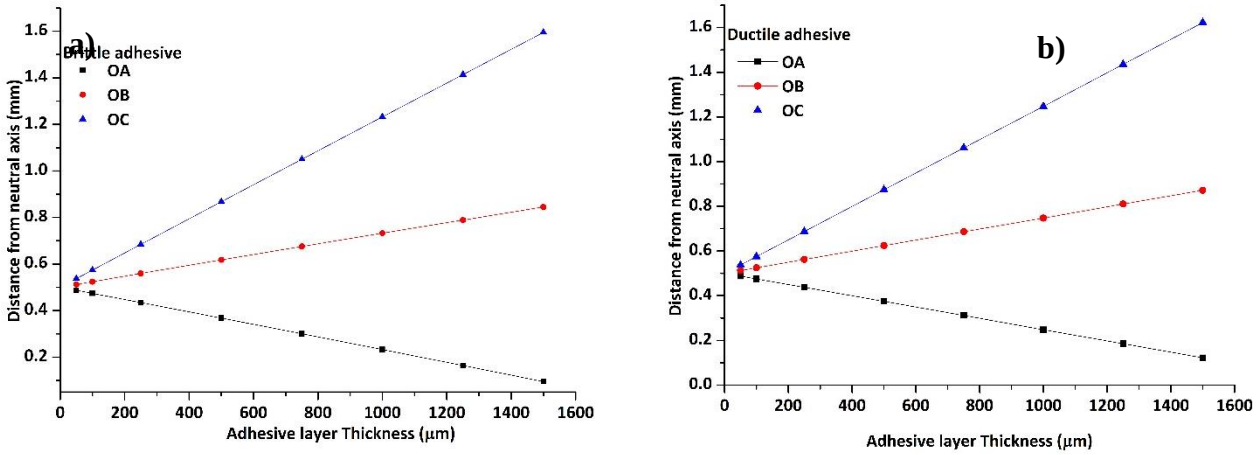

Figure 4.11. Distance of OA, OB and OC from neutral axis: (a) brittle adhesive, and (b) ductile adhesive.

The steady increase in the stress along the upper interface (OC) can be observed with increasing thickness until the stress crosses the yield point beyond which the entire upper interface can be assumed to have failed. The rate of increase of the mid-span stress with the adhesive layer thickness decreases from the upper interface (OC) to lower interface (OA). A simple explanation of this behaviour has been investigated by looking at the joint as a composite beam under flexural load. **Fig 4.11a** and **Fig 4.11b** show the position of OA, OB and OC with respect to the neutral axis of the composite beam with the brittle and ductile adhesives, respectively. The position of the neutral axis has been calculated according to simple beam theory. As can be seen, the peak mid-span von-Mises stress along the three layers follows a similar trend as the corresponding distance from the calculated neutral axis. The same behaviour can be seen in both the ductile and brittle adhesive layers, although the peak stresses in the ductile adhesive layers are quite low compared to those in the brittle adhesive.

4.2.2. Indentation testing of perfectly bonded adhesive joints

A preliminary study was conducted to understand the indentation stress distributions in the adhesive layer and to identify the possible failure and deformation mechanics. This section presents the results obtained from the simulations on indentation testing of adhesive joints with the adherends and the adhesive perfectly bonded across the interfaces. In this study, the values assigned to the normalised elastic modulus (E_{adh}/σ_{adh}^{y}) of the adhesive were 10, 50, 100, 200 and 500. The values assigned to the normalised thickness of the adhesive layer (h_{adh}/R) were 0.025, 0.0625 and 0.125. The rest of the parameters from **Equation 4.10** were assumed to have no effect on the indentation response as the interface was assumed to be perfectly bonded. The simulations were carried out with various adhesive layer thicknesses and elastic moduli. To assess the strength of the adhesive bond interface itself, simulations were also carried out on adhesive bonds where one of the interfaces is completely debonded. By comparing the load-displacement profiles of the fully bonded joints to those of the fully debonded joints, the energy absorbed by the adhesive layer interface in addition to the associated plastic deformation energy can be extracted.

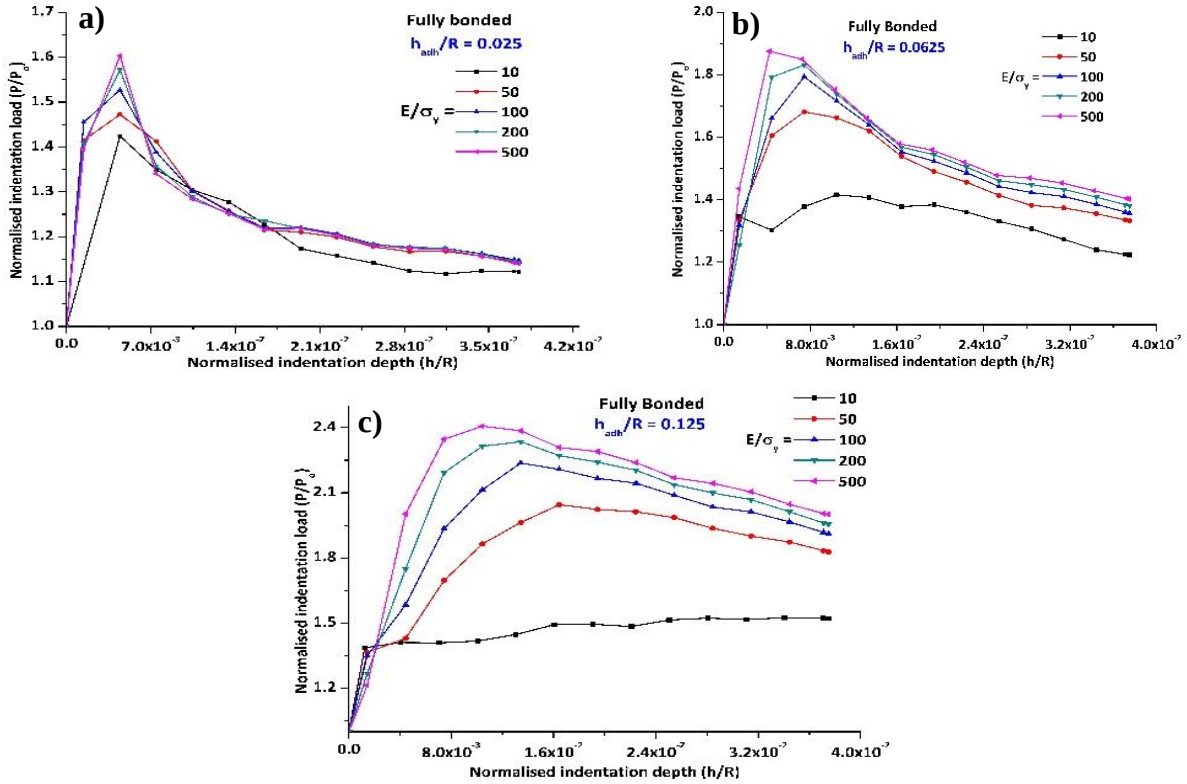

Figure 4.12. Normalised load-normalised displacement plots of adhesive joints with h_{adh}/R values of **a.** 0.025, **b.** 0.0625 and **c.** 0.125

The maximum normalised displacement (*h/R)* of the indenter was fixed at 0.0375 for all the simulations carried out. The load-displacement curve, interface shear and opening stress profiles and the indent profile on the top adherend were recorded from each simulation at various indentation depths. This allows us to understand the evolution of the stress profile with respect to the indentation depth and possibly predict a critical indentation depth and the corresponding indentation load. The load at a given depth was normalised with respect to the load of the fully-debonded adhesive joints at the corresponding depth. **Figure 4.12** presents the normalised load-displacement profiles of simulations with various E_{adh}/σ_{adh}^{y} values for each normalised adhesive layer thickness (h_{adh}/R) values. The increase in the thickness increases the peak normalised load especially in adhesive layers with high elastic modulus (E_{adh}/σ_{adh}^{y}=500). Also, the role of the adhesive layer elastic modulus in the load carrying capability of the adhesive joint becomes more apparent at higher thicknesses.

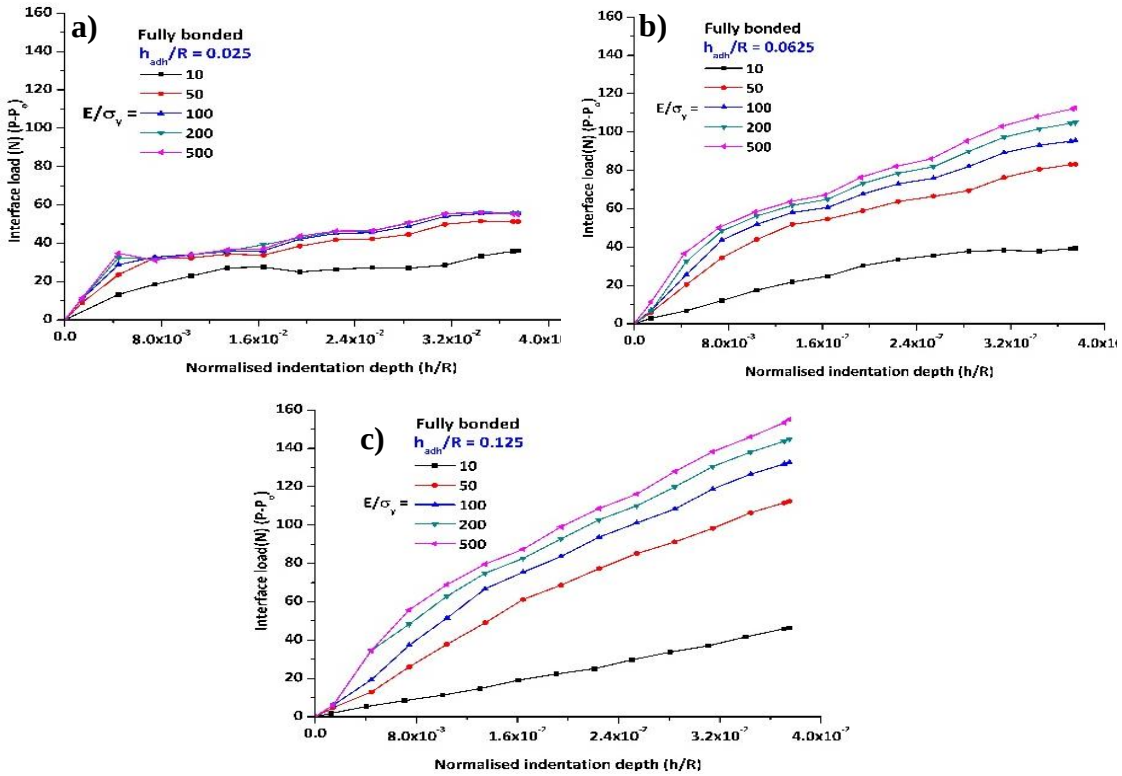

Figure 4.13. Interface loads (P-P_o) of adhesive joints with various E_{adh}/σ_{adh}^{y} values and h_{adh}/R values of **a.** 0.025, **b.** 0.0625 and **c.** 0.125.

The difference between the normalised load-displacement curves is more apparent at higher adhesive layer thickness (h_{adh}/R=0.125). Thus, the inference that the indentation method can be used to qualitatively distinguish between ductile and brittle adhesive joints can be drawn from the above observation. Furthermore, the deterioration of the elastic modulus due to environmental factors can also be quantified using this method.

The increase in the adhesive layer thickness does not seem to have a significant effect on the peak stress in the adhesive layers with higher elastic moduli (E/σ_y = 500). However, at lower elastic modulus (E/σ_y = 10), the peak stress decreases with increasing adhesive layer thickness.

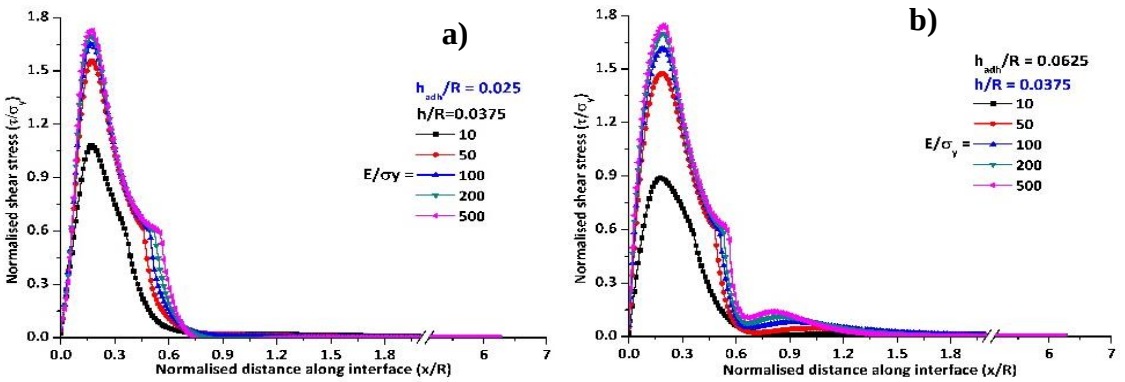

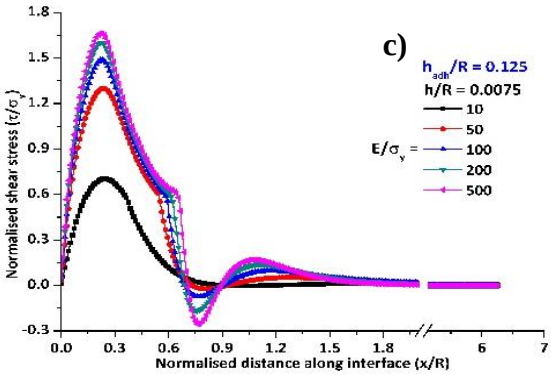

Figure 4.14. Variation of normalised shear stress along the interface **a.** for h_{adh}/R=0.025 at *h/R*=0.0625, **b.** for h_{adh}/R=0.0625 at *h/R*=0.0625, and **c.** for h_{adh}/R=0.125 at *h/R*=0.0375.

It can also be said that at higher adhesive layer thicknesses, the interfacial deformation increases, especially at higher elastic modulus of the adhesive layer. To further illustrate, the difference between the indentation loads, the fully bonded and fully de-bonded adhesive joints is plotted against the corresponding indentation depth as shown in **Figure 4.13**. This is a measure of the total energy spent on the interfacial deformation and includes both the elastic and plastic deformation of the adhesive along the interface. In other words, as the thickness increases, the significance of the interfacial quality, represented by its strength and toughness, also increases.

The normal stress in the adhesive layer is primarily compressive around the indenter. The deformation profile shows that the principal failure mechanism is the extrusion of the adhesive layer from underneath the indenter away from the axis of symmetry. The extruded adhesive piles up around the indenter leading to a build-up of shear stress along the interface leading to delamination. Hence, the adhesive layer is primarily expected to fail in shear mode (mode-II) with the crack propagating along the interface. To identify the critical indentation depth, the interfacial stress is plotted with respect to the length along the interface. The shear stress was normalised with respect to the yield stress of the adhesive. These plots show the evolution of the shear stress with respect to the indentation depth (**Fig 4.12)**. The normalised shear stress at a given indentation depth and adhesive layer thickness increases with increasing elastic modulus of the adhesive.

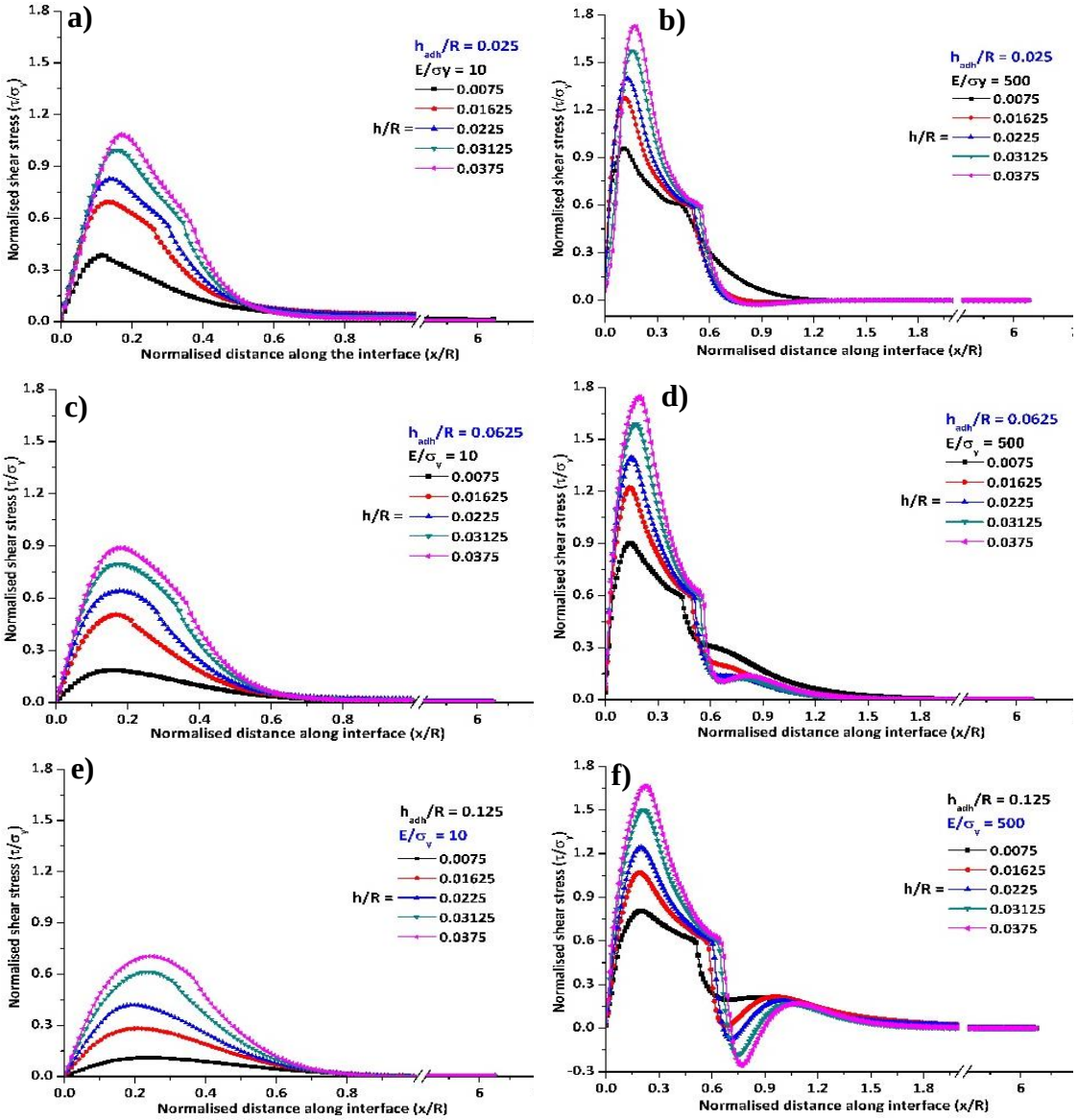

Figure 4.15. Evolution of shear stress with respect to indentation depth in adhesive joints with **a.** E_{adh}/σ_{adh}^{y}=10, h_{adh}/R=0.025, **b.** E_{adh}/σ_{adh}^{y}=500, h_{adh}/R= 0.025, **c.** E_{adh}/σ_{adh}^{y}=10, h_{adh}/R=0.0625, **d.** E_{adh}/σ_{adh}^{y}=500, h_{adh}/R= 0.0625, **e.** E_{adh}/σ_{adh}^{y}=10, h_{adh}/R=0.125, **f.** E_{adh}/σ_{adh}^{y}500, h_{adh}/R= 0.125.

Hence for a given yield limit of a material, a lower elastic modulus of the adhesive layer implies that there might not be any crack initiation under indentation loading as the shear stress never exceeds the yield limit. Referring to the above plot it can be concluded that the adhesive bond with the adhesive layer with the normalised elastic modulus, E/σ_y = 10 will not exhibit any crack initiation for a fixed indentation depth. This is especially the case with the higher adhesive layer thicknesses. To identify the depth at which the crack initiates, the stress evolution is plotted with respect to indentation depth. **Figure 4.14** shows these plots for three adhesive layer

thicknesses at the lowest and highest normalised modulus values. The plots for the remaining values of the normalised modulus are not shown here for brevity. **Figure 4.15** shows the evolution of shear stress distribution with indentation depth for different thicknesses and highest and lowest adhesive elastic moduli. The above analysis helps in predicting the approximate failure initiation load and depths by using the stress states in the adhesive.

The peak stress values at various indentation depths were used to extract the critical indentation depth which is plotted against the normalised elastic modulus for various adhesive layer thicknesses in **Fig 4.16**. The plot shows that as the modulus decreases, the critical indentation depth tends to an asymptote. The same is the case at the other end on the normalised modulus scale. As the elastic modulus increases, the critical indentation depth tends to reach a constant value.

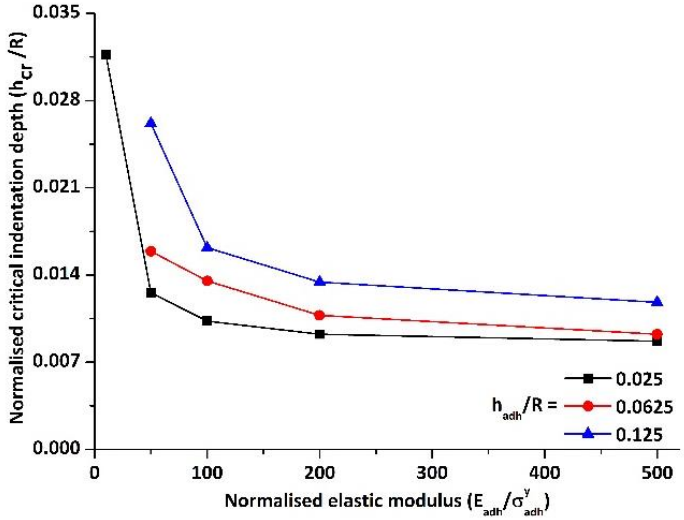

Figure 4.16. Variation of critical normalised indentation depth with normalised elastic modulus at various normalised adhesive layer thicknesses.

As mentioned earlier the normalised displacement of the indenter has been limited to a value of 0.0375. The crack initiation criteria (τ_y/σ^{y}_{adh}=1) was not satisfied at the lowest normalised elastic modulus (E_{adh}/σ^{y}_{adh}=10) at higher adhesive layer thicknesses. However, it must be noted here that the interface was assumed to be perfectly bonded in all the simulations. This assumption is hypothetical and in the real case scenario, the interface has defects introduced because of fabrication or environmental effects. It has been observed that prolonged exposure of adhesive bonds to high moisture and elevated temperature conditions leads to interfacial bond quality deterioration. This is because of degradation of the adherends along the interface and the formation of an oxide layer. Hence, the stress distributions in such cases might be quite different from the above shown plots.

To accurately predict the interfacial delamination behaviour however, the FE model should be able to accommodate the interfacial behaviour in terms of delamination initiation and propagation. The interface could be thought of as a series of springs whose initial stiffness and softening behaviour dictate the interfacial delamination. This behaviour can be simulated using the cohesive zone model with a series of elements along the specified interface geometry. The element behaviour follows a specified traction-separation curve. The complete explanation of this model is given in **section 4.1.3**. Several traction-separation laws are available to be utilised. The shape of the curve has little to no effect on the fracture behaviour of an adhesive joint as previously proven [**130**]. For this study, the simple triangular or bi-linear law has been chosen, the input parameters being the critical traction and the delamination displacement. The triangular law has been chosen as it gives faster convergence of the solution compared to trapezoidal and elliptical laws. Delamination or damage initiates at the critical traction and completes at the critical displacement. **Figure 4.2** shows the shape of the traction separation law used.

The delamination study was carried out by assigning a set of values to each of the non-dimensional parameter in the **Equation 4.10**. In addition to the values assigned to E_{adh}/σ_{adh}^{y} and h_{adh}/R, the values assigned to the normalised interfacial strength ($\sigma_c/\sigma_{adh}^{y}$) were 1, 0.75, 0.5 and 0.25. The values assigned to the normalised interface toughness ($\Gamma_c/\sigma_{adh}^{y}R$) were $1.8\text{x}10^{-4}$,$1.2\text{x}10^{-4}$, $6\text{x}10^{-5}$ and $3\text{x}10^{-5}$. The value of 'R', the radius of the indenter was kept constant at 4 mm. Similarly, the yield limit and the poisson's ratio of the adhesive layer were kept constant at 32 MPa and 0.38 respectively. The material properties of the adherends were the same as those used in the flexure simulations. The effect of each of the non-dimensional parameter on the load-displacement behaviour, critical indentation depth, total crack length and interfacial crack energy release rate was studied.

4.2.3. Effect of normalised interfacial strength

The normalised load-displacement plots of the adhesive joints with various values of interfacial strengths, thicknesses and modulus are shown in **Fig 4.17**. Only the highest and lowest normalised modulus values were chosen for brevity. However, all the possible combinations of the afore mentioned parameters were studied. From the figure, the normalised load displays linear behaviour in the beginning till a peak value where the crack initiates. Upon further increase in the indentation depth, the crack propagates along the interface of the adhesive joint and the residual strength of the adhesive joint slowly drops. There is no crack initiation in the adhesive joints with the lowest normalised elastic modulus. This corresponds to the observation made before in the perfectly bonded adhesive bonds.

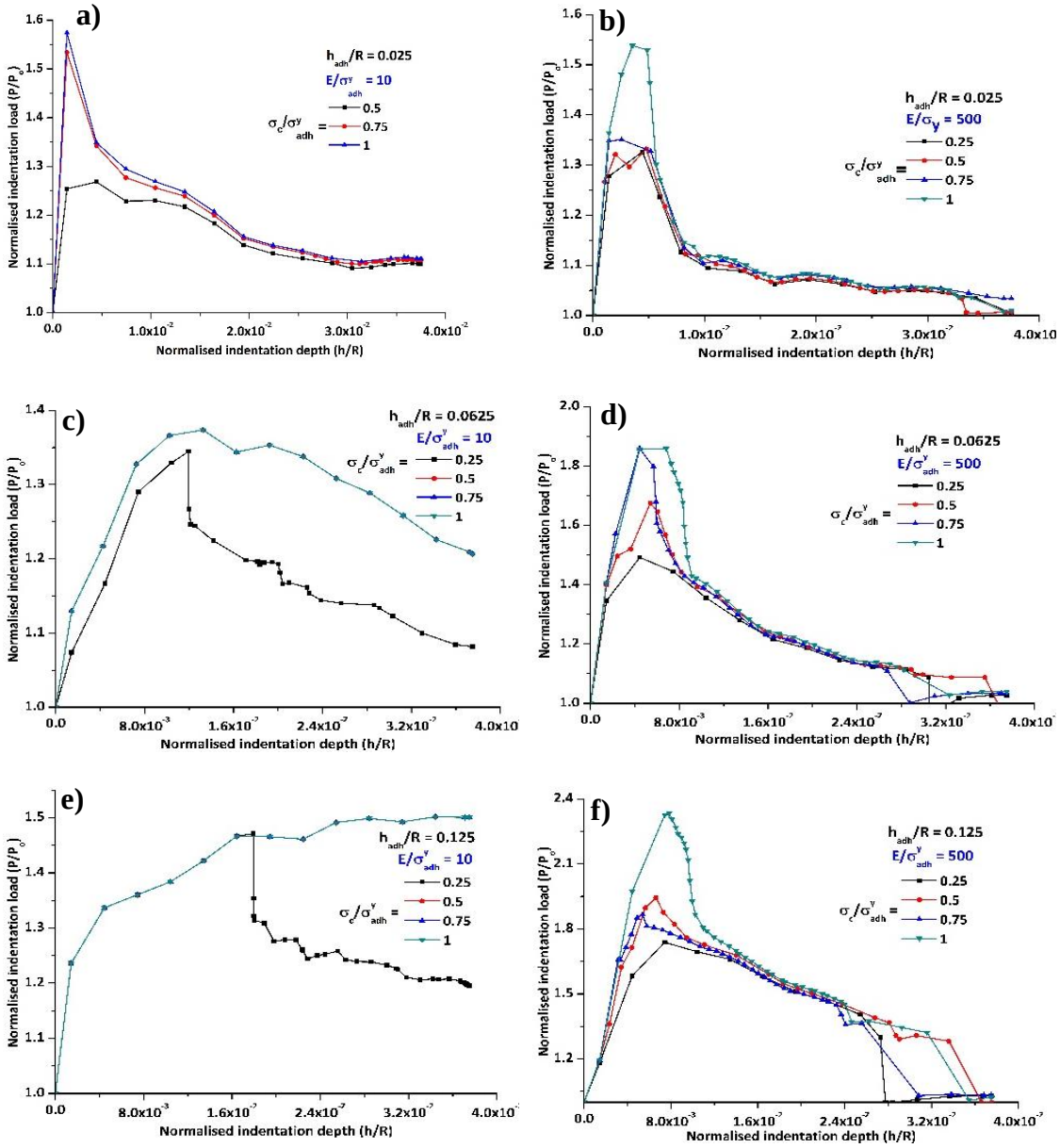

Figure 4.17. Normalised load-displacement curves of indentation testing on adhesive layer with different normalised interfacial strengths and with **a.** E_{adh}/σ_{adh}^{y}=10, h_{adh}/R=0.025, **b**. E_{adh}/σ_{adh}^{y}=500, h_{adh}/R=0.025, **c.** E_{adh}/σ_{adh}^{y}=10, h_{adh}/R=0.0625, **d.** E_{adh}/σ_{adh}^{y}=500, h_{adh}/R=0.0625, **e.** E_{adh}/σ_{adh}^{y}=10, h_{adh}/R=0.125, **f.** E_{adh}/σ_{adh}^{y}=500, h_{adh}/R=0.125.

The normalised load tends to reach the value '1' towards the end of the indentation process. This value corresponds to the residual strength of an adhesive joint without any interfacial bonding along one of the interfaces. This behaviour can be seen in all the simulations carried out. Another observation from these plots is that the critical indentation depth increases with increase in interfacial strength. The same is the case with increasing adhesive layer thickness. The normalised load drops after the peak load point and the rate of drop is steeper at

lower adhesive layer thicknesses. The inference that can be drawn from this observation is that the load transferred to the interface is concentrated to a smaller zone at lower adhesive layer thicknesses, the argument being that the residual strength depends on the load carrying capability of the interface. All the adhesive joints at a given adhesive thickness with different interfacial strengths tend towards the same normalised load value after some degree of indentation loading. This shows that the interfacial loading plays a key role in determining the crack initiation load, but may not significantly affect the crack propagation.

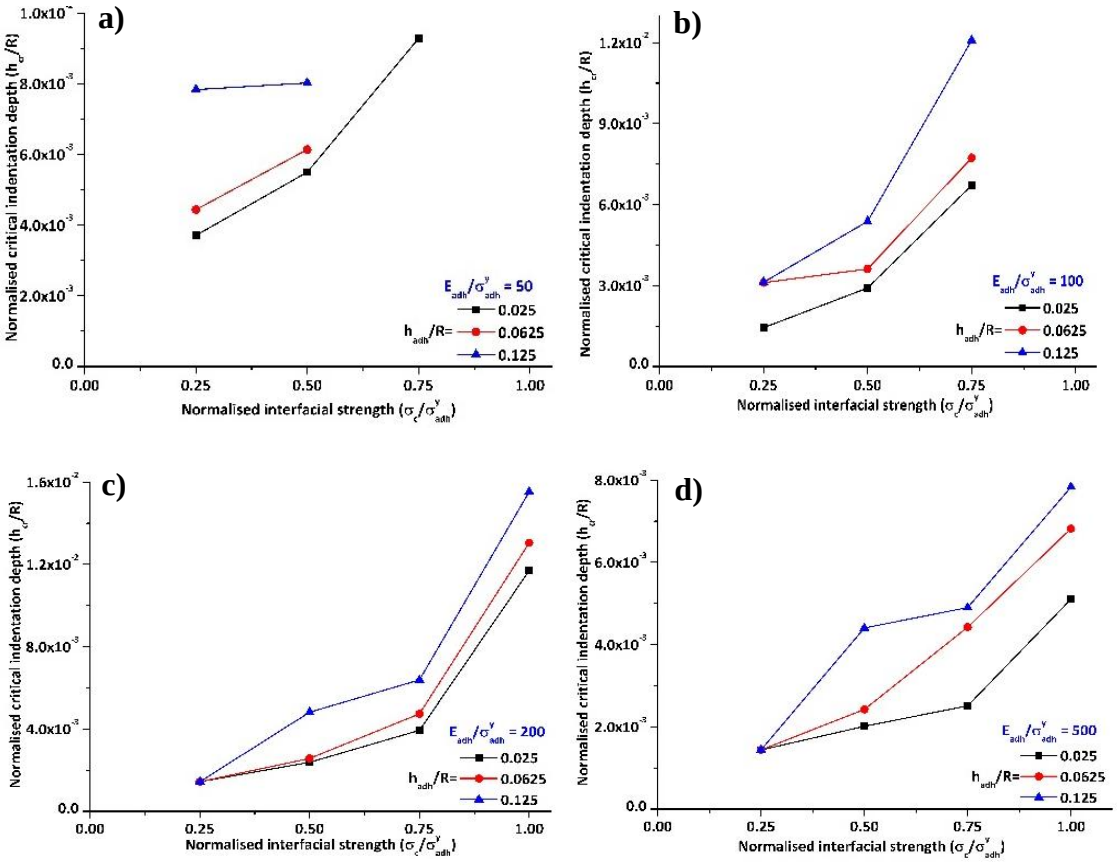

Figure 4.18. Critical indentation depths at various σ_c/σ^y_{adh} values and h_{adh}/R values for E_{adh}/σ^y_{adh} value of **a.** 50, **b.** 100, **c.** 200, **d.** 500.

The effect of the interfacial strength on the crack initiation and propagation is quantified by identifying the critical normalised indentation depth. **Figure 4.18** shows the variation of the critical normalised indentation depth with respect to the normalised interfacial strength at various normalised thicknesses and normalised elastic modulus values. As seen, the critical normalised depth decreases with decreasing normalised thickness. Similarly, the critical normalised depth decreases with decreasing normalised interfacial strength.

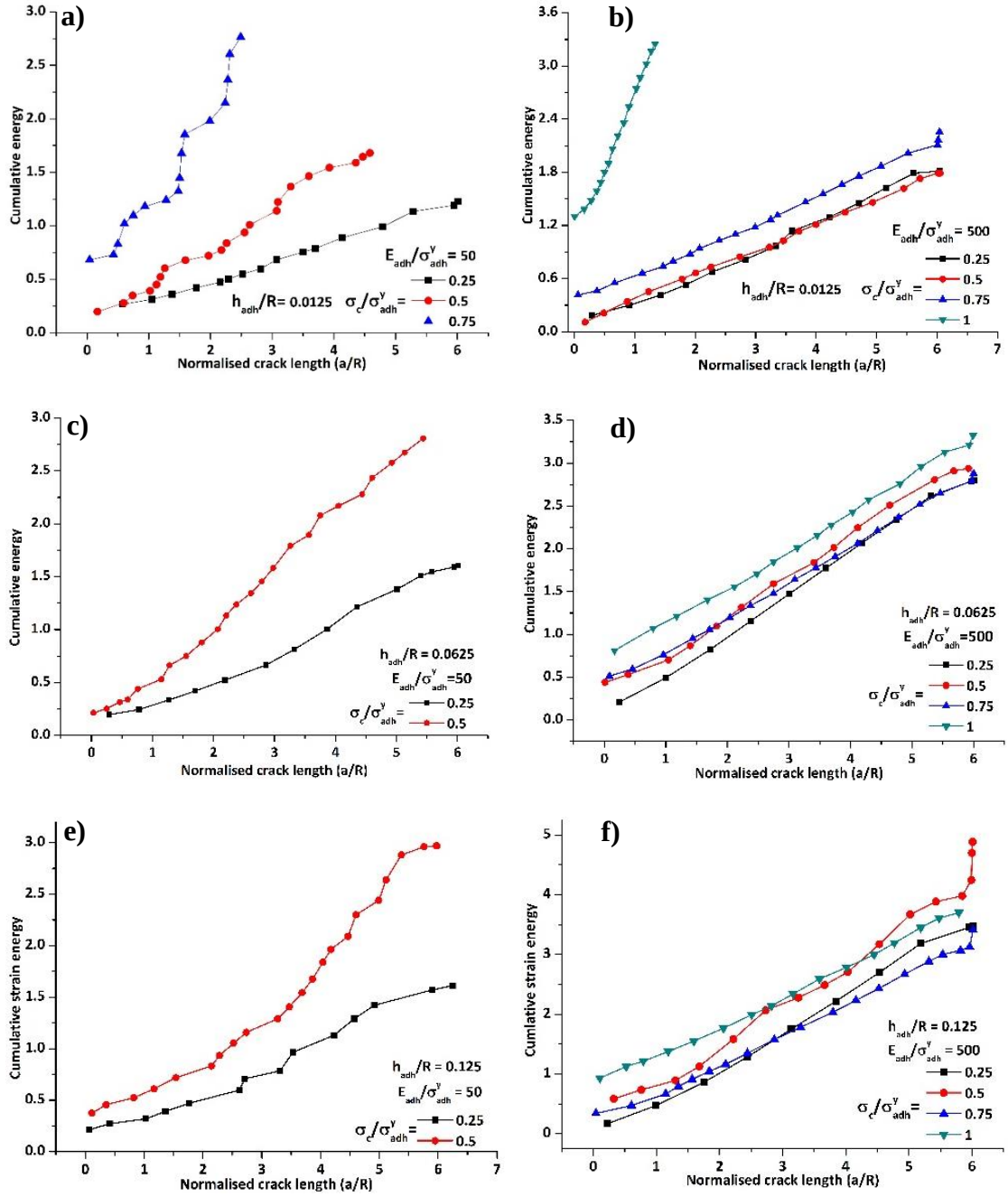

Figure 4.19. Cumulative strain energy vs crack length curves of adhesive joints with h_{adh}/R=0.0125 and **a.** E_{adh}/σ^{y}_{adh}=50, **b.** E_{adh}/σ^{y}_{adh}=500, with h_{adh}/R=0.0625 and **c.** E_{adh}/σ^{y}_{adh}=50, **d.** E_{adh}/σ^{y}_{adh}=500, with h_{adh}/R=0.125 and **e.** E_{adh}/σ^{y}_{adh}=50, **f.** E_{adh}/σ^{y}_{adh}=500.

This observation further supports the previous observation that the interfacial strength affects the crack initiation in adhesive joints. Again, as mentioned before, at lower elastic modulus, no crack propagation was observed except at lower values of normalised interfacial strength. This observation is supported by the fact that the critical normalised indentation depth increases with decreasing normalised elastic modulus. The interfacial strength, adhesive layer

thickness and the elastic modulus have a compounded effect on the crack propagation, which can be stable or unstable. To explain further, the simulations in this work have been carried out under displacement control condition. Hence the slope of the available energy vs crack length curve is negative. This means that the crack propagation always tends to be stable.

To further understand the effect of the interfacial strength on the crack propagation, the cumulative strain energy (U) is plotted against the normalised crack length (a). It should be noted here that the cumulative energy is a measure of the energy available for the crack propagation and not necessarily the energy released. The slope of this curve for a set of adhesive joint properties can be used as an indicator of the stability of the crack. Higher is the slope, more stable is the crack.

Figure 4.19 shows the cumulative strain energy vs a/R curves of various normalised interfacial strengths for various thicknesses and normalised elastic modulus values. The first observation that can be made from these plots is that the cumulative strain energy required to drive the crack increases with increasing normalised interfacial strength at lower values of the normalised elastic modulus. Secondly, at higher normalised elastic moduli however, the cumulative strain energy required to drive the crack in the adhesive joints with lower normalised interfacial strengths raises above the energy required in adhesive joints with higher normalised interfacial strengths. This can be observed in **Fig 4.19d** and **Fig 4.19f** and can be specific to indentation loading. From **Fig 4.19a**, there seems to be a crack arrest where the cumulative strain energy required to drive the crack raises to a point where there is a slight crack growth. This behaviour can be seen only in this set of parameters where the normalised modulus of the adhesive is low and the normalised interfacial strength is high.

Figure 4.20 shows the mode mix ratio calculated (**Equation 4.16**) for the crack tip stress state at various indentation depths. The normalised crack length is also plotted. Plots are shown for various normalised thicknesses of the adhesive layer only at the lowest value of the normalised interfacial strength and the lowest and highest values of the normalised elastic modulus. From the plots, the initial crack mode tends towards mode-II and slowly changes to the opening mode as the crack propagates along the interface.

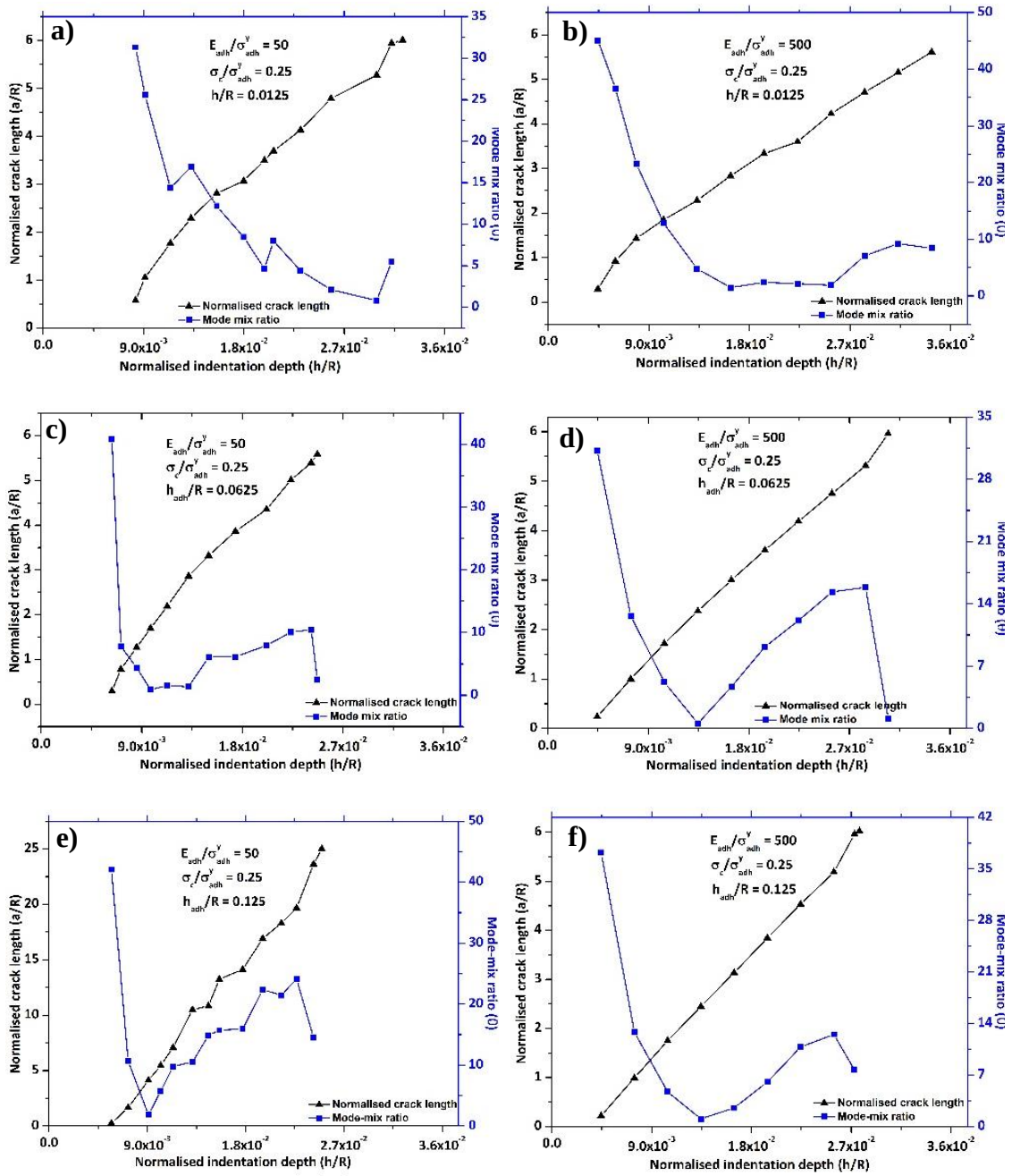

Figure 4.20. Mode-mix ratios of crack tip stresses in adhesive joints with h_{adh}/R=0.0125, $\sigma_c/\sigma^{y}_{adh}$ =0.25 and **a.** E_{adh}/σ^{y}_{adh}=50, **b.** E_{adh}/σ^{y}_{adh}=500, with h_{adh}/R=0.0625, $\sigma_c/\sigma^{y}_{adh}$ =0.25 and **c.** E_{adh}/σ^{y}_{adh}=50, **d.** E_{adh}/σ^{y}_{adh}=500, with h_{adh}/R=0.125, $\sigma_c/\sigma^{y}_{adh}$ =0.25 and **e.** E_{adh}/σ^{y}_{adh}=50, **f.** E_{adh}/σ^{y}_{adh}=500.

At the lowest normalised thickness of the adhesive, the mode-mix ration monotonously decreases. At higher normalised thicknesses however, the mode-mix ratio increases again. Looking at the shear stress distributions along the interface in perfectly bonded joints (**Fig 4.15**), it can be said that the crack initiates due to the accumulation of shear strain within the adhesive layer along the interface to a point at which the adhesive separates from the underlying adherend.

This could be reason for the high mode-mix at the crack initiation point. As the crack propagates, the top adherend along with the adhesive layer buckles and lifts off the bottom adherend. As the crack length increases, the delaminated length of the top adherend and adhesive layer assembly acts as a cantilever beam. Thus, as the crack propagates, the mode-mixity decreases and approaches the value of 0^o corresponding to mode-I type propagation. The effect of the model boundaries (edges) on the mode-mix also needs to be considered. The edge effects seem to be more apparent in the case of the adhesive layers with higher normalised thicknesses and higher normalised elastic moduli. At lower normalised thickness and lower normalised elastic modulus, the edge effect is not noticeable on the mode-mix ratio.

4.2.4. Effect of interfacial toughness

The effect of the interfacial toughness on the load-displacement behaviour, crack initiation and propagation, the total deformation energy are explained in this section. It should be noted that the simulations were carried out under displacement control conditions.

Figure 4.21 presents the normalised load-normalised displacement plots from adhesive joints with various interfacial toughness values as mentioned before. The normalised interfacial strength is kept constant at 0.5 for all the simulations discussed in this section.

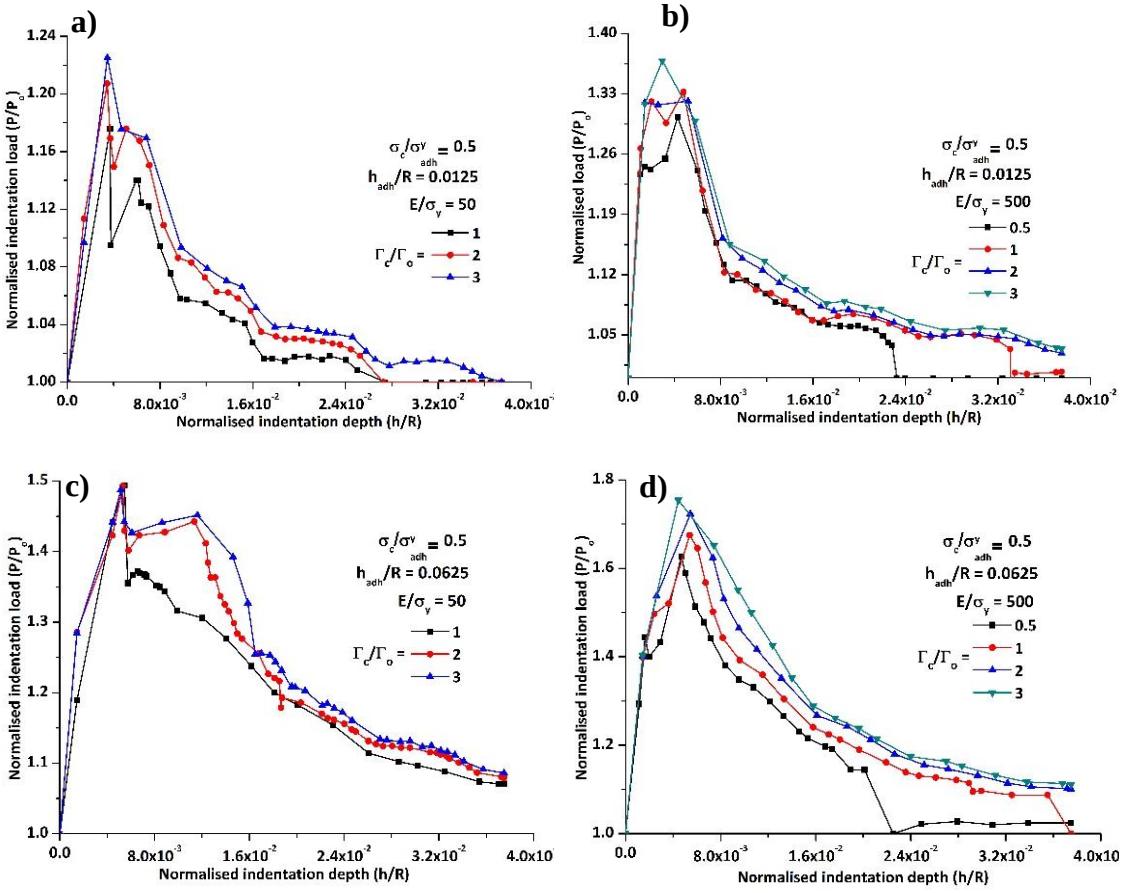

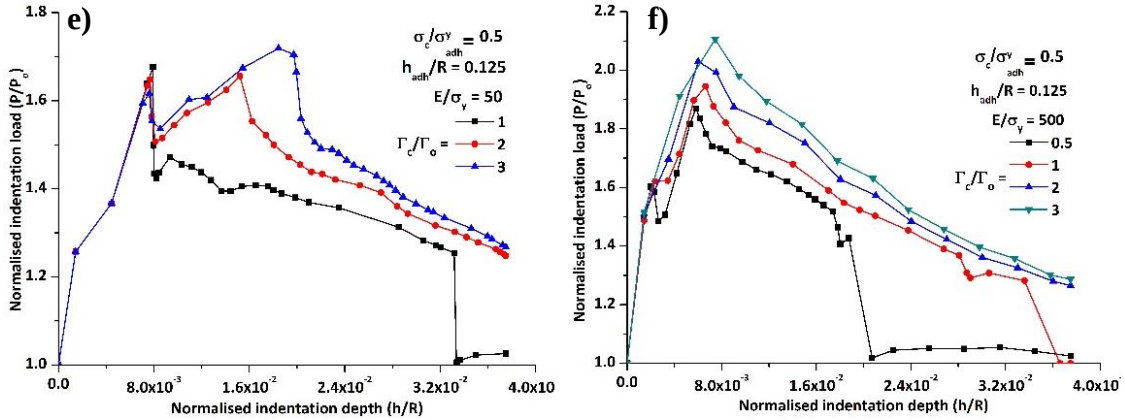

Figure 4.21. Normalised loads of adhesive joints with normalised thickness h_{adh}/R=0.0125 and **a.** E_{adh}/σ^y_{adh}=50, **b.** E_{adh}/σ^y_{adh}=500, with normalised thickness h_{adh}/R=0.0625 and **c.** E_{adh}/σ^y_{adh}=50, **d.** E_{adh}/σ^y_{adh}=500, with normalised thickness h_{adh}/R=0.125 and **e.** E_{adh}/σ^y_{adh}=50, **f.** E_{adh}/σ^y_{adh}=500.

The normalised load value plotted here are the ratios of the load values of a bonded adhesive joint to the load values of completely unbonded adhesive joint at the corresponding indentation depth.

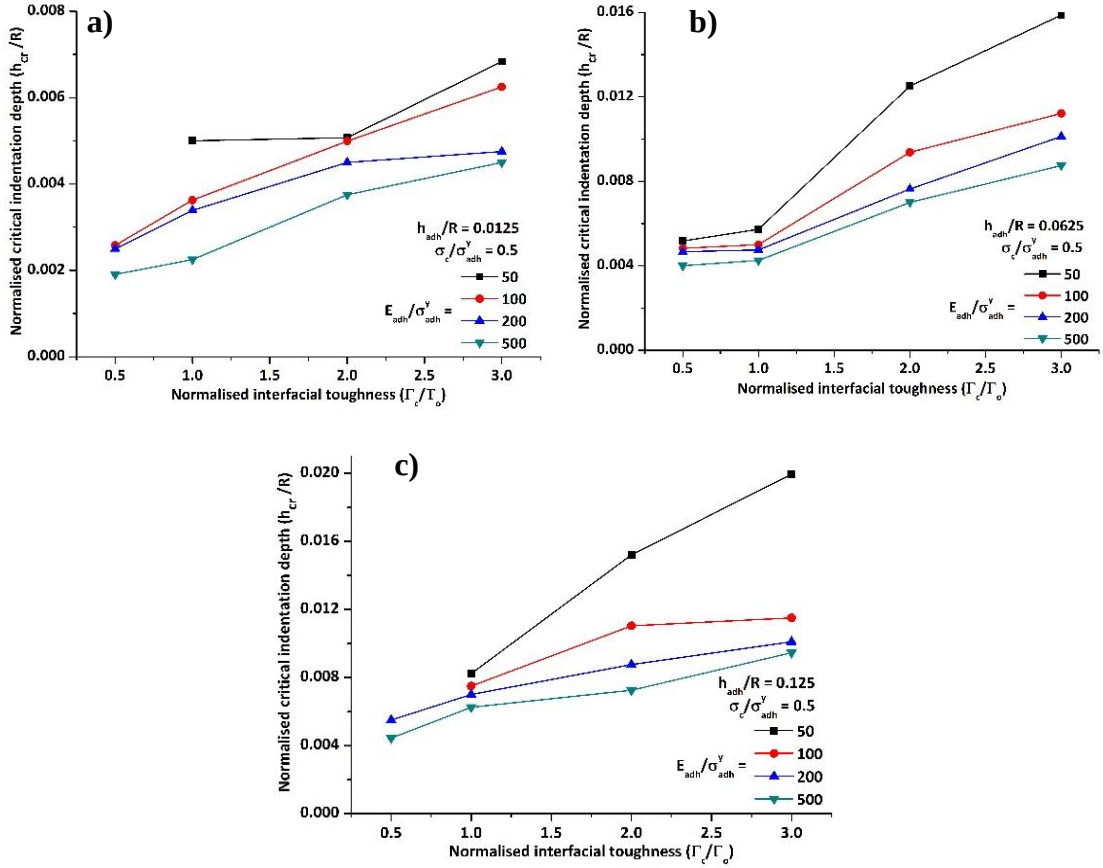

Figure 4.22. Effect of interfacial toughness on the critical indentation depth in adhesive joints with normalised adhesive layer thickness **a.** 0.0125, **b.** 0.0625, **c.** 0.125.

From the plots, the peak normalised load increases with increasing interfacial toughness for all the adhesive layer thickness and elastic modulus values. Another observation that can be made is that at lower interfacial toughness (0.5, 1), the normalised load value drops to the value '1'. This implies that the crack propagating along the interface has traversed the entire length of the adhesive joint model and the load-depth response of the adhesive joint is now similar to that of the adhesive joint with no interfacial bonding. This also means that there is no residual strength in the adhesive bond.

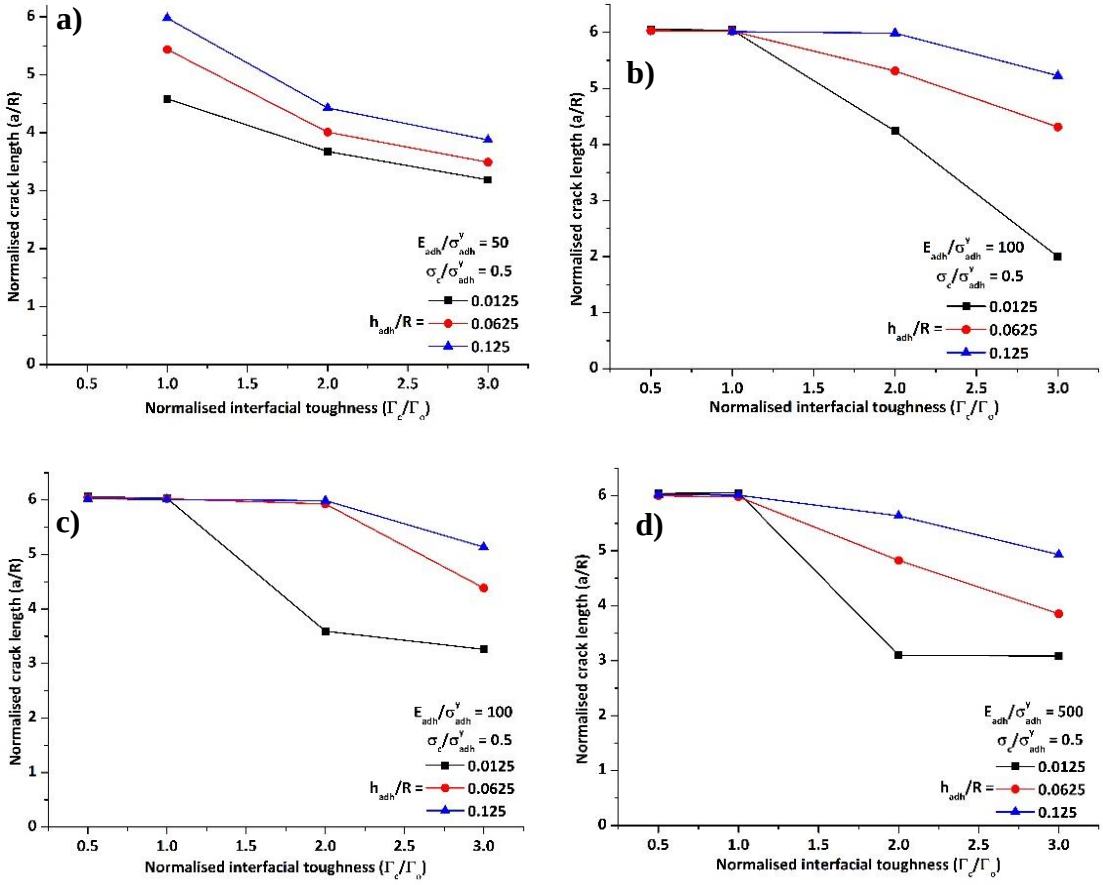

Figure 4.23. Effect of interfacial toughness on the total crack length for adhesive joints with various thicknesses and E_{adh}/σ^y_{adh} values of **a.** 50, **b.** 100, **c.** 200, **d.** 500.

Recalling the behaviour of the adhesive joints with the same interfacial toughness and different interfacial strengths (**Fig 4.17**), the normalised load-normalised depth behaviour of the adhesive joints tends to be the same after a certain depth of loading. However, in the case of adhesive joints with similar interfacial toughness and different interfacial strength, the normalised load-depth curves do not merge and can be clearly distinguished. This part of the curve represents the crack propagation along the interface of the adhesive joint. In other words, adhesive joints with the same value of the interfacial toughness exhibit a similar crack growth behaviour in terms

of the load-depth response. This is not the case with adhesive joints with different interfacial toughness as can be seen from **Fig 4.21**.

The effect of the interfacial toughness on the crack initiation and propagation were investigated next. The critical indentation depth of the various parameter combinations was plotted with respect to the interfacial toughness as shown in **Fig 4.22**. From the figures, the following observations can be made:

1. The normalised critical indentation depth increases with increasing interfacial toughness.
2. The normalised critical indentation depth decreases with increasing normalised elastic modulus.
3. The normalised critical indentation depth increases with increasing normalised adhesive layer thickness.

The behaviour observed here is similar to what was observed in the case of increasing interfacial strength. The first among the above observations helps conclude that the interfacial strength has a considerable effect on the crack initiation in adhesive joints. To study the effect on the crack propagation, the total crack length has been plotted against the normalised interfacial toughness at various thicknesses and normalised elastic moduli.

From **Fig 4.23**, the following observations can be made:

1. The normalised crack length decreases with increasing interfacial toughness.
2. The normalised crack length increases with increasing adhesive layer thickness.

Another observation that can be made from the above plots is that the increase in the interfacial toughness does not seem to have a significant effect on the normalised crack length at higher adhesive layer thickness ($h_{adh}/R=0.125$). However, it should be noted that the restrictions on the model length may have been the reason behind this behaviour. It should be noted that the crack propagated along the complete length of the model and complete delamination of the interface was observed in most of the cases. Thus, keeping the above fact in mind, it can be concluded that the increased interfacial toughness has an arresting effect on interfacial crack propagation.

4.2.5. Effect of adhesive elastic modulus

The effect of adhesive layer elastic modulus is explained in the following section.

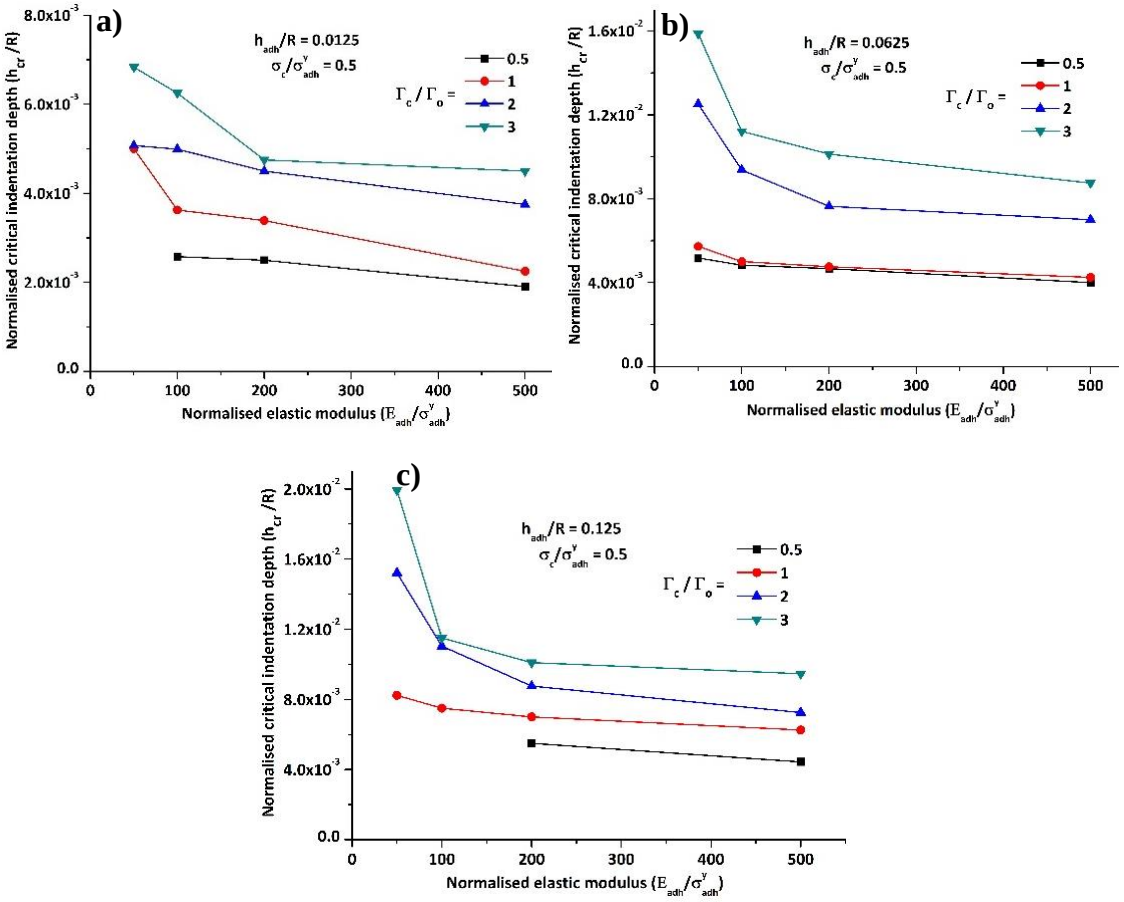

Figure 4.24. Variation of the normalised indentation depth with normalised elastic modulus at h_{adh}/R values of **a.** 0.0125, **b.** 0.0625 and **c.** 0.125

The variation of the critical indentation depth with the elastic modulus of the adhesive layer is shown in **Fig 4.24**. The plotted values are the normalised values. The plots show that the critical value increases with decreasing elastic modulus. At higher interfacial toughness values, the critical normalised indentation depth tends towards an asymptotically high value indicating that for a given set of interfacial parameters, lower is the adhesive modulus, the probability of crack initiation under indentation loading drastically decreases.

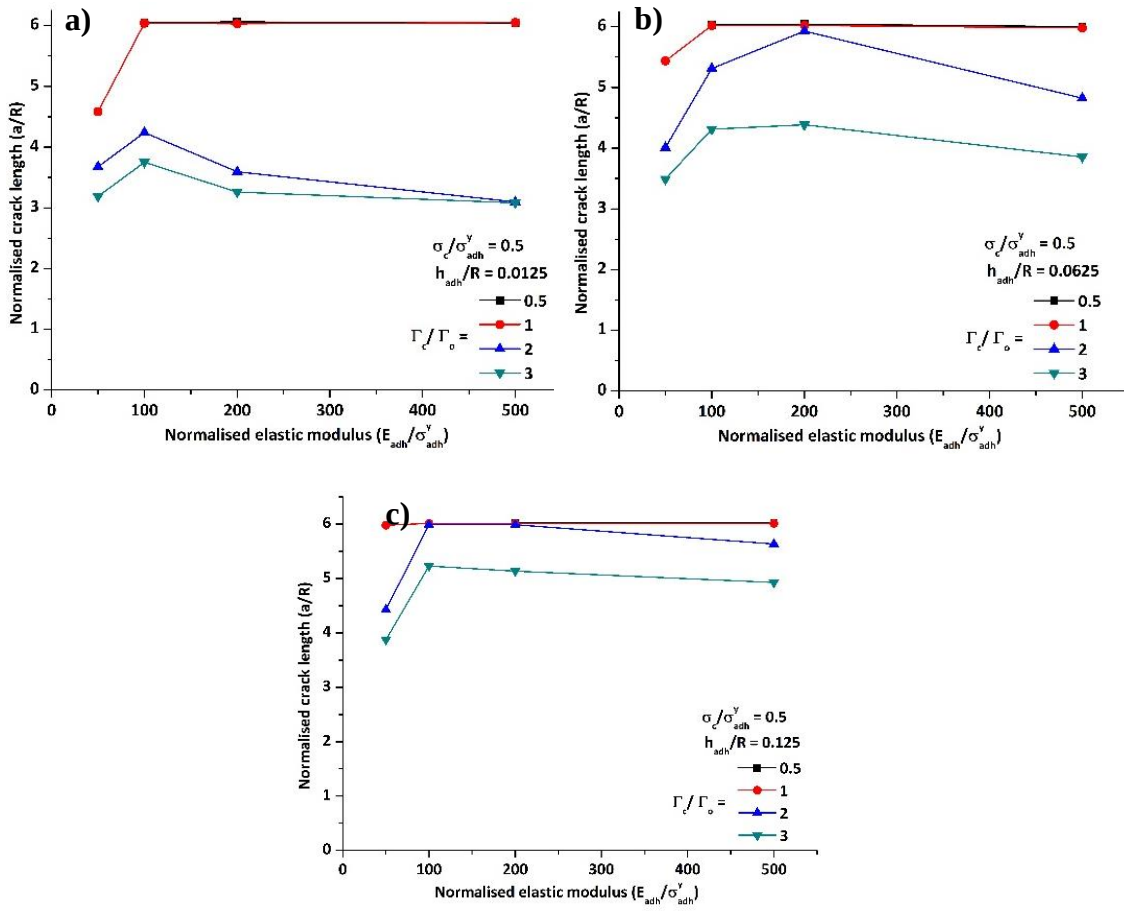

Figure 4.25. Variation of the normalised crack length with normalised elastic modulus at h_{adh}/R values of **a.** 0.0125, **b.** 0.0625 and **c.** 0.125

Also, the rate of change of the 'h_{cr}' decreases with increasing adhesive modulus. This shows that 'h_{cr}' reaches an upper limit with increasing adhesive modulus. Hence, it can be deduced that for a given set of interfacial parameters, the 'h_{cr}' value becomes independent of the elastic modulus at a high enough modulus of the adhesive. From the plots, this behaviour is true only for h_{adh}/R values of 0.0625 and 0.125. Also, the effect of the interfacial toughness needs to be taken into consideration while studying the role of the adhesive elastic modulus. From the plots, the asymptotic behaviour can only be seen at higher interfacial toughness values. This can be understood as follows: The ease of crack initiation increases with decreasing interfacial toughness and with increasing elastic modulus. At lower elastic moduli, lower interfacial toughness value helps in the initiation of the crack, but a drastic raise in the 'h_{cr}' value can be seen with increasing toughness. These plots represent the tendency of crack initiation at various values of 'E_{adh}/σ^{y}_{adh}'. To understand its effect on the crack propagation, the total normalised crack length values are plotted against the same. The variation of the normalised crack length with the normalised elastic modulus is shown in **Fig 4.25.** There is an increase and then a gradual decrease

in the normalised crack length value with increasing 'E_{adh}/R'. The variation of the mode-mix ratio with the elastic modulus is shown in **Fig 4.26** for various 'h_{adh}/R' values. From the plot, the mode-mix ratio decreases with crack propagation distance at lower adhesive thickness.

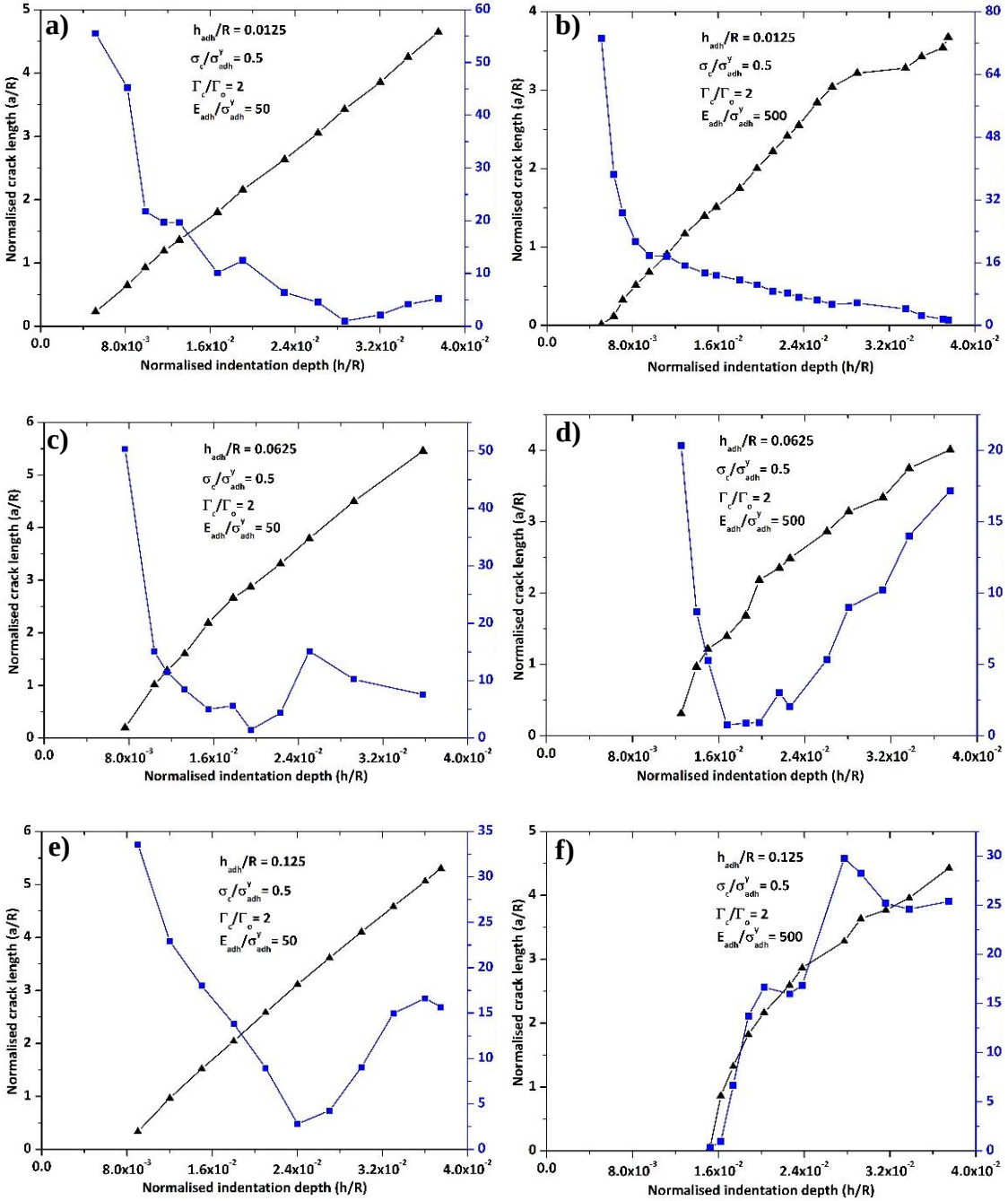

Figure 4.26. Normalised crack length and mode-mix ratio vs normalised indentation depth for h_{adh}/R=0.0125, **a.** E_{adh}/σ^{y}_{adh}=50, **b.** E_{adh}/σ^{y}_{adh}=500, for h_{adh}/R=0.0625, **c.** E_{adh}/σ^{y}_{adh}=50, **d.** E_{adh}/σ^{y}_{adh}=500, for h_{adh}/R=0.125, **e.** E_{adh}/σ^{y}_{adh}=50, **f.** E_{adh}/σ^{y}_{adh}=500.

However, at higher normalised thicknesses, the mode ratio can be seen to be increasing as the crack length increases. This is similar to what was observed in the case of increasing interfacial strength and interfacial toughness, which leads to the conclusion that the variation of

the mode-mix ratio with respect to crack length varies only with the adhesive layer thickness. This plot show that the crack initiation is predominantly under shear mode. As discussed previously, the adhesive directly underneath the indenter is being extruded out of the compression zone and this leads to high shear stress at the adhesive-adherend interface. As the crack length increases, the top adherend lifts off creating a cantilever like crack propagating mechanism. Thus, the initial mode-mix is highly shear in nature in the beginning and slowly reduces to mode-I.

4.2.6. Effect of adhesive layer thickness

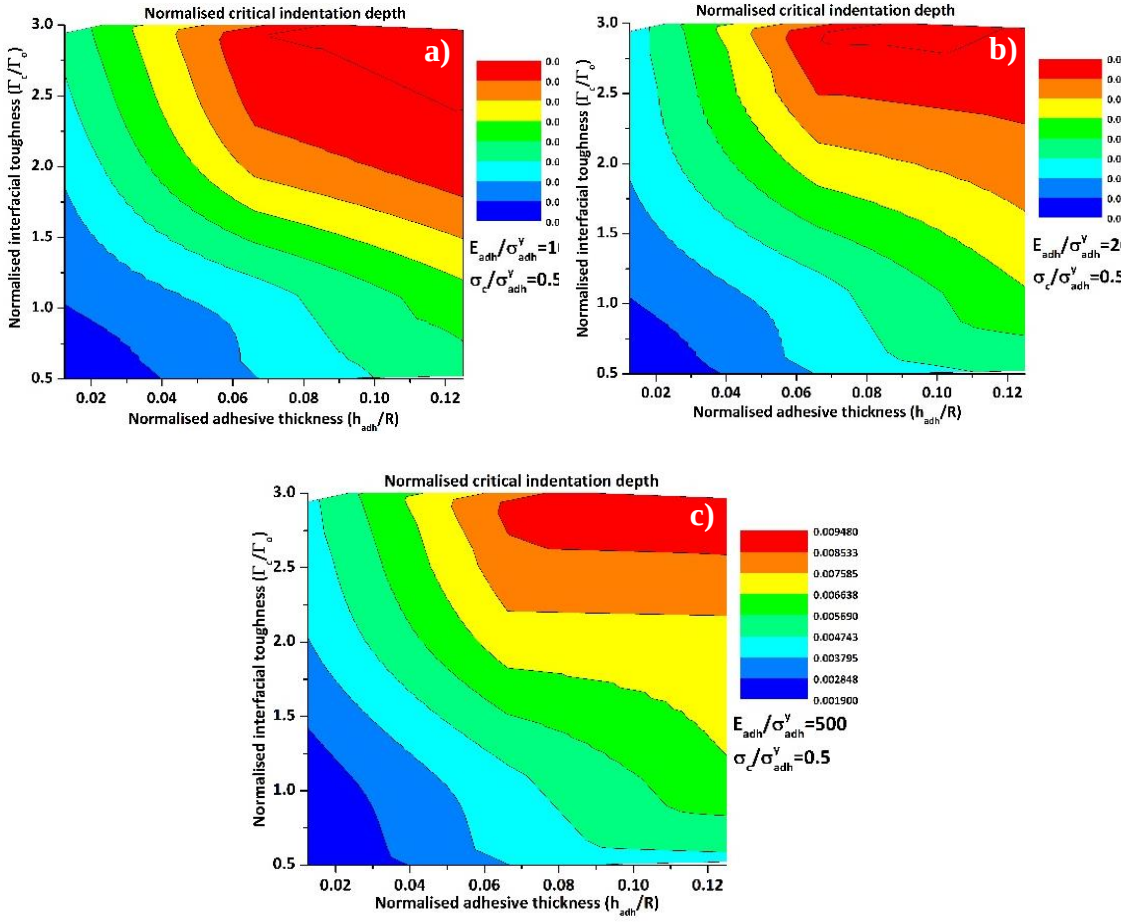

Figure 4.27. Variation of normalised critical indentation depth with adhesive layer thickness and toughness for E_{adh}/σ^{y}_{adh} values of **a.** 100, **b.** 200, **c.** 500

Increasing the adhesive layer thickness increases the flexibility, deformability and the load carrying capability of adhesive joints. From the above analysis conducted so far, it can be surmised that the more ductile the adhesive is, the more crack retarding the adhesive joint is. Moreover, with the increase in the adhesive layer thickness, the energy absorbing capacity of the adhesive joint also increases. The interfacial plastic deformation increases with increasing

thickness. This is attributed to the reduction of the constraint exerted by the adherends on the adhesive deformation. To observe the effect of the adhesive thickness and modulus on the deformability of the adhesive joints, the normalised strain energy is plotted against the above parameters in **Fig 4.28.** From this plot, adhesive layer thickness has a major role in determining the strain energy absorption of the adhesive layer. The near vertical bands in the plot indicate that for a given adhesive layer thickness, the variation of the adhesive elastic modulus does not have a considerable effect on the strain energy. It should be mentioned here that the effect of the adhesive layer should be discussed in combination with other parameters studied in this investigation. **Figure 4.27** explains the combined effect of the interfacial toughness and the adhesive layer thickness on the critical indentation depth. Both these parameters have a similar effect. Increase in one of these parameters increases the retardation of the crack. The large red area on each of the plots show that the critical indentation depth becomes independent of the parameter combination and reaches a threshold value. Beyond this point, increasing either of the parameters does not have a significant effect on the crack initiation.

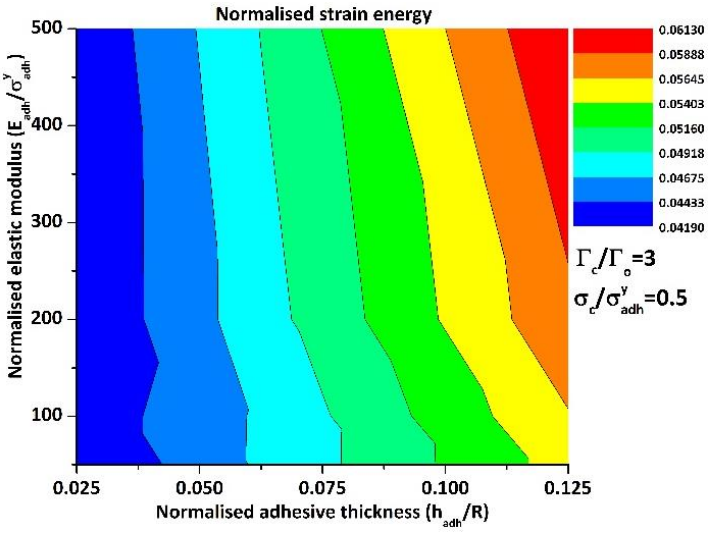

Figure 4.28. Variation of normalised strain energy with normalised elastic modulus and normalised adhesive layer thickness.

The effect of the combination of the interfacial strength and adhesive layer thickness is presented in **Figure 4.29**. From the figure, the effect of the adhesive layer thickness is smaller compared to that of the interfacial strength. Furthermore, the change in 'h_{cr}/R' with respect to 'h_{adh}/R' is more apparent only at higher values of '$\sigma_c/\sigma^{y}_{adh}$' (> 0.8). This behaviour is similar across different values of 'E_{adh}/σ^{y}_{adh}' as shown in **Fig 4.28.** However, as the modulus increases, there is a considerable shift in the parameter range in which there is no notable change in the 'h_{cr}' value. Hence, it can be said that the dependency of crack initiation on the adhesive layer thickness

becomes more apparent at higher elastic modulus values. The same goes for the dependency on the interfacial strength.

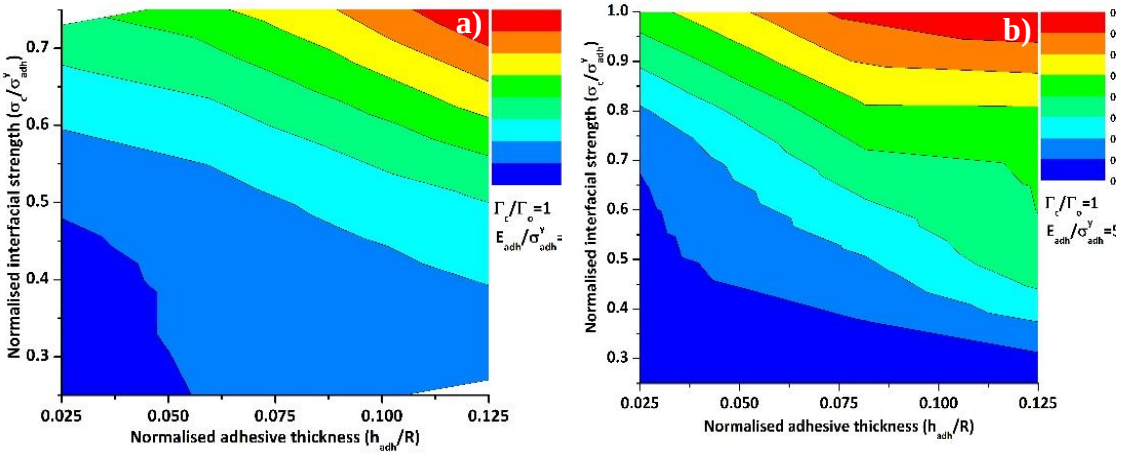

Figure 4.29. Variation of *'h_{cr}/R'* with *'h_{adh}/R'* and 'σ_c/σ^y_{adh}' for 'E_{adh}/σ^y_{adh}' values of **a.**100 and **b.**500.

Also, the dependence of the critical indentation depth on the modulus-thickness combination is shown in **Fig 4.30.** It is quite apparent that the critical indentation depth increases with increasing adhesive layer thickness. However, the total increase in the 'h_{cr}' value for a given range of the 'h_{adh}/R' values is dependent on the elastic modulus of the adhesive layer. At lower elastic modulus ('E_{adh}/σ^y_{adh} = 50) of the adhesive layer, the 'h_{cr}' value increases by almost 4 times as the thickness increases by 5 times. The same increase in the thickness at an 'E_{adh}/σ^y_{adh}' value of 500 increases the 'h_{cr}' value by 2 times. This behaviour changes at lower value of the normalised interfacial toughness ('Γ_c/Γ_o'=1), where the dependency of the 'h_{cr}' value on the adhesive layer thickness is comparatively smaller.

From **Fig 4.30a** and **Fig 4.30b**, the '*hcr*' value becomes independent of both the elastic modulus and the adhesive layer thickness beyond a threshold value of either parameter. At the highest value of 'Γ_c/Γ_o' (**Fig 4.30a**), the 'h_{cr}' value is independent of the adhesive modulus at the lowest adhesive layer thickness (h_{adh}/R =0.025), and at the lowest normalised modulus (E_{adh}/σ^y_{adh}=100), the 'h_{cr}' value is highly dependent on the *'h_{adh}/R'* value. The change in the parametric dependency of 'h_{cr}' with toughness is due to the change in the restraint on the deformation of the adhesive layer. This restraining effect can be seen at lower adhesive layer thicknesses and at high toughness values.

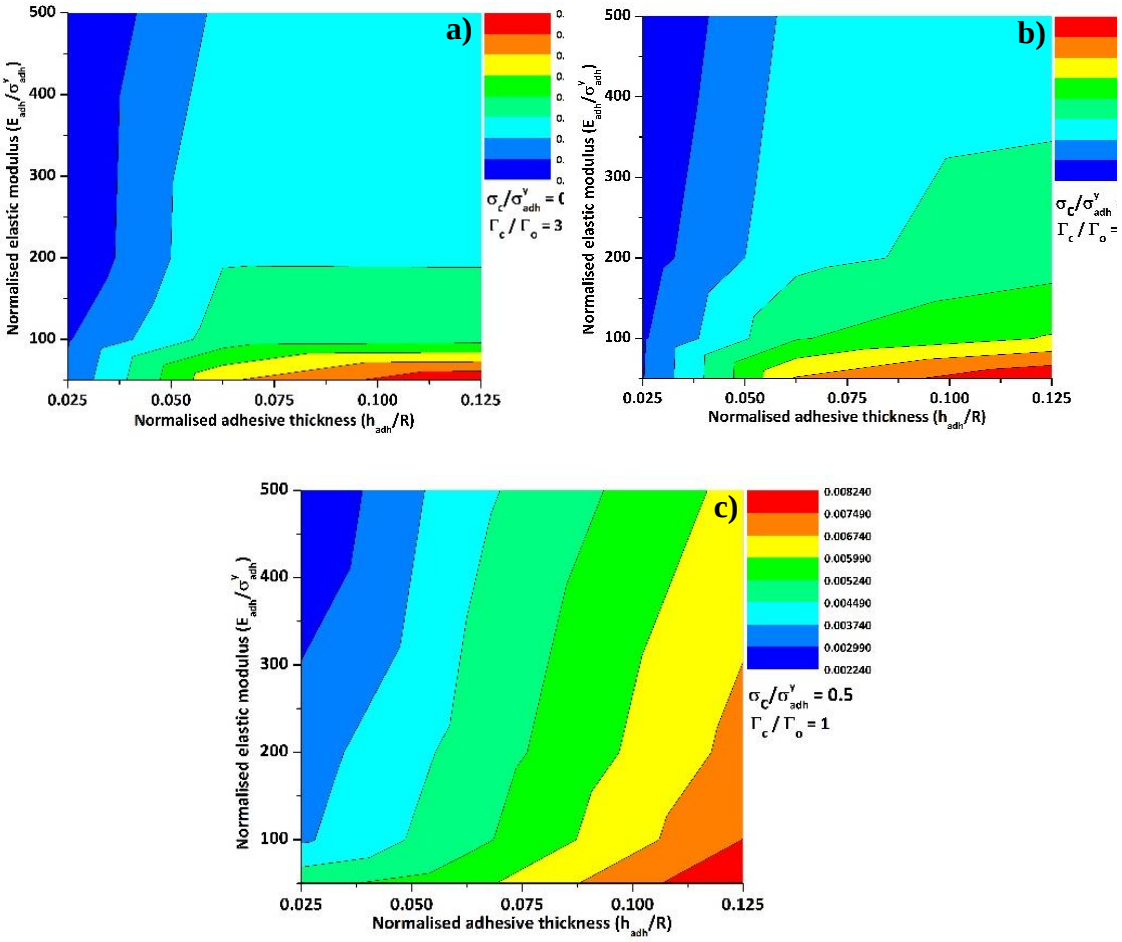

Figure 4.32. Variation of 'h_{cr}' with combination of the parameters 'h_{adh}/R' and 'E_{adh}/σ^{y}_{adh}' at 'Γ_c/Γ_o' values of **a.**3, **b.**2 and **c.**1

4.3. Summary

4.3.1. Summary of results from 4-point flexural simulation

a. The adhesive thickness and modulus play a key role in determining flexibility and the load carrying capability of the adhesive joint. The effect of the modulus is not distinguishable at lower thicknesses of the adhesive layer, but increases with increasing thickness. The adhesive layer has some load carrying capability of its own which increases with increasing adhesive thickness and also the adhesive modulus.

b. The constraint exerted by the adherends limits the deformation of the adhesive layer especially at lower adhesive thicknesses, thus restricting the failure.

c. The stress states induced in the adhesive can also be explained by bi-material beam bending theory. The distance of the concerned layer (OA, OB or OC) from the corresponding neutral axis affects the stress state as both the stress state and the distance follow similar trend.

d. Although the mid-span shear stress values are consistently close to zero in both the brittle

and ductile adhesives, the distribution is affected by the load concentration around the loading pin. The effect is more pronounced in the brittle adhesive, where steep changes in the shear stress distribution around the load point can be seen at higher thicknesses of the adhesive layer. At lower thicknesses, the adhesive layer is constrained by the adherends and hence the effects are localised around the load pin.

e. The stress distribution in all the combinations simulated is affected by the loading pin and to an extent by the support pin. The adhesive volume directly below the loading point is under a high degree of stress concentration and the stress changes its nature drastically in many of the cases considered. Hence this region may act as the failure initiation region.

4.3.2. Summary of results from indentation simulation

a. Increasing the interfacial strength increases the critical indentation depth for a given parameter combination. However, it does not have a significant effect on the total crack length at a given indentation depth. Similarly, the energy release rate calculated is not significantly affected by the interfacial strength.

b. Increasing the interfacial toughness increases the critical indentation depth and decreases the total crack length. This is attributed to the increase in the net energy required per unit crack length. Similarly, the energy release rate also increases with increasing interfacial toughness.

c. Increasing the adhesive layer thickness increases the strain energy absorption of the adhesive joint. Similarly, the critical indentation depth increases with increasing adhesive thickness. However, this is valid only at very low elastic modulus of the adhesive. At higher modulus values, the critical depth does not change significantly with increasing thickness.

d. The adhesive elastic modulus increase increases the strain energy absorption of the adhesive joint. It also decreases the energy release rate for a given set of parameters. It does not have a significant effect on the crack initiation indentation depth except at higher adhesive layer thickness.

The results and analysis presented in this chapter show that the adhesive bond interfacial failure can be predicted using CZM based numerical models. The crack propagation energy release rates were estimated using conventional fracture mechanics combined with the crack propagation predicted by the numerical models. These can be compared with the experimental energy release rate values to create an estimate of the residual strength of the defective adhesive bond.

Chapter-5

5. Experimentation

This chapter presents experimental results, mostly on the AE response from instrumented 4-point flexural and indentation test. This chapter starts with specimen preparation, experimental test set-up (flexural and indentation) and data analysis methodology. Following section includes results from 4-point flexural and indentation tests, including results from PLB testing on selective specimens. The PLB tests were conducted so as to simulate the mode-I and mode-II type signal propagation in the metal plates. The data from these tests was used in classification of the crack event signals acquired from the flexural and indentation tests. To test the validity of the method used to simulate the adhesive bond interfacial quality, single lap joint tension tests were also conducted on adhesively bonded joints with various simulated interfacial conditions.

5.1. Specimen preparation

The specimens used for the AE based PLB testing were used for the flexure experiments too. Thus, the same specimen preparation methodology as explained in chapter-3 applies here. The indentation specimens were prepared in the same manner as the flexure specimens. Two types of defective surfaces were created for the experiments to represent different levels of degradation of the interfacial condition. The ingestion of moisture along the interface of an adhesive bond leads to the formation of a very thin oxide layer that induces the formation of a disbond along the interface [2]. Hence, the specimen preparation methodology was aimed at simulating this kind of an interfacial condition. In the first type of specimens, the adhesive was directly applied on to the metal plate without any pre-treatment of the surface. This leads to improper bonding across the interface because of the thin oil film present on the as-manufactured specimens. These specimens were given a name with ‘NST’ (no surface treatment). To simulate the moisture induced de-bonding across the interface, a thin layer of oil was applied onto the 0.5 mm plate surface. The amount of oil applied was kept constant across different specimens. This was done on the surface of the 0.5 mm plate. These specimens were given the name with ‘OF’ (oil film).

To test the effectiveness of the method used to simulate the various interfacial conditions, single lap joints were fabricated using 2 mm thick aluminium plates. The specimen preparation technique was the same as that for the indentation specimens. The overlap length of the SLJ specimens was 40 mm and the width of the specimens was 50 mm. The other dimensions were according to the standard ASTM D1002 [131].The interface conditions tested in this case were NST, OF and WST. WST being the adhesive bond where surface pre-treatment was applied. The details of the number of specimens prepared for each mechanical test method is presented in

Table.5.1. In total, 32 experiments were performed across various test methods. A minimum of 2 specimens were tested in each test case. The number of variables is 3 including the adhesive layer thickness, defect area percentage and the adhesive modulus.

Test	Configuration	Adhesive layer thickness	Interface condition	Number of specimens
4-point flexure	0.5-A-1.5-Defect density	100 µm	0%, 25%, 40%	2, 2, 2
		250 µm	0%, 25%, 40%	2, 2, 2
		500 µm	0%, 25%, 40%	2, 2, 2
SLJ tension	2 mm-A-2 mm	250 µm	OF, NST, WST	2, 2, 2
Indentation	0.5-A-1.5-D	250 µm	OF, NST	2, 2
		500 µm	OF, NST	2, 2

Table 5.1. Number of specimens prepared for each test method.

5.2. Experimental setup

PLB tests on metal plates: Pencil lead breaks (PLB's) were done on several locations of the plate specimens corresponding to mode-I and mode-II type sources. The PLB tests conducted were of two types. One on the face of the specimen and the other on the side wall of the specimen. The face PLB tests correspond to the mode-I type signals and the edge PLB tests correspond to the mode-II type signals. The plates were placed on a wooden block with a V-shaped groove. Paper was placed between the wooden block and the metal plates to remove any reflections along the plate surface. The edge PLBs were conducted on the centre of the plate width. The AE sensor was mounted on one of the faces of the plates at a distance of 20 mm from the farthest edge away from the pencil breaks.

Flexural experiments: The flexure experiments were performed on an in-house assembled test rig. The rig was designed based on the maximum loads calculated for the specimens from the simulations. The 4-point test set up, including the distances between the support and load points was as shown in **Fig 4.1**. The experimental set up is shown in ***Appendix-C***. The displacement rate of the experiment was set at 5 mm/min. This is slightly higher than the standard displacement rate of 2 mm/min used in flexure testing of metals and composites. However, to reduce the amount of AE data to be recorded during the experiment, a slightly higher value was chosen.

Indentation experiments: The indentation testing was done by using a cylindrical indenter with a radius of 4 mm to simulate plane strain indentation during loading cycle only. The specimens were placed on a flat plate. The AE sensor was mounted onto the specimens using silicone grease and adhesive tape. The clamping force was low enough so as not to decrease the sensitivity of the sensor. The transmission of AE signal along the specimen under load has been tested prior to the experiments. This was done by loading a plate to various levels using the indenter. The PLB source and the AE sensor were placed on both sides of the load line. It was found that the attenuation of the signal because of the applied load was insignificant compared to the total signal energy. This was tested by loading the specimen to different indentation loads and conducting PLB tests and measuring the signal maximum amplitude.

Instrumentation: Both the flexure and indentation experiments have been carried out on an Instron 3342 machine. This machine has the capability of recording both the load and displacement at 1000 samples/sec. The load cell used for recording the load data during the flexure experiments was the SEN2008 (SLC41/000500) model supplied by RDP electronics, UK. This load cell is a tension/compression type and has the load range of ±2.2kN. The calibration curve of the load cell is shown in ***Appendix-E***. The voltage from the load cell was amplified using the S7DC amplifier. For the indentation experiments however, the load data has been acquired directly from the test machine as the maximum load is higher than the peak rated load of the load cell. The displacement in both the cases was taken from the test machine directly. The mechanical test procedure and the data acquisition were started and stopped simultaneously to ensure synchronisation between the various data channels.

Data acquisition*:* The AE data was recorded at a rate of 2 M samples/sec using two sensors along two channels simultaneously. In addition, the load data was recorded on the third channel. The sensors were mounted onto the specimens using silicon grease and aluminium tape. The sensors were mounted at 20 mm from the outer edge on the longer axis of the specimen on either side. The total downward displacement was 10 mm for each specimen. The recorded data was stored as a single '*.tdms'* file which was then split into multiple file. The VI used is shown in ***Appendix-F***. Each of these files corresponds to data recorded on all the channels for ½ sec. Thus, it consists of 1000000 data points from each channel. These files were later converted to '*.xlsx*' format that can be opened using Microsoft Excel. This made data processing easier as large '*.tdms'* files cannot be processed using MATLAB.

5.3. Data analysis methodology

Each *'.xlsx'* file obtained as explained in the previous section was then processed for the AE parameters namely number of hits, total duration of each hit, peak amplitude of each hit, peak

frequencies in the low and high frequency ranges and finally the ratio of the high and low frequency energy values.

These values were then used to classify the events into two or more clusters. The expected number of clusters is two at the least, corresponding to the mode-I and mode-II type crack propagation. In the case of the existence of mixed-mode failure, another cluster of data was expected to exist. However, the distribution of the data in this cluster was expected to be wide spread because of the several possible mode-mix ratios. From the simulation results however, crack initiation and propagation in both flexure and indentation (**section 4.3**) is expected to be in mode-II. To confirm the validity of the cluster data, these signal records were then processed for the same parameters as mentioned above and clusters were created using this data. These were then compared to the experimental data to understand the dominant mode of crack propagation in the adhesive bonds under the given loading conditions. This helps in understanding the suitability of the said methods in assessing the mode dependent residual strength of the adhesive bonds tested. However, it should be mentioned that the PLB tests conducted had a constant impulse (amplitude) source (PLB). The experimental record on the other hand, has AE hits from crack events of variable amplitudes depending on the strain energy release. Hence, the energy ratio of the high and low frequency bands was taken as the important characterising features as it nullifies the effect of the amplitude.

Clustering has been performed on the PLB test data using the k-means algorithm embedded in MATLAB. This is an unsupervised clustering technique based Four variables were the basis for clustering, energy ratio (175 kHz-highpass/175 kHz-lowpass), peak amplitude ratio (175 kHz-highpass/175 kHz-lowpass) and ratio of the total event duration to the peak amplitude. These ratios were expected to normalise the effect of the event magnitude on the classification. In addition, the peak amplitude and event duration have also been evaluated as the characterising parameters instead of the amplitude ratio and event duration to peak amplitude ratio. The use of the k-means clustering algorithm in the fracture monitoring of adhesive bonds has previously implemented by Jefferson *et al* [17].

5.4. Results

5.4.1. 4-point flexure testing (load-displacement curves)

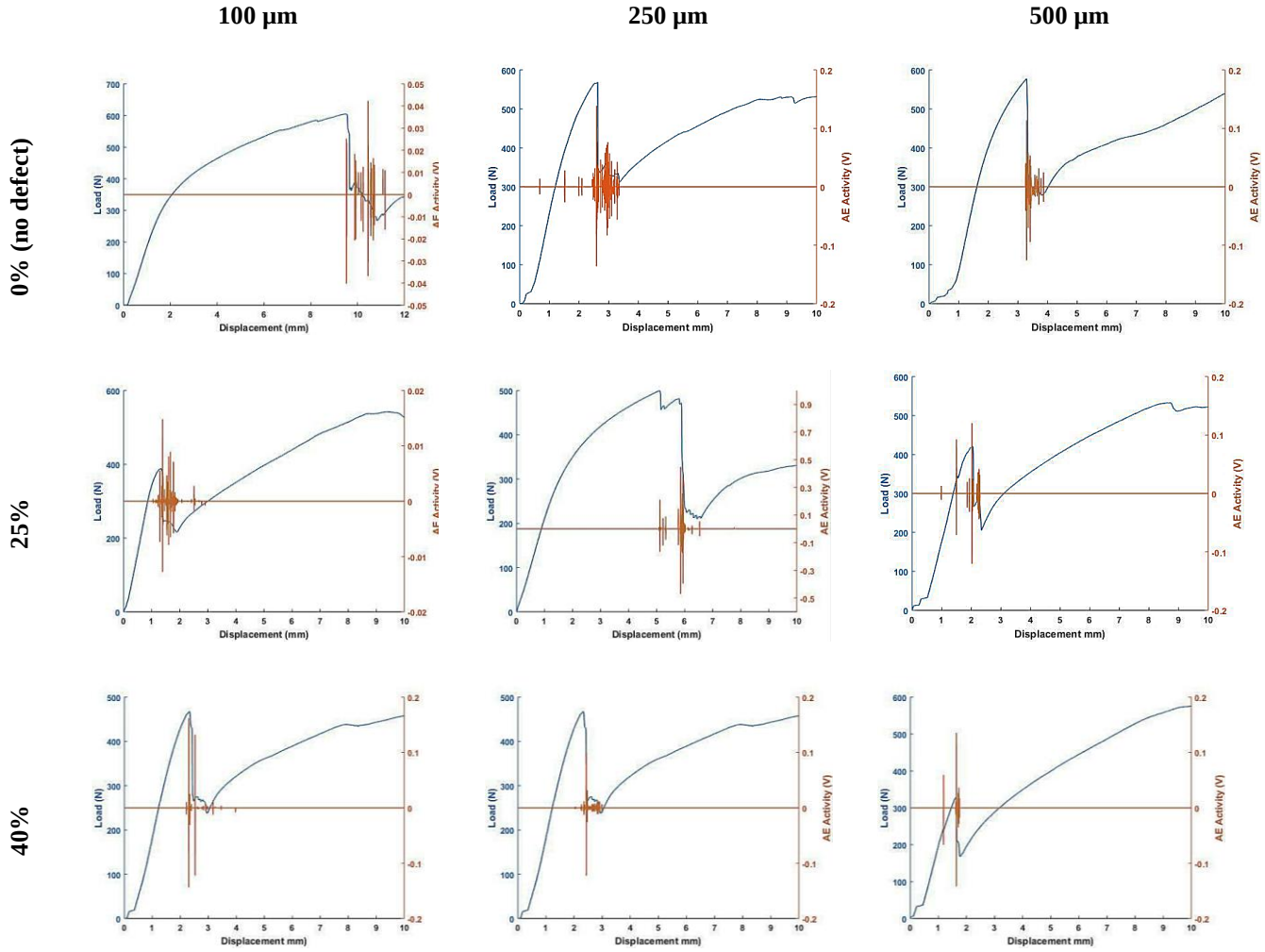

Figure 5.1. Load-AE-extension plots of the flexure experiments.

Figure 5.1 shows the load-displacement plots (at 5 mm/min displacement rate) of the flexure experiments along with the AE activity. The AE activity decreases with increasing adhesive layer thickness. Also, the crack initiation or failure load decreases with increasing defect area percentage. However, peak amplitude associated with the crack initiation was the same across the various adhesive joints. Similarly, the crack initiation displacement stayed the same across the experiments. The crack initiation was expected to happen predominantly in mode-II. This was because a high shear stress concentration was observed at the loading points on the specimen. Chai [57**]** reported a mode-II crack initiation when the interfacial shear strain reaches a critical value. Hence this crack initiation criterion can be applicable to the present scenario as well. The crack propagation, as seen from the plots, is rapid.

Fig 5.2 shows the 4-point bending force against span deflection profile for all the different specimens. There exists a very good agreement between the experimental and simulation load-displacement profiles. The discrepancies between the both are due to the assumptions of the finite element model, the important one being the bi-linear modelling of the elastic-plastic nature of aluminium and the adhesives. The specimens with the adhesive layer thickness of 250 µm exhibited failure with both the adhesives. This can be seen as a sudden drop in the load during the test. However, the load kept steadily increasing even after failure because of the load bearing capacity of the aluminium plates.

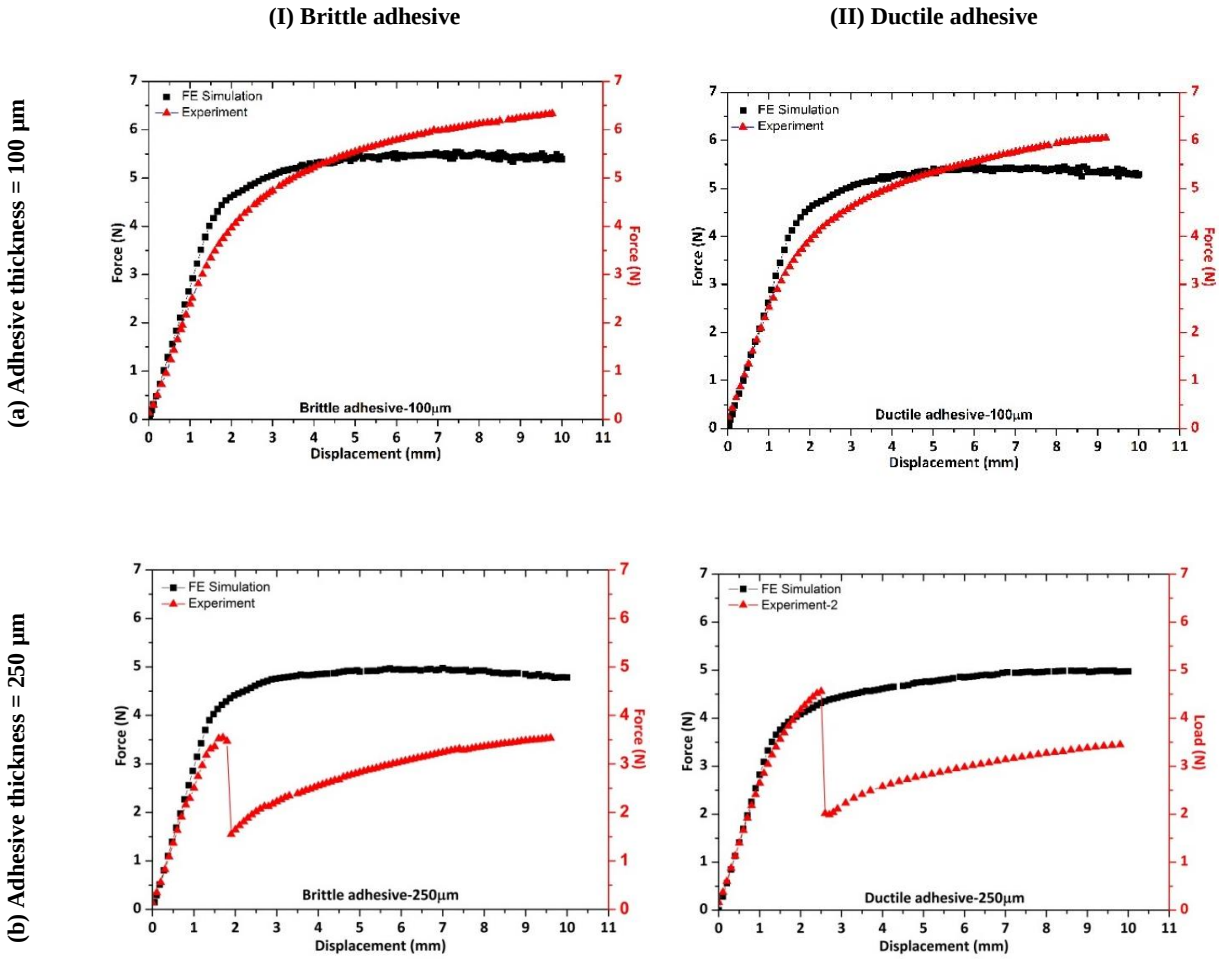

Figure 5.2. Experimental validation of FE model during 4-point bending: Comparison of force-displacement profile for Al-to-Al adhesively bonded specimens with brittle (Loctite®3430TM) and ductile (Loctite®326TM) adhesives of thicknesses 100 µm and 250 µm.

The initiation and further propagation of the failure can be seen as a reduced stiffness of the specimen compared to the simulation data for the 250 µm specimens. These specimens seem to fail as soon as the metal plates entered the plastic regime. Upon observation of the failed specimens, the crack seems to originate along the upper interface near the load locations and travel towards the centre of the span. This agrees with the predictions of the simulations where a

high stress concentration was seen immediately adjacent to the load points.

The simulations assume that there exists a perfect bonding between the adhesive and the adherends along the interfaces and does not account for the existence of defects both within the adhesive and along the interface. Hence the failure of the specimen, as predicted by the simulations depends completely on the stress states within the adhesive layer and evaluation of failure must be carried out based on a pre-selected failure criterion such as von-Mises stress criterion or maximum principal stress criterion [132]. However, in both the experimental specimens tested, failure was along the interface and this could be primarily because of the strain mis-match between the adhesive and the metal. The presence of defects might also lead to localised stress concentrations and crack propagation by the agglomeration of these defects. Incorporation of these defects within the model will be an intriguing study. As seen, from the experimental curves, the load raises till a value where there is sudden and rapid crack propagation along the interface of the adhesive bond leading to a sudden drop in the load. This sudden crack propagation leads to a drastic release of stored elastic energy from within the metal plates. The amount of elastic energy stored in the adhesive layer is negligible keeping in mind the elastic modulus and the yield strength of the adhesive. After the crack propagates along the entire span of the interface, the top plate (0.5 mm thick) completely separates from the adhesive bonded sandwich. Thus, upon further loading, the assembly behaves as two plates stacked one on top of the other.

The agreement between the simulation and the experimental results validate the simulation technique though the simulation slightly underestimates the load-carrying capability of the specimens in cases where there is no discernible failure of the adhesive layer.

5.4.2. PLB testing (edge and face) on metal plates and bonded joints

PLB testing was conducted on the metal plates as described previously (section **5.2**). **Figure 5.3** shows the representative signal records and the corresponding power spectral density plots for the edge and face PLB tests on the metal plates. In the edge PLB tests, the low frequency content of the signal records has lower energy compared to the higher frequency component of the signal record. For the face PLB tests, however, both the peaks have similar or comparable magnitudes. **Figure 5.4** shows the wavelet transforms of the signal records from the metal plates. The dispersion curves of the corresponding metal plates have been superimposed on each WT. From these plots, in addition to the frequency of the peak amplitude, the energy associated with the high and low frequency ranges also changes with the location of the PLB.

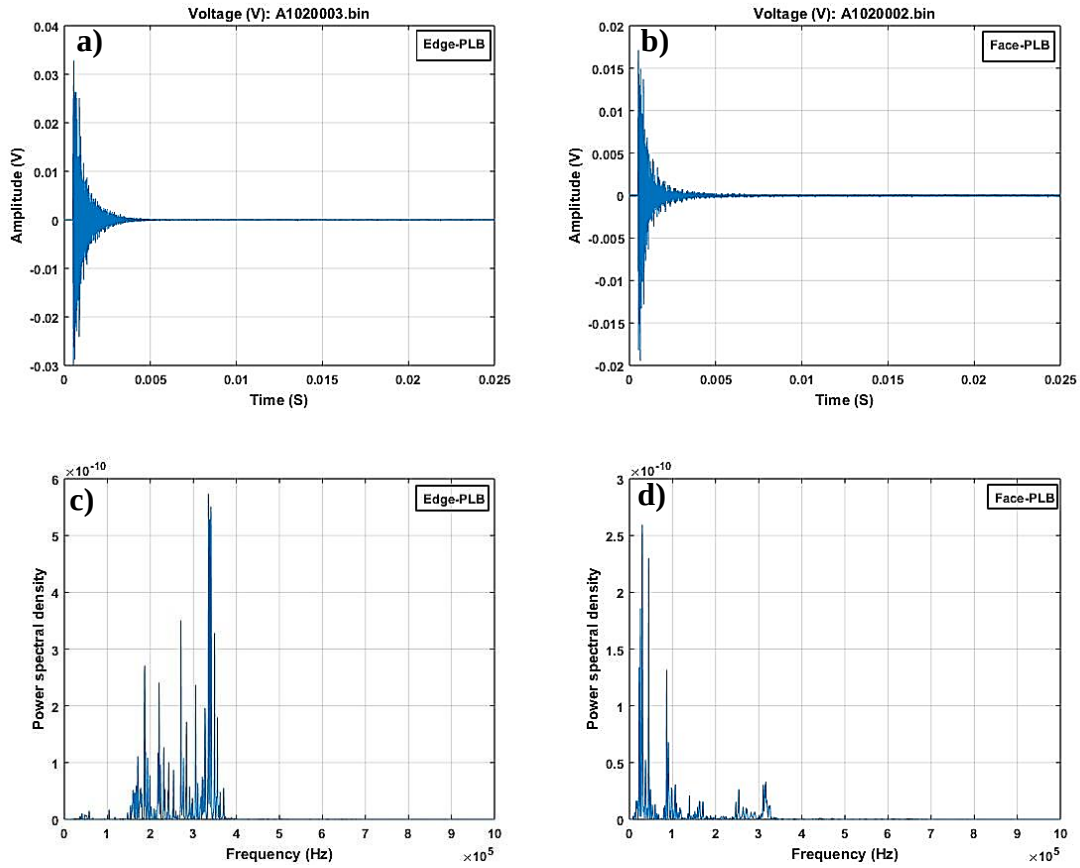

Figure 5.3. Signal record of **a.** Edge (Mode-II) type PLB, **b.** Face (Mode-I) type PLB and PSD plots of **c.** Edge (Mode-II) type PLB, and **d.** Face (Mode-I) type PLB.

The collected data was then classified into clusters using the k-means clustering technique based on the squared-Euclidian distance estimate. This unsupervised technique classifies the data into clusters by maximising the mean Euclidean distance between the centroids of the clusters. Thus, the distance between each data point and its neighbours within the same cluster, and those in other clusters is calculated. The AE data acquired from the PLB test on the 0.5 mm and 2 mm thick plates was analysed to identify any possible clusters. The AE parameters chosen were the peak amplitude, total event duration above threshold and energy ratio of the low and high frequency band energies. The frequency bands for the energy ratio were chosen based on the observation that mode-II sources (edge PLB) predominantly produce signals with frequency response in the 175 kHz to 400 kHz range. This can be seen from **Fig 5.3**. The validity of the number of clusters was evaluated using the Davies-Bouldin and silhouette coefficients [17]. The optimum number of clusters is when the Davies-Bouldin coefficient is the lowest and the silhouette coefficient is the highest. The variation of these parameters with respect to the number of clusters was evaluated to estimate the optimum number of clusters, and as expected, this number was found to be 2.

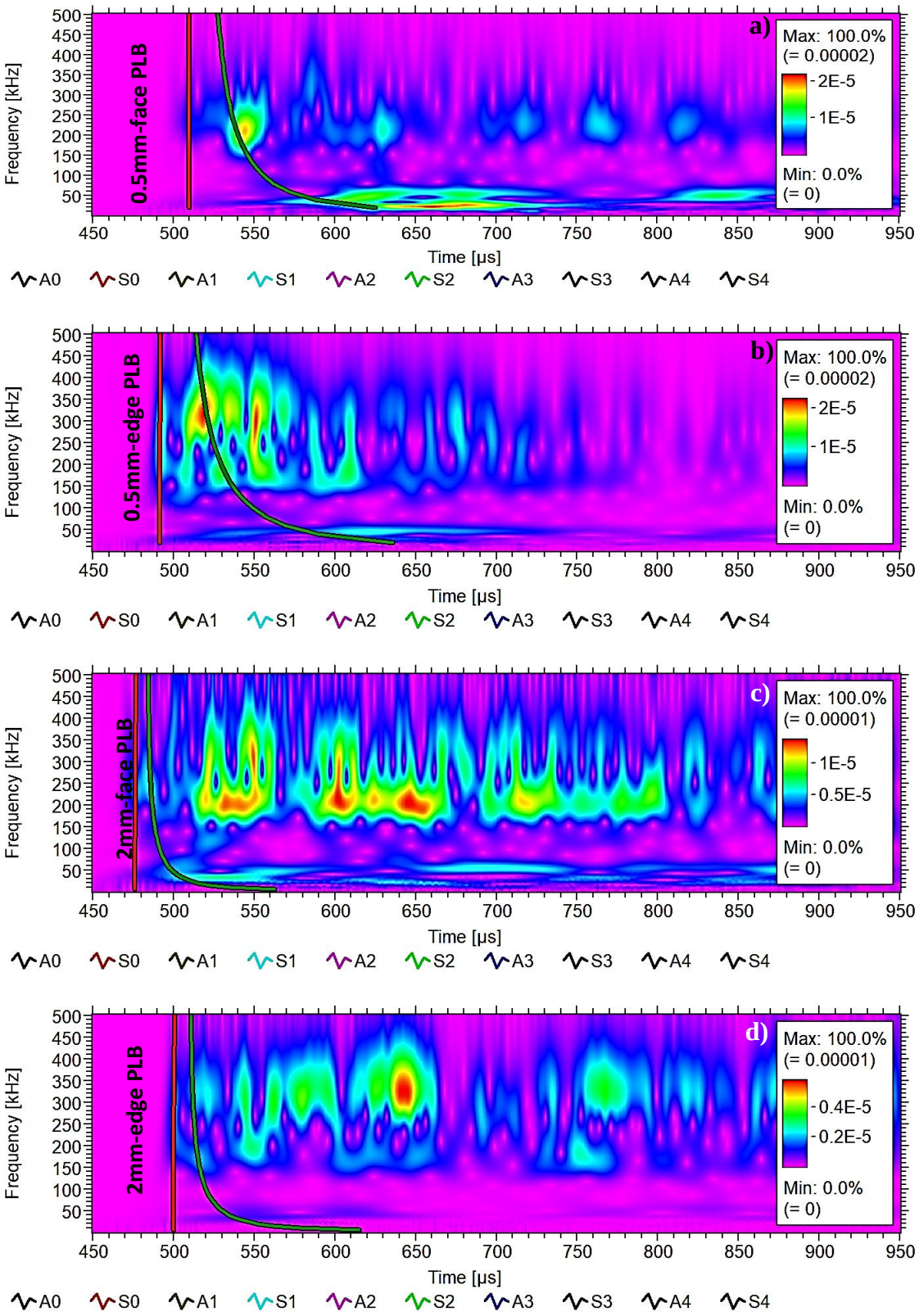

Figure 5.4. WTs of **a.** face PLB test on 0.5 mm plate, **b.** edge PLB test on 0.5 mm plate, **c.** face PLB test on 2 mm plate, and **d.** edge PLB test on 2 mm plate.

Figure 5.5 presents the cluster data of the 0.5 mm plate using three and two variables respectively. The first cluster plot uses total event duration, peak amplitude and energy ration of

each PLB test. As seen, this technique was clearly able to distinguish between the edge and face PLB tests. However, an overlap can be seen between the two clusters along the peak amplitude axis which shows that the location of the PLB test has no effect on the peak amplitude of the signal. However, both the event duration and the energy ratio can be taken as the classifying parameters between the edge and face PLB tests. The parameters event duration and peak amplitude are two parameters that are specific to the PLB tests as the input is of a fixed amplitude and input response. To classify crack events of varying amplitudes, energies and decay rates, the parameters need to be of a relative rather than an absolute nature. Hence, in addition to the energy ratio, two other parameters namely the peak amplitude ratio of the low and high frequency components of the signal and the ratio of event duration and the peak amplitude of the signal were considered**. Figure 5.5** shows the cluster plot of the signal using these three parameters. As seen, the overlap between the clusters is significantly reduced and there is a clear distinction between the edge and face PLB tests.

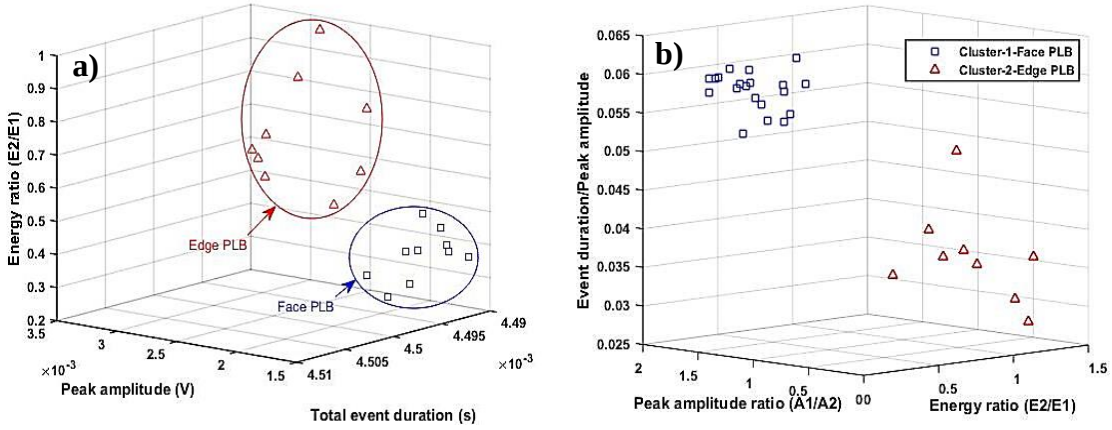

Figure 5.5. Clustering of edge and face PLB test signal records on the 0.5 mm thick plate based on the **a.** peak amplitude, total duration and energy ratio (175 kHz-highpass (E2) /175 kHz-lowpass (E1)), and **b.** based on energy ratio (E2/E1) and peak amplitude of the 175 kHz-lowpass component.

5.4.3. AE data analysis of 4-point flexure experiments

Three types of signals were observed in the 4-point flexural signal record (time and frequency domain). These are shown in **Fig 5.6**. The first signal was expected to be corresponding to the mode-I type crack propagation where the energy associated with the low frequency band is significantly higher than that of the high frequency band. Similarly, the second type of signal was expected to be of the mode-II type where the energy associated with the high frequency range is significantly higher than that of the low frequency range. The third type of signal was expected to be of the mixed-mode type. However, from the PLB tests, the mode-II type PLB tests produced signals with energy ratios slightly higher than 1. Another observation is that the AE event

corresponding to the mode-I type crack has a longer duration compared to the other two types of events. The failure of the specimens always occurred at the interface between the 0.5 mm thick plate and the adhesive layer.

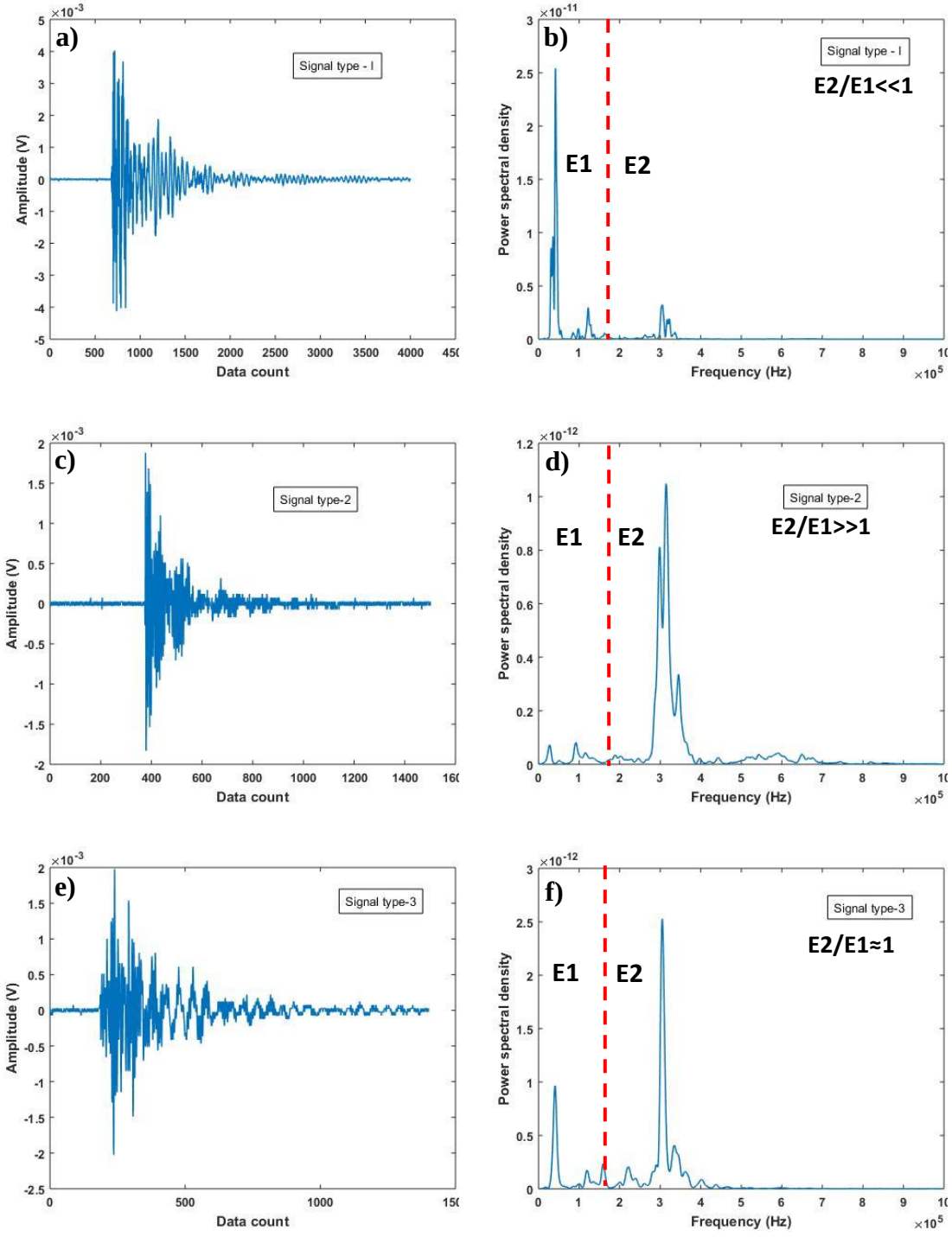

Figure 5.6. Various signal types recorded during the flexure tests. **a.** Signal record, **b.** PSD plot of mode-I type signal, **c.** Signal record, **d.** PSD plot of mode-II type signal, **e.** Signal record, and **f.** PSD plot of mode-I type signal.

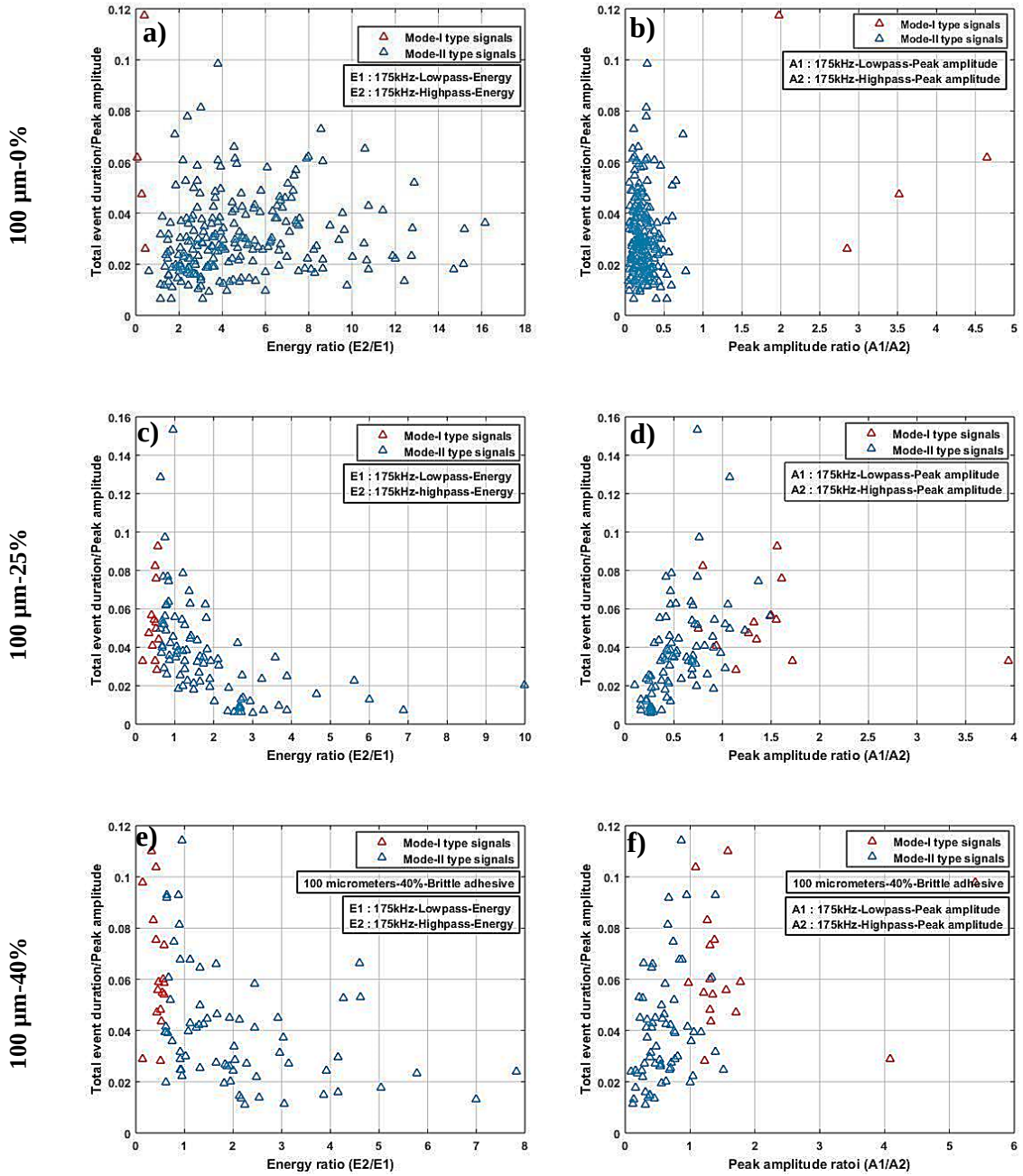

Figure 5.7. Plots of normalized event duration vs energy ratio and normalized event duration vs peak amplitude ratio respectively for **a,b.** 0.5-0.1-1.5-BA, **c,d.** 0.5-0.1-1.5-25%-BA, and **e,f.** 0.5-0.1-1.5-40%-BA.

Hence, as the interfacial crack propagates, the 0.5 mm thick plate becomes free and behaves as an individual plate. The AE signals presented here were collected by the sensor mounted on the 0.5 mm thick plate. Hence, the recorded signals were compared to the PLB tests conducted on the 0.5 mm plate. The first signal type, as seen from **Fig 5.6**, is characterised by a low frequency response. From the PLB tests, this frequency response matches closely with that of the PLB test on the face of the specimen. The comparison with the edge PLB tests is not straight

forward. Whereas, the metal plates were freely rested in the PLB tests, the adhesive bonding restricts the vibrations towards the edges in the experimental specimens. The crack propagation in the flexure specimens never reached the specimen edges.

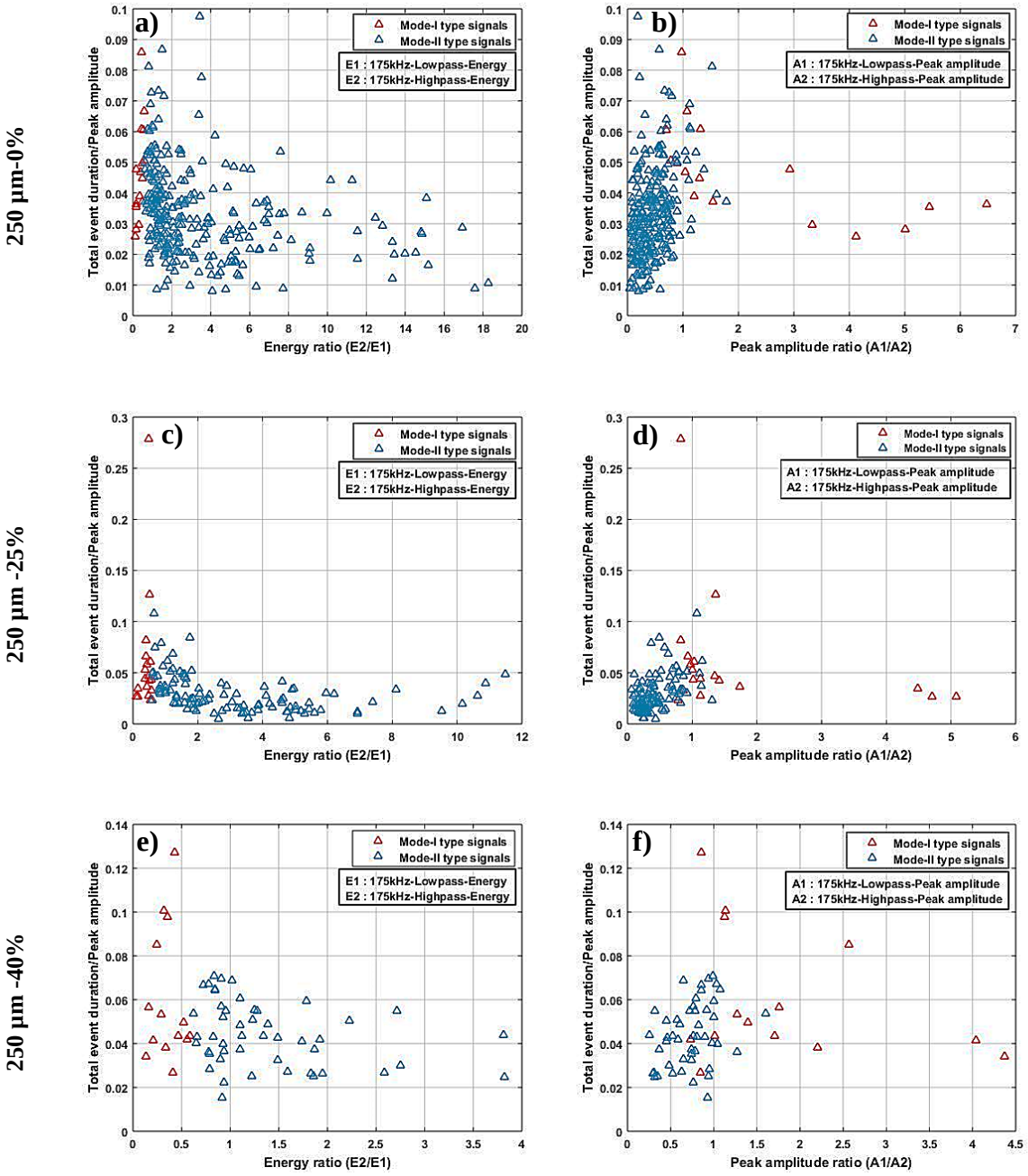

Figure 5.8. Plots of normalized event duration vs energy ratio and normalized event duration vs peak amplitude ratio respectively for **a,b.** 0.5-0.25-1.5-BA, **c,d.** 0.5-0.25-1.5-25%-BA, and **e,f.** 0.5-0.25-1.5-40%-BA.

The entire signal record was then split into individual hits and the data analysis was done as described previously. The event classification plots for various specimens are shown in **Fig 5.7** to **Fig 5.9**. As seen, two distinct clusters were observed in each specimen. As can be seen, the

energy ratio features in each case, emerged to be the most significant features. The same features emerged to be most suitable for distinguishing between the clusters formed from the face and edge PLB tests. The value of this features ranged from ~0.05 to 50 for most of the test specimens. The higher the value, the higher the energy associated with the high frequency component of the hits.

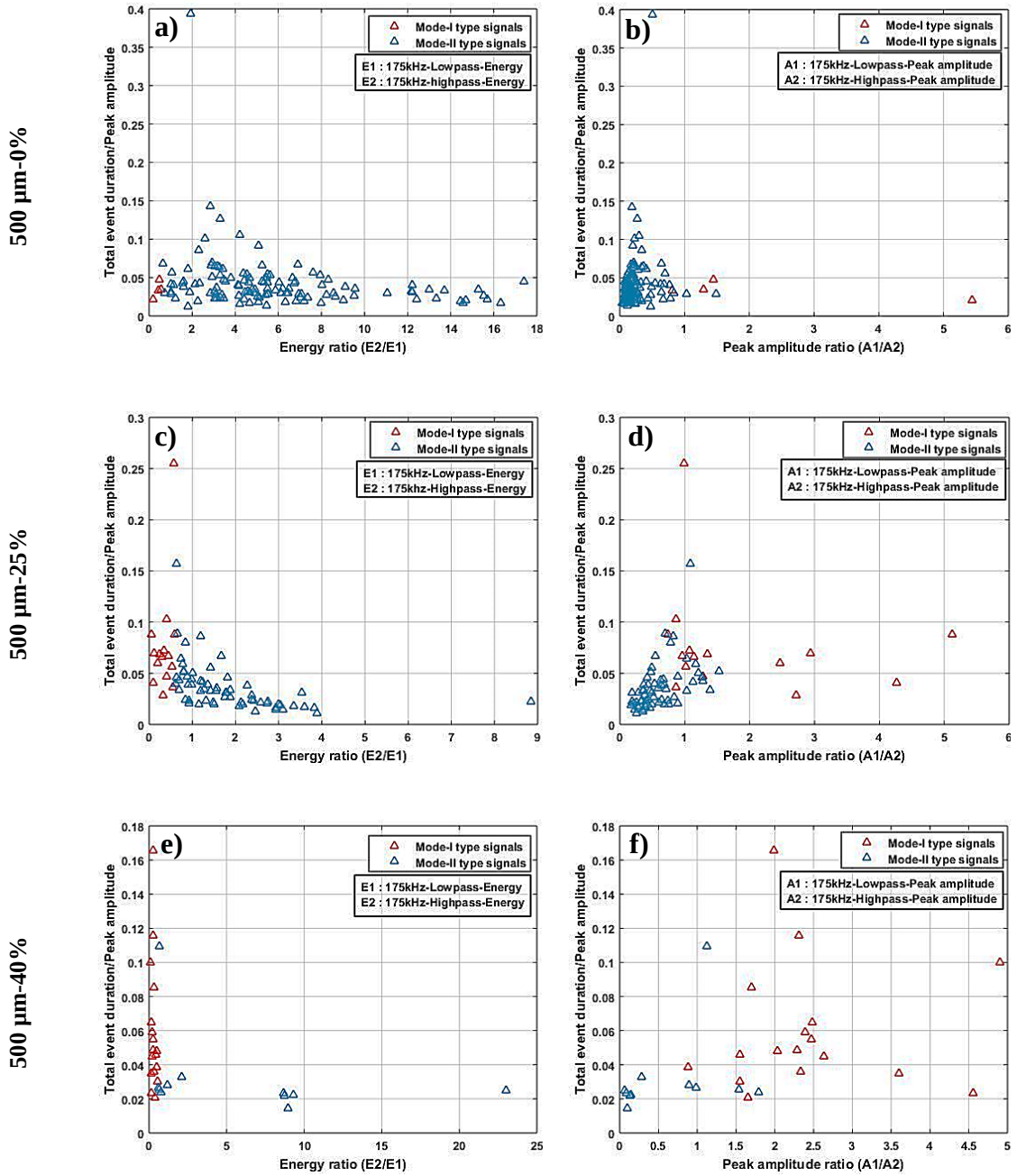

Figure 5.9. Plots of normalized event duration vs energy ratio and normalized event duration vs peak amplitude ratio respectively for **a,b.** 0.5-0.5-1.5-BA, **c,d.** 0.5-0.5-1.5-25%-BA, and **e,f.** 0.5-0.5-1.5-40%-BA.

From the PLB tests, the higher value of the energy ratio features corresponds to the edge PLB (mode-II) tests. **Figure 5.8** shows the classification of events from the various flexural tests based on the energy ratio (E2/E1), peak amplitude ratio (A1/A2) and ratio of the event duration to the peak amplitude. The events were classified into mode-I and mode-II type signals. As seen, most of the events are mode-II in nature. The increase in the number of events with the decrease in the defect area percentage is quite apparent from the plots. The dominance of the mode-II type events was as expected from the simulations where a shear stress concentration along the interface leading to a high shear strain mismatch was expected to be responsible for the crack initiation. From the plots, the maximum value of the energy ratio observed within an experiment decreases with the increasing defect area percentage. The normalized event duration (total event duration/peak amplitude) decreases with increasing energy ratio. This trend can be clearly seen in the defective adhesive bonds. Another observation that can be made from the above figures (**Fig 5.7 - Fig 5.9**) is that as the adhesive layer thickness increases, the number of hits decreases and the same can be seen from the increasing defect area percentage.

5.4.4. Single lap joint tension tests

The surface treatments applied on the metal plates to vary the interface quality and strength were tested mechanically. Single lap joints (as per standard ASTM D1002) [131] were manufactured with an adhesive layer thickness of 250 µm and an overlap length of 50 mm. Specimens were prepared with the three interface conditions as described before and tested in tension. As with the indentation specimens, the interface towards the 0.5 mm plate was treated according to the required surface condition.

The displacement rate applied was 0.5 mm/minute which is about half the standard displacement rate mentioned in the above standard. The reason for choosing this low displacement rate is so that the crack events will be spaced wider apart in the temporal space. This ensures that the AE events produced do not overlap under gradual loading conditions. The load and displacement values were monitored throughout the tests. Similarly, the AE activity was also recorded at a rate of 2 MS/sec. **Figure 5.10** shows the energy ratio vs displacement plots for the single lap joint tension tests conducted. **Figure 5.11a** shows the number of AE hits during each type of test. Each data point corresponds to one AE event. It is expected that as the interfacial quality increases, the number of AE events associated with the crack propagation will also increase. As shown, the number of hits increases with increasing interfacial strength.

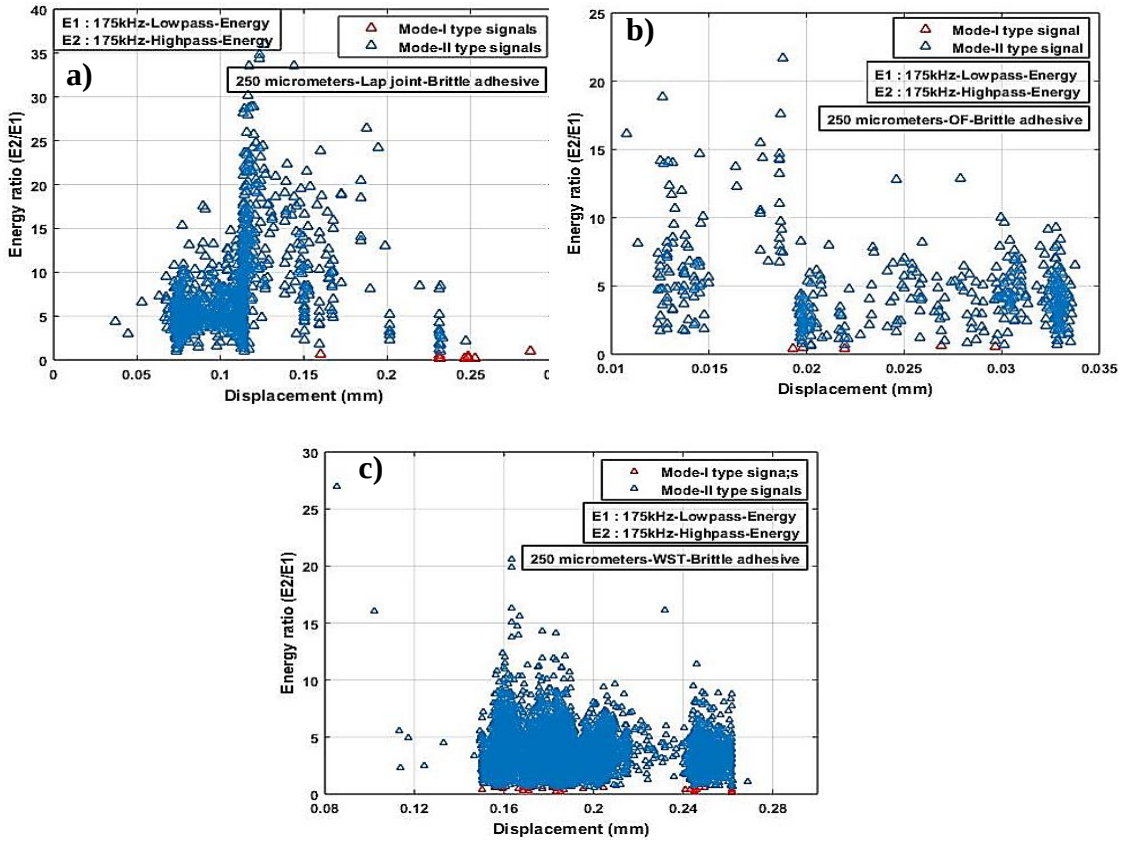

Figure 5.10. Displacement vs hit energy ratio plots for lap joint specimens with **a.** No surface treatment, **b.** Oil film along interface, and **c.** With Surface treatment.

A drastic drop in the number of hits can be seen the interfacial quality decreases. However, traditionally, lap joints have been reported to exhibit mode-I type failure in the beginning of the failure. This was because of a bending moment acting at the edge of the overlap. This was not observed in the lap joint tensile tests carried out. This was because of the comparatively weak interfaces of the manufactured specimens.

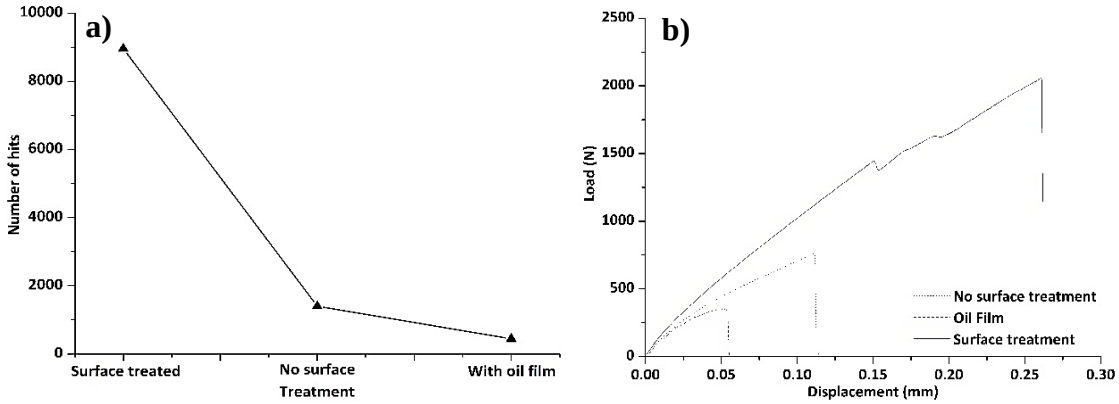

Figure 5.11.a. Variation of the number of hits with the surface treatment, and **b.** load-displacement curves of the SLJ tensile tests.

Hence, the number of hits during the load testing can be taken as an indicator of the interfacial strength of an adhesive bond. This is further supported by the load-displacement curves shown in **Fig 5.11b** which shows that the adhesive bonds with weaker interfaces exhibit lower failure loads. As expected, all the lap joints exhibited a predominantly mode-II type of failure.

5.4.5. Indentation testing and data analysis

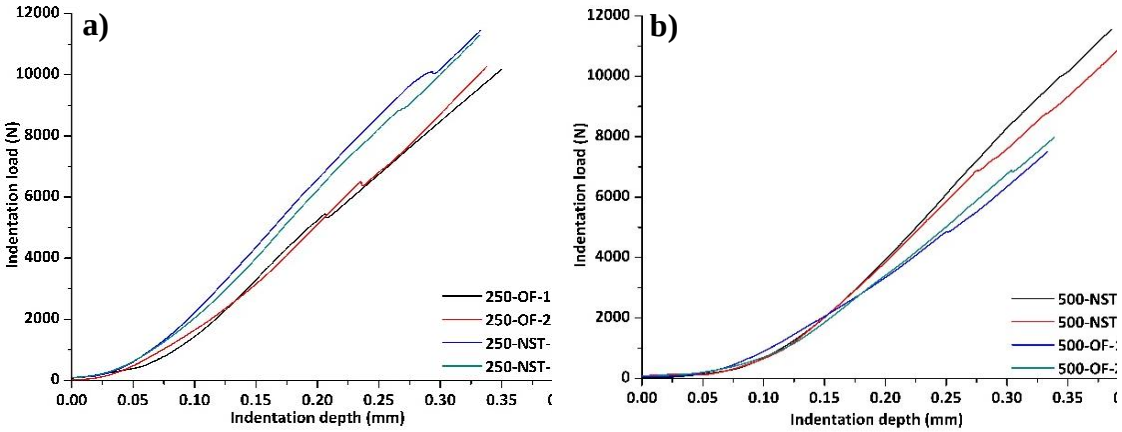

Figure 5.12. Load displacement curves of brittle adhesive bonds with and without interfacial oil film for adhesive layer thicknesses **a.** 250 µm and **b.** 500 µm.

As mentioned two adhesively bonded specimen types (**Table 5.1**) were tested for both the brittle and ductile adhesives. However, none of the ductile adhesive specimens exhibited any interfacial failure even with the weaker interfaces. This was expected to be because of the localization of the deformation in the ductile adhesive under indentation loading. Hence, no results were shown for these specimens. **Figure 5.12** presents the load-displacement profiles of the indentation tests carried out on the various adhesive joints (brittle) with various surface treatments. As seen, the curves exhibit a typical indentation loading behaviour. The adhesive joints with the oil film along the interface were weaker compared to those without an oil film. The inflexion in each curve corresponds to the load at which the crack exhibits rapid propagation. However, the crack initiation happened well before the inflexion point. This cannot be seen in the load-displacement plots.

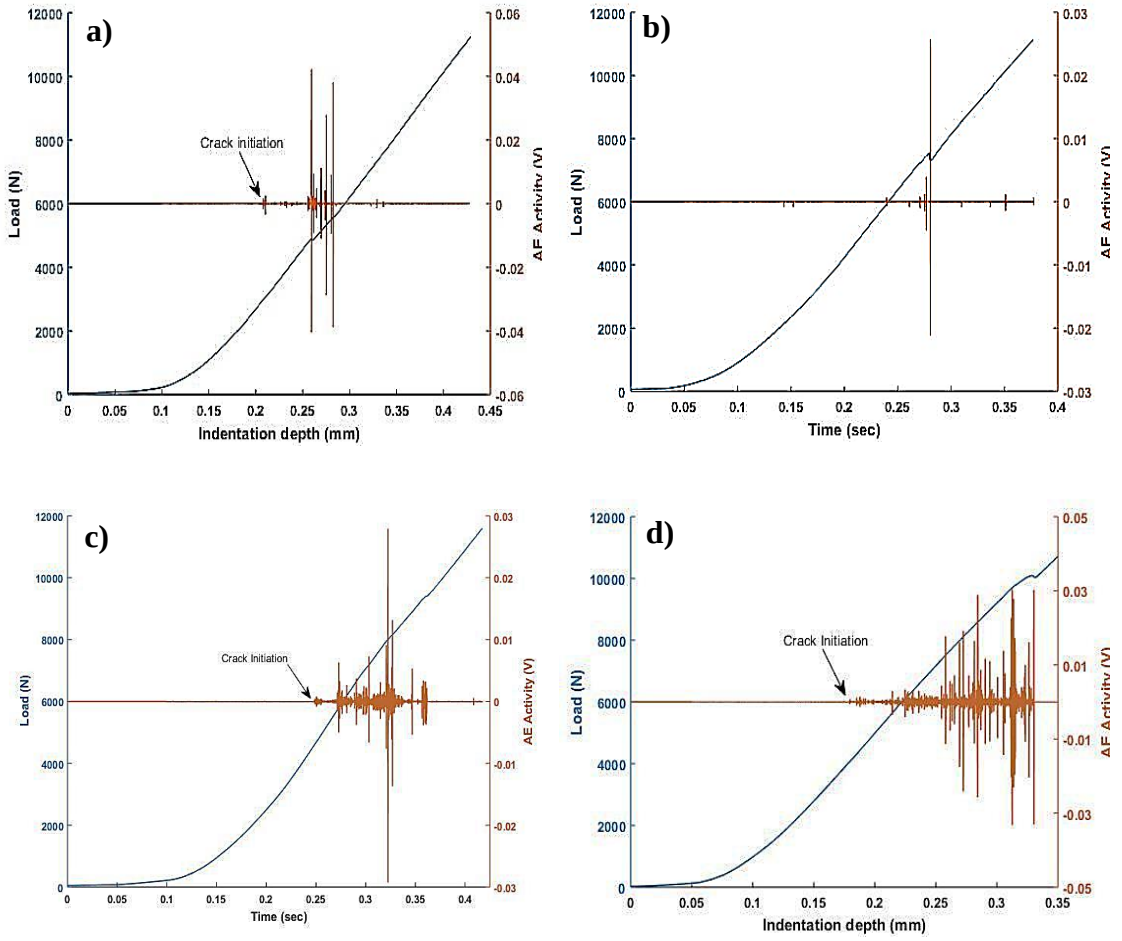

Figure 5.13. Load-AE activity-displacement profiles of **a.** 250 microns-OF-1, **b.** 250 microns-OF-2, **c.** 250 microns-NST-1, and **d.** 250 microns-NST-2.

The AE activity plots (recorded continuously with no data loss) however, show the crack initiation very clearly. The load and AE activity with respect to the indentation depth for the two adhesive layer thicknesses and two surface treatments are shown in **Fig 5.13** for the adhesive bonds with 250 µm thick adhesive layer and in **Fig 5.14** for the adhesive bonds with 500 µm thick adhesive layer. From the figures, in the case of adhesive bonds with oil film along interface, the AE activity is concentrated around the load inflexion point which corresponds to the sudden crack extension.

In the case of adhesive bonds without the oil film however, the crack initiates quite before the sudden crack extension event and a significant amount of loading is required to drive the crack further. This is slightly in contrast to what was observed in the FE simulations (**Fig 4.17**) where a rapid crack growth was observed at higher interfacial strengths because of the accumulation of the strain energy within the adherends prior to crack initiation.

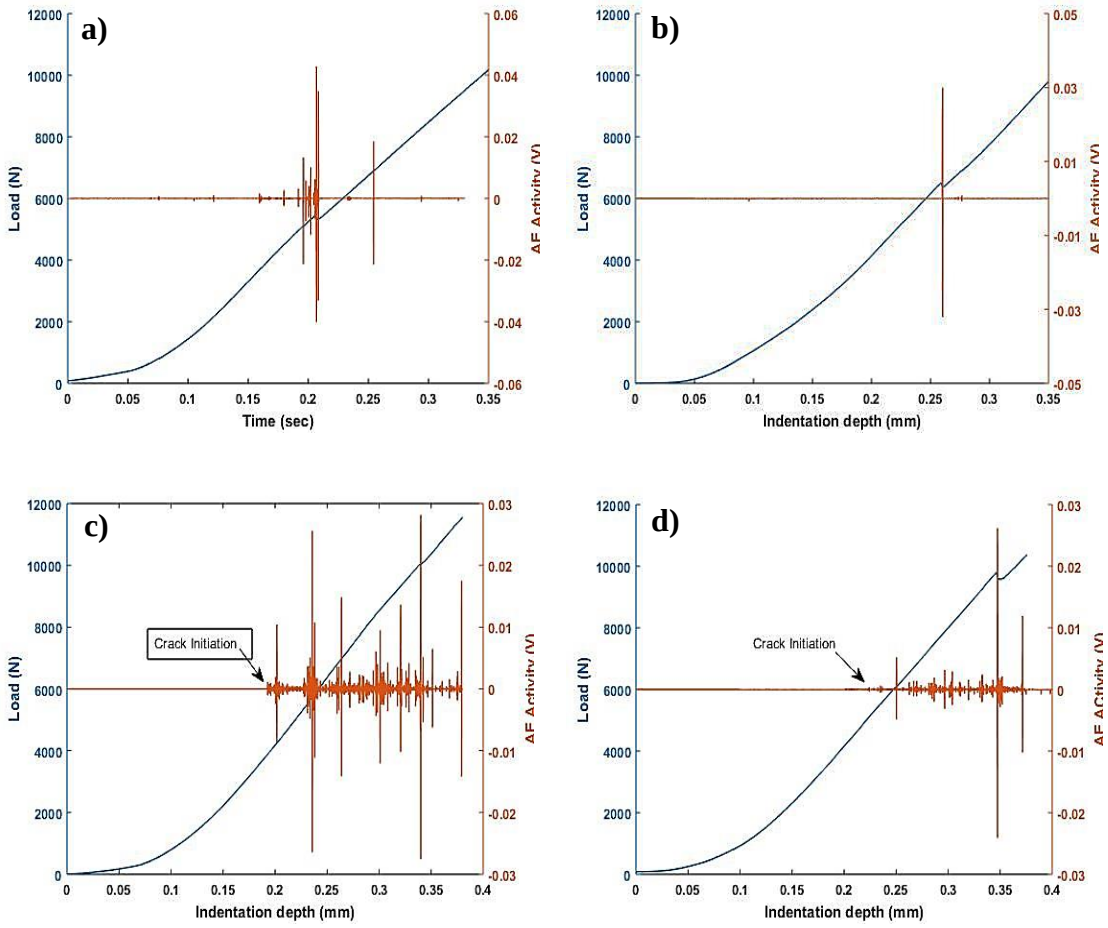

Figure 5.14. Load-AE activity-displacement profiles of **a.** 500 microns-OF-1, **b.** 500 microns-OF-2, **c.** 500 microns-NST-1, and **d.** 500 microns-NST-2.

Figure 5.15 shows the average number of hits for the different experiments. As seen, the number of hits is higher at lower adhesive layer thicknesses and at stronger surface conditions. However, the adhesive layer thickness does not seem to have any effect on the number of hits with adhesive joints with oil film along the interface. The presence of the oil film leads to an early crack initiation which in turn leads to lower elastic energy being stored in the adhesive joint. With a stronger interface however, the crack initiation is slightly delayed and the elastic energy stored within the adhesive layer increases. The effect of the adhesive layer thickness, on the other hand is to increase the elastic energy being absorbed by the adhesive layer.

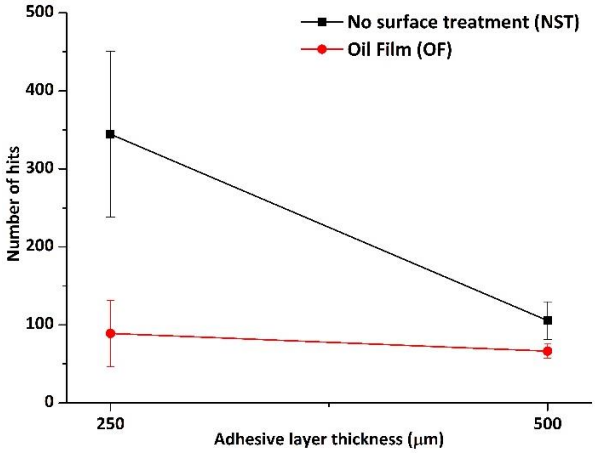

Figure 5.15. Variation of the number of hits with the adhesive layer thickness and surface treatment under indentation testing.

At lower adhesive layer thickness, the stress being transferred to the adherends is higher whose capability of elastic energy storage is higher. At higher thicknesses however, the adhesive being more ductile, absorbs the load and hence a major portion of the elastic energy released upon crack initiation is from the adhesive layer. The variation of the number of hits with the interfacial condition agrees with that observed in the lap joint tests. The classification of the events was based on the pencil break tests made on the metal plates on the transverse and longitudinal faces. The plots showing the distribution of the events in the time, energy ratio, Event duration-peak amplitude space are shown in **Fig 5.16** for adhesive bonds with 250 μm thick adhesive layer and in **Fig 5.17** for adhesive bonds with 500 μm thick adhesive layer. As seen, almost all the events are of the mode-II type. Mode-I type signals, though existent, are sparsely distributed.

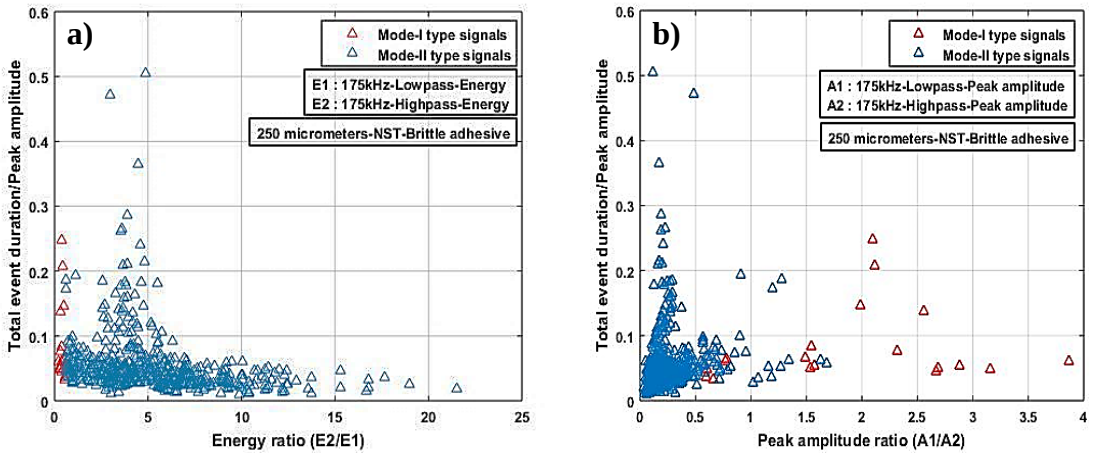

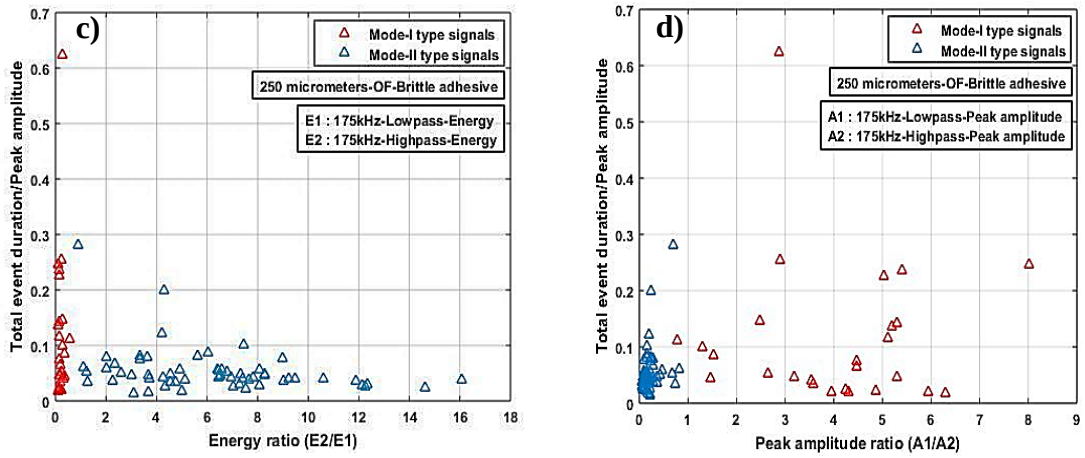

Figure 5.16. Crack event distribution with respect to indentation depth and the variation of event duration to peak amplitude with respect to peak amplitude ratio for **a,b**. 250 µm-NST, and **c,d.** 250 µm-OF.

The crack initiation is predominantly under mode-II. It can be clearly seen that the peak value of the energy ratio (E2/E1) is higher with adhesive bonds without an oil film along the interface thus showing that as the interfacial quality increases, the crack extension event becomes extensively of mode-II type. Also, the number of events corresponding to mode-I type crack extension is higher at lower interfacial quality. Also, the peak amplitude ratio corresponding to the mode-I type signals is higher in the case of the adhesive joints with the oil film along the interface than those with without the oil film.

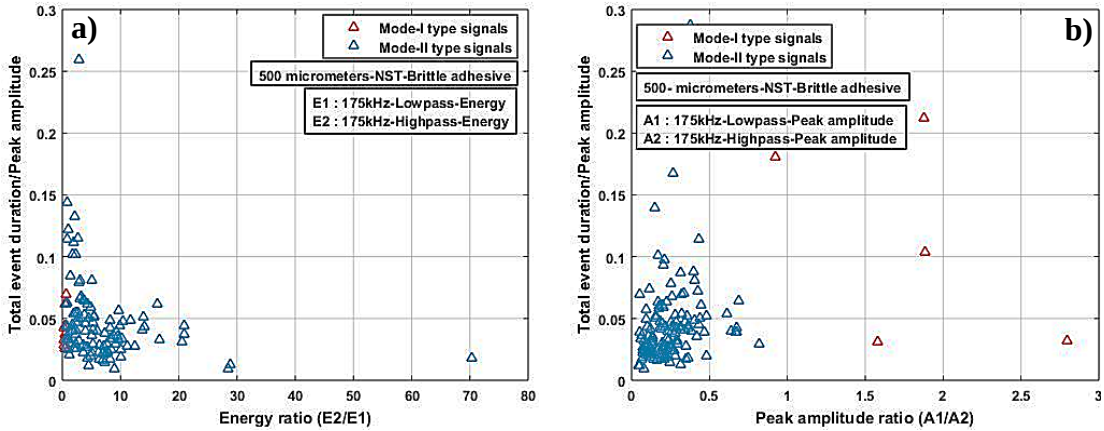

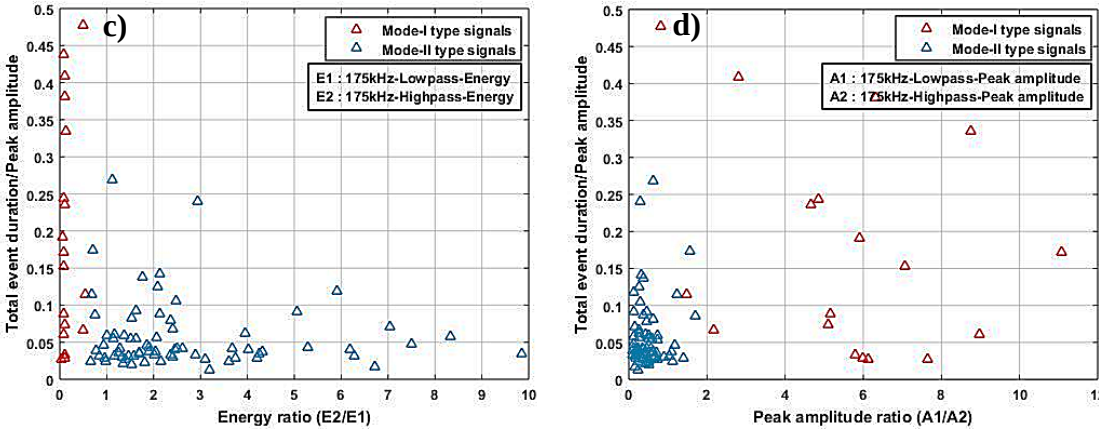

Figure 5.17. Crack event distribution with respect to indentation depth and the variation of event duration to peak amplitude with respect to peak amplitude ratio for **a,b.** 500 µm-NST, and **c,d.** 500µm-OF.

This corresponds to more mode-I type energy release during the crack propagation. However, in adhesive joints with and without oil film, the crack initiation is predominantly mode-II natured. As with the flexure experiments, the normalised event duration follows a decreasing trend with increasing energy ratio. The increase in the mode-I type crack events with decreasing interfacial strength implies the mixed mode nature of the crack propagation. It has been previously established that the resistance of the mode-I type crack extension is usually much lower than the mode-II type crack extension. As was seen from the simulations, the crack tends towards the mode-I type as the crack propagates along the interface. In the adhesive bonds with oil film along the interface, the interfacial resistance is low enough that the mode-I type crack propagation is easily achieved compared to the mode-II type extension.

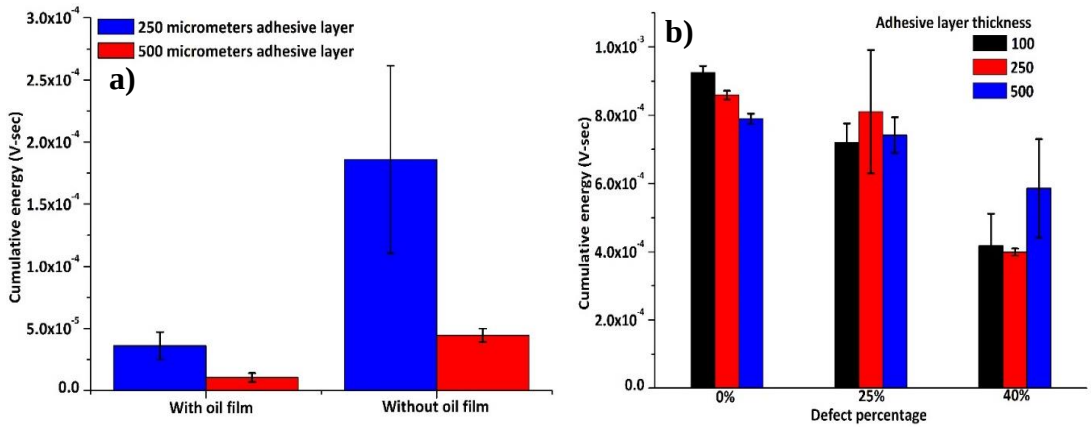

Figure 5.18. Cumulative AE energy calculated for different **a.** indentation specimen types, **b.** flexure type specimens.

5.5. Summary

1. The use of 4-point flexure and indentation testing in the interfacial strength evaluation of adhesive bonds has been tested and analysed.
2. Adhesive bonds with defect area distribution along the interface have been tested in flexure. The experimental results agree very well with the FE simulation results in predicting the load-displacement behaviour. The predictability of the simulations depends on the ability of the simulation in capturing the effect of defects.
3. The crack events were recorded using AE technique and the resulting hit data was classified into mode-I type and mode-II type signals. Both flexure and indentation experiments exhibited mode-II type crack propagation as was predicted by the FE simulations. More than 95% of all the AE events recorded were classified to be of mode-II type in both the experiment types.
4. Increase in the adhesive layer thickness decreases the number of AE hits in both the test methodologies. This indicates the increase in the attenuation of the AE signals with increasing adhesive layer thickness. The same result was seen with the pencil break tests. In indentation experiments, this indicates a lower tendency of interfacial crack propagation because of localisation of deformation under the indenter.
5. The failure of an adhesive bond can be easily detected using the AE technique well before the rapid crack propagation occurs. However, this is true only with adhesive bonds with higher interfacial strength.
6. Hence, both flexure and indentation can be used as alternate methods to test the interfacial strength of adhesive bonds using features such as the number of hits and the mode of crack propagation can be easily detected using the energy ratio parameter.

Figure 5.18 shows the variation of the cumulative energy release rate from the AE measurements. The conclusion that can be drawn from this plot is that as the defect density along the interface increases, the AE energy release rate decreases, thus proving that the AE can characterise the adhesive bond interfacial quality. For example, the introduction of oil film along the interface of an adhesive bonded joint with a 250μm thick brittle adhesive layer decreases the cumulative AE energy release rate from 1.9×10^{-4} a.u. to 4×10^{-5} a.u. These when correlated with the numerical predicted energy release rates shall quantify the residual strength of the defective adhesive bonds.

Chapter-6

6. Discussions

This chapter provides an interpretation of the experimental results covering defect detection of adhesive bonds, instrumented testing of adhesive bonds, including measurement of bond quality using a combination of simulation and experimental techniques. Comparisons will be made between the results of the present study and published literature. A step-by-step procedure is put forth to estimate the structural and residual strength of adhesively bonded joints.

6.1. Defect detection in adhesive bonds

The detection of adhesive layer defects such as porosity, voids (or absence of adhesive), kissing bonds, etc. is very crucial in ensuring the integrity of an adhesive bonded structure [133]. The most suitable defect detection technique would be able to assess both the cohesion and the adhesion within the adhesive bond. The use of shear horizontal waves [127], ultrasonic techniques [96] and guided lamb waves [21] in the detection of cohesive type defects has been extensively studied before.

The ratio of the reflection coefficients of both shear and normal wave propagation through an adhesive bonded joint has been found to be sensitive to the various defect types [134]. In specific, shear horizontal waves have been found to be highly sensitive to the interfacial quality [134].

This study also proposed a method to quantify the interfacial quality using FEA. The interface was modelled as a series of springs whose stiffness in the normal and shear directions dictates the wave propagation through the joint. These values were adjusted so that the simulated waveforms of the propagating impulse match the experimental values. Though this technique is highly reproducible, it requires an iterative procedure of tuning the FE model parameters to match the experimental values. The use of other experimental techniques in place of FE methods to assess the interfacial quality has not been explored in this context. **Table 6.1** gives an overview of studies on kissing bond detection using lamb waves. Various techniques have been previously studied for adhesive bond defect detection. These include ultrasonic scanning, infrared thermography, guided lamb wave based scanning, optical fibre interferometry, etc. **Table 2.4** (literature review) gives a brief overview of some of the studies conducted in this area. The adhesive strength of an adhesive bond is dependent on several parameters such as the surface treatment, the surface finish and the surface energies of the two components. The detection of kissing bonds is the most difficult compared to other type of adhesive bond defects. The use of AE in adhesive bond defect detection has never been extensively investigated before. Though some studies have been made on the use of AE based mechanical testing of defective adhesive

bonds, the possibility of defect detection prior to mechanical testing was not evaluated. Few authors have addressed the detection and location of kissing bonds (**Table 6.1**).

Adhesive	Adherend	Technique	Type of defect	Reference
Epoxy-AF3109	Aluminium	Guide SH wave (A_0, S_0 modes)	Kissing bonds	[134]
--	Aluminium	Guided lamb wave, guided SH-wave	Cohesive defects	[22]
Epoxy-AF3109	Aluminium	Guided SH-wave	Imperfect adhesion, interfacial oil film	[127]
--	Glass	Leaky lamb wave	Interface adhesion	[135]
Epoxy-AY103	Aluminium	Ultrasonic C-scan	Kissing bonds, Environmental degradation	[78]

Table 6.1. Detection of kissing bonds in adhesive joints.

The size of the kissing bonds in these studies ranges from 10 x 10 mm^2 to 50 x 50 mm^2. The technique being proposed in this study depends on the AE parameters such as the total duration above a set threshold of the signal, number of counts and energy to identify the kissing bonds along the interface of an adhesive bond. The present technique was able to detect a kissing bond of area 10 x 10 mm^2 area on a specimen of the area 120 x 50 mm^2. Hence, it is comparable to other defect detection techniques though the specimen size effect also needs to be taken into consideration. Since the specimens tested were of a small size, the edge reflections also play a key role in determining the AE parameters. In short, this technique considers the energy associated with all the reflections from the specimen edges. In a large enough specimen, the edge reflections may not be observed or might be of a very low amplitude owing to the damping of the adhesive material. However, it should be mentioned that PLB tests on an aluminium plate of dimensions 500 x 500 x 2 mm^3 revealed the presence of multiple reflections off the edges of the plate. Thus, it is possible that this technique is equally applicable on plates of said dimensions. However, this claim needs to be tested.

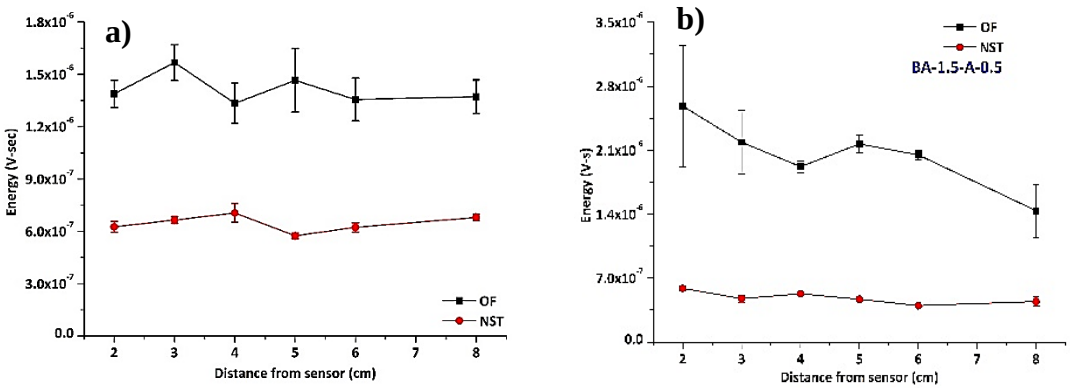

Figure 6.1. AE energies from PLB tests on adhesive bonds with and without oil films along interface, in configuration **a.** 0.5-A-1.5, **b.** 1.5-A-0.5.

In addition, PLB tests conducted on adhesive bonds with a very thin oil film along the interface, prepared to simulate moisture induced interfacial delamination, revealed that this technique can differentiate these defective adhesive bonds from those with perfect bonding across the interface. The plot corresponding to these tests is shown in **Fig 6.1**. Two configurations were tested in this case, 0.5-A-1.5 and 1.5-A-0.5. The specimen was prepared with the brittle adhesive with a thickness of 0.25 mm. The observation from this plot is that for a given energy input, the energy of the recorded signal is higher in the adhesive bond with interfacial imperfections. Though this might seem counter-intuitive, it can be inferred that the addition of the oil film along the interface leads to the energy not being properly transmitted into the adhesive layer and hence the additional damping associated with the lower adherend is bypassed in this case. This can be further explained by considering the top adherend and the adhesive layer together as a composite plate. Where there is a defect along the interface along the lower adherend, this composite plate acts as if it is freely suspended and fixed along the defect boundary. Upon propagation of plate waves, this plate tends to vibrate freely. This explanation is supported by the results reported by Xu *et al* [128]. They observed that the amplitude of vibration measured using optical fibre interferometry directly on top of an interfacial defect is higher compared to that measured on a fully bonded specimen and this increased with the energy input.

The use of AE signal detection had previously been implemented in a technique called acousto-ultrasonics [106] wherein an ultrasonic pulse is sent into the structure using a broadband transducer and a receiving AE transducer placed on the same side of the specimen intercepts the propagating stress waves. The collected waveform consists of multiple reflections from the various edges of the specimen and hence consists of the information pertaining to multiple interactions with the adhesive layer. The parameters of interest in this technique are the signal amplitude, ringdown counts and the total duration. Vary *et al* [136] defined a stress wave factor

(SWF) to quantify the information in the acousto-ultrasonic pulse. The SWF is determined by the ringdown count calculated based on a chosen threshold value and a chosen time duration.

Williams and Rampert [137] introduced another parameter called the acousto-ultrasonic parameter (AUP) which considers the number of oscillations at various threshold levels thus quantifying the stress wave propagation across a specimen. Higher AUP value implies a higher bond strength. Tanary *et al* [106] utilised this parameter in assessing the integrity of adhesive bonded graphite/epoxy composites. They correlated AUP to the shear strength of single lap joints.

Adhesive type-Thickness	Fit equation
BA-100μm	Defect % = (Event duration - 0.00192) / 1.9396
BA-250μm	Defect % = (Energy + 7.63E-7) / 1.728E-8
BA-500μm	Defect % = (Energy – 4.1209E-7) / 1.4574E-7
DA-100μm	No. of hits = 17.491*(Defect %)^2 -0.234*(Defect %)+489
DA-250μm	Defect % = (Energy - 6.2884E-7) / 1.5544E-7
DA-500μm	Event duration = 2.36E-7*(Defect %)^2 + 9.15E-7*(Defect %) + 4.021E-4

Table 6.2. Fit equations for different thicknesses of the brittle and ductile adhesive types (BA: brittle adhesive, DA: ductile adhesive).

The present technique utilises PLBs as a signal source and follows a similar data analysis technique as acousto-ultrasonics. The multiple reflections recorded contain information about the interaction of the principal wave modes with the interfacial defects. The characterisation of these signal recordings by identifying the effect of the defect distribution on the AE features helps in the identification and classification of the defective adhesive bonds. The AE features namely the duration above a chosen threshold, the number of threshold crossings (hits) and the energy of low and high frequency components of the signal have been identified to be sensitive to the presence of both distributed defects along the interface and interfacial quality. **Figure 3.49** shows the effect of defect area percentage on the time duration and energy parameters of the recorded AE signals for different adhesive layer thicknesses. This supports the claim that AE based PLB tests could be used for defect detection in adhesively bonded joints. The curves have been fitted with either linear or curvilinear equations. It should be noted that these equations are not to be used for extrapolation beyond the tested range of defect density. In each case, the intercept corresponds to the AE parameter value from the PLB test on an adhesive bond without any defects. The equations of the fit curves in each case are shown in **Table 6.2**.

6.2. Instrumented testing of adhesive bonds

The previous section outlined the suitability of AE based PLB testing as a defect detection technique in adhesive bonds. The above methodology though gives an idea of the presence of defects, does not quantify the effect of these defects on the strength of the adhesive bond. In some cases, where the adhesive bond strength is not critical for load transmission and is

a secondary load path, it might be that the presence of a certain defect area percentage is still acceptable. Thus, the tolerance levels for the adhesive bond strength reduction due to defect growth needs to be assessed. In other words, the residual strength of the adhesive bond with a certain defect area needs to be quantified. Test methods such as single lap tensile testing have been assessed as suitable candidates for residual strength measurement [14].

In addition, several numerical studies have been conducted on the effect of defects such as voids and disbonds on the adhesive bond failure [138]. Traditionally, indentation has been used to assess the hardness and fracture toughness of materials, including other contact mechanics features. In recent years, it is being used to understand the delamination behaviour of multi-layered materials. In particular, the fracture toughness and crack propagation behaviour of thin films have been investigated using wedge indentation [38,40]. The indentation induced shear stress field is ideal to induce interfacial crack propagation in multi-layer materials. To understand the effect of interface quality itself on the interfacial crack propagation, FE analysis is best suited given the number of variables to be considered.

The crack initiation in adhesive bonds under indentation loading is because of the extrusion of the adhesive layer from underneath the indenter and outwards causing a shear stress concentration along the interface. Thus, the crack initiates under mode-II type of loading. As the crack propagates along the interface, the volume of the adhesive being extruded out of the compressive zone underneath the indenter also increases. This leads to the buckling of the adhesive layer creating a mode-I type opening of the crack faces. Thus, as the crack length increases, the mode-mix ratio taken as the ratio of the mode-II type deformation to the mode-I type deformation decreases.

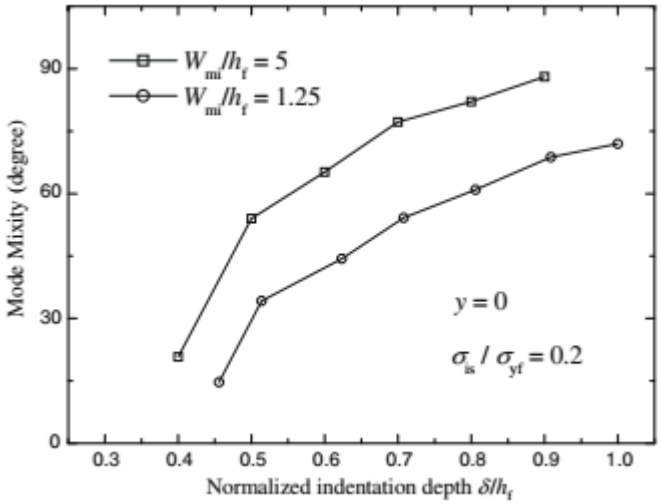

Figure 6.2. Variation of mode-mix ratio with normalised indentation depth in wedge indentation. The two plots correspond to wedge indenters of different widths [126].

This can be seen from **Fig 4.20**. This theory is confirmed by the previous research on the wedge indentation of thin films on hard substrates [29,36]. Several authors reported similar mechanisms of interfacial crack propagation under indentation loading. Furthermore, **Fig 6.2** presents the variation of the mode-mix ratio with indentation depth in thin film wedge indentation reported by She *et al* [126]. Here, the mode-mix ratio was taken as the ratio of mode-I deformation to the mode-II deformation. Thus, this agrees with the mode-mix ratio variation with crack length presented in **Fig 4.19.**

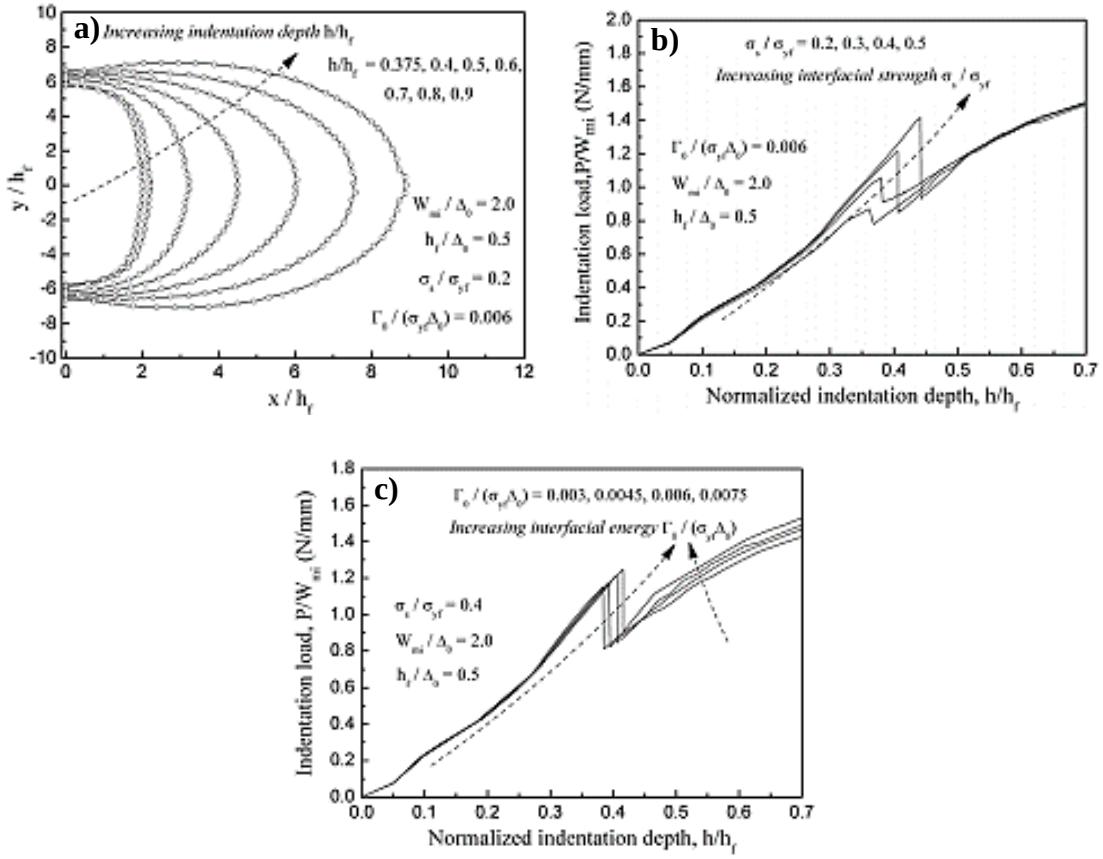

Figure 6.3.a. Variation of indentation profile with indentation depth at constant parameters and geometry, **b.** P-h curves with constant toughness and varying interfacial strength, **c.** P-h profiles with constant interfacial strength and varying toughness [30].

Previous studies on the effect of the interfacial strength on the steady state energy release rate of adhesive bonds under various loading configurations have revealed there is a linear relationship between the two [53] till a critical point is reached. However, in the mentioned studies, the interfacial strength was higher than the yield strength of the adhesive material. Hence, in such cases, high degree of plastic deformation can be expected in the adhesive layer leading to

an increase in the steady state toughness. In the present study, the interfacial strength was assumed to be lower and equal to the yield strength.

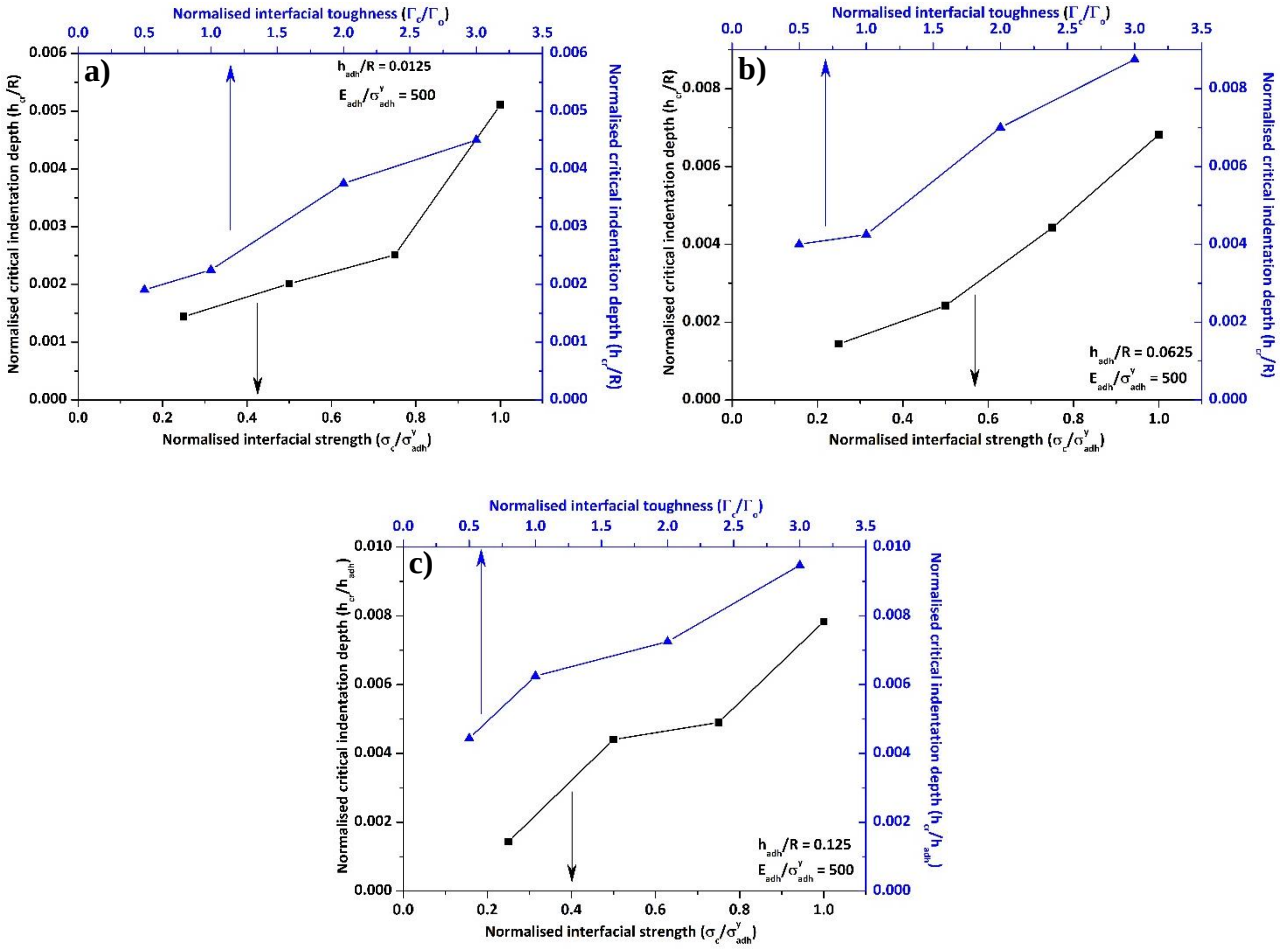

Figure 6.4. Variation of 'h_{cr}/R' with respect to 'σ_c/σ^y_{adh}' and *'Γ_c/Γ_o'* for *'hadh/R'* values of **a.** 0.0125, **b.** 0.0625, **c.** 0.125 (Indentation FEA)

Hence, except in the case of the adhesive bond with the interfacial strength equal to the yield strength, the energy release rate is equal to the toughness value assigned through the CZM. Finite element analyses of the wedge indentation of thin films have revealed a transformation of the crack propagation process from being a 2-D phenomenon to a 3-D phenomenon depending on the length of the wedge indenter under use [30]. She *et al* [126] reported that as the length of the wedge indenter increases the stress state tends towards a plane strain condition. Furthermore, the indentation depth also influences the stress state. At lower indentation depth, the stress state tends to be closer to the plane strain condition and as the depth increases, it exhibits a 3-D behaviour (**Fig 6.3**). Also, for a given interface condition, the critical indentation depth decreases with increasing indenter length which shows that the crack initiates earlier under plane strain conditions. The 2-D simulations carried out in this study were assumed to be under plane strain conditions.

Figure 6.4 shows the effect of the interfacial strength and interfacial toughness on the critical indentation depth for a given adhesive modulus and different adhesive layer thicknesses. From the plots, the interfacial strength has a more prominent effect on the crack initiation than the interfacial toughness. For example, from Fig.6.5a, increasing the normalised interfacial strength 4 times increases the normalised critical indentation depth by around 5 times, whereas increasing the normalised interfacial toughness to 6 times increases the normalised critical indentation depth by around 2.5 times. This is evident at higher adhesive layer thicknesses too.

Chen *et al* [30] reported that the interfacial strength has a significant effect on the crack initiation but not on the crack propagation. The interfacial toughness, however, affects both the crack initiation and propagation. These observations validate the findings of this study as seen from **Fig 4.24**. Increasing the interfacial strength increases the steady state toughness of crack propagation [54]. Tvergaard and Hutchinson [54] reported that for a given thickness of the adhesive layer, increasing the interfacial strength parameter of the cohesive zone model increases the deformation of the adhesive layer around the crack tip. Similar results were reported by Madhusudhana *et al* [139]. Moreover, for a given interfacial strength, increasing the adhesive layer thickness decreases the deformation zone within the adhesive layer [140]. Thus, at lower adhesive layer thickness, the peak stress zone extends till the extremities of the adhesive layer across the span of the adhesive layer whereas at higher adhesive thickness, the deformation zone surrounding the crack tip does not reach the opposite interface. Similar observations were made in the present study. **Figure 6.5** shows the deformation contours around the crack tip for similar interfacial properties and different adhesive layer thicknesses.

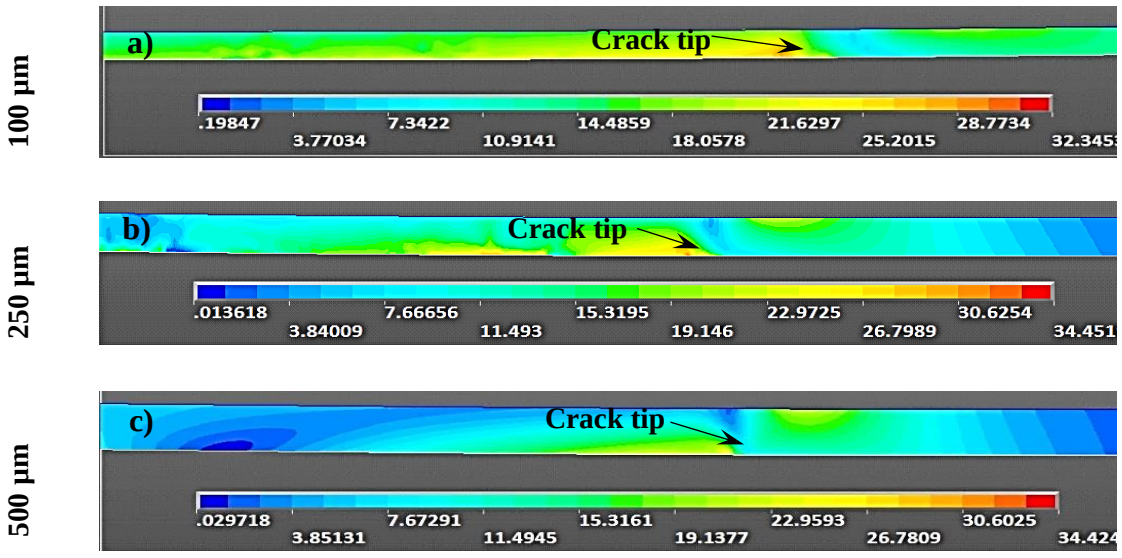

Figure 6.5. Deformation zone around the crack tip with same interfacial properties and adhesive and adherend properties for adhesive layer thicknesses **a.** 100µm, **b.** 250µm, **c.** 500µm. (Indentation FEA)

As seen, as the adhesive layer thickness increases, the deformation zone size reduces and does not reach the opposite interface. This is due to the constraining effect of the adherends on the adhesive layer deformation. At lower thicknesses, the adhesive deformation is restricted by the adherends because of their higher elastic modulus compared to the adhesive. At higher thicknesses, the constraint of the adherends reduces and hence the adhesive deformation is easier. The same can be said from the stress profiles in adhesive joints with thin and thick adhesive layers (**Fig 6.6**) during 4-point flexural analysis. At lower adhesive layer thickness, the stress profile is dominated by the constraint exerted by the adherends, whereas, at higher adhesive layer thickness, the stress distribution becomes independent of the adherend effect. The deformation mechanism of the indentation testing is outlined in the following paragraphs. The application of indentation load creates a compressive zone directly underneath the indenter. Because of the high compressive stress, the adhesive is extruded out of this zone. The lateral displacement of the adhesive induces a shear stress along the interface because of the displacement mismatch.

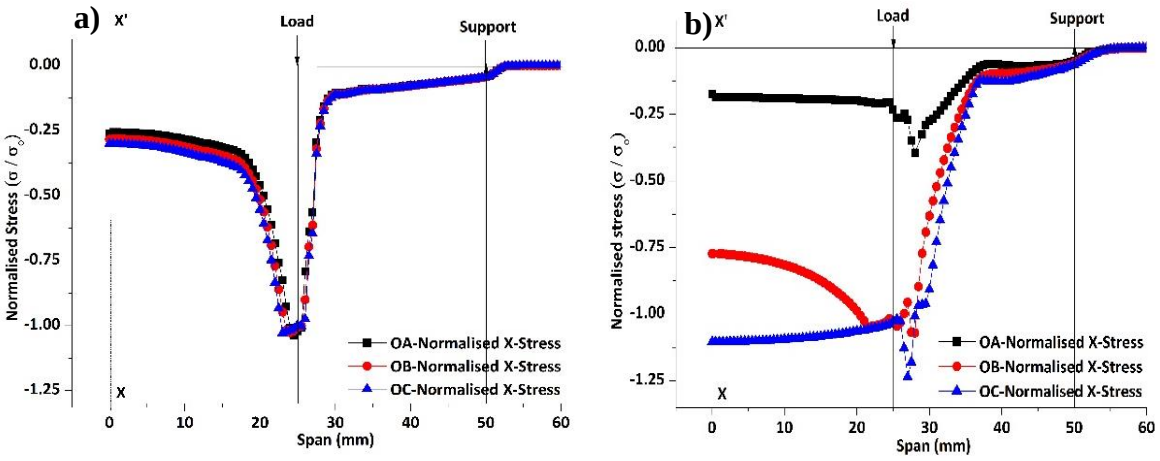

Figure 6.6. Variation of x-directional stress across the adhesive layer thickness in **a.** 100 µm thick brittle adhesive, **b.** 1500 µm thick brittle adhesive (4-point flexure FEA).

However, since the difference of elastic modulus between the adhesive and adherend material, the lower adherend does not exhibit a similar deformation. As the indentation load increases, the degree of buckling increases and the interfacial deformation shifts from shear type to opening type. This justifies the change in the mode-mix ratio with increasing indentation depth as seen in **Fig 4.20.** Furthermore, in the later stages of loading, the top adherend in combination with the adhesive undergoes flexure type loading because of the top adherend and adhesive buckling. **Figure 6.7** shows the deformation profile of indentation loaded adhesive bonds of various thicknesses.

The profiles are shown at similar crack lengths. As seen, the degree of buckling decreases with increasing adhesive layer thickness. The reason behind this is that the increase in the adhesive layer thickness increases the area of the zone that is under compressive loading upon application of the indentation load. This decreases the extrusion of the material as the deformation is spread over a larger volume.

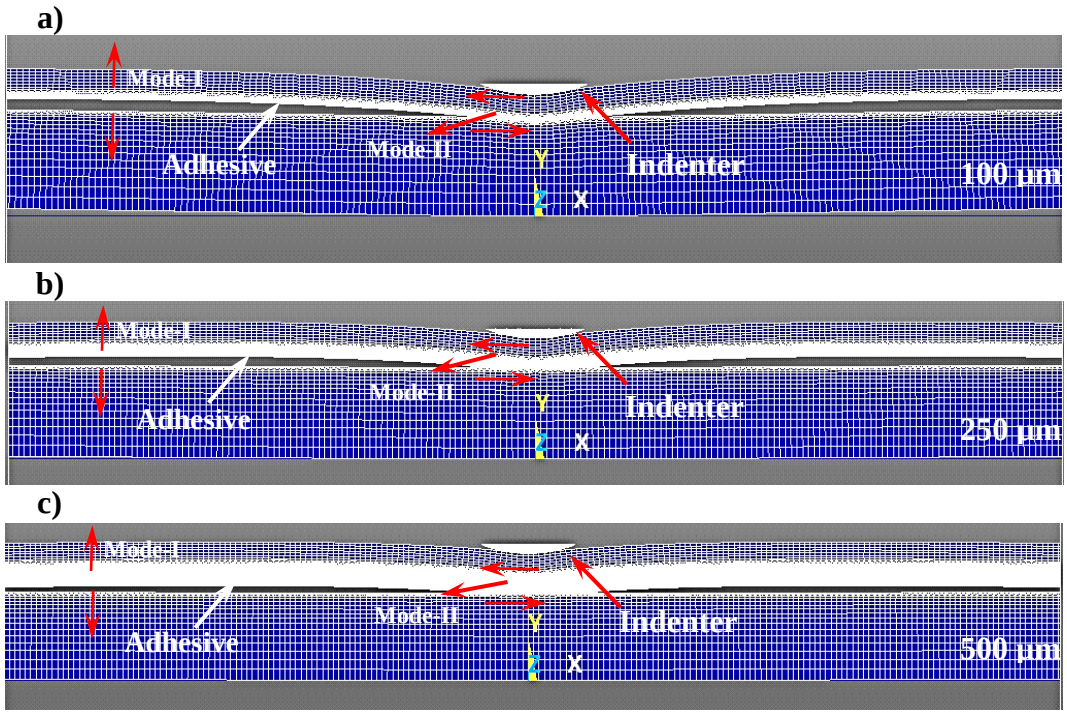

Figure 6.7. Deformation profiles showing buckling of adhesive layer for adhesive bonds with normalised adhesive thicknesses of **a.** 0.025, **b.** 0.0625, **c.** 0.125. (Indentation FEA)

The deformation of the lower adherend needs to be discussed in the context of indentation testing of adhesive bonds. Lower is this thickness, higher is the substrate depth effect on the indentation loading behaviour. This deformation is affected by the adhesive layer thickness. This can be seen from **Fig 6.7**. This figure shows the deformation profile of the lower adherend along the interface at various adhesive layer thicknesses. As seen, as the adhesive layer thickness increases, the deformation of the lower adherend decreases. It can be inferred that the adherend modulus increase also decreases the deformation of the lower adherend.

The residual strength of adhesive bonds can be directly assessed using the indentation methodology by simply comparing the load-displacement plot of a test against the corresponding plot of an adhesive bond with no interfacial bond. Though this means that a different specimen needs to be prepared, this method gives a direct assessment of the quality of the interfacial

bonding. The cumulative energy calculated from the AE record of each experiment gives the total elastic energy stored within the specimen structure. This energy value can then be used to calculate the energy release rate of the interfacial crack extension using transfer functions. In this case, delamination has been observed on both sides of the specimen in each case. The average cumulative energy for each type of specimen has been calculated and presented in **Fig 5.18**.

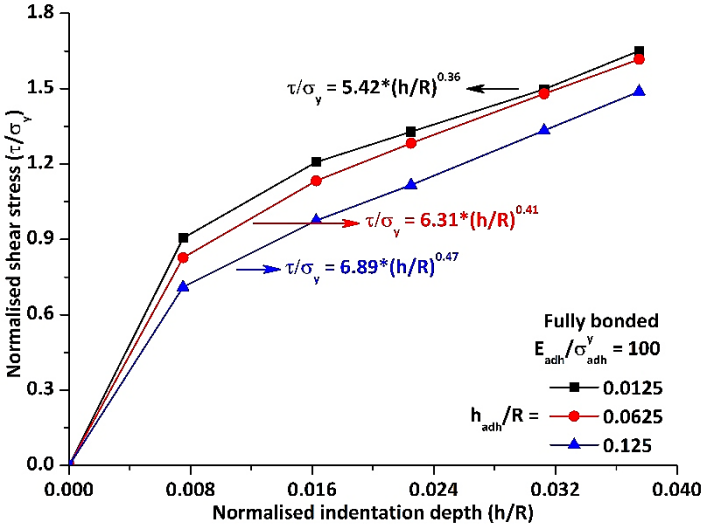

Figure 6.8. Normalised shear stress along the interface at different adhesive layer thicknesses at a given indentation depth (Indentation FEA).

This plot shows that the AE energy can be used to estimate the interfacial quality of an adhesive bond. The energy value reduces with decreasing interfacial quality in indentation specimens and increasing defect area density in flexure specimens. The differences in the cumulative energy values between the 250 µm and 500 µm thick adhesive layers were attributed to the differences in the stress states in the adhesive layer. **Figure 6.8** shows the peak normalised shear stress variation along the interface with respect to the indentation depth. The plot shows that for a given indentation depth the peak stress in the thicker adhesive layer is lower compared to that in the thinner adhesive layer. Also, at higher thickness, the adhesive tends to deform more and hence the elastic energy being transferred to the adherends is lower in this case, whereas, at a lower adhesive layer thickness, most of the load is born by the adherend which store higher elastic energy compared to the adhesive. This could be the other reason for the higher AE energy at lower adhesive layer thickness. Power law curves have been fit to the shear stress variation curves. The fit equations are shown in **Fig 6.8**. The cumulative energy values have been calculated from the lap joint tension experiments presented in *Chapter 5*. CZM simulations were then performed on models with boundary conditions corresponding to the lap joint test. The CZM parameters were tuned in each case such that the load-displacement curve from the simulation

matches the experimental curve. **Figure 6.9** shows the experimental AE cumulative energy and the corresponding energy release rate from the simulations. The AE energy has been divided by the total crack area to give an energy release rate. It should be mentioned here that the energy calculated from the AE data has arbitrary units. Since all the failed specimens exhibited total interfacial delamination in all the different specimen types, the total crack area can be taken as the total interfacial area of the specimen.

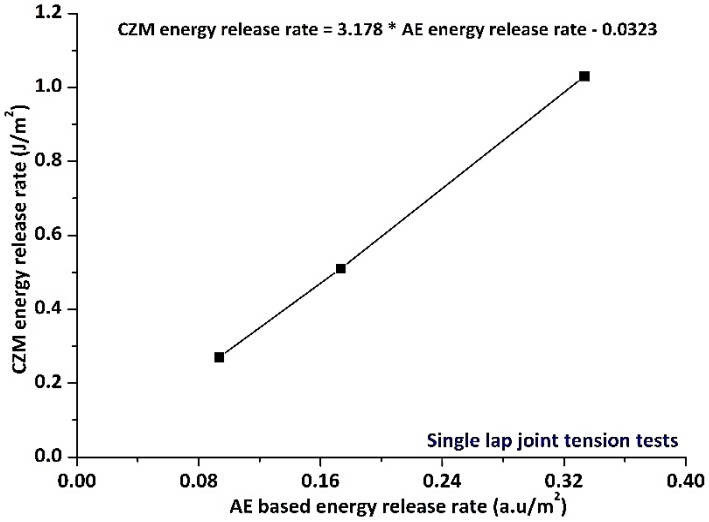

Figure 6.9. Cumulative AE energy vs energy release rate from CZM model (lap joint tension).

This plot proves that there is a direct correlation between the AE cumulative energy and the FEA calculated energy release rate. A straight line has been fit to this plot and the equation is presented in the plot itself (**Equation 6.1**).

$$CZM\ energy\ release\ rate = 3.178 * AE\ energy\ release\ rate - 0.0323$$

.....Equation 6.1

The negative intercept here does not make physical sense as a negative CZM energy release rate (Γ_o) is not be possible. Hence, it should be read as a positive x-intercept (intercept on the AE energy axis) which in an experimental condition can be associated with the signals generated by the friction, adhesive and adherend material deformation and failure in a multi-layer structure with the adherends and adhesive in-between. From **Fig 6.1** and **Fig 6.5**, the interfacial quality of an adhesive joint can be quantified using AE based PLB tests. The PLB test energy can directly correlated to the interfacial quality. Thus, the FEA based energy release rate can be related to the interfacial quality through the PLB tests. The indentation experimental method along with the AE based instrumentation can be utilised here to estimate the AE energy release rate for a given crack area. The relation presented in **Fig 6.9** can then be used to estimate a CZM

energy release rate which can then be implemented in FE based failure analysis and interfacial strength estimation. Thus, the residual strength of any adhesive bonded structure can be quantified. The flow chart (**Fig 6.10**) presents the step-by-step procedure of defect detection and residual strength estimation.

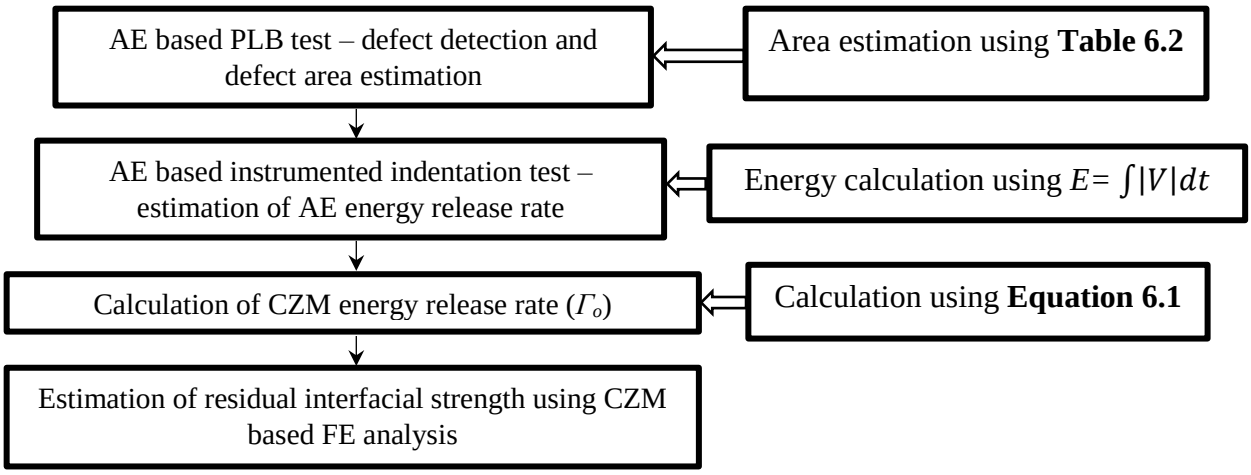

Figure 6.10. Proposed flow chart depicting defect detection and residual strength of adhesively bonded joints (metal-to-metal).

The use of PLB as an AE source to simulate failure modes in metal plates has been given little attention. Though some studies exist that use edge (in plane) and face (out of plane) PLB sources to simulate the different AE sources that emanate from material failure, this technique has not been applied in adhesive bonding to distinguish between mode-I and mode-II type crack propagation. The principal drawback in using PLB as AE source in conventional material testing is that PLB is a monopole type of signal source, whereas, the energy released due to the crack propagation inside a material is a dipole source. Hamstad [141] conducted a study on the difference between PLB based monopole sources and FE simulated dipole sources using wavelet transforms. They postulated that in most of the cases, the dipole sources (both in plane and out of plane) can be represented by PLB monopole sources on the plate edge and surface.

In adhesive bonds, three types of signal sources are possible. Interfacial and cohesive failure of the adhesive and adherend yield. The cohesive failure of the adhesive is because of void nucleation and coalescence leading to the formation of two crack faces. Hence this signal source is located within the adhesive. The interfacial failure caused by moisture ingestion begins at the edges first and penetrates the interface gradually [4]. Thus, the interfacial crack propagation is principally a monopole type source. Hence, in this study, the edge and face PLB tests have been used to simulate the mode-II and mode-I type signal sources respectively. Previously, Gorman and Prosser [142] investigated the use of in-plane and out-of-plane PLB tests on an aluminium plate to investigate the variation of the flexural and extensional wave propagation amplitudes with respect to the source angle. They found out that with the source oriented parallel to the plane

of the plate, the extensional mode is dominant, and the flexural mode is of a low amplitude. The opposite is true when the source is perpendicular to the plane of the plate. They theorised that the vector of the particle displacement responsible for wave propagation tends to be parallel to the force vector applied. The use of AE parameters to classify the failure events has previously been implemented by several studies [18,143-145]. Identification of different frequency ranges for different modes of failure has been attempted with partial success. This study is especially difficult in composites as multiple failure mechanisms exist such as matrix cracking, matrix delamination, fibre breakage, fibre pull out etc. The use of AE in adhesive bond failure characterisation has primarily been limited to the evaluation of the number of hits and the cumulative energy calculation [20,105,108,144]. To the author's knowledge no attempt has so far been made to differentiate the different crack propagation mechanisms based on the AE parameters. Thus, the present study outlines an approach towards characterising the structural and residual strength of adhesive bonds by combining instrumented mechanical testing and FE based strength evaluation methodologies. The defect detection method presented in this study is the first to utilise pencil lead breaks as signal source and AE as the signal detection technique. Finally, in this study, the use of AE signal parameters to characterise adhesive bonding failure has been proposed based on simulated mode-I and mode-II type signals.

Chapter-7

7. Conclusions and recommendations

This chapter outlines the key conclusions from the experiments and simulations, including recommendations for future work. The principal aim of this study was to device a simple methodology to detect the presence of defects and degradation along the interface of an adhesive bond and characterise the effect of the interfacial defects on the adhesive bond strength. To this end, three different methodologies have been proposed. The first using AE along with PLB tests to detect a series of small defects distributed along the interface and to detect a degraded interface, the second using 4-point flexure to characterise the strength of adhesive bonds with the defect distribution along the interface and the third using plane strain indentation (spherical) to characterise the residual strength of adhesive bonds with degraded interfaces. The conclusions from the study on each proposed methodology are presented separately.

Conclusions

Conclusions from AE-PLB defect detection in adhesive bonds

a. The AE based PLB testing can be used to differentiate between the brittle and ductile adhesive types. The signal energy can be made use of for this purpose.

b. The 200 kHz-highpass and lowpass components of the recorded signals were found to be highly sensitive to the interfacial quality. AE parameters namely energy, time duration above threshold and number of hits can be used to differentiate between defective joints with 0%, 25% and 40% defect area distribution. The reflections of the propagating signal consist of the defect related information.

c. At lower adhesive thickness, the time duration and the number of hits can be made use of in defect detection with the brittle adhesive and ductile adhesive respectively. At higher thickness, the number of hits (threshold crossings) and filtered component energies can be made use of with the brittle adhesive whereas the signal energy can be directly made use of with the ductile adhesive.

d. The AE signal energy can directly be used without any further signal processing to differentiate between adhesive bonds with an oil film (simulated moisture ingested interface) along the interface and adhesive bonds with a strong interfacial bond. The energy calculated is of the entire signal record including all the reflections.

e. The configuration with the source and sensor on the thinner (i.e. 0.5 mm thick) adherend side of the specimen was found to be the best to detect interfacial defects. Relations between AE parameters and defect densities were derived.

Conclusions from FE analysis

a. The flexure simulations assume perfect bonding across the interface. Analysis of the stress states along the interfaces reveals the failure initiation location to be near the loading points. The high stress state extends through the thickness of the adhesive layer and till the extremes of the constant bending moment zone, at lower adhesive layer thicknesses. Hence failure, after initiation at the loading points, is expected to propagate fast towards the centre of the specimen.
b. Adherend constraint plays a major role in determining the stress state in the adhesive layer at lower adhesive layer thickness. Increasing the thickness reduces the constraint because of increased flexibility.
c. Plane strain (spherical) indentation testing was found to be highly sensitive to variation in the interfacial strength and toughness. In addition, this methodology is sensitive to the adhesive modulus and thickness.
d. Failure of the adhesive bond is primarily because of the extrusion of the adhesive material from underneath the indenter away from the centreline leading to shear strain accumulation along the interface and consequent interfacial delamination. Increase in the interfacial strength, toughness and thickness has a retarding effect on the crack initiation. Increase in the modulus, however, has the opposite effect.
e. The crack propagation under indentation loading in the initial stages is of mode-II in nature and shifts to mode-I behaviour in later stages of loading. This behaviour is predominant at lower adhesive layer thicknesses.

Conclusions from experimentation and correlation

a. Both the instrumented indentation (spherical) testing and instrumented flexural (4-point) testing were found to be sensitive to the presence of defects along the interface. Flexural testing however did not exhibit differences in the failure displacement. However, cumulative AE energy can be used as the distinguishing parameter between various defective adhesive joints.
b. The use of PLB tests to simulate the mode-I and mode-II type signals led to classification of crack propagation mechanisms. Mode-II type failure was found to be dominant in both indentation and flexure testing.

c. Increasing the adhesive layer thicknesses decreases the AE cumulative energy released. This is associated with the stress states observed from the FE simulations.
d. The degradation of the interface simulated by introduction of oil film led to decrease in crack initiation load under indentation loading thus showing that this test methodology can be used to quantify the residual strength of adhesive bonds.
e. A correlation has been drawn between the CZM energy (Γ_o) and the AE energy release rate. This correlation can be used in estimating the residual interfacial strength of defective adhesive bonds.

Recommendations

Sensor based instrumented measurement and metrology (possibly combined test methodologies, both non-destructive and semi-destructive) is an important proposition for future re-use or recycling of adhesive joint structures. Such structures can provide numerous failure sites and it may become difficult to track and examine the quality or residual strength by conventional standardised tests. Overall aim of any future framework model development should be developing novel diagnostic tool for enhanced characterisation of adhesive joints for re-use applications. This will be an important step towards development of adhesive joint decommissioning strategy and policy. The study will further help in a review and preparation of worldwide strategy for decommissioning of various structures, potentially addressing recycling and re-use technologies and associated manufacturing challenges.

1. The applicability of PLB-AE (in combination with other sensing techniques) defect detection technique needs to be evaluated over specimens of different materials and dimensions. The present study evaluates the suitability of the technique for two different adhesives and different adhesive layer thicknesses. Though the adhesive thicknesses chosen are within the range of what is being presently used in the industry, the study of the effect of higher adhesive layer thicknesses on the effectiveness of the technique would be beneficial.
2. The use of indentation testing needs to be evaluated over a wider range of specimen sizes. The effect of the specimen dimensions and the indenter radius needs to be evaluated. Similarly, the adherend thickness effect on the stress distribution along the adhesive-adherend interfaces needs to be studied.
3. Research work while using fully instrumented mechanical testing for other types of adhesively bonded joints (e.g. metal-to-composite, composite-to-composite during mode-I, mode-II, mixed-mode) can be a part of future work.
4. Application of self-healing adhesives in above testing procedures can also be part of further work.

Appendix - A

Acoustic emission sensor

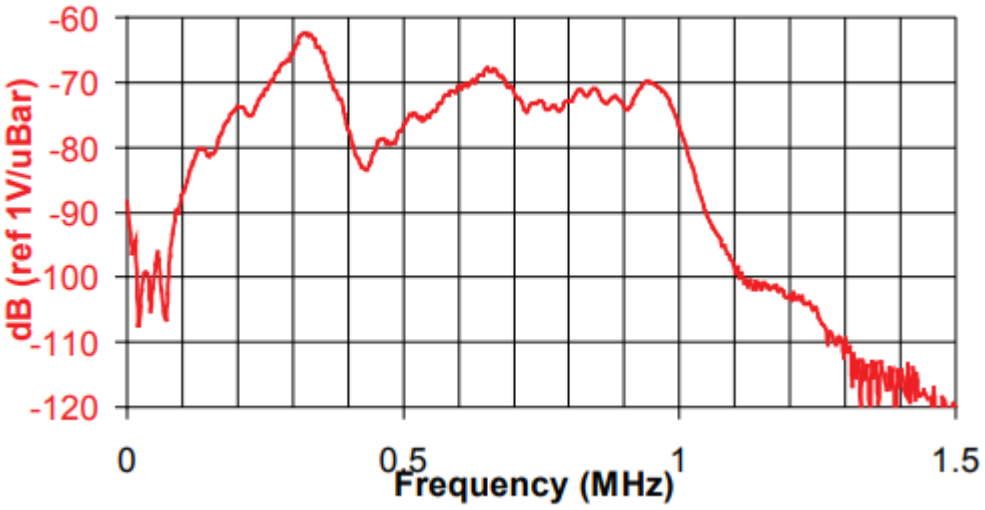

Figure A1. AE sensor calibration curve

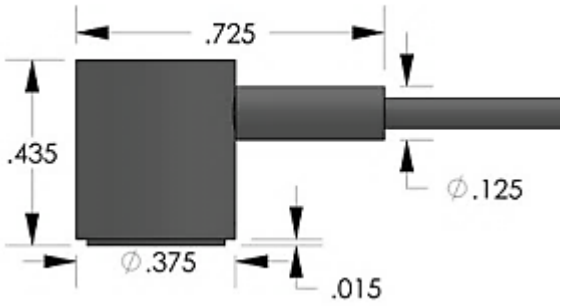

Figure A2. AE sensor dimensions

Appendix - B

VI used for AE based PLB testing

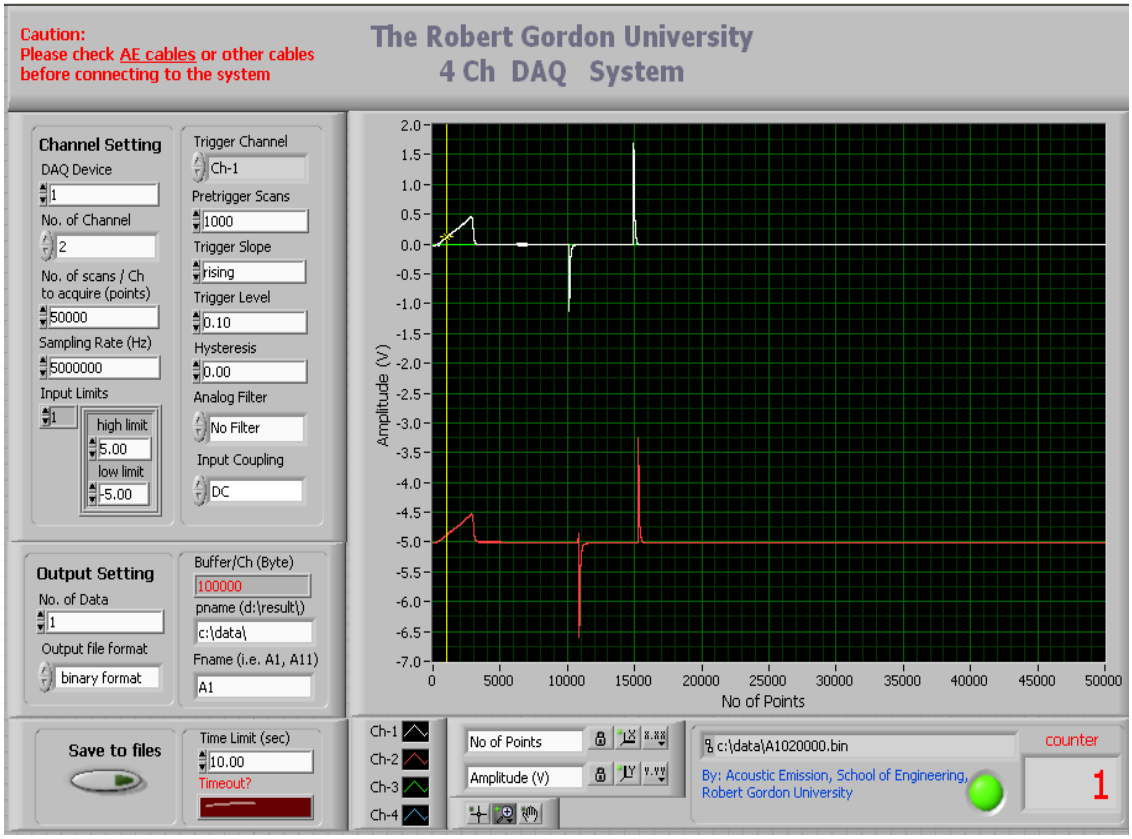

Figure B1. VI used for AE based PLB tests for defect detection

The above picture shows the snapshot of the VI that was used for the AE PLB testing of the adhesive bonds. This VI is capable of recording data at the chosen sampling rate. The trigger level, the number of pre-trigger data points for each channel and the number of data points that need to be recorded can be chosen along with the file storage path. The trigger channel can also be chosen. The output is stored as .bin files. This VI can record data only for one second at a time. The data transfer from the buffer storage to the data storage location takes another second and hence this VI cannot be used for continuous data recording.

Appendix - C

Experimental setup

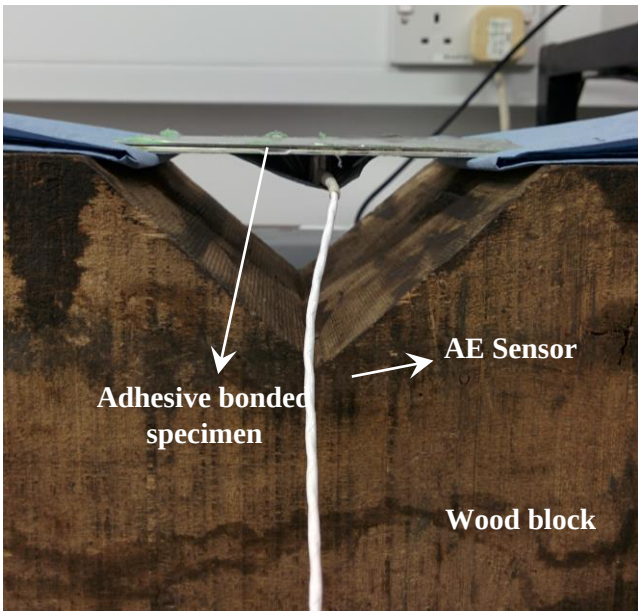

Figure C1. PLB test specimen set up

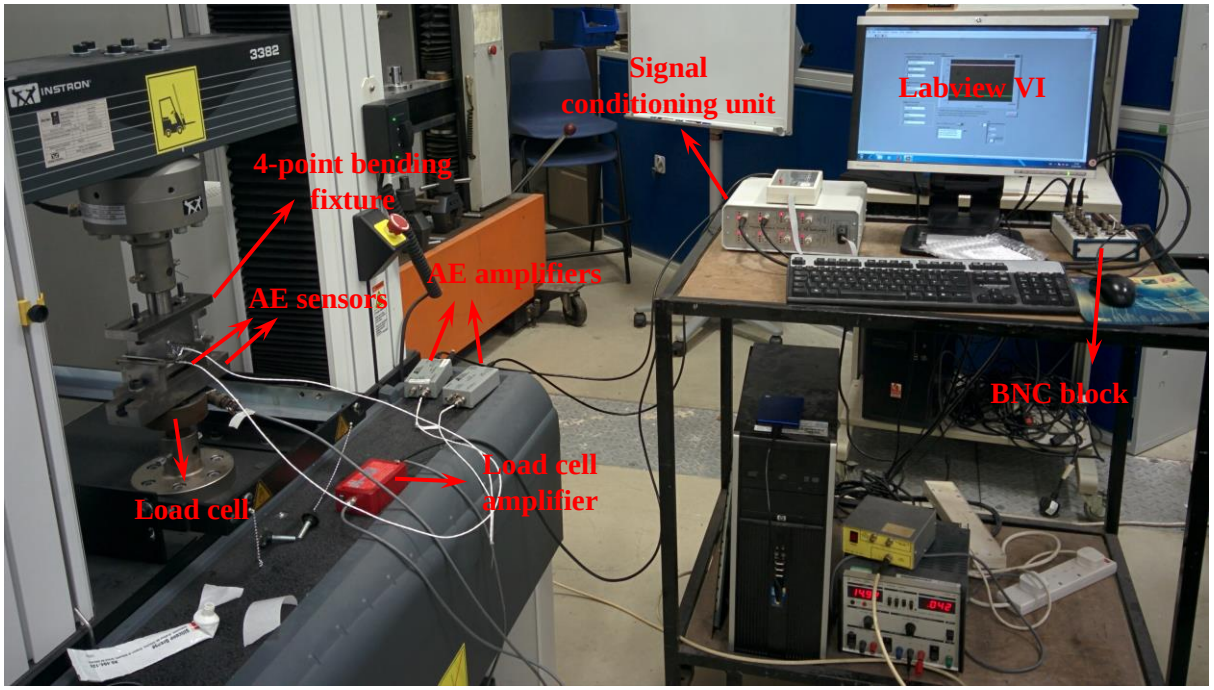

Figure C2. Experimental setup with the different components indicated

Appendix - D

Matlab code used for data analysis and signal classification

```
clear all;
pname='E:\MATLAB\Matlab_progs\Data\New Sensors\Brittle adhesive\100
microns\1.5-0.1-0.5-40%\';
l=6;
for i=1:l
    source_dir = sprintf('%s%d%s', pname,i,'\');
    source_files = dir(fullfile(source_dir, '*.bin'));
    n=length(source_files);
    for k=1:n
        fname=source_files(k).name;
        fname2=[source_dir fname];
        fid = fopen(fname2,'r','b');
        para=fread(fid,4,'float');
        fs=para(4);
        fseek(fid,16,'bof');
        a = fread(fid,inf,'float');
        fclose(fid);
        clear fid;
        j=1;
        ndata=length(a)/para(1);
        for m=1:para(1):ndata
            n=1;
            for t=m:(m+para(1)-1)
                y(j,n)=a(t);
                n=n+1;
            end
            j=j+1;
        end
        clear j t n m;
        ndata = length(a);
        x = 0:1/fs:(ndata-1)/fs;
        x = x';
        g31 = 20; % Gain at SCU.0
        g32= 0;
        for m = 1:para(1)
            y(:,m)=y(:,m)/((10^(g32/20))*(10^(g31/20)));
            for j=1:10
                avg=(max(y(200:600,m))+min(y(200:600,m)))/2;
                y(:,m)=y(:,m)-avg;
            end
            clear j;
            s=max(abs(y(:,m)));
```

```
param(num,1,m)=s;
threshold=s*0.02;rise=0;fall=0;index_at_max=0;
for j=2:(10000)
if((abs(y(j,m))<=threshold) && (abs(y(j+1,m))>threshold))
   rise=rise+1;
   risetime(rise)=j;
elseif((abs(y(j,m))>threshold) && (abs(y(j+1,m))<=threshold))
   fall=fall+1;
   falltime(fall)=j;
end
end
param(num,2,m)=(falltime(length(falltime))-risetime(1))/fs;
for j=1:(ndata-1)
    if (abs(y(j)) == max(abs(y)))
        index_at_max=j;
    end
    if (index_at_max~=0)
        break;
    end
end
rise_time(i,k)=(index_at_max-risetime(1))/fs;
fall_time(i,k)=(falltime(length(falltime))-index_at_max)/fs;
Hd1=Cheby_2M_50K_Lowpass;
Hd2=Cheby_2M_50K_200K;
Hd3=Cheby_2M_200K_Highpass;
y11(:,m)=filter(Hd1,y(:,m));
y12(:,m)=filter(Hd2,y(:,m));
y13(:,m)=filter(Hd3,y(:,m));
energy(i,k,m)=trapz_r2(y(1:7000,m))*(1/fs);
energy1(i,k,m)=trapz_r2(y11(1:7000,m))*(1/fs);
energy2(i,k,m)=trapz_r2(y12(1:7000,m))*(1/fs);
energy3(i,k,m)=trapz_r2(y13(1:7000,m))*(1/fs);
 param(num,4,m)=max(abs(y11(:,m)))/max(abs(y12(:,m)));
%             param(num,5,m)=param(num,2,m)/param(num,1,m);
%             param(num,5,m)=max(abs(y12(:,m)));
 tname=sprintf('%s%d%s%s',source_dir,m,fname,'.txt');
 fid = fopen(tname,'wt');
fseek(fid,0,'eof');
fprintf('\n');
fprintf(fid,'%g\n',1/fs);
fprintf(fid,'%d\n',15000);
for j = 1:15000
    fprintf(fid,'%g\n',y(j,m));
end
status=fclose('all');
```

```
            baseFileName1 = sprintf('Figure_%d%d%d.jpg',m,k,1);
            baseFileName2 = sprintf('Figure_%d%d%d.jpg',m,k,2);
            fullFileName1 = [source_dir baseFileName1];
            fullFileName2 = [source_dir baseFileName2];
           [pyy,f] = pwelch(y(1:15000,m),[],[],4098,fs);%Matlab 6.5 (R13)
            p1=plot(f,pyy);
            set(gca,'fontsize',18);
            title('Power spectral density');
            xlabel('frequency (Hz)');
             ylabel('PSD');
            grid on
            saveas(p1,fullFileName1)
            p2=plot(x(1:15000),y(1:15000,m));
            set(gca,'fontsize',18);
            title('Signal');
            xlabel('Time(s)');
            ylabel('Voltage(V)');
            grid on
            saveas(p2,fullFileName2)
            clear index_at_max risetime falltime;
        end
        %         num=num+1;
        clear fid fs status a para y x y1 y11 y12 y13 avg fname2 f pyy;
    end
    average(i,1)=mean(energy(i,:));
    average(i,2)=std(energy(i,:));
    average1(i,1)=mean(energy1(i,:));
    average1(i,2)=std(energy1(i,:));
    average2(i,1)=mean(energy2(i,:));
    average2(i,2)=std(energy2(i,:));
    average3(i,1)=mean(energy3(i,:));
    average3(i,2)=std(energy3(i,:));
end
ptsymb = {'bs','r^','md','go','c+'};
[cidx1,cmeans1] = kmeans(param(:,3:5,1),2,'dist','sqeuclidean');
figure
for i = 1:2
    clust1 = find(cidx1==i);
     plot3(param(clust1,3,1),param(clust1,4,1),param(clust1,5,1),ptsymb{i});
hold on
end
grid on
hold off
[cidx2,cmeans2] = kmeans(param(:,3:5,2),2,'dist','sqeuclidean');
figure
```

```
for i = 1:2
     clust2 = find(cidx2==i);
       plot3(param(clust2,3,2),param(clust2,4,2),param(clust2,5,2),ptsymb{i});
       hold on
end
grid on
hold off
```

Appendix - E

Load cell calibration plot

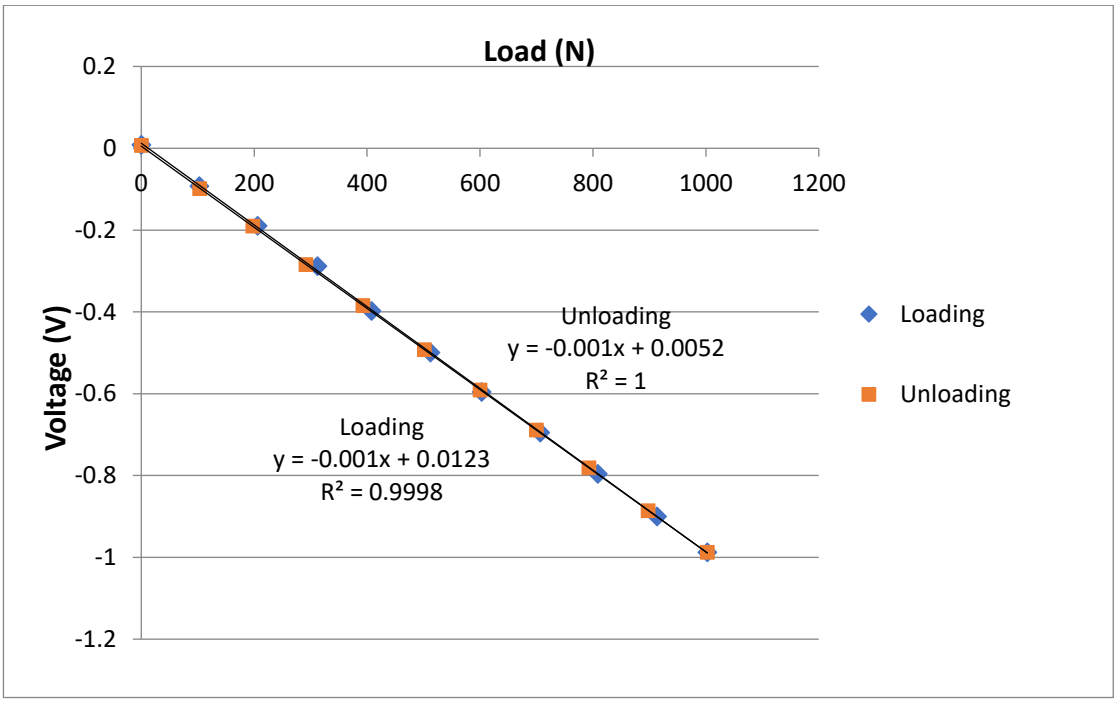

Figure E1. Load cell calibration plot

The above plot shows the calibration curve of the load cell. The calibration was done under compression loading as the intended use of the load cell is under compression. The load was applied using an Instron 3385 machine. The load was applied in steps of 100N and the voltage output from the load cell was recorded at each step continuously over a minute. The average value of the voltage was then calculated thus giving the above plot. This procedure was repeated under both loading and unloading. As shown, the fit to the calibration data was a perfect straight line with an excellent R^2 value.

Appendix - F

VI used for flexure and indentation experiments

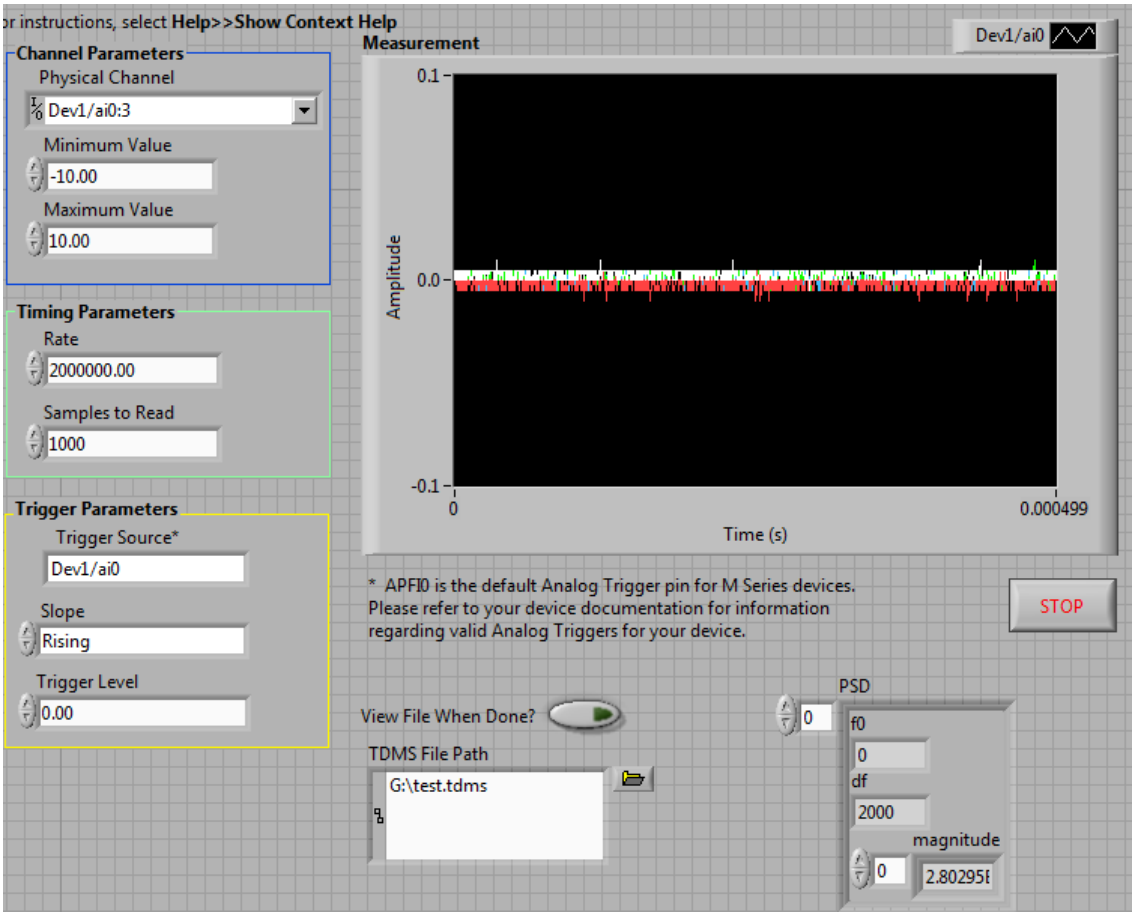

Figure F1. VI used for indentation and flexure experiments

The above picture shows the VI that was used for the experimental testing of the adhesive bonds. The AE in addition to the load were recorded over the entire experiment. This VI outputs data in .tdms format. The VI has options to choose the data acquisition rate, the trigger channel and the data storage path.

References

[1] L.J. Hart-Smith, "Adhesive-bonded double lap joints," 1973.

[2] F Benyahia, F M Bounani, A Albedah, B B Bouiadjra, and T Achour, "Effect of water adsorption on the adhesive damage in bonded composite repair of aircraft structures," *Materials and Design*, vol. 57, pp. 435-441, 2014.

[3] T de Frietas, M D Banea, S Budhe, and S de Barros, "interface adhesion assessment of composite-to-metal bonded joints under salt spray conditions using peel tests," *Composite Structres*, article in press.

[4] P Hu, X Han, W.D Li, L Li, and Q Shao, "Research on the static strength performance of adhesive lap joints subjected to extreme temperature for automotive industry," *International Journal of Adhesion & Adhesives*, vol. 41, pp. 119-126, 2013.

[5] B R K Blackman, A J Kinloch, and M Paraschi, "The determination of the mode II adhesive fracture resistance, GIIc, of structural adhesive joints: an effective crack length approach," *Engineering Fracture Mechanics*, vol. 72, no. 6, pp. 877-897, 2005.

[6] B Blackman, J P Dear, A J Kinloch, and S Osiyemi, "The calculation of adhesive fracture energies from double-cantilever beam test specimens," *Journal of Materials Science Letters*, vol. 10, no. 5, pp. 253-256, 1991.

[7] H C Cao and H G Evans, "An experimental study of fracture resistance of bi-material interfaces," *Mechanics of Materials*, vol. 7, pp. 295-304, 1989.

[8] H Chai, "On teh correlation between the mode-I failure of adhesive joints and laminated composites," *Engineering Fracture Mechanics*, vol. 24, no. 3, pp. 413-431, 1986.

[9] F Ducept, P Davies, and D Gamby, "Mixed mode criteria for a glass/epoxy composite and an adhesively bonded composite/composite joint," *International Journal of Adhesion & Adhesives*, vol. 20, pp. 233-244, 2000.

[10] P Feraboli and K.T Kedward, "Four-point bend interlaminar shear testing of uni- and multi-directional carbon/epoxy composite systems," *Composites: Part A*, vol. 34, pp. 1265-1271, 2003.

[11] M Wang, A Liu, Z Liu, and P -C Wang, "Effect of hot humid environmental exposure on fatigue crack growth of adhesively bonded aluminium A356 joints," *International Journal of Adhesion & Adhesives*, vol. 40, pp. 1-10, 2013.

[12] F M F Ribeiro, R D S G Campilho, R J C Carbas, and L F M Da Silva, "Strength and damage growth in composite bonded joints with defects," *Composites Part B*, vol. 100, pp. 91-100, 2016.

[13] W Xu and Y Wei, "Strength analysis of metallic bonded joints containing defects," *Computational Materials Science*, vol. 53, pp. 444-450, 2012.

[14] E F Karachalios, R D Adams, and Lu F M Da Silva, "Strength of single lap joints with artificial defects," *International Journal of Adhesion & Adhesives*, vol. 45, pp. 69-76, 2013.

[15] J Galy, J Moysan, A E Mahi, Noellie Ylla, and Nicolas Massacret, "Controlled reduced-strength epoxy-aluminium joints validated by ultrasonic and mechanical measurements," *International Journal of Adhesion & Adhesives*, 2016.

[16] L Michalkova and M Kadlec, "Carbon/Epoxy composite delamination analysis by acoustic emission method under various environmental conditions," *Engineering Failure Analysis*, vol. 69, pp. 88-96, 2016.

[17] J J Andrew, V Arumugam, D J Bull, and H.N Dhakal, "Residual strength and damage characterisation of repaired glass/epoxy composite laminates using A.E and D.I.C," *Composite Structures*, vol. 152, pp. 124-139, 2016.

[18] C Baker, G N Morscher, V V Pujar, and J R Lemanski, "Transverse cracking in carbon fiber reinforced polymer composites: Modal acoustic emission and peak frequency analysis," *Composites Science and Technology*, vol. 116, pp. 26-32, 2015.

[19] C J Brotherhood, B W Drinkwater, and S Dixon, "The detectability of kissing bonds in adhesiev joints using ultrasonic techniques," *Ultrasonics*, vol. 41, no. 7, pp. 521-529, 2003.

[20] A J Brunner, G P Terrasi, T V Allee, and T Keller, "Acoustic emission analysis and acousto-ultrasonics for damage detection in GFRP adhesive joints," in *28th European conference on AE testing*, 2008.

[21] M Castaings, D Singh, and P Viot, "Sizing of impact damage in composite materials using ultrasonic guided waves," *NDT&E International*, vol. 46, pp. 22-31, 2012.

[22] S De Barros, A L Gama, M Rousseau, and B Collet, "Characterisation of bonded plates with Lamb and SH waves using a quasi-static approximation," *Latin American Journal of Solids and Structures*, vol. 1, pp. 379-399, 2004.

[23] L Goglio and M Rosetto, "Ultrasonic testing of adhesive bonds of thin metal sheets," *NDT&E International*, vol. 32, pp. 323-331, 1999.

[24] Y Xu, R Chen, Z Liu, and C Shao, "An acousto-optical fibre NST technique for interfacial debonding detection in FRP-retrofitted structures," *NDT&E International*, vol. 72, pp. 50-57, 2015.

[25] K Heller, L J Jacobs, and J Qu, "Characterisation of adhesive bond properties using lamb waves," *NDT&E International*, vol. 33, pp. 555-563, 2000.

[26] G R Markus Sause, "Investigation of pencl-lead breaks as acoustic emission sources," *Journal of Acoustic Emission*, vol. 29, pp. 184-196, 2011.

[27] ASTM E976-15, "Standard guide for determining the reproducibility of acoustic emission sensor response".

[28] K Senthil, A Arockiarajan, and R Palaninathan, "Experimental determination of fracture toughness for adhesively bonded composite joints," *Engineering Fracture Mechanics*, vol. 154, pp. 24-42, 2016.

[29] H Chai, "Fracture mechanics analysis of thin coatings under plane-strain indentation," *International Journal of Solids and Structures*, vol. 40, pp. 591-610, 2003.

[30] L Chen, K B Yeap, C M She, and G R Liu, "A computational and experimental investigation of three-dimensional micro-wedge indentation-induced interfacial delamination in a soft-film-on-hard-substrate system," *Engineering Structures*, vol. 33, pp. 3269-3278, 2011.

[31] M Desaeger and I Verpoest, "On the use of micro-indentation test technique to measure the interfacial shear strength of fibre-reinforced polymer composites," *Composites Science and Technology*, vol. 48, pp. 215-226, 1993.

[32] N H Faisal, R Ahmed, and R L Reuben, "Indentation testing and it's acoustic emission response: applications and emerging trends," *International Materials Review*, vol. 4, no. 2, pp. 98-142, 2011.

[33] Y Gu, T Nakamura, L Prchlik, S Sampath, and J Wallace, "Micro-indentation and inverse analysis to characterise elastic-plastic graded materials," *Materials Science and Engineering*, vol. A345, pp. 223-233, 2003.

[34] H Ho and L T Drzal, "Evaluation of interfacial mechanical properties of fibre reinforced composites using microindentation method," *Composites Part A*, vol. 27, pp. 961-971, 1996.

[35] K Sriram, R Narasimhan, and S K Biswas, "A numerical fracture analysis of indentation into thin hard films on soft substrates," *Engineering Fracture Mechanics*, vol. 70, pp. 1323-1338, 2003.

[36] P Liu, Y W Zhang, K Y Zeng, C Lu, and K Y Lam, "Finite element analysis of interface delamination and buckling in thin film systems by wedge indentation," *Engineering Fracture Mechanics*, vol. 74, pp. 1118-1125, 2007.

[37] M J Matthewson, "Axi-symmetric contact on thin compliant coatings," *Journal of Mechanics and Physics of Solids*, vol. 29, no. 2, pp. 89-113, 1981.

[38] M Zhao, H Liu, C Fan, E Pan, and T Zhang, "Indentation stress in multi-layer delaminated thin film induced by a microwedge indenter," *Composites Part B*, vol. 45, pp. 845-851, 2013.

[39] S Mustapha, L Ye, X Dong, and M M Alamdari, "Evaluation of barely visible indentation damage (BVID) in CF/Ep sandwich composites using guided wave signals," *Mechanical Sysytems and Signal Processing*, vol. 76-77, pp. 497-517, 2016.

[40] Y Xiao, W Shi, and J Luo, "Indentation for evaluating cracking and delamination of thin coatings using finite element method," *Vacuum*, vol. 122, pp. 17-30, 2015.

[41] M Goland and E Reissner, "The stresses in cemented joints," *Journal of Applied Mechanics*, vol. 11, no. 1, pp. 17-27, 1944.

[42] H Adin, "The investigation of the effect of the angle on the failure load and strength of scarf lap joints," *International Journal of Mechanical Sciences*, vol. 61, pp. 24-31, 2012.

[43] S Azari, A Ameli, M Papini, and J K Spelt, "Adherend thickness influence on fatigue behaviour and fatigue failure prediction of adhesively bonded joints," *Composites: Part A*, vol. 48, pp. 181-191, 2013.

[44] S Azari, M Papini, and J K Spelt, "Effect of adhesive thickness on fatigue and fracture of toughened epoxy joints - Part I: Experiments," *Engineering fracture mechanics*, vol. 78, pp. 153-162, 2011.

[45] R D S G Campilho, D C Moura, M D Banea, and L F M da Silva, "Adherend thickness effect on the tensile fracture toughness of a strucutural adhesive using an optical data acquisition method," *International Journal of Adhesion & Adhesives*, vol. 53, pp. 15-22, 2014.

[46] H Dan, T Sawa, T Iwamoto, and Y Hirayama, "Stress analysis and strength evaluation of scarf adhesive joints subjected to static tensile loadings," *International Journal of Adhesion & Adhesives*, vol. 30, pp. 387-392, 2010.

[47] L D R Grant, L D R Adams, and L F M Da Silva, "Experimental and numerical analysis of single-lap joints for the automotive industry," *International Journal of Adhesion & Adhesives*, vol. 29, pp. 405-413, 2009.

[48] N A Fleck, J W Hutchinson, and Z Suo, "Crack path selection in a brittle adhesive layer," *International Journal of Solids and Structures*, vol. 27, no. 13, pp. 1683-1703, 1991.

[49] M S Kafkalidis, M D Thouless, and Q D Yang, "Deformation and fracture of adhesive layers constrained by plastically deforming adherends," *Journal of Adhesion Science and Technology*, vol. 14, no. 13, pp. 1593-1607, 2000.

[50] T Pardoen, T Ferracin, C M Landis, and F Delannay, "Constraint effects in adhesive joint fracture," *Journal of Mechanics and Physics of Solids*, vol. 53, pp. 1951-1983, 2005.

[51] V Tvergaard and J W Hutchinson, "On the toughness of ductile adhesive joints," *Journal of Mechanics and Physics of Solids*, vol. 44, no. 5, pp. 789-800, 1996.

[52] H Chai, "Observation of deformation and damage at the tip of cracks in adhesive bonds loaded in shear and assessment of a criterion for fracture," *International Journal of Fracture*, vol. 60, no. 4, pp. 311-326, 1993.

[53] V Tvergaard, "Resistance curves for mixed mode interface crack growth between dissimilar elastic-plastic solids," *Journal of Mechanics and Physics of Solids*, vol. 49, pp. 2689-2703, 2001.

[54] V Tvergaard and John W. Hutchinson, "The influence of plasticity on mixed mode interface toughness," *Journal of Mechanics and Physics of Solids*, vol. 41, no. 6, pp. 1119-1135, 1993.

[55] Q D Yang, M D Thouless, and S.M. Ward, "Numerical simulations of adhesively bonded beams failing with extensive plastic deformation," *Journal of Mecahnics and Physics of Solids*, vol. 47, pp. 1337-1353, 1999.

[56] C Buo and D A Dillard, "The effect of T-stress on crack path selection in adhesively bonded joints," *International Journal of Adhesion and Adhesives*, vol. 21, pp. 357-368, 2001.

[57] H Chai, "A note on trajectory in an elastic strip bounded by rigid substrates," *International Journal of Fracture*, vol. 32, pp. 211-213, 1987.

[58] G Jhin et al., "Crack growth rate and crack path in adhesively bonded joints: Comparison of creep, fatigue and fracture," *International Journal of Adhesion & Adhesives*, vol. 46, pp. 74-84, 2013.

[59] A Ameli, S Azari, M Papini, and J K Spelt, "Crack path selection in the fracture of fresh and degraded epoxy adhesive joints," *Engineering Fracture Mechanics*, vol. 78, pp. 1986-2003, 2011.

[60] B Chen and D A Dillard, "The effect of T-stress on crack path selection in adhesively bonded joints," *International journal of adhesion & adhesives*, vol. 21, pp. 357-368, 2001.

[61] Z Q Qian, "On the evaluation of wedge corner stress intensity factors of bi-material joints with surface tractions," *Composites and Structures*, vol. 79, pp. 53-64, 2001.

[62] W Xu and Y Wei, "influence of adhesive thickness on local interface fracture and overall strength of metallic adhesive bonding structures," *International journal of adhesion & adhesives*, vol. 40, pp. 158-167, 2013.

[63] S Yang, W Xu, L Liang, T Wang, and Yueguang Wei, "An experimental study on the dependence of the strength of adhesively bonded joints with thickness and mechanical

properties of the adhesives," *Journal of Adhesion Science and Technology*, vol. 28, no. 11, pp. 1055-1071, 2014.

[64] R O Shah and M Tarfaoui, "Effect of adhesive thickness on the mode I and II strain energy release rates. Comparative study between different approaches for the calculation of Mode I & II SERR's," *Composites Part B*, vol. 96, pp. 354-363, 2016.

[65] K Naito, M Onta, and Y Kogo, "The effect of adhesive thickness on tensile and shear strength of polyimide adhesive," *International Journal of Adhesion & Adhesives*, vol. 36, pp. 77-85, 2012.

[66] L Liao, C Huang, and T Sawa, "Effect of adhesive thickness, adhesive type and scarf angle on teh mechanical properties of scarf adhesive joints," *International Journal of Solids and Structures*, vol. 50, pp. 4333-4340, 2013.

[67] P Davies et al., "Influence of adhesive bond line thickness on joint strength," *International Journal of Adhesion & Adhesives*, vol. 29, pp. 724-736, 2009.

[68] S Marzi, A Biel, and U Stigh, "On experimental methods to investigate the effect of layer thickness on the fracture behavior of adhesively bonded joints," *International Journal of Adhesion & Adhesives*, vol. 31, pp. 840-850, 2011.

[69] G Ji, Z Ouyang, Guoqiang Li, Samuel Ibewke, and Su-Seng Pang, "Effects of adhesive thickness on global and local mode-I interfacial fracture of bonded joints," *international journal of solids and structures*, vol. 47, pp. 2445-2458, 2010.

[70] M Lee, C H Wang, and E Yeo, "Effects of adherend thickness and taper on adhesive bond strength measured by portable pull-off tests," *International Journal of Adhesion & Adhesives*, vol. 44, pp. 259-268, 2013.

[71] M D Thouless et al., "Determining the toughness of plastically deforming joints," *Journal of Materials Science*, vol. 33, pp. 189-197, 1998.

[72] S Azari, A Ameli, M Papini, and J K Spelt, "Adherend thickness influence on fatigue behaviour and fatigue failure prediction of adhesively bonded joints," *Composites Part A*.

[73] E D Reedy Jr, "Cpnnection between interface corner and interfacial fracture analyses of and adhesively-bonded butt joint," *International Journal of Solids and Structures*, vol. 37, pp. 2429-2442, 2000.

[74] E R Reedy Jr and T R Guess, "Comparison of butt tensile strength data with corner stress intensity factor prediction," *International Journal of Solids and Structures*, vol. 30, no. 21, pp. 2929-2936, 1993.

[75] R D Adams and P Cawley, "defect types and non-destructive techniques for composites and bonded joints," *Construction & Building Materials*, vol. 3, no. 4, pp. 170-182, 1989.

[76] L D R Grant, R D Adams, and L F M Da Silva, "Effect of the temperature on the strength of adhesively bonded single lap and T joints for the automotive industry," *International Journal of Adhesion and Adhesives*, vol. 29, no. 5, pp. 535-542, 2009.

[77] F Zhang et al., "Experimental study of initial strengths and hygrothermal degradation of adhesive joints between thin aluminium and steel substrates," *International Journal of Adhesion & Adhesives*, vol. 43, pp. 14-25, 2013.

[78] G Viana, M Costa, M D Banea, and L F M da Silva, "Moisture and temperature degradation of double cantilever beam adhesive joints," *Journal of adhesion Science and Technology*, 2017.

[79] R Zheng, J -P Lin, P -C Wang, and Y -R Wu, "Effect of hot-humid exposure on static strength of adhesive-bonded aluminium alloys," *Defence Technology*, vol. 11, pp. 220-228, 2015.

[80] J Weiss et al., "Ageing mechanisms of polyurethane adhesive/steel interfaces," *International Journal of Adhesion & Adhesives*, vol. 70, pp. 167-175, 2016.

[81] A H Korayem et al., "Failure of CFRP-to-steel duble strap joint bonded using carbon nanotubes modified epoxy adhesive at moderately elevated temepratures," *Composites Part B*, vol. 94, pp. 95-101, 2016.

[82] M A G Silva and H Biscaia, "Degradation of bond between FRP and RC beams," *Composite Structures*, vol. 85, pp. 164-174, 2008.

[83] F I Soykok, "Degradation of single lap adhesively bonded composite joints due to hot water ageing," *Journal of Adhesion*, vol. 93, no. 5, pp. 357-374, 2017.

[84] Z Abdo and H Aglan, "Analysis of aircraf adhesive joints under combined thermal and mechanical loads," *Journal of Adhesion Science and Technology*, vol. 11, no. 7, pp. 941-956, 1997.

[85] A Al-Ostaz, P R Mantena, M Anakapalli, and S J Hwang, "Evaluation of high-performance pressure-sensitive adhesives and VHB acrylic foam tapes bonded aluminium joints subjected to environmental aging," *Journal of Adhesion Science and Technology*, vol. 21, no. 3-4, pp. 339-361, 2007.

[86] F Stazi, M Giampoli, M Rossi, and P Munafo, "Environmental ageing on GFRP pultruded joints: Comparison between different adhesives," *Composite Structures*, vol. 133, pp. 404-414, 2015.

[87] P Liu, L Cheng, and Y W Zhang, "Measuring interface properties and toughness - A computational study," *Acta Materialia*, vol. 49, pp. 817-825, 20001.

[88] N Badwe, R Mahajan, and K Sieradzki, "Interfacial fracture strength and toughness of copper/epoxy-resin interfaces," *Acta Materialia*, vol. 103, pp. 512-518, 2016.

[89] K Vine, P Cawley, and A J Kinloch, "Comparison of normal and oblique incidence ultrasonic measurements for the detection of environmental degradation of adhesive joints," *NDT&E Internationsl*, vol. 35, no. 4, pp. 241-253, 2002.

[90] S I Rokhlin, W Wang, B Xie, V A Yakolev, and L Adler, "Modulated angle beam ultrasonic spectroscopy for evaluation of imperfect interfaces and adhesive bonds," *Ultrasonics*, vol. 42, no. 1, pp. 1037-1047, 2004.

[91] P Mylavarapu and E Woldesenbet, "Non-destructive characterisation of bondlines in composite adhesive joints," *Journal of Adhesion Science and Technology*, vol. 20, no. 7, pp. 647-660, 2006.

[92] W Wang and S I Rokhlin, "Evaluation of interfacial properties in adhesive joints of aluminium alloys using angle-beam ultrasonic spectroscopy," *Journal of Adhesion Science and Technology*, vol. 5, no. 8, pp. 647-666, 1991.

[93] S -C Her and Y -C Lin, "Assessment of adhesive bond strength using the ultrasonic scanning," *Journal of Adhesion*, vol. 90, pp. 545-554, 2014.

[94] Kumar R L V, M R Bhat, and C R L Murthy, "Evaluation of kissing bond in composite adhesive lap joints using digital image correlation: Preliminary studies," *International Journal of Adhesion & Adhesives*, vol. 42, pp. 60-68, 2013.

[95] X Ma, K Bian, J -Y Lu, and K Xiong, "Experimental research on detection for interface debond of CFRP T-joiuns under tensile load," *Composite Structures*, vol. 158, pp. 359-368, 2016.

[96] Kumar R L V, M R Bhat, and C R L Murthy, "Some studies on evaluation of degradation in composite adhesive joints using ultrasonic techniques," *Ultrasonics*, vol. 53, pp. 1150-1162, 2013.

[97] R C Tighe, J M Dulieu-Barton, and S Quinn, "Identification of kissing defects in adhesive bonds using infrared thermography," *International Journal of Adhesion & Adhesives*, vol. 64, pp. 168-178, 2016.

[98] M Santos and J Perdigao, "Leaky lamb wave for the detection and sizing of defects in bonded aluminium lap joints," *NDT&E International*, vol. 38, pp. 561-568, 2005.

[99] R Tamborino et al., "Assessment of the efefct of defects on mechanical properties of adhesive bonded joints by using non destructive methods," *Composites Part B*, vol. 91, pp. 337-345, 2016.

[100] S I Rokhlin and M Rosen, "An ultrasonic method for the evaluation of interface elastic properties," *Thin Solid Films*, vol. 89, no. 2, pp. 143-148, 1982.

[101] S V Teles and D E Chimenti, "closed disbond detection in marine glass-epoxy/balsa composites," *NDT&E International*, vol. 41, no. 2, pp. 129-136, 2008.

[102] J Yu, P Ziehl, B Zarate, and J Caicedo, "Prediction of fatigue crack growth in steel bridge components using acoustic emission," *Journal of Constructional Steel Research*, vol. 67, no. 8, pp. 1254-1260, 2011.

[103] R Hill, "The use of acoustic emission for characterising adhesive joint failure," *NDT International*, pp. 63-72, 1977.

[104] G J Curtis, "Acouatic emission energy relates to bond strength," *Non-Destructive testing*, pp. 249-257, 1975.

[105] Y A Dzenis and I Saunders, "On the possibility of discrimination of mixed mode fracture mechanisms in adhesive composite joints by advanced acoustic emission analysis," *International Journal of Fracture*, vol. 117, pp. L23-L28, 2002.

[106] S Tanary, Y M Haddad, A Fahr, and S Lee, "Nondestructive evaluation of adhesively bonded joints in graphite/epoxy composites using acousto-ultrasonics," *Journal of Pressure Vessel Technology*, vol. 114, pp. 344-352, 1992.

[107] Z Chen, D Li, Y Li, and Q Feng, "Damage analysis of CFRP/steel composite plates using acoustic emission," *Pacific Science Review*, vol. 16, pp. 193-200, 2014.

[108] C Santulli and A C Lucia, "Relation between acoustic emission analysis during cure cycle and bonded joints performance," *NDT&E International*, vol. 32, pp. 333-341, 1999.

[109] A G Magalhaes and M F S F de Moura, "Application of acoustic emission to study creep behaviour of composite bonded lap shear joints," *NDT&E International*, vol. 38, pp. 45-52, 2005.

[110] E F Karachalios, R D Adams, and L F M Da Silva, "Single lap joints loaded in tension with ductile steel adherends," *International Journal of Adhesion & Adhesives*, vol. 43, pp. 96-108, 2013.

[111] L Liao, T Sawa, and C Huang, "Experimental and FEM studies on mechanical properties of single-lap adhesive joint with dissimilar adherends subjected to impact tensile loadings," *International Journal of Adhesion & Adhesives*, vol. 44, pp. 91-98, 2013.

[112] H Nakano, Y Omiya, Y Sekiguchi, and T Sawa, "Three dimensional FEm stress analysis and strength prediciton of scarf adhesive joints with similar adherends subjected to static tensile loadings," *International Journal of Adhesion & Adhesives*, vol. 54, pp. 40-50, 2014.

[113] A Leski, "Implementation of the virtual crack closure technique in engineering FE calculations," *Finite Elements in Analysis and Design*, vol. 43, pp. 261-268, 2007.

[114] P A Gustafson and A M Waas, "The influence of adhesive constitutive parameters in cohesive zone finite element models of adhesively bonded joints," *International Journal of Solids and Structures*, vol. 46, pp. 2201-2215, 2009.

[115] R Dimitri, M Trullo, L De Lorenzis, and G Zavarise, "Coupled cohesive zone models for mixed-mode fracture: A comparative study," *Engineering Fracture Mechanics*, vol. 148, pp. 145-179, 2015.

[116] Z Mohammadi, A A Z -Moayyed, and S -M A. Mesgar, "Adhesive and cohesive properties by indentation method of plasma-sprayed hydroxyapatite coatings," *Applied Surface Science*, vol. 253, pp. 4960-4965, 2007.

[117] J Y Cognard, "Numerical analysis of edge effects in adhesively-bonded assemblies application to the determination of the adhesive behaviour," *Computers & Structures*, vol. 86, pp. 1704-1717, 2008.

[118] L Liao, T Sawa, and C Huang, "Numernical analysis on load-bearing capacity and damage of double scarf adhesive joints subjected to combined loadings of tension and bending," *International Journal of Adhesion & Adhesives*, vol. 53, pp. 65-71, 2014.

[119] H J Park, H J Choi, and H J Kweon, "Evaluating the strengths of thick aluminium-to-aluminium joints with different lengths and thicknesses," *Composite Structures*, vol. 92, no. 9, pp. 2226-2235, 2010.

[120] T Sawa, K Ichikawa, Y Shin, and T Kobayashi, "A three-dimensional finite element stress analysis and strength prediction of stepped-lap adhesive joints of dissimilar adherends subjected to bending moments," *International Journal of Adhesion & Adhesives*, vol. 30, pp. 298-305, 2010.

[121] ASTM D6272-17, "Standard test method for flexural properties of unreinforced and reinforced plastics and electrical insulating materials by four-point bending".

[122] W C Cui and M R Wisnom, "Contact finite element analysis of three- and four point short-beam bending of unidirectional composites," *Composites Science and Technology*, vol. 45, pp. 323-334, 1992.

[123] M Xie and D F Adams, "Study of three- and four-point shear testing of unidirectional composite materials," *Composites*, vol. 26, pp. 653-659, 1995.

[124] A B De Morais and A B Pereira, "Mode II interlaminar fracture of carbon/epoxy laminates using four-point bending plate test," *Composites: Part A*, vol. 40, pp. 1741-1746, 2009.

[125] M Kharrat, A. Chateauminois, L Carpentier, and P Kapsa, "On the interfacial behaviour of glass/epoxy composite during a micro-indentation test: assessment of interfacial shear strength using reduced indentation curves," *Composites Part A*, vol. 28, pp. 39-46, 1997.

[126] C She, Y W Zhang, and K Y Zeng, "A three-dimensional finite element analysis of interface delamination in a ductile film/hard substrate system induced by wedge indentation," *Engineering Fracture Mechanics*, vol. 76, pp. 2272-2280, 2009.

[127] M Castaings, "SH ultrasonic guided waves for teh evaluation of interface adhesion," *Ultrasonics*, vol. 54, pp. 1760-1775, 2014.

[128] Y Xu, R Chen, Z Liu, and C Shao, "An acousto-optical fiber NDE technique for interfacial debonding detection in FRP-retrofitted structures," *NDT&E International*, vol. 72, pp. 50-57, 2015.

[129] H Yuan and X Li, "Effects of cohesive law on ductile crack propagation simulation by using cohesive zone models," *Engineering Fracture Mechanics*, vol. 126, pp. 1-11, 2014.

[130] M F S F De Moura, J P M Goncalves, J A G Chousal, and R.D.S.G. Campilho, "Cohesive and continuum mixed-mode damage models applied to the simulation of the mechanical behaviour of bonded joints," *International Journal of Adhesion & Adhesives*, vol. 28, pp. 419-426, 2008.

[131] ASTM D1002, Apparent shear strength of single-lap adhesively bonded metal specimens by tension loading (Metal-to-Metal).

[132] E Sancaktar and U Karmarkar, "Mechanical behaviour of interlocking multi-stepped double scarf adhesive joints including void and disbond effects," *International Journal of Adhesion & Adhesives*, vol. 53, pp. 44-56, 2014.

[133] A Higgins, "Adhesive bonding of aircraft structures," *International Journal of Adhesion & Adhesives*, vol. 20, no. 5, pp. 367-376, 2000.

[134] E Siriyabe, M Renier, A Meziane, and M Castaings, "The transmission of lamb waves across adhesively bonded lap joints to evaluate interfacial adhesive properties," in *International Congress on Ultrasonics*, vol. 70, 2015, pp. 541-544.

[135] T Kundu, A Maji, T Ghosh, and K Maslov, "Detection of kissing bonds by lamb waves," *Ultrasonics*, vol. 35, no. 8, pp. 573-580, 1998.

[136] A Vary and K J Bowles, "An ultrasonic-acoustic technique for nondestructive evaluation of fiber composite quality," *Polymer Science and Engineering*, vol. 19, no. 5, pp. 373-376, 1979.

[137] J H Williams Jr and N R Lampert, "Ultrasonic evaluation of impact-damaged graphite fiber composite," *Materials Evaluation*, vol. 38, pp. 68-72, 1980.

[138] A Chadegani and R C Batra, "Analysis of adhesive-bonded single-lap joint with an interfacial crack and a void," *International Journal of Adhesion & Adhesives*, vol. 31, pp. 455-465, 2011.

[139] K S Madhusudhana and R Narasimhan, "Experimental and numerical investigations of mixed mode crack growth resistance of a ductile adhesive joint," *Engineering Fracture Mechanics*, vol. 69, pp. 865-883, 2002.

[140] M Y, M Chiang and H Chai, "Plastic deformation analysis of cracked adhesive bonds loaded in shear," *International Journal of Solids and Structures*, vol. 31, no. 18, pp. 2477-2490, 1994.

[141] M A Hamstad, "Acoustic emission signals generated by monopole (pencil-lead break) versus dipole sources: finite element modelling and experiments," *Journal of Acoustic Emission*, vol. 25, pp. 92-106, 2007.

[142] M R Gorman and W H Prosser, "AE source orientation by plate wave analysis," *Journal of Acoustic Emission*, vol. 9, no. 4, pp. 283-288, 1991.

[143] P J de Groot, P A M Wijnen, and R B F Janssen, "Real-time frequency determination of acoustic emission for different fracture mechanisms in carbon/epoxy composites," *Composites Science and Technology*, vol. 55, pp. 405-412, 1995.

[144] P Alander, L V J Lassila, A Tezvergil, and P K Vallittu, "Acoustic emission analysis of fiber-reinforced composite in flexural testing," *Dental Materials*, vol. 20, pp. 305-312, 2004.

[145] M G R Sause, A Gribov, A R Unwin, and S Horn, "Pattern recognition approach to identfy natural clusters of acoustic emission signals," *Pattern Recognition Letters*, vol. 33, pp. 17-23, 2012.